The role of pectin metabolism in the control of cell wall pH and rheology

Fan Xu

université PARIS-SACLAY

NNT : 2019SACLS019

UNIVERSITÉ PARIS SUD
Comprendre le monde, construire l'avenir

Le rôle du métabolisme des pectines dans le contrôle du pH et de la rhéologie de la paroi

Thèse de doctorat de l'Université Paris-Saclay
préparée à l'Université Paris-Sud

École doctorale n°567 Sciences du Végétal : du gène à l'écosystème (SDV)
Spécialité de doctorat : Biologie

Thèse présentée et soutenue à Versailles, le 15/01/2019, par

Fan Xu

Composition du Jury :

Sébastien Thomine Directeur de recherche,	Université de Paris-Saclay	Président
Nadine Paris Directrice de recherche,	Université de Montpellier	Rapporteur
Kris Vissenberg Professeur,	Université de Antwerp	Rapporteur
Valérie Lefebvre Maître de conférence,	Université de Picardie Jules Verne	Examinateur
Herman Höfte Directeur de recherche,	INRA (IJPB, Versailles)	Directeur de thèse

Thèse de doctorat

Acknowledgements

I would like to convey my gratitude to all those who made this thesis possible, contributed to the build-up of my scientific personality and also to those who made my days unforgettable during PhD.

My deepest gratitude is to my supervisor, Dr Herman Höfte, who gives me an opportunity to study in Primary Cell Wall group. Your guidance and stimulating interest of science are of great importance in my scientific career. Your encouragement, energetic, personality and enthusiasm stimulated me to improve my scientific background and also to enjoy my research output. I have learned a lot from you and realize how kind and generous you've been teacher and supervisor. I have really enjoyed working with you.

I thank all the members of the Primary Cell Wall group for their friendly support and discussion in lab meeting. I especially thank Julien Renou for help in both life and work. You were always patient for my questions. Your help lets me rapidly get used to new culture in France and working environment in INRA Versailles. I thank Marjorlaine Martin and Thierry Desprez for teaching me many experiments that allowed me to work independently during my PhD. I thank Martine Gonneau and Samantha Vernhettes for expert assistance and constructive comments on my works. I thank Fabien Miart for teaching my many imaging techniques and for discussion about my experiment in details. I really appreciated the sound advice and critical comments from Tian, Aline, Veronica, and Ying. I learned a lot while working with all of you.

This thesis would not have been possible were it not for collaboration with the Biologie des plantes et Innovation group in Universite de Picardie, Amiens. My visits allowed me to make important progress at critical times of my project. I especially thank Olivier Habrylo for teaching protein expression in yeast, Fabien Sénéchal for Microscale thermophoresis and Jerome Pelloux for giving me the opportunity and valuable advice.

I thank the jury members who have accepted to evaluate this thesis. I thank reviewers Nadine Paris and Kris Vissenberg and examiners Sébastien Thomine and Valérie Lefebvre. I thank members of my thesis committee: Sebastian Wolf, Kian Hématy, Jeffrey Leung and Estelle Bonnin, who followed my work for three years. Your suggestions and comments are useful for my thesis.

I would like to acknowledge many colleagues in INRA Versailles: Magelie Uyttewaal, Katia Belcram, Gwendal Cueff, David Bouchez, Taline Elmaya, Ivan Le Masson, Véronique Pautot, Phillipe Le Bris, Aurelie Hurel and Olivier Grandjean, for technical favor.

I cherished the moments with my friends: Chuande, Qinwu, Jie, Jing, Zeyun, Yannick, Claudia, Federica, Laia, Kostlend, Samantha, Fadi, Olivier, Nicolas, Camille, with whom I celebrated dinners, birthday parties, graduation ceremonies and many more. Thank you for making life in France feel more like home.

I am greatly thankful to the China Scholarship Council, for funding me to pursue my scientific dream. I also thank Institut Jean-Pierre Bourgin, INRA Versailles and University of Paris Sud for hosting me.

My deepest gratitude goes to my family without whom I have nothing. Without the encouragement and support from my family, it would be impossible to finish my PhD. My grandmother, mother and wife are important for PhD and all my life. My grandmother gives me the courage to study abroad and pursue what I really like although it is hard. My mother warmly gives me lots of positive energy and teaches me to be genius and kind. My wife accompanied with me during the PhD and always encourage me whenever I need. Thank you for your love, understanding, and endless patience. I love you all beyond words.

Abbreviations

A, C, G, T	Adenine, cytosine, guanine, thymine
AFM	Atomic force microscopy
AHA2	Plasma membrane H^+-ATPase 2
APAP1	ARABINOXYLAN PECTIN ARABINOGALACTAN PROTEIN1
ATP	Adenosine triphosphate
BSA	Bovine serum albumin
BR	Brassinosteroid
CAX	Ca^{2+}/H^+ antiporters
cDNA	complementary DNA
Col-0	Columbia-0 Arabidopsis accession
CrRLK1L	*Catharanthus roseus* RLK1-like
Ct	Cycle threshold
DB	Degree of blockiness
DEX	Dexamethasone
DNA	Deoxyribonucleic acid
DZ	Differentiation zone
EGCG	(−)-epigallocatechin gallate
EGFP	Enhanced GFP
et al.	and others
EZ	Elongation zone
FER	FERONIA
FRET	Förster resonance energy transfer
GalA	Galacturonic acid
GDA	Gel diffusion assay
GFP	Green fluorescent protein

HDM	High degree of methylesterification
HG	Homogalacturonan
HG^{HDM}	Homogalacturonan in high degree of methylesterification
HG^{LDM}	Homogalacturonan in low degree of methylesterification
HPTS	8-hydroxypyrene-1, 3, 6-trisulfonic acid trisodium salt
K_d	Dissociation constant
LDM	Low degree of methylesterification
LRX	LEUCINE-RICH REPEAT EXTENSIN
mRFP1	Monomeric red FP
MS	Mass spectrometry
MS medium	Murashige and Skoog medium
MST	Microscale thermophoresis
MT	Meristem
NADPH	Nicotinamide adenine dinucleotide phosphate
PCR	Polymerase chain reaction
pH^{apo}	Apoplastic pH
PM	plasma membrane
PME	Pectin methylesterase
PMEI	Pectin methylesterase inhibitor
PMF	Proton motive force
PT	Pollen tube
QC	Quiescent center
RALF	Rapid Alkalinization Factor
RG-I and -II	Rhamnogalacturonans -I and-II
RH	Root hair
RNA	Ribonucleic acid

ROI	Regions of interest
rpm	Revolution per minute
RT-PCR	Reverse transcriptase polymerase chain reaction
Tm	Melting temperature
TMD	Transmembrane domain
TZ	Transition zone
v/v	volume per volume
WB	Western Blotting
w/v	Weight per Volume
w/w	Weight per Weight
XG	Xyloglucan
$\Delta\psi$	Electrostatic potential difference

Contents

List of Figures

List of Tables

Chapter 1 Introduction

1.1. Primary cell wall

Plant cells are surrounded by strong cell walls, which allow turgor pressure to be built up, determine cell and organ shape and provide protection against biotic stresses. Cell walls also must be able to expand to allow growth (Cosgrove 2005; Hofte and Voxeur 2017). How cell walls are modified to enable cellular expansion, while maintaining their integrity remains an important and fascinating scientific question.

The dual function of walls of growing cells (so-called primary walls) relies on the formation of reinforced gel structures consisting of cellulosic microfibrils, connected to matrix phase that consists mainly of hemicellulose and pectins (Somerville et al. 2004; Burton et al. 2010). Cellulose microfibrils with their extreme tensile strength are the main load-bearing elements of the cell wall. They are composed of β-1,4-linked glucose, and are synthesized by cellulose synthase complexes embedded in the plasma membrane (PM) (Somerville et al. 2004). Hemicellulose and pectin are synthesized in the Golgi apparatus and then secreted into the apoplast (Figure 1.1). Primary cell walls also contain a small amount (10%) of proteins, which can connect to the polysaccharides network and can modify the wall structure during development and in reaction to diverse environmental changes.

An important challenge is to understand how the cell wall extensibility is regulated. Recent studies showed that cell wall loosening agents target the load-bearing cellulose-xyloglucan interaction sites, also called ‘biomechanical hotspots’, to regulate cell wall loosening (Cosgrove 2014 and 2015). Although some evidence suggested that pectin also has a load-bearing role in expanding cells, this point remained controversial. In this Introduction, I will provide an update of the literature on the link between pectin modification and cell wall loosening, with a focus on the contradictions and challenges presented in these studies, and discuss evidence showing how pectin metabolism is intimately linked to the pH and the rheology of the cell wall.

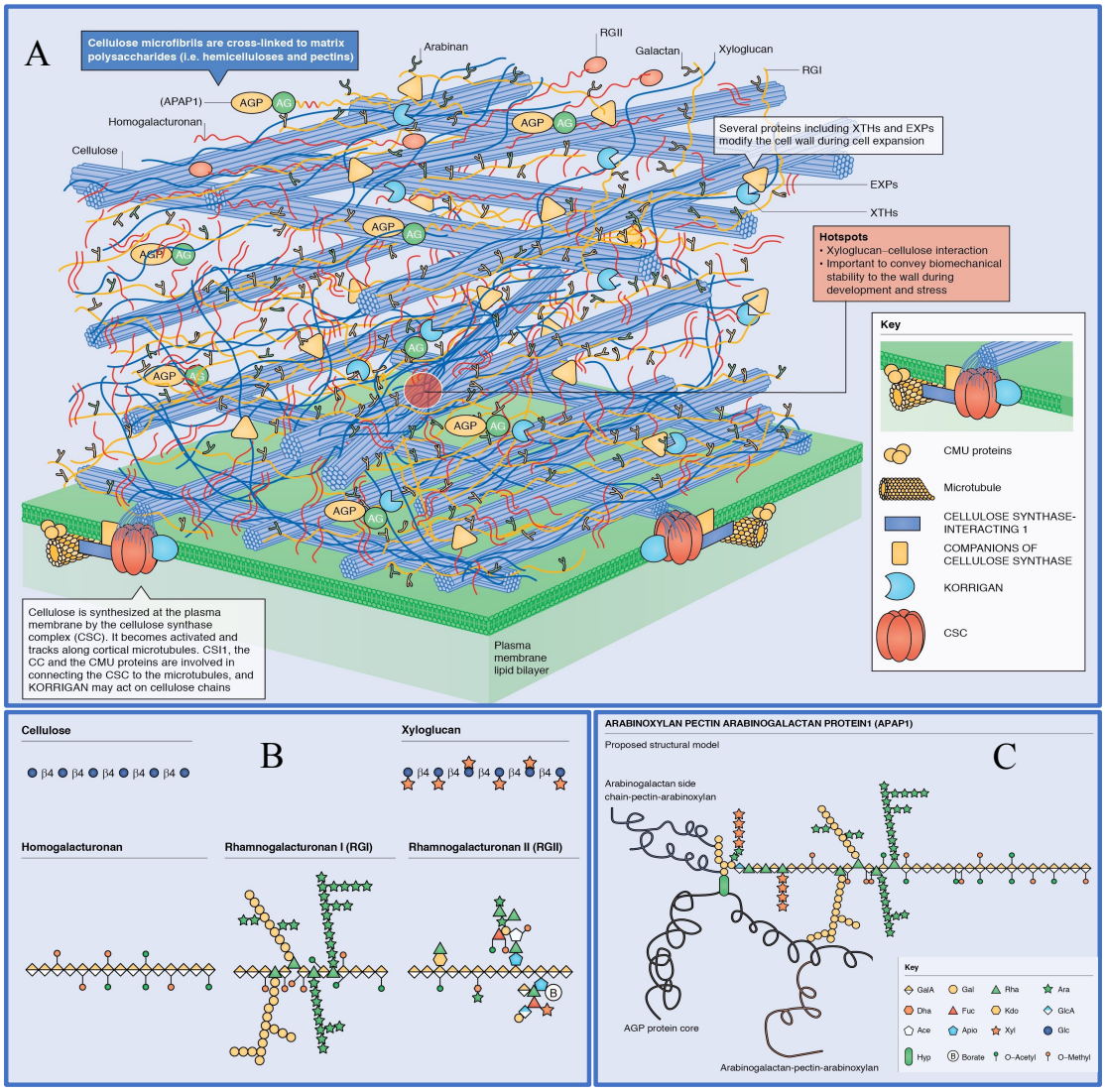

Figure 1.1: Model of primary cell wall (A) and structure of cell wall polysaccharides (B) and proteoglycan APAP1 (C). Modified from (Lampugnani et al. 2018)

1.2. Pectins and homogalacturonan modification

Pectins influence various cell wall properties such as porosity, surface charge, pH, and ion balance by forming networks and trapping solute molecules (Harholt et al. 2010). Pectins are block co-polymers, characterized by the presence of galacturonic acid (GalA). They represent up to 40% of the dry mass in primary cell walls of dicots. Three types of pectin polymers can be distinguished: homogalacturonan (HG), rhamnogalacturonans (RG)-I and RG-II (Figure 1.1). HG is the most abundant form, representing around 20% of the dry cell wall in *Arabidopsis* leaves (Zablackis et al. 1995).

1.2.1 HG synthesis and secretion

The main steps of HG synthesis include polymerization, methylesterification and acetylation, all of which occur in the Golgi apparatus (Caffall and Mohnen 2009; Wolf et al. 2009). The HG backbone is a polymer of alpha-1, 4-linked GalA residues, which is synthesized from the nucleotide-sugar precursor, UDP-D-GalA, which is in turn synthesized from UDP-D-Glucose via a UDP-D-GlcA intermediate. Galacturonosyltransferases (GAUTs) specifically catalyze the transfer of D-GalA from UDP-D-GalA to the non-reducing end of a growing stretch of HG via a luminally facing GAUT catalytic domain, in the *cis*-Golgi (Sterling et al. 2001). So far, GalA transferase activity has been confirmed *in vitro* for GAUT1 and GAUT4 (Sterling et al. 2001; Biswal et al. 2018). Two polypeptides of GAUT1 bind to one polypeptide of GAUT7, and this heterocomplex is responsible for retaining GAUT1 in the Golgi membranes (Atmodjo et al. 2011). In the medial-Golgi, the HG backbone is methylesterified at the C6 position by pectin methyl transferase (PMT), which transfers a methyl group from S-adenosyl methionine. The *QUASIMODO-2/TUMOROUS SHOOT DEVELOPMENT-2 (QUA2/TSD2)* has been proposed to a pectin

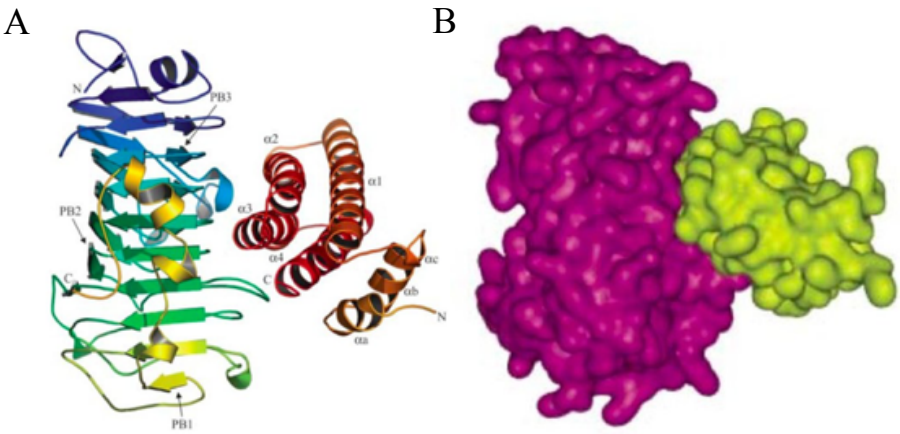

Figure 1.2: Structure of the PME-PMEI complex. (A) Ribbon representation illustrating the relative positions of PMEI and PME in the complex. PME is shown in green-blue on the left side. PMEI is represented in yellow-red on the right side; the α -helices of the four-helix bundle are indicated as α1 to α4, whereas helices of the N-terminal region are named αa, αb, and αc. (B) Molecular surface of the PME-PMEI complex. Representation of the molecular surface of PME (violet) and PMEI (yellow) in the complex. Modified from (Di Matteo et al. 2005).

methyltransferase (Krupkova et al. 2007; Mouille et al. 2007). The *qua2* mutant showed a phenotype similar to that of *qua1*, another putative HG GAUT, including a 50% reduction in HG content. The latter suggests that the methylesterification of HG is a critical step for the GAUT-catalyzed polymerization reaction. Another family of HG methylesterases is encoded by cotton Golgi-related (CGR) 2/3 (Kim et al. 2015). It is interesting to note that non-methylesterified HG accumulated in a double *cgr 2/3* mutant in contrast to *qua2*, which had reduced HG levels without a change in the degree of methylesterification (DM). The reason for this difference is not known but it is possible that GAUTs and CGRs synthesize HG in the context of different polymers. Alternatively, the HG produced in *cgr 2/3* may be more prone to HG demethylesterification in the cell wall for some unknown reason. The acetylation of HG is catalyzed by pectin O-acetyltransferase (PAT), which transfers an acetyl group from acetyl CoA to a HG acceptor. Acetyl groups can decorate the GalA residues of HG at the O-2 or O-3 positions (Ishii 1997).

The secretion process of HG remains poorly understood. HG has been clearly shown to localize in vesicular structures using immunoelectron microscopy (Kim and Brandizzi 2014). HG-specific antibody labeling revealed a non-uniform distribution of HG in pea parenchyma cells (Willats et al. 2001) as well as *Nicotiana tabacum* and *Solanum chacoense* pollen tubes (PTs) (Bosch and Hepler 2005; Parre and Geitmann 2005). This supports the existence of a mechanism for localized HG secretion to the cell wall, or the concentration of HG in specific cell wall regions *in muro* after secretion. An example of directional pectin secretion is observed during the deposition of *Arabidopsis* seed coat mucilage, which is mainly composed of RG-I, whereas HG is deposited specifically at the outward facing cell walls, through polarized secretion (Haughn and Western 2012). The trans-Golgi network-localized ECHIDNA/YIP4a and 4b protein complex is required for correctly localized secretion of cell wall polysaccharides, including HG, in the *Arabidopsis* seed coat cells (Gendre et al. 2013). The *echidna*

mutant shows a highly reduced accumulation of mucilage in the cell walls of the seed coat, but mucilage can be detected in the vacuole, highlighting the importance of a strict cellular control of cell wall secretion (McFarlane et al. 2013).

1.2.2 HG demethylesterification

Upon secretion, HG can be selectively demethylesterified *in muro* by pectin methylesterases (PMEs) (Pelloux et al. 2007). PMEs are essential for the gelling behavior of pectins and the rheology (see below) of the cell wall. PMEs are encoded by large multigene families (e.g. 69 members in *Arabidopsis*). They are classified into two groups based on the presence (type I) and absence (type II) of a PRO domain, which shares similarities with the PME inhibitor (PMEI) domain (Pelloux et al. 2007). For type I PMEs, two conserved cleavage motifs were identified between PRO and PME domains, which can be cleaved in a secretory compartment by AtS1P, a subtilisin-like protease (Wolf et al. 2009). The 3D crystallographic structure of plant PME shows that mature PME has three parallel right-handed β-sheets. The pectin-binding cleft is formed by two loops that are composed of aromatic residues (Figure 1.2, Di Matteo et al. 2005; Pelloux et al. 2007).

Most plant PMEs studied so far are processive, remove methylester groups from stretches of GalA residues, resulting in a blockwise distribution of methylester groups, whereas fungal PMEs are mostly non-processive, they dissociate from the substrate after each enzymatic reaction, leading to random demethylesterification patterns. The terms “blockiness” (Degree of blockiness (DB)) defines the ratio of contiguous free GalA units relative to the total amount of free GalA residues in the HG. This value is calculated from the amount of monomer, dimer, and trimer of GalA, produced when pectin is incubated with endopolygalacturonase, divided by the total amount of GalA present in the pectin sample (Daas et al. 2009). The processivity of the plant PMEs, however, can be influenced by the reaction conditions. For instance, in high pectin concentrations and in the presence of Ca^{2+}, a processive PME can become non-

processive (Vincent and Williams 2009).

In many developmental processes, PMEs are regulated by either differential transcription or posttranslational control by protein inhibitors (PMEIs). In *Arabidopsis*, 76 genes have been annotated as encoding putative PMEIs. PMEIs inhibit plant PMEs through interaction in a complex of 1:1 stoichiometry, in which PMEI covers the pectin-binding cleft of PME and hides its putative catalytic site, thereby impairing access to the substrate (Di Matteo et al. 2005). The structure of the PME-PMEI complex is shown in Figure 1.2. Until now, 14 PMEIs have been functionally analyzed and shown to play different functions in *Arabidopsis* growth and development (Table.1.1).

1.2.3 Pectin network and connections to cellulose, hemicellulose and proteins

HG is found in a variety of cell wall fractions, from water- or chelator-soluble, alkaline extractable to strongly cellulose-associated fractions (Caffall and Mohnen 2009). This most likely reflects the methylesterification pattern and the covalent association of HG with the other pectic polymers RG-I and RG-II (Vincken et al. 2003; Atmodjo et al. 2013; Popper and Fry 2005) and proteoglycans (Caffall and Mohnen 2009), which in turn can form covalent and non-covalent cross-links with other cell wall polymers. RG-II can form dimers via borate diester linkages. More than 95% of RG-II exists as dimers, which determine strength and pore size of the cell wall and are essential for cell wall integrity as shown by the disorganized walls in plants starved for boron and the lethality of mutants lacking RG-II dimers. RG-I can bind to cellulose *in vitro* through its arabinan, galactan or xylan side chains and close pectin-cellulose interactions have been observed in intact, never-dried cell walls using NMR. HG also interacts with xyloglucan (XG) as shown by the release of XG fragments from the cell wall by endo-polygalacturonase treatment, but no covalent crosslinks between the two polymers have been observed so far (Talmadge et al. 1973; Popper and Fry 2005). XG strongly binds to cellulose *in vitro* and cellulose-XG-cellulose connections are observed in intact cell walls. The latter form the so-called biomechanical hotspots, which are thought to be the

targets of specialized microbial endoglucanases and expansins, which can promote wall "creep" at low pH in extensibility tests (Cosgrove 2014 and 2015). An alternative way to crosslink pectins to other cell wall polymers is via structural proteins of the cell walls. Structural proteins make up 2 ~ 10% of wall dry weight (O'Neill et al. 2003) and are classified into four groups. Three of them are named for their uniquely enriched amino acid: the hydroxyproline-rich glycoproteins (HRGPs), the proline-rich proteins (PRPs), and the glycine-rich proteins (GRPs). Arabinogalactan proteins (AGPs) form the fourth class. AGPs are more aptly named proteoglycans because they can be more than 95% carbohydrate (Buchanan et al. 2000). Recently, linkages between pectins and HRGPs and AGPs have been identified. Extensin is one of the best-studied HRGPs of plants, which consists of repeating Serine-$(Hydoxyproline)_4$ and Tyrosine-Lysine-Tyrosine sequences (Buchanan et al. 2000). Loss-of-function mutants for AtEXT3 are embryo lethal with incomplete cell plates, indicating the important role of extensins (Cannon et al. 2008). Pectin-extensin binding was suggested by an *in vitro* study on the physical properties of a thin film made by the successive adsorption of low methylesterifed pectin and extensin. It was observed that the positively charged extensins create an interpenetrating network with negatively charged pectin and that extensin promotes the dehydration and compaction of the pectin (Valentin et al. 2010). The discovery of the remarkable ARABINOXYLAN PECTIN ARABINOGALACTAN PROTEIN1 (APAP1) from the medium and cell walls of *Arabidopsis* cell cultures revealed pectin-AGPs linkages (Figure 1.1). APAP1 consists of an AGP backbone, which is linked to RG-I/HG through a rhamnosyl residue in the AG and with arabinoxylan attached either to a rhamnosyl residue in the RG-I domain or directly to the arabinosyl residue in the AG domain (Tan et al. 2013). The importance of APAP1 in the cell wall architecture is shown by the increased extractability of pectic polysaccharides in APAP1 mutants and the observation that more than 95% of RG-I released from cell walls of *Arabidopsis* suspension-cultured cells was covalently attached to APAP1 (Tan et al. 2013).

Table 1.1 Overview of characterized pectin methylesterase inhibitors (PMEIs) in *Arabidopsis*.

Gene name	Gene ID	Genotype	Expression pattern	Phenotype	DM*	Publication
PMEI1	AT1G48020	Overexpression 35S::PMEI1	Pollen	Increased root growth, promote resistance to the necrotrophic fungus *Botrytis cinerea*; expression restricted to pollen	Increase	Wolf et al.2003; Lionetti et al. 2007
PMEI2	AT3G17220	Overexpression 35S::PMEI2	Pollen, seed	Increase root growth, promote resistance to the necrotrophic fungus *Botrytis cinerea*; expression restricted to pollen; promote growth of tobacco pollen tubes	Increase	Wolf et al.2003; Lionetti et al.2007; Rockel et al.2008
PMEI3	AT5G20740	Overexpression pAlcA::PMEI3	Developing meristemoids zone, flower	Decreased primordia growth; perturbed phyllotaxis and organ initiation, increased stiffness, shorter cells	Decrease	Peaucelle et al. 2008, 2011 and 2015
PMEI4	AT4G25250	Overexpression 35S::PMEI4	Root, hypocotyl	Dark-grown hypocotyls, controls the initiation of the acceleration but not the growth process itself	Increase	Pelletier et al. 2010
PMEI5	AT2G31430	Overexpression pMDC7::PMEI5	Flower, bud, seed	Irregular root waving; faster seed germination, bigger seeds and bigger embryos; drastic reduction in dark-grown hypocotyl length, no reduced root length; overexpression promotes BR signaling	Increase	Wolf et al. 2012 and 2015; Muller et al. 2013; Levesque-Tremblay et al. 2015
PMEI6	AT2G47670	Mutant *pmei6* and Overexpression 35S::PMEI6	Stem, seed	*pmei6*: mucilage release was delayed and outer cell walls of epidermal cells did not fragment; 35S::PMEI6: increased labeling of cell wall fragments.	Decrease or increase resp.	Saez-Aguayo et al. 2013
PMEI7	AT4G25260	no mutant reported	Leaf, root, seed	Binding to PME3 is pH dependent	Increase	Senechal et al. 2015

PMEI8	AT3G17130	Overexpression on 35S::PMEI8 in *cob-6* background	Leaf, silique	Promote growth: partial suppression of the *cob-6* phenotype, PMEI8 is up-regulated in sfr6-3 when treated with isoxaben	Increase	Sorek et al. 2015
PMEI9	AT1G62770	Overexpression on 35S::PMEI9 in *cob-6* background	Root, shoot, hypocotyl	Inhibits growth: partial suppression of the cob-6 phenotype, PMEI9 is up-regulated in sfr6-3 when treated with isoxaben	Increase	Sorek et al. 2015
PMEI10	At1g62760	Mutant *pmei10*	Leaf, hypocotyl, silique	Less resistance to *B. cinerea.* no evident defects in rosette leaves, floral stems, flowers, seeds, and all developmental stages, Higher resistance to the necrotrophic fungus *B. cinerea*, a mediators of CW integrity maintenance in plant immunity	Decrease	Lionetti et al. 2017
PMEI11	At3g47380	mutant pmei11	Root, leaf	Higher resistance to the necrotrophic fungus *B. cinerea*, a mediators of CW integrity maintenance in plant immunity	Decrease	Lionetti et al. 2017
PMEI12	At5g46960	mutant pmei12	Seed, leaf, silique	Less resistance to *B. cinerea.* no evident defects in rosette leaves, floral stems, flowers, seeds, and all developmental stages, Higher resistance to the necrotrophic fungus *B. cinerea*, a mediators of CW integrity maintenance in plant immunity	Decrease	Lionetti et al. 2017
PMEI3	At5g62360	Overexpression on 35S::PMEI13	Seed, leaf, shoot apex	Less resistance to cold stress, more tolerance to salt stress, PMEI13-YFP localized on plasma membrane rather than cell wall. PMEI13 is expressed leaves, roots, developing siliques	Increase	Chen et al. 2018
PMEI14	At1g56100	Mutant *pmei14*	Seed, silique	Decrease seed mucilage, Similar to PMEI6, PMEI14 regulates seed coat mucilage and is target gene of MYB52 transcription factor.	Decrease	Shi et al. 2018

***DM: Degree of methylesterification**

In summary, in contrast to previous models in which cellulose-hemicellulose forms the load-bearing network embedded in, but independent from the pectin network, which primarily has a role in controlling the porosity of the cell wall, recent finding showed that pectic polysaccharides form one interconnected network with cellulose and hemicellulose and cell wall structural proteins in the walls through covalent and non-covalent linkages. As a result, the whole cell wall behaves as a fiber-reinforced hydrogel.

1.3. Pectin gels and rheology

1.3.1 Gels and phase transition

A gel is a form of matter intermediate between a solid and a liquid. It consists of polymers, or long-chain molecules, cross-linked to create a tangled network immersed in a liquid medium. The properties of the gel depend strongly on the interaction between polymers and liquid. Interestingly, around phase transition points, drastic changes in gel volume can be brought about by small changes in the external conditions. For example (Figure 1.3), the hydrophobicity of the medium, the pH, ionic strength, temperature or mechanical stresses can influence the gel volume and one can observe phase transition points were extremely small changes in any of these parameters induce abrupt volume changes. The gel volume appears to be governed by three forces that act to expand or shrink the polymer network: the rubber elasticity of the polymers, the polymer-polymer affinity and the hydrogen-ion pressure (Tanaka 1980). Interestingly, many biological gels are poised around such phase transitions, which provides a mechanism to render the associated responses exquisitely sensitive to small changes in the intra- or extra-cellular environment (Pollack 2001).

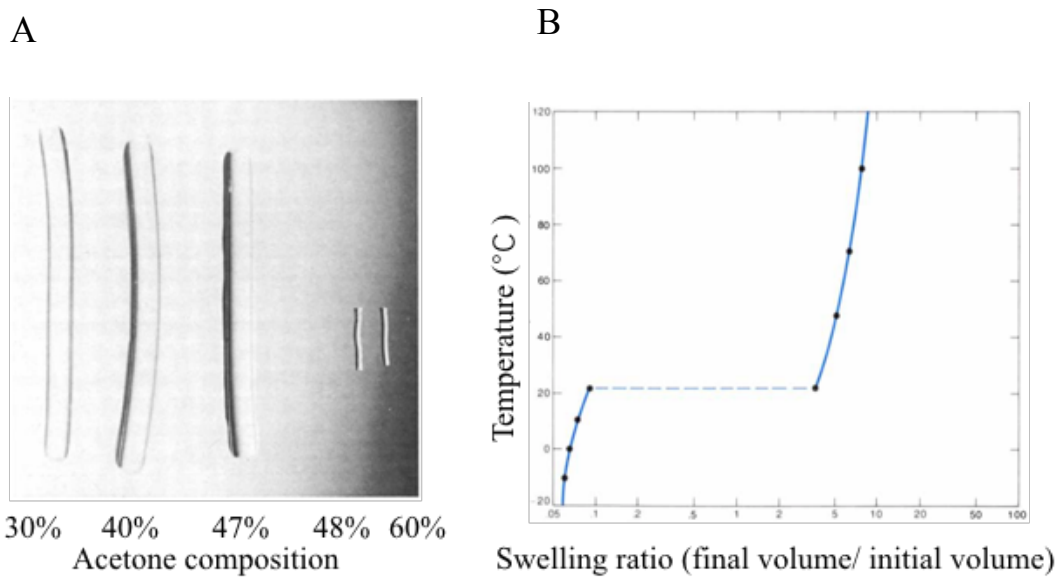

Figure 1.3: Gel phase transition (A) Acrylamide gel strips are incubated in a medium of increasing hydrophobicity (increasing aceton concentrations). The dramatic volume decrease between 47% and 48% aceton reflects a phase transition. (B) Small change in temperature elicits a phase transition in a gel in an acetone-water mixture of fixed composition. Modified from (Tanaka 1980).

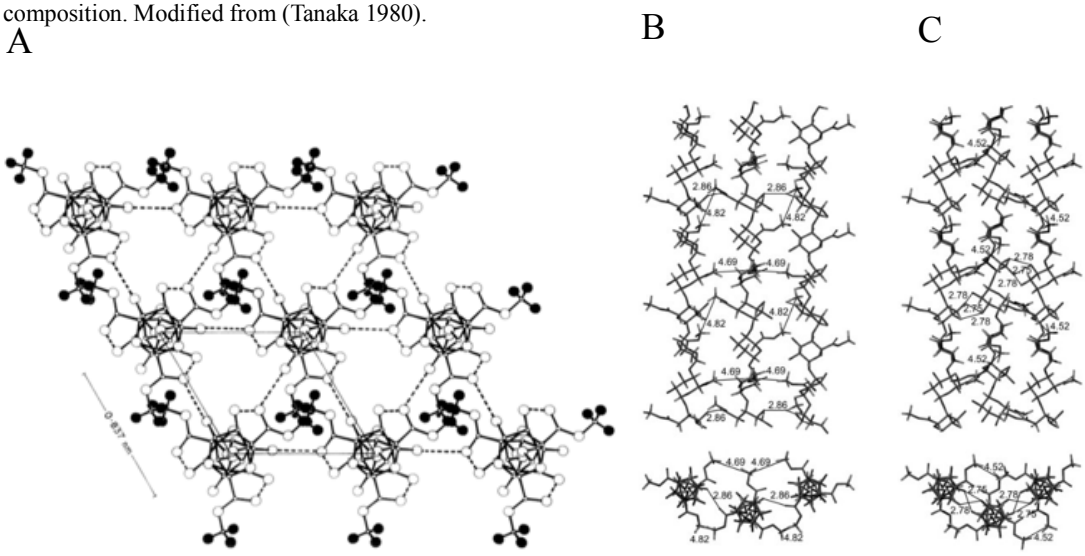

Figure 1.4: Model for methyl polygalacturonate structure. (A) Parallel chains are packed in a hexagonal lattice. (B) and (C) Best associations of three interacting methyl polygalacturonate chains for (B) parallel and (C) antiparallel arrangements. Distances are given in Å. For the sake of simplicity, the hydroxylic hydrogen atoms are not represented. Modified from (Walkinshaw and Arnott. 1981; Braccini et al. 2005).

1.3.2 Pectin gels and their properties

***In vitro*:** Pectins are typical gelling agents, traditionally used to make jams and jellies. Pectins also play a critical role *in planta* in the control of the hydration and the rheology of the cell wall (Parre and Geitmann 2005; Suárez et al. 2013; Willats et al. 2001). *In vitro* studies showed that pectin at low concentrations in water cannot gelate but forms a solution, because the pectin molecules are too far apart to interact with one another (Guimara et al. 2009). The viscosity of pectin solutions increases with increasing pectin concentration. When the pectin concentration exceeds a certain percentage (depending on other conditions), a hydrogel is formed consisting of a 3D network of polymer chains, that entraps solvent and solutes (Loh et al. 2014; Tanaka 1980).

Depending on the DM and the presence of Ca^{2+}, pectin gels can be classified into two types: Low DM (LDM, DM < 30%) and High DM (HDM, DM > 55%) gels (Figure 1.4 and 1.5).

HDM gel: To form a HDM gel, the pH has to be adjusted to below 3.5 and a large amount of co-solute has to be added. Two speculative structure models for HDM gel were established based on fiber diffraction studies (Walkinshaw and Arnott 1981; Braccini et al. 2005). In these models, the polygalacturonate chains forms a 3-fold helix with a rise per residue of 4.3 Å (Figure 1.4). Walkinshaw and Arnott. (1981) reported that HDM gels condensed into uniaxially oriented fibers and that the parallel arrangement of the chains provided the most efficient packing for the postulated net on the basis of theoretical calculations. One model of the junction zones in HDM gels is shown in Figure 1.4b. Braccini et al. (2005) instead, found that the antiparallel arrangement of methyl polygalacturonate chains is much more favorable than the parallel one, with nearly a 2-fold ratio between the interaction energies of the best associations, as shown in Figure 1.4c.

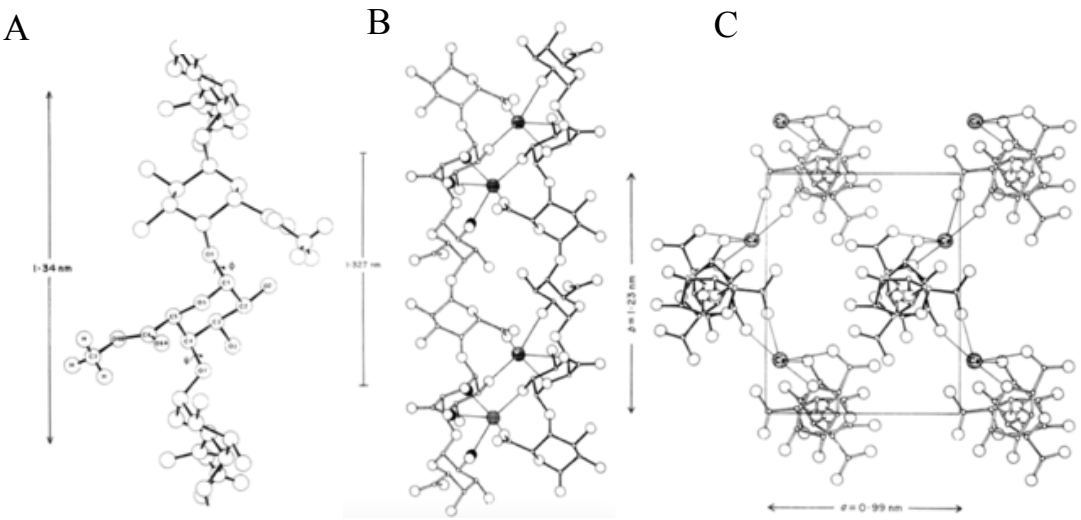

Figure 1.5: Model for methyl Ca^{2+}-pectate. (A) Molecular conformation of fully methylesterified HG showing atom labeling for the helical repeating unit. (B) The Ca^{2+} -pectate molecular conformation. Coordination of Ca^{2+} (striped circles) to polymer oxygen functions is denoted by thin unbroken lines. (C) The Ca^{2+}-pectate unit cell viewed parallel to the helix axis. Ca^{2+} coordination to the polyanion oxygen atoms is denoted by thin unbroken lines. At least 2 water molecules would be required to complete the Ca^{2+} coordination shells. Modified from (Walkinshaw and Arnott 1981).

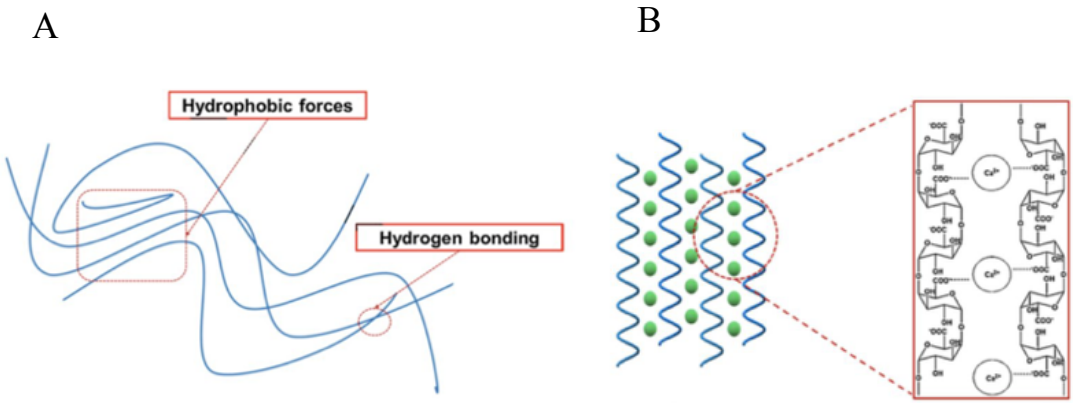

Figure 1.6: High degree-of-methylesterification (HDM) and LDM gelation. (A) HDM gelation is governed by intermolecular hydrogen bonds and hydrophobic interactions between methylesters. (B) LDM gelation mechanism is governed by ionic cross-linking via Ca^{2+} between two carboxyl groups from two different chains in close proximity. Modified from (Chan et al. 2017).

HDM gels are stabilized by intermolecular hydrogen bonds and hydrophobic bonds between methylesters (Figure 1.6). Hydrogen bonds between pectin molecules, favored by the conformation of adjacent GalA units, are the main interaction that sustains the HDM gel structure. Individual hydrogen bonds are relatively weak, but a large number of them confer significant thermodynamic stability to the gel. Hydrogen bonds only are insufficient to overcome the entropic barrier to gelation. HDM gels need the methylesters to coalescence, which can reduce the surface area exposed to water and therefore overall decrease the entropy of HG molecules. The contribution of hydrophobic interactions to the free energy of junction zones in HDM is half that arising from hydrogen bonding (Oakenfull and Scott 1984). An increase in hydrophobic interactions can make HDM more viscous (Guimara et al. 2009).

The conditions required for gelation and the properties of the gel ultimately depend on intrinsic and extrinsic factors. Intrinsic factors include the number and distribution pattern (the DB) of free carboxyl groups, the molecular weight and pectin concentration, while extrinsic factors include the types of other pectin polymers, co-solute concentration, ionic strength (Ca^{2+} concentration and pH), and temperature (Gigli et al. 2009). A high co-solute concentration, such as sucrose, promotes gelling through reducing water activity, which promotes chain-chain interactions (Thibault and Ralet 2003). An intermediate temperature range, from 10°C to 30°C can facilitate both hydrogen bonds and hydrophobic interactions (da Silva et al. 1995). Lowering the pH below the pKa of GalA (3.24) protonates carboxylic groups, reducing electrostatic repulsions along and between pectin chains and promotes the formation of inter- and intra-molecular hydrogen bonds between non-dissociated carboxylic and alcohol groups (Thakur et al. 1997).

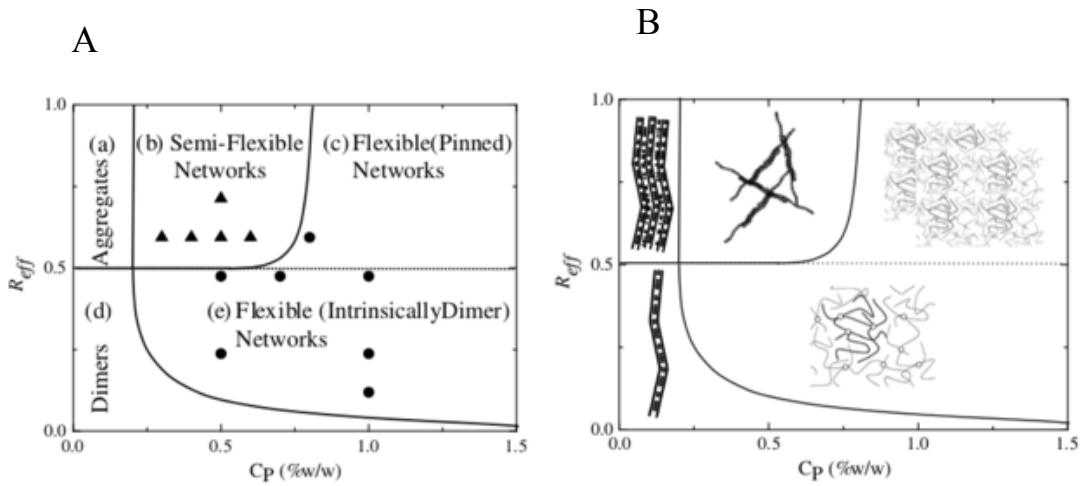

Figure 1.7: Different types of LDM pectin gel depending on Ca^{2+} concentration, consecutive demethylesterified residues and HG polymer concentration. (A) Gel state diagram. (B) Schematic of gel state diagram corresponding to (A). R_{eff} value: the ratio of Ca^{2+} concentration to the quantity contained in blocks of consecutive demethylesterified residues longer than the amount required to bind Ca^{2+} into an egg-box. Cp: HG polymer concentration. Modified from (Vincent and Williams 2009).

LDM gel: LDM gels are mainly stabilized by ionic cross-links via Ca^{2+} bridges between two carboxylates from two different chains (Axelos and Thibault 1991) (Figure 1.5 and 1.6) and only partially through hydrophobic interaction, given the number of methylester groups is relatively low (Kastner and Senge 2012). In LDM gels, the binding of arrays of Ca^{2+} between antiparallel chains of 3_1 symmetry form extended, corrugated sheets with a characteristic spacing of a = 1.23 nm (Figure 1.5b, c), as opposed to the closer spacing of parallel HDM HG chains (a = 0.8 nm). Given the differences in space between HG backbones of HDM and LDM gels, HG demethylesterification within a HDM gel can lead to an increase in gel volume even in the presence of Ca^{2+}.

The properties of LDM gels depends on GalA and, degree of polymerization (DP), DM (Figure 1.7, Vincent and Williams 2009), co-solute concentration, ions strength (Ca^{2+} concentration and pH), and temperature (Chan et al. 2017). The gel strength of LDM gels increases with increasing GalA concentration and with increasing DB (Basak and Bandyopadhyay 2014; Ngouémazong et al. 2012; Vincent and Williams 2009). If the DM is too low, HG can precipitate out of solution instead of forming a stable gel, in which the polymers are dynamically pinned and the system mobility is reduced significantly, and extensive lateral association of the dimers is dynamically forbidden (Region c in Figure 1.7, Vincent and Williams 2009). Similar to HDM gels, the presence of co-solute can also promote inter-chain interactions (Fu and Rao 2001), bivalent ions such Fe^{2+}, Mg^{2+} or heavy metals can alter the viscosity of LDM gels (Mierczynska et al. 2015). Whether these ions bind to pectin in an egg-box-like model is still unknown. Higher ambient temperature can accelerate gelation through promoting the formation of egg-box junction zones. Low temperature facilitates hydrogen bonds, which are weaker than Ca^{2+} bonds, and therefore weakens the gel (Chan et al. 2017). HG gels undergo a conformational transition below a pH value corresponding to the pKa of GalA: carboxyl groups are protonated and the chains are essentially uncharged. Gelation occurs by dimerization of (antiparallel) 3-fold helices as a result of the

suppression of electrostatic repulsion, and the formation of hydrogen bonds between the protonated carboxylic acids (Gilsenan et al. 2000; Mansel et al. 2015; Li et al. 2013)

***In vivo*:** Changes in the abiotic environment (temperature, ion concentrations, osmolarity or mechanical stresses) can affect plant growth by changing the rheology of the cell wall. For instance, high concentrations of NaCl in the medium of *Arabidopsis* root cells, caused a transient decrease in wall stiffness (Feng et al. 2018). The recovery of wall stiffness did not occur in mutants for the CrRLKL1 receptor kinase FERONIA (FER), causing root cells to burst in the presence of NaCl. This bursting could be prevented by supplying extra Ca^{2+} and boron (promoting crosslinks between RG-II molecules) to the medium. These observations are consistent with the idea that monovalent Na^{+} ions interfere with load-bearing Ca^{2+}-pectate bonds; that plant cells actively recover cell wall strength by promoting the formation of additional crosslinks in the cell wall and that this cell wall repair activity requires FER activity (Feng et al. 2018). In this context, HG modification most likely plays a critical role in the homeostasis of the cell wall rheology.

1.4. HG interacts with cell surface receptors

HG also binds to many cell surface receptors, such as *Catharanthus roseus* RLK1 (CrRLK1) -like family (Lin et al. 2018; Feng et al. 2018; Sebastjen et al. 2018), extensin containing receptors (Valentin et al. 2010; Mecchia et al. 2017), LRR receptor-like protein 44 (RLP44) (S. Wolf, personal communication) and Wall Associated Kinases (WAKs, Kohorn and Kohorn 2012). CrRLK1L proteins have a signal peptide, an extracellular domain consisting of two tandem malectin-like domains A and B (MALA, MALB), an extracellular juxtamembrane region, a transmembrane domain, and a kinase domain (Frank et al. 2018; Li et al. 2016). The Xenopus malectin domain binds to alpha-1,3-linked diglucosides on N-linked glycans and plays a role protein quality control in the ER (Schallus et al. 2008). Unlike animal malectin, these malectin-like domains lack critical residues involved carbohydrate binding (Du et al. 2018).

Nevertheless, the ectodomain of FER interacts directly with HG *in vitro*, although no genetic evidence exists so far for a signaling role for HG binding (Feng et al. 2018). Likewise, *in vitro* pull-down assays showed that FER preferentially binds to HG^{LDM} (Lin et al. 2018). Furthermore, it is worthwhile to note that oligogalacturonides (OGs) bind to members of the WAKs family, which appear to play a role in growth regulation and defense signaling (Kohorn and Kohorn 2012).

1.5. Apoplastic pH

Cell walls and spaces between cells make up the apoplast. The pH of the apoplast (pH^{Apo}) is tightly regulated and contributes to the control of the mechanical properties of the cell walls and, as a result, affect growth and development. About 50 years ago, the acid growth theory was proposed to explain this mechanism. The core of the acid growth theory is that a decrease in pH^{Apo} as a result of the activation of the PM-localized H^+-ATPase (also called proton pump) by auxin, results in the activation of cell wall-loosening enzymes, which in concert with the turgor pressure, enable cell expansion (Hocq et al. 2016).

1.5.1 Regulation CW enzyme activity by pH

In vitro experiments showed that many cell wall remodeling agents and their inhibitors are regulated by pH^{Apo} (Table 1.2). Among them, a principal role in cell wall loosening is played by expansin, which is a protein that disrupts cellulose-hemicellulose bonds with a low pH optimum (pH 4.5) (Mc-Queen-Mason and Cosgrove 1994; Mc-Queen-Mason et al. 1992; Cosgrove 2014 and 2015). The pH-dependence has also been characterized for some PMEs and PMEIs. For instance, AtPME3 activity has a pH-optimum of 7.5 (Sénéchal et al. 2015), AtPMEI4 and AtPMEI7 showed a similar pH-dependence for their inhibiting capacity (Hocq et al. 2017; Sénéchal et al. 2017) while AtPMEI9 is less pH-dependent (Hocq et al. 2017).

Table 1.2 Cell wall proteins sensitive to apoplastic pH.

Protein name	Gene ID	Functions	pH optimum	Assay	Species	Comment	Reference
PttCel9A	CA926262	Endo 1,4-glucanase	5.5-6.0 (30°C)	*In vitro*, expressed in *Pichia pastoris*	*Populus tremula*	Plasma membrane localized, cellulose synthesis, Arabidopsis KOR homologous	Master et al. 2004
AtXTH12	At5g57530	Xyloglucan endotransglucosylase/hydrolase (XTH)	5.0-6.0 (28°C)	*In vitro*, expressed in *Pichia pastoris*	*Arabidopsis thaliana*	Trichoblast	Maris et al. 2011
AtXTH13	At5g57540	XTH	5.0-6.0 (28°C)	*In vitro*, expressed in *Pichia pastoris*	*Arabidopsis thaliana*	Trichoblast	Maris et al. 2011
AtXTH17	At1g65310	XTH	7.0 (20°C)	*In vitro*, expressed in *Pichia pastoris*	*Arabidopsis thaliana*	Root	Maris et al. 2011
AtXTH18	At4g30280	XTH	7.0 (28°C)	*In vitro*, expressed in *Pichia pastoris*	*Arabidopsis thaliana*	Root	Maris et al. 2011
AtXTH19	At4g30290	XTH	7.0 (28°C)	*In vitro*, expressed in *Pichia pastoris*	*Arabidopsis thaliana*	Root	Maris et al. 2011
Cel16	AJ242807	Endo 1,4-glucanase	6.0	*In vitro*, expressed in *Pichia pastoris*	*Brassica napus*	Strong dependence on Calcium	Mølhøj et al. 2001
TCH4	AC004512.2	XTH	6.0-6.5 (18°C)	*In vitro*, expressed in baculovirus/ insect cell system	*Arabidopsis thaliana*	Acid-induced and cold-tolerant enzyme	Campbell and Braam. 1999; Purugganan et al.1997
AtXTH24 (Meri-5)	AT4G30270	XTH	6.0-6.5 (28°C)	*In vitro*, expressed in baculovirus/insect cell system	*Arabidopsis thaliana*	-	Campbell and Braam. 1999
EXGT	AT2G06850	XTH	6.0-6.5 (37°C)	*In vitro*, expressed in baculovirus/insect cell system	*Arabidopsis thaliana*	-	Campbell and Braam. 1999
XTG14 (XTR9)	AT4G25820	XTH	6.0-6.5 (18°C)	*In vitro*, expressed in baculovirus/insect cell system	*Arabidopsis thaliana*	-	Campbell and Braam. 1999

XET	-	XET	5.5	*In vitro*, extract enzyme from pea	*Pisumsativum*,cv.Alaska	XET is not bound to cell wall.	Fry et al. 1992
Expansin	-	Expansin	4.5	*In vitro*, extract enzyme from cucumber	(*CucumissativusL.*, cv. *Burpee Pickler*	Molecular weight 29-30 KDa	Mc-Queen-Mason and Cosgrove 1994; Mc-Queen-Mason et al. 1992
BcPG1	BCIN_14g00850	*Botrytis cinerea* endopolygalacturonase	4.2	*In vitro*, expressed in *Pichia pastoris*	*Botrytis cinerea*	The necrotizing activity is dependent on BcPGs enzyme activity.	Kars et al. 2005
BcPG2	BCIN_14g00610	*Botrytis cinerea* endopolygalacturonase	4.5	*In vitro*, expressed in *Pichia pastoris*	*Botrytis cinerea*	The necrotizing activity is dependent on BcPGs enzyme activity.	Kars et al. 2005
BcPG4	BCIN_03g01680	*Botrytis cinerea* endopolygalacturonase	4.9	*In vitro*, expressed in *Pichia pastoris*	*Botrytis cinerea*	The necrotizing activity is dependent on BcPGs enzyme activity.	Kars et al. 2005
PGs	-	Strawberry endopolygalacturonase	5.5	*In vitro*, extracted from strawberry fruit	Not mentioned	PG activity was inhibited by EDTA and citrate and activated by Ca^{2+}	Nogata et al.1993
PGs	-	Tomato endopolygalacturonase	4.5 (in Na^{+}) and 6.0 (in K^{+})	*In vitro*, extracted from tomato fruit	*Lycopersicon esculentum*	pH and cation can modulate PG2 activity.	Chun and Huber. 1998
PG1	-	Banana endopolygalacturonase	3.3	*In vitro*, extracted from banana fruit	*Musa acuminata*	-	Pathak and Sanwal. 1998
PG2	-	Banana endopolygalacturonase	3.7	*In vitro*, extracted from banana fruit	*Musa acuminata*	-	Pathak and Sanwal. 1998
PG3	-	Banana endopolygalacturonase	4.3	*In vitro*, extracted from banana fruit	*Musa acuminata*	-	Pathak and Sanwal. 1998
PG	-	Tomato endogalacturonase	4.4-4.8 (35°C)	*In vitro*, extracted from tomato fruit	*Lycopersicon esculentum*	Temperature optimum 55 ~ 60 °C	Verlent et al. 2004
BGLC1	At5g20950	β-glucosidase	5.5	*In vitro*, expressed in *N. benthamiana*	*Arabidopsis thaliana*	-	Sampedro et al. 2017

BGLC3	At5g04885	β -glucosidase	5.0	*In vitro*, expressed in *N. benthamiana*	*Arabidopsis thaliana*	-	Sampedro et al. 2017
β-glucosidase Eox 1	-	β-glucan exohydrolases	5.25	*In vitro*, purified from barley	*Laminaria digitata*	-	Hrmova and Fincher. 1997
β-glucosidase Eox 2	-	β-glucan exohydrolases	5.25	*In vitro*, purified from barley	*Laminaria digitata*	-	Hrmova and Fincher. 1997
β-glucosidase	-	β-glucosidase	4.5	*In vitro*, purified from nasturtium	*Tropaeolum majus*	Temperature optimum 30°C	Crombie et al. 1998
AtXYL1	AT1G68560	α-xylosidase	> 4.5	*In vitro*, purified from cabbage and expressed in yeast	*Arabidopsis thaliana*	-	Sampedro et al. 2001
AtPME3	AT3G14310	Pectin methylesterase	7.5 (among 3 pH, 37°C)	*In vitro*, expressed in *N. tabacum*	*Arabidopsis thaliana*	pH 5.0, 6.3 and 7.5 were tested	Sénéchal at al. 2015
AtPMEI7	At4g25260	Pectin methylesterase inhibitor	5.0 (among 3 pH, 37°C)	*In vitro*, expressed in *E. coli*	*Arabidopsis thaliana*	pH 5.0, 6.3 and 7.5 were tested	Sénéchal at al. 2015
AtPMEI4	At4g25250	Pectin methylesterase inhibitor	5.0 (among 3 pH, 37°C)	*In vitro*, expressed in *E. coli*	*Arabidopsis thaliana*	pH 5.0, 6.3 and 7.5 were tested	Hocq et al. 2017

1.5.2 Proton motive force and turgor pressure regulation

Protons constitute one of the major energy currencies of the plant cell. H^+-ATPase powers the transport of H^+ out of the cytosol, establishing an electrochemical potential across the membranes. This transmembrane H^+ potential is then used to power the transport of other ions or solutes across the membranes (Figure 1.8). The net direction of transport across a membrane is dictated by the driving force on the transport system. Two factors contribute to the overall driving force: the solute concentration difference across the membrane and the membrane electrical potential difference (membrane potential, V_m). In the particular case of H^+, a simplified expression based on the pH, can be obtained for the electrochemical potential difference. In *Arabidopsis thaliana* root cells, a membrane potential in excess of approximately 200 mV and a ΔpH (proton chemical concentration gradient) of approximately 2 (equivalent to approximately 120 mV) both contribute to the large proton motive force (PMF) (Buchanan et al. 2000).

Proton motive force regulates turgor pressure through mediating ion transport： Turgor pressure, an essential feature of plants, is often considered as the motor of growth (Beauzamy et al. 2014). This force within the cell pushes the PM against the cell wall and plays a key role in plant cell growth where the cell wall undergoes irreversible expansion due to the force of turgor pressure as well as structural changes in the cell wall that alter its extensibility (Cosgrove 2015). Turgor pressure is caused by the osmotic flow of water. The three major classes of osmo-active molecules modulated in osmoregulation are ions, sugars and amino acids. Plant cell have two mechanisms to regulate turgor pressure: one is transpiration, which results in water loss and decreases turgidity in cells. The other relies on its semipermeable membrane, which only allows some solutes to travel in and out of the cell. Most

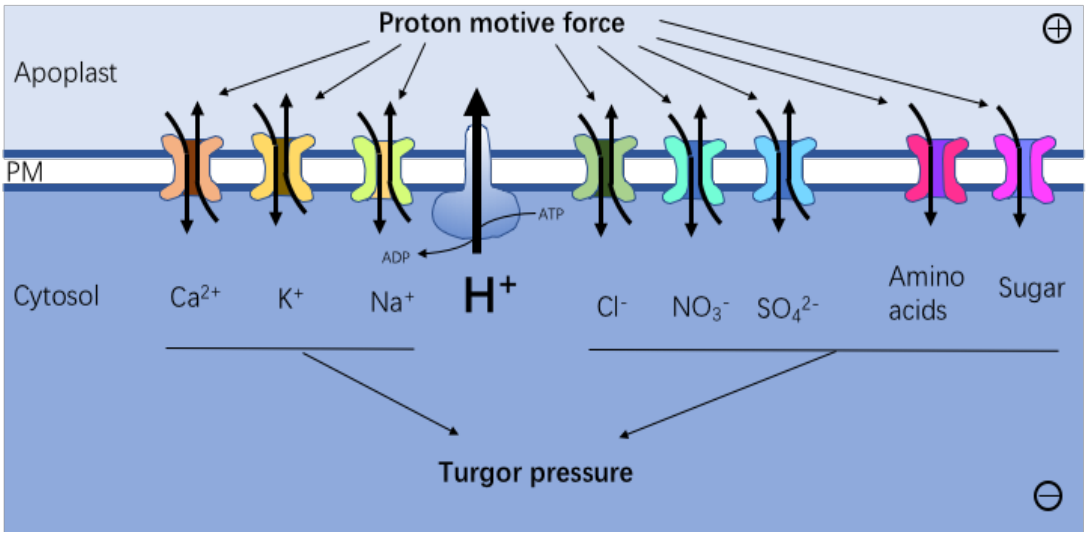

Figure 1.8: Proton efflux by H^+-ATPase affects cation and anion transportation cross plasma membrane through elevating proton motive force. The cytosolic ion concentrations determine turgor pressure. PM: plasma membrane.

PM solute transport systems in plants are H^+ coupled, and an ATP-coupled proton pump creates the PMF that energizes these systems (Bush 1993; Sussman 1994), resulting in the elevated turgor pressure that drives cell expansion (Figure 1.8).

Cation transport

K^+: PMF drives K^+ transport through channels and transporters against its concentration gradient. According to a current model (Nieves-Cordones et al. 2014; Wang and Wu 2017), non-selective channels are the main pathways for K^+ uptake at high concentrations, while at intermediate concentrations, the inward rectifying channel AKT1 dominates K^+ uptake (Lagarde et al. 1996; Sentenac et al. 1992). Under lower concentrations of external K^+, AKT1 channels, together with the high-affinity K^+ uptake system HAK5 (Rubio et al. 2000) contribute to K^+ acquisition, and at extremely low concentrations the only system capable of taking up K^+ is HAK5. As a cation, K^+ can be passively driven into the cell down the ΔVm, via a secondary transport system such as a uniport, AKT1. When the K^+ supply is reduced to 0.1 mM, the ΔVm becomes closer to K^+ diffusion potential and K^+ influx through the AKT1 complex decreases. The H^+/ K^+ symport activity of HAK5, is up-regulated under a low K^+ supply, allowing K^+ uptake. In tomato (*Solanum lycopersicum*), the change in ΔVm lead to increased LeHAK5 expression as well (Nieves-Cordones et al. 2014). Moreover, 50% of reduced H^+-ATPase concentration in an *Arabidopsis* knockdown mutant, *aha2-4*, caused the upregulation of the HAK5 compared with wild-type seedlings under normal growth conditions (Haruta and Sussman 2012). Therefore, the AKT1- and HAK5-dependent K^+ transport is affected by the PMF.

Cation/H^+ exchangers (CHX) are antiporters that are involved in K^+ transport (Sze and Chanroj 2018). For instance, PTs express 18 genes encoding putative cation-H^+ antiporter CHX family members (Sze et al. 2004). Of these genes, CHX13 and CHX14 are PM transporters involved in K^+ homeostasis (Sze et al. 2004; Zhao et al. 2008 and 2015). In the *aha2-4* mutant, CHX17 was also up-regulated under normal growth

conditions in the same way as HAK5 (Haruta and Sussman 2012). In summary, both K^+ symporters and antiporters are coupled to the PMF.

Na^+: Na^+ is deleterious to many organisms. Under salt and drought stress, plant cells exhibit three major mechanisms to avoid excessive Na^+ accumulation in the cytosol and reach ion homeostasis, plant cells exhibit three major mechanisms: restriction of Na^+ permeation and uptake catalyzed by Na^+ transporters; sequestration of Na^+ into the vacuole; and efflux of excess Na^+, with cytosolic Na^+ being transported back to the apoplast through PM Na^+/H^+ antiporters (Conde et al. 2011). In *Arabidopsis*, Na^+ efflux is catalyzed by the PM Na^+/H^+ antiporter encoded by *SOS1 (SALT OVERLY SENSITIVE1)* (Zhu 2003). PM H^+-ATPases generate the PMF for Na^+ transport by SOS1. Disruption of the root-endodermis-specific PM H^+-ATPase, AHA4, in mutant *Arabidopsis* plants causes increased salt sensitivity (Vitart et al. 2001). The inward rectifying channels KATl and KST in *Arabidopsis* and potato are activated by external H^+ via a positive shift of the activation potential (Amtmann and Sanders 1999). Moreover, the transcriptional upregulation of PM H^+-ATPases in saline environments is also consistent with a role for the PMF in the regulation of Na^+ influx and efflux (Amtmann and Sanders 1999).

Ca^{2+}: Unlike K^+ and Na^+, Ca^{2+} indirectly affects the turgor pressure by acting as a negative regulator (Okazaki and Tazawa 1990). In the plant *Lamprothamnium*, an increase in turgor pressure activated the PM Ca^{2+} channels, such as cylic nucleotide-gated channels (CNGC) and glutamate-like receptor families (GLR) (González-Fontes et al. 2017). The elevated Ca^{2+} influx increased the cytosolic Ca^{2+}, which activates K^+ and/or Cl^- channels in PM and/or tonoplast. Consequently, the passive effluxes of K^+ and Cl^- leads to a decrease in turgor pressure (Okazaki and Tazawa 1990).

In the soil, Ca^{2+} entry into the root is strongly favored by PMF (González-Fontes et al. 2017). Even though cell walls contains high concentrations of Ca^{2+}, cytosolic Ca^{2+} is maintained at a low level (about 100 nM). The Ca^{2+} system has two components: Ca^{2+}

-ATPases and Ca^{2+}/H^{+} antiporters (CAX) (Bose et al. 2011). CAXs are PMF-energized Ca^{2+} transporters. The stoichiometry of the dominant H^{+}/Ca^{2+} antiporter in the tonoplast is $3H^{+}/1Ca^{2+}$ (González-Fontes et al. 2017; Blackford et al. 1990).

Anion transports: Anion channels/transporters are key to osmoregulation (Barbier-Brygoo et al. 2011). Anions such as chloride, nitrate, or malate constitute a major part of the plant cell osmoticum. Anion movements through membranes, when coordinated with a cation flux, are thus expected to play a key role in the regulation of cell turgor. Plant cells contain the Rapid-type (R-type) and Slow-type (S-type) anion channels (Hedrich et al. 1990; Linder and Baschke 1990). The S-type current was proposed as the main mechanism for the depolarization, the loss of anions, and ultimately the decrease in guard cell turgor. The R-type anion channel accommodates, in the millisecond range, its gating to the membrane potential and shows a V-shaped current-voltage relationship with a steep voltage dependency. The S-type channel shows slow activation/deactivation kinetics in the 10-s range and a weak voltage dependency.

Sugar and amino acid transports: Sugar production or breakdown can elevate turgor pressure. In sink tissues, storage polysaccharides break down to increase the osmotic potential; for example, starch split is converted into glucose, fructose and/or malic acid, increasing the concentration of osmo-active solutes (Taiz and Zeiger 2010). The sucrose concentration can increase in the cytosol because of sucrose transport. One major way to regulate proton-coupled sugar transporters is indirectly by regulating H^{+}-ATPase activity (Lalonde et al. 1999). For instance, sucrose transporter, a high-affinity sucrose-H^{+} symporter, which transport sucrose and protons in the same direction across a membrane is regulated by the PMF (Lalonde et al. 1999). The stoichiometry of the proton-sucrose symport is 1:1 (Bush 1993). Furthermore, the phloem contains an

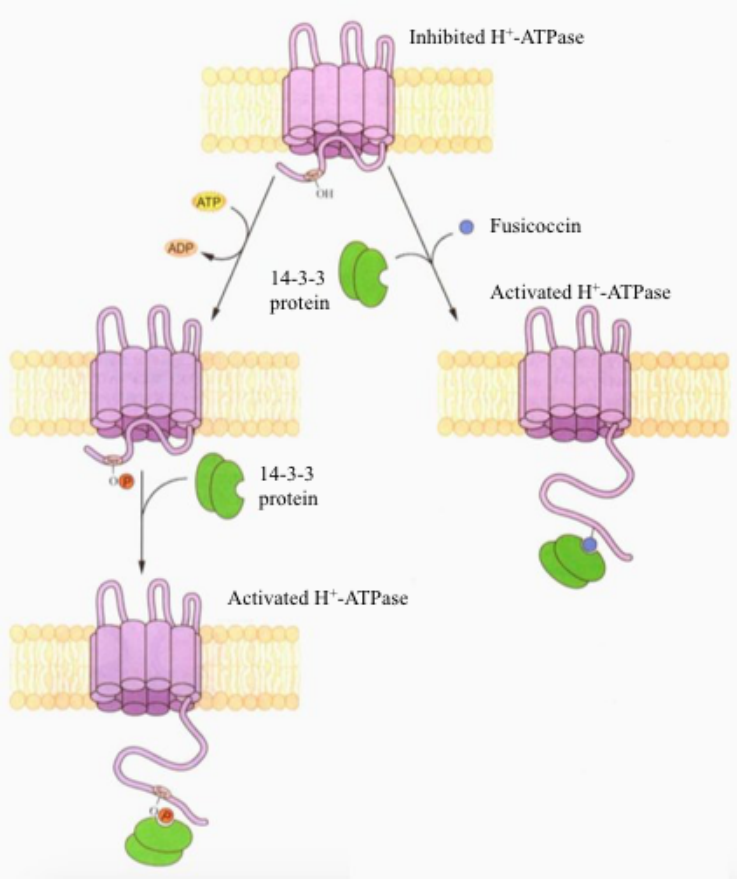

Figure 1.9: Models for the activation of plasma membrane H^+-ATPase by phosphorylation and fusicoccin. The C terminus of the enzyme functions as an inhibitory domain. Phosphorylation of a serine in the C terminus and binding of two 14-3-3 proteins remove this inhibition and activate the enzyme. The enzyme is also activated by binding of fusicoccin and 14-3-3 protein. Modified from (Buchanan et al. 2000)

osmotic pump whose efficacy rests primarily on the cooperative functions of three types of PM proteins: (1) H^+/sucrose symporters; (2) H^+-ATPases; and (3) water transporters (Sze et al. 1999; Lalonde et al. 1999). The pH^{Apo} ranges from 5.0 to 6.0, which is of importance for the proton binding of H^+/sucrose symporters which have an acidic pH optimum (Bush 1990). Besides, the transport of hexose, such as glucose, was driven not only by the size of the imposed gradient, but also by either H^+ or Vm (Bush 1993).

Amino acids are osmo-active, and their concentrations are modulated during osmoregulation. Amino acids are transported into plant cells by proton-coupled symports. Alanine accumulation against a significant concentration gradient and saturation kinetics indicated active amino acid transport (Bush 1988). The proton-alanine symport is located in the PM (Bosh 1988). Li and Bush (1990) investigated the proton-amino acid symport activity using purified PM vesicles isolated from sugar beet leaf tissue. In these experiments, a pH-dependent alanine, leucine, glutamine, glutamate, isoleucine, and arginine transport was demonstrated.

1.5.3 Regulation of apoplastic pH

The cell wall pH regulates the cell wall modifying proteins (Table 1.2), which alter the extensibility of the walls, allowing cellular expansion. A deep understanding of the pH^{Apo} regulation is required to answer the question of how plant cells grow.

H^+-ATPases: The long-standing acid growth theory postulates that the PM-localized H^+-ATPase, activated by plant hormone auxin, is the primary factor to acidify the apoplast. *Arabidopsis* contains 11 genes encoding PM H^+-ATPases (AHA1-11; Baxter et al. 2003). So far, AHA1 and AHA2 encode the two most highly expressed isoforms (Baxter et al. 2003; Haruta et al. 2010). The H^+-ATPase possesses 10 transmembrane domains and an autoinhibitory domain at the C-terminus (Figure 1.9, Buchanan et al. 2001). This autoinhibitory domain plays a pivotal role in regulating H^+-ATPase activity. Tobacco (*Nicotiana tabacum*) plants engineered to express a constitutively active PM H^+-ATPase derivative lacking the C-terminal inhibitory domain exhibit increased cell expansion (Gévaudant et al. 2007). In addition, the autoinhibitory domain can bind to

conserved regulatory molecule,14-3-3 proteins, which are expressed in all eukaryotic cells, where they regulate many cellular targets. These regulatory proteins bind to the autoinhibitory domain of H^+-ATPase, forming a complex, thus activating H+ transport (Kanczewska et al. 2005). The complex can be stabilized by fusicoccin, a toxic compound produced by fungus *Fusicoccum amygdali* (Figure 1.9) (Morsomme and Boutry 2000). Auxin regulates H^+-ATPases through phosphorylation of the autoinhibitory domain. Type 2C protein phosphatase PP2C-D dephosphorylates the penultimate threonine at the C-terminus of H^+-ATPase (in *Arabidopsis*, Thr 948 and Thr 947 for AHA1 and AHA2, respectively) and leads to H^+-ATPase activation (Takahashi et al. 2012). Auxin-induced SAUR19 is able to inhibit PP2C-D activity (Spartz et al. 2014), leading to the activation of H^+-ATPase, apoplast acidification and cell expansion (Spartz et al. 2014; Takahashi et al. 2012).

Besides auxin, other plant hormones, such as brassinosteroid (BR, Caesar et al. 2011), ABA (Merlot et al. 2007, Hayashi et al., 2014) and methyl jasmonate (MeJA) (Zhu et al., 2015), can also regulate H^+-ATPase activity. The BR receptor protein (BRI1), can activate a H^+-ATPase, AHA1. BRI1 interacts with AHA1 on the PM, phosphorylating its C-terminal autoinhibitory domain (Caesar et al. 2011). ABA inhibits PP2C protein (Hayashi et al. 2014). ABA binds to its receptors to inhibit PP2C-A, releasing the protein kinase SnRK2 into an active form that can directly inhibit AHA2-mediated acidification and thereby repress root growth (Merlot et al. 2007; Hayashi et al. 2014). MeJA treatment stimulated PM H^+-ATPase activity in parallel with H^+ efflux from the root tips of lettuce seedlings and rhizosphere acidification (Zhu et al. 2015).

Rapid alkalinization factor and FERONIA: Rapid alkalinization factor (RALF) is a 49-amino-acid secreted peptide first discovered in a screen for endogenous plant peptides with the ability to increase the pH of the media of cultured cells (Pearce et al. 2001). Silencing the NaRALF in *N. attenuata* caused roots to grow longer and trichoblasts that developed into abnormal root hairs (RHs) (Wu et al. 2007). *Arabidopsis* has 36 RALFs regulating developmental and physiological processes (Ge et al. 2017; Haruta et al. 2014; Mecchia et al. 2017; Stegmann et al. 2017). Overexpression and silencing of AtRALF1 respectively resulted in reduced and increased root cell size and lateral root number (Bergonci et al. 2014). All RALF peptides tested induced alkalinization (Morato do Canto et al. 2014; Pearce et al. 2010).

A specific-YISY-motif located at positions 5 through 8 from the N-terminus, which is highly conserved within the plant kingdom, is required for productive binding of RALF to its putative receptor (Pearce et al. 2010). All characterized RALF receptors belong to the CrRLK1L family (Ge et al. 2017; Haruta et al. 2014; Mecchia et al. 2017; Stegmann et al. 2017). For instance, FER is a receptor for RALF1 and RALF23 (Haruta et al. 2014; Stegmann et al. 2017), BUPS1/2 and ANX1/2 for RALF4, RALF19 and RALF34 (Ge et al. 2017; Mecchia et al. 2017) and THESEUS (THE1) for RALF34 (Gonneau et al. 2018). Although two different peptides applied sequentially were able to induce a higher alkalinization response than that produced when the same peptide was applied (Morato do Canto et al. 2014), RALFs also showed competitive relationships, such as RALF34 competing for RALF4 and RALF19 binding to their receptors (Ge et al. 2017). Based on the alkalinization, pollen germination and Ca^{2+} mobilization assays, it is assumed that at least two or three different pathways for sensing the peptides are functioning in the same tissue (Morato do Canto et al. 2014). Indeed, in addition to RALF binding to different CrRLK1Ls, RALF4 and RALF19 also interact with LEUCINE-RICH REPEAT EXTENSIN (LRX) in PTs (Mecchia et al. 2017). RALFs regulate extracellular alkalinization through the inhibition of H^+ transport. For example, RALF1 treatment promoted phosphorylation of Ser-899 in PM H^+-ATPase 2 (AHA2) (Haruta et al. 2014), leading to inhibition of H^+-ATPase activity, medium alkalinization and growth suppression. In contrast, the pump activity was constitutively up-regulated in loss-of-function *fer* mutant (Haruta et al. 2014). Interestingly, the fungal pathogen *Fusarium oxysporum* secretes a RALF homolog, F-RALF, which also elicited a rapid alkalinization response in tomato and inhibited root elongation in both tomato and *Arabidopsis* (Masachis et al. 2016), indicating that pathogens can highjack this endogenous pH regulating system to their advantage.

FER is a regulator of many biological processes, ranging from fertilization to inhibition of cell elongation and growth (Li et al. 2016). Besides cell wall alkalinization, FER plays essential roles in other signaling pathways. For instance, FER acts as a RALF-regulated scaffold that modulates the assembly of immune receptor kinase complex consisting of EF-TU RECEPTOR (EFR) and FLAGELLIN-SENSING 2 (FLS2) with their co-receptor BRASSINOSTEROID INSENSITIVE 1–ASSOCIATED KINASE 1

(BAK1) (Stegmann et al. 2017). FER, together with its co-receptor LORELEI (LRE), is also required for cytosolic Ca^{2+} oscillations in male gametophyte (pollen) and female tissues during fertilization, PT rupture and programmed cell death of one of two synergid cells (Duan et al. 2014; Ngo et al. 2014). This explains the defect in fertilization in *fer* mutants (Escobar-Restrepo et al. 2007). FER is required for the production of high levels of reactive oxygen species (ROS) at the entrance to the female gametophyte. ROS accumulation is thought to be responsible for PT rupture in a Ca^{2+} dependent process involving Ca^{2+} channel activation (Duan et al. 2014). FER is required for RALF-induced Ca^{2+} spikes that further produce an inhibitory effect on root growth (Haruta et al. 2014). The RALF-induced Ca^{2+} increase observed in the wild type was absent in the *fer-4* mutant, indicating that this fer4 mutant is deficient in the RALF-dependent Ca^{2+} signaling system. FER is required for mechanical signal transduction in *Arabidopsis* roots (Shih et al. 2014). A *fer* mutant shows severely altered cytosolic Ca^{2+} signaling, pH and growth responses to different forms of mechanical perturbation. Ca^{2+} signals and pH responses are either abolished or exhibit qualitatively different signatures in *fer-4* mutants exposed to local touch or bending stimulation (Shih et al. 2014). Interestingly, FER kinase activity was not essential for FER-dependent mechanical Ca^{2+} signaling, suggesting either an interaction between FER and another kinase or that FER plays a role as a scaffold not only for pathogen-associated molecular patterns (PAMPs) triggered immunity complexes but also for mechanosensing protein complexes.

ROS: Plant cell growth requires constant balancing between cell wall strength, to resist the turgor pressure, and extensibility, to allow expansion. ROS are important regulators of this balance. ROS comprise several molecules, which may contribute to wall stiffening (e.g. H_2O_2, through peroxidase-promoted oxidative crosslinking of polymers (extensins or in grasses, feruoylated arabinoxylans)) or wall loosening ($HO^{\bullet}$, through polymer severing, (Fry et al. 1998)). FER functions as a cell surface regulator in a FER-ROPGEF-ROP complex required for auxin-promoted to nicotinamide adenine

dinucleotide phosphate (NADPH) oxidase-dependent ROS accumulation in roots, which is also required for normal RH growth (Duan et al. 2014). FER is also required for the production of high levels of ROS at the entrance to the synergid cell through a NADPH reductase and the authors hypothesize that $HO^{\bullet}$ accumulation may explain the rupture of the PT upon arrival at the synergid cell (Duan et al. 2014).

BR: FER can also promote cell growth through integrating different hormone signaling pathways (Duan et al. 2014; Guo et al. 2009). FER is transcriptionally induced by BRs, and are down-regulated in the loss-of-function BR mutant *bri1* and up-regulated in the constitutive BR-response mutant *bes1-D*. Besides *FER*, the CrRLK1Ls *THE1* and *HERK1* are also transcriptionally upregulated by BR through BRI1 and BES1. *herk1/the1* double mutants enhance loss of function *bri1* and suppress *bes1-D* mutant phenotypes. The two pathways regulate a common set of 127 target genes, including those involved in cell elongation (Deslauriers and Larsen 2010; Duan et al. 2014; Guo et al. 2009).

Abscisic acid: Phosphatase ABA INSENSITIVE 2 (ABI2) negatively regulates abscisic acid (ABA) signaling (Yu et al. 2012), which physically interacts with and be activated by RHO GTPase, such as *ROP11/ARAC10* (*RHO OF PLANTS 11/RAC-LIKE GTP BINDING PROTEIN 10*) (Yu et al. 2012). RHO GTPase, considered as a molecular switch, shuttles between the GDP-bound inactive state and the GTP-bound activated state and its activation is predominantly mediated by a family of guanine nucleotide exchange factors (GEFs) referred to as ROPGEFs. FER activates ABI1 through regulating RHO GTPase activity via its interaction with ROPGEFs, being a negative regulator of ABA signaling (Duan et al. 2010; Yu et al., 2012). Seedlings of loss-of-function mutants in *FER* or downstream interactors *GEF1/4/10* or *ROP11/ARAC10*, respectively, are hypersensitive to ABA (Yu et al. 2012). In response to ABA, they display higher ROS levels in guard cells, increased stomatal closure, and stronger growth inhibition of seedlings and roots. In return, ABI2 directly interacts with

and dephosphorylates FER thus counteracting RALF1-mediated FER phosphorylation and activation (Chen et al. 2016).

Auxin: FER seems to be positively influencing auxin signaling. *fer* seedlings are insensitive to auxin-stimulated RH elongation and ROS accumulation; however, not all FER dependent functions (such as precocious RH bursting) can be explained by auxin-signaling insensitivity (Duan et al. 2014; Li et al. 2015). In addition, FER is required for auxin-induced transient alkalinization of the extracellular matrix and inhibition of cell elongation in roots, for instance during the gravitropic response (Barbez et al. 2017).

Ethylene: FER might negatively regulate *S*-adenosylmethionine (SAM) synthesis by interacting with SAM1 and SAM2. *fer* plants are also hypersensitive to ethylene, showing severe hypocotyl shortening in the presence of saturating ethylene levels in the dark (Deslauriers et al. 2010). Additionally, *fer* mutants contain higher levels of SAM and ethylene, with SAM being part of the ethylene biosynthetic pathway (Mao et al. 2015). Interestingly, overexpression of *SAM SYNTHASE1* (*SAM1*) or *SAM2* trigger growth-related phenotypes similar to those of the *fer* mutant.

1.5.4 Matrix charge

Due to the presence of HG in the plant cell wall, the apoplast is negatively charged and behaves as an insoluble polyanion under most pH conditions (Ricard et al. 1981 and 1984). The fixed negative charges create an electrostatic potential difference ($\Delta\psi$) between inside and outside of the wall and contribute to the local pH by sequestering H^+. This in turn affects the cell expansion rate by controlling the pH-dependent activity of cell wall modifying agents (Moustacas et al. 1986, Table 1.2), where acidic (pH 4 ~ 5) and alkaline pH (> 6) promote and inhibit growth, respectively. With the cell wall volume increase in growing cells, and the arrival of newly synthesized HG^{HDM}, the matrix charge density is expected to decline and the pH to increase (Moustacas et al. 1986; Ricard and Noat 1986). Therefore, the cell wall must have subtle molecular mechanisms to maintain the acidic milieu for cell wall extension. Ricard and co-

workers (Crasnier et al. 1985; Moustacas et al. 1986 and 1991; Nari et al. 1986 and 1991; Ricard and Noat 1986) combined *in vitro* enzymological approaches on isolated walls and mathematical modeling to study this mechanism and reported an exquisite relationship among the $\Delta\psi$, PME, metal ions and cell wall extension rate (Figure 1.10). The results show:

(1) The decrease or increase in $\Delta\psi$ controls the increase or decrease in pH, respectively (Moustacas et al. 1991; Nari et al. 1991).

(2) PME catalyzed the HG demethylesterification with a high pH optimum (pH 7.5), which produces H^+ and additional anionic sites, causing a decrease in pH^{Apo} (Nari et al. 1991) and its own inhibition. The subsequent decrease in fixed charge density in growing cells leads to a pH increase, the activation of PME and the restoration of the charge density and so forth (Moustacas et al. 1986; Nari et al. 1986; Ricard and Noat 1986).

(3) This process is amplified by the attraction of metal ions (such as Ca^{2+}) in the poly-anionic cell-wall matrix. Ca^{2+}, which tightly binds to cell wall pectate affects the net charge of the cell wall and therefore the amplitude of electrostatic repulsion effects (Crasnier et al. 1985; Moustacas et al. 1991). In addition, whereas metal ions do not intrinsically activate PME, they tend to dissociate enzyme molecules from 'blocks' of carboxy groups of the cell wall (Nari et al. 1991). As a result, metal ions increase the number of enzyme molecules that are available for the HG demethylesterification.

In this context it is interesting to consider a role for RALF/CrRLK1L signaling as an amplifier of the cell wall-associated pH homeostatic mechanism, through the recruitment of the H^+-ATPase in the system. Indeed, most RALFs are poly-cationic peptides that are thought to segregate between their CrRLK1L receptor complex and negatively charged HG. Upon co-secretion with HG^{HDM}, RALF peptides would be

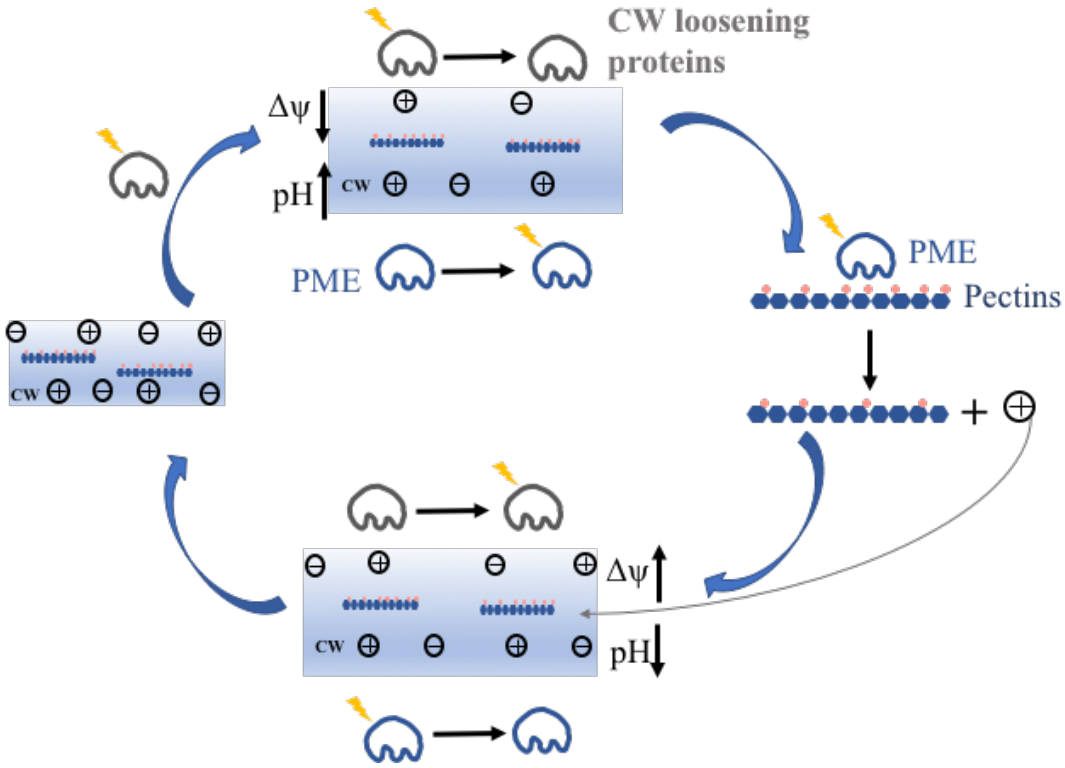

Figure 1.10: **Theoretical model of the electrostatic and ionic control of cell wall loosening.** PME activity catalyzing HG demethylesterification has a high pH optimum. The H^+ released from this reaction increases the electrostatic potential Δψ of the cell wall relative to the medium and reduces the pH. This in turn activates cell wall loosening proteins with low pH optimum, leading to cell wall extension. Cell wall extension combined with the deposition of new wall material leads to the dilution of the H^+ and the alkalination of the cell wall. The yellow "lightning" refers to the active version of the protein. (Adapted from Crasnier et al. 1985; Moustacas et al. 1986 and 1991; Nari et al., 1986 and 1991; Ricard and Noat, 1986)

available for CrRLK1L binding. This would amplify the cell wall alkalinization response, associated with the decay in cell wall charge density, through the inhibition of the H^+-ATPase. Subsequent activation of PME and the increase in negative charge density of HG would cause not only passive acidification through the sequestering of H^+, but also the amplification of this response through the sequestering of the poly-cationic RALF and the derepression of the H^+-ATPase (Doblas et al. 2018).

It is worth noting that these studies of Ricard and colleagues were carried out *in vitro* on the extracted cell wall of soybean and that the cell wall pH was estimated from the H^+ release in the bulk phase. Very little information exists however on the cell wall pH *in vivo* and its effect on plant cell growth.

1.6. How to measure apoplastic pH

Given the key role for pH in cell wall metabolism and in growth, its measurement has been an important goal of plant biologists. The pH difference between cellular compartments, however, can reach as much as 6 pH units, posing a challenge to imaging approaches to visualize the pH of the various regions in these compartments (Swanson et al. 2011). Intracellular pH measurement methods were first developed to study animal systems and were adapted later on for cytoplasmic and vacuolar pH measurements in plants (Kurkdjian and Guern 1989). Recently, methods have emerged for the measurement of the pH^{Apo} of plant cells based on pH-sensitive fluorescent dyes or proteins in addition to the older methods based on H^+-selective microelectrodes, the isolation of apoplastic fluid, bromocerol purple in agar (Geilfus 2017; Martinière et al. 2013; Swanson et al. 2011). I will focus here on the first three, most commonly used, approaches (Table 1.3).

1.6.1 H^+-selective microelectrodes

H^+-selective microelectrodes allow pH measurements over time *in vivo*, enabling the temporal mapping of pH kinetics from milliseconds to hours. The most common type

are H^+-sensitive glass microelectrodes, which cover the entire physiological pH range that may prevail in any plant tissues or cellular compartments (Ammann 2013). An estimate of pH^{Apo} can be recorded by placing the electrode on the cell wall of leaf mesophyll or root cortex cells using a micromanipulator to position the microelectrode with micrometer accuracy (Felle et al. 2009). To measure pH^{Apo} dynamics that are under the influence of the mesophyll cells, it may be necessary to remove the epidermis to position the electrode on top of the apoplastic region (Rubio et al. 2017). By placing the microelectrode on the surface of growing *Arabidopsis* RHs, it was found that ROS-related RH elongation is coupled to spatially distinct regulation of extracellular pH (Monshausen et al. 2007). Using this approach, Felle et al (2009) found that the mycorrhiza fungus *Piriformospora indica* induces root surface alkalinization that was hypothesized to support the systemic stress response of barley (*Hordeum vulgare*) to *B. graminis f. sp. hordei*. Furthermore, *in planta* measurements are available with microelectrodes to investigate the stomatal cavity, because the microelectrodes can be inserted through the opened stomata (Guzel Deger et al. 2015; Zimmermann et al. 2016), allowing the pH in the sub-stomatal cavity to be quantified (Hanstein and Felle 1999; Pitann et al. 2009; Zimmermann et al. 2009). This application has led to many significant findings that have improved the mechanistic understanding of the role of the sub-stomatal cavity pH in stress responses (Felle and Hanstein 2002). The drawback of this approach is that the inserted microelectrodes present a physical barrier that inhibits full stomatal closure, affecting gas exchange of closed stomates. Moreover, the fabrication of microelectrodes and their insertion into the cavity are labor intensive and not every attempt is successful. The pH recordings yield information about the pH in the close vicinity of the microelectrode with low spatial resolution. However, the accuracy of the microelectrode-based acquired data is high and reliable (Felle 1998; Ammann 2013).

Table 1.3 Fluorescent pH indicators used in plant cell walls.

Probes	Type	Excitation (nm)	Emission (nm)	pH range	Usage range	Advantages / disadvantages	Reference
SNARF	Ratiometric	488 or 514	580/640	6.0-8.0	Leaf	Simple and cheap, in vivo measurement. Imprecise estimation of pH	Jia and Davis 2007
BCECF	Ratiometric	508	530	6.0-8.0	Leaf, root, pollen tube,	Simple and cheap, in vivo measurement. Imprecise estimation of pH	Jia and Davis 2007; Feijó et al. 1999
Fluorescein	Ratiometric	490/450	515	6.0-7.2	Root, root hair, leaf	Simple and cheap, in vivo measurement. Imprecise estimation of pH	Monshausen et al. 2007 and 2009; Hoffmann and Kosegarten 1995
Oregon Green	Ratiometric	480/440	520	4.2-5.7	Root, leaf	Simple and cheap, in vivo measurement. Imprecise estimation of pH	Fasano et al. 2001 ; Javed et al. 2014
Bromocerol purple	-	-	-	5.2-6.8	Root, root hair	Simple and cheap, in vivo measurement. Imprecise estimation of pH	Pacheco-Villalobos et al. 2016 ; Zhu et al. 2015 ; Masachis et al. 2016
HPTS	Ratiometric	405/458(470)	514/514	4.5-6.5	Root	Reliable, *in vivo* and with high spatiotemporal resolution. Confocal or fluorescence microscopy needed, calibration might be inaccurate due to unknown effects of the apoplastic milieu on the dye, limited pH range of responsiveness, cross-sensitivity to other ions is merely possible	Barbez et al. 2017

pHluorin	Ratiometric	395/475	510	5.4-8.4	Root	Reliable, in vivo measurement possible with high spatiotemporal resolution (milliseconds to hours), different organs and tissues can be monitored. Confocal or fluorescence microscopy needed, long time required to produce transgenic plants, hardly suitable for plants that are not readily transformable, calibration might be inaccurate due to unknown effects of the apoplastic milieu on the protein, cross-sensitivity to other ions is merely possible, proteins might emit light from subcellular compartments during sorting, limited pH range of responsiveness	Gao et al. 2004 ; Martinière et al. 2018
pHusion	Ratiometric	488/558	510/600	4.5-8.0	Hypocotyl, root	Same as for pHluorin.	Gjetting et al. 2012 ; Fendrych et al. 2016

1.6.2 pH-sensitive fluorescent dyes

A second method combines pH-sensitive fluorophores and confocal or fluorescence microscopy. This fluorophore should fulfill several requirements. (i) It must not penetrate into the symplast. This can be prevented by conjugating the dye to a 10-kDa-sized dextran (Monshausen et al. 2007 and 2009). (ii) The probe must change a physicochemical attribute, such as emission intensity, in a strict dependency to the free H^+ concentration. (iii) It should not be cross-sensitive to other ions, metabolites, or chemical parameters such as the redox state of the biological system.

Methods based on the pH dependency of the emitted light intensity, have to correct for variations in the probe concentration itself. To this end, the protonated form of the fluorophore is excited by light of a specific wavelength, while a different wavelength is used to measure a pH-independent signal. The pH-sensitive/pH-insensitive channel ratio is then determined for each pixel (Gilroy et al. 1990). Calibration *in vivo* is then required to convert this ratio into pH (Geilfus et al. 2014). The fluorescein derivatives fluorescein isothiocyanate, Oregon green 488, or 2', 7'-bis-(2-carboxyethyl)-5-(6)-carboxy fluorescein (BCECF) have been frequently used as dyes to monitor the pH of the leaf apoplast via the dual-excitation technique (Pitann et al. 2009; McLachlan et al. 2016; Hoffmann and Kosegarten 1995). An alternative method is based upon the excitation of the fluorophore at one wavelength and the emission at 2 different wavelengths only one which is correlated with pH. To measure the surface pH of roots, Monshausen et al. (2009) bathed *Arabidopsis* roots in a medium containing the ratiometric pH indicator fluorescein dextran (10 kDa). By observing changes in the emission intensity of the dye, which is dissolved in the bathing solution that harbors the roots, it was possible to analyze the root surface pH. This revealed that the root surface pH is regulated by calcium signals during mechanosensing in *Arabidopsis* roots. Barbez et al. (2017) were able to load the ratiometric pH indicator 8-hydroxypyrene-1,3,6-trisulfonic acid trisodium salt (HPTS) into the root apoplast by immerging seedlings of *Arabidopsis* for 30 min in liquid growth medium that contained the dye. By using this

loading technique in combination with two- excitation-wavelength-ratio imaging, this research revealed that auxin signaling triggered cell-wall acidification, leading to increased cellular expansion.

1.6.3 pH-sensitive fluorescent proteins

Genetically encoded pH sensors that have been designed to overcome the limitations of pH sensitive dyes, such as the leakage into the symplast or the impermeability of certain tissues (Table 1.3). Green fluorescent protein (GFP) absorbs light at two maxima: 395 nm when protonated and 475 nm when deprotonated (Bizzarri et al. 2009). This shift in absorption has been extensively used to record pH in living organisms (Kneen et al. 1998) and optimized versions of GFP for pH measurement have been generated. Ecliptic and superecliptic pHluorins display almost no fluorescence when protonated, allowing sensitive pH measurements. Gao et al. (2004) fused the pHlourin to a chitinase signal sequence to target this pH indicator directly to the cell wall. This study revealed that the salt stress-induced pH^{apo} signature differed from that induced by osmotic stress. Martinière et al. (2018) fused pHlourin to a modified transmembrane domain containing 26 amino acids of the PM-localized TM23. This pH^{Apo} sensor, briefly called PM-Apo, is able to record the pH value at a position of a few nanometer away from the PM. The results with PM-Apo revealed pH of 6.5 to 6.7 close to the PM, suggesting a large difference in pH between PM and cell wall (pH ~ 4.0). Combined PM-Apo and an interface-localized pH sensor, PM-cyto, which consists of pHlourin and a farnesylation sequence of Ras, the transmembrane H^+ gradient (= pH_{cyto} - pH_{Apo}) was precisely measured in mature root cells from the epidermis to stele Martinière et al. (2018). Although pHluorin and its derivative sensors have proven their utility (Martinière et al. 2013 and 2018), they also have a number of disadvantages, such as (1) the equilibrium between the protonated and deprotonated states of these proteins is affected by temperature and ionic strength. (2) the light emitted by sensor is dependent on its own concentration. (3) the fluorescence sensor is easily degraded or quenched in acidic milieu. To circumvent these issues, other sensors are based on the measure of

pH by Förster resonance energy transfert (FRET) between two fluorescent proteins or by the emission intensity ratio of two fluorescent proteins. In particular, the tandem of enhanced GFP (EGFP) and pH insensitive monomeric red FP (mRFP1) is suitable for measuring pH in the apoplast (Gjetting et al. 2012). apopHusion is targeted to the apoplast thanks to a chitinase signal peptide (Gjetting et al. 2012), as confirmed in leaf epidermis, the guard cells, the mesophyll, and root apex in *Arabidopsis*. Using this genetically encoded sensor, Gjetting et al. (2012) discovered a fast alkalinization response in the epidermal apoplast of elongating roots to the external addition of indole-3-acetic acid. Fendrych et al. (2016) found that apoplastic acidification, elongation, and auxin transcriptional responses all happen ~20 min after auxin application in the etiolated *Arabidopsis* hypocotyl. The power of the apopHusion approach was especially evident when auxin-induced pH changes in the apoplast were examined *in vivo* during gravitropic responses.

Genetically encoded pH probes have the drawback, however, that they may accumulate in an active form within the secretory system. As a result, quantification of the pH^{Apo} requires correction for the intracellular signal (Swanson et al. 2011). A second drawback is that it is not known to what extent other physico-chemical parameters can influence the behavior of sensors. A further disadvantage is that genetically-encoded probes require plants that are readily transformable, complicating their use in non-model plants. In order to circumvent the problem, Geilfus et al. (2014) purified ratiometric dual-excitation pH-sensor GFPs from a bacterial expression system and loaded them non-invasively through the open stomata into the apoplast of intact plants. With this approach, however, the big advantage of genetically encoded sensors is lost in that they cannot be targeted to specific microdomain in the apoplast. Care must be taken, however, because at pH < 5, GFPs exhibit irreversible conformational changes leading to protein instability (Kneen et al. 1998). This problem must be taken into account since the pH^{Apo} often reaches values is below pH 5 (Grignon and Sentenac 1991). No matter the type of genetically-encoded pH sensor, estimation of the local pH

value from the fluorescence data is not straightforward. It requires *in vitro* or *in vivo* calibration to characterize the relationship between the fluorescence properties of the sensor and pH^{Apo} (Gao et al. 2004; Schulte et al. 2006; Shen et al. 2013). *In vitro* calibration uses heterologously expressed sensors in buffers of different pH. Such a calibration does not take into account the ionic strength and buffering capacity of the cell and thus can lead to substantial artifacts (Schulte et al. 2006). *In vivo* calibration uses sensor-expressing plant cells that are treated with buffer solution at certain pH points. This approach should be favored whenever possible, but also has its limitation. First, there is no objective way to ensure that the equilibrium has indeed been reached between the bathing media and the cell compartment where the sensor is located. Second, the buffer solution can modify the ion content of the cell and consequently native buffering capacity and ionic strength (Martinière et al. 2013).

In summary, among the discussed methods for the measurement of pH^{apo}, H^+-selective microelectrodes are relatively precise in the entire physiological pH range but the setup of instruments and fabrication microelectrodes is labor-intensive and its spatial resolution is low. pH-sensitive fluorescence dyes have higher spatiotemporal resolution but a limited pH range of responsiveness. pH-sensitive genetically encoded florescence proteins can be used in different organs and can be targeted to distinct domains in the apoplast, but they require the generation of transgenic plants, may emit light from subcellular compartments during sorting and also have a limited pH range.

1.7. Relationships between growth, apoplastic pH, and HG demethylesterification

As above-mentioned, pH^{Apo} is an essential factor to control cell growth. The mechanism that underlies this regulation has been studied in great detail in tip-growing PTs and RHs. The rapid, directed growth of the PTs is a central event in the sexual reproduction of higher plants. RHs play critical roles in water and nutrient uptake, and in anchoring the plant in the soil. PT and RH provide important models for study of the cellular

processes underlying growth. Here I focused on the relationship between pH^{Apo}, pectin metabolism and tip growth in these contexts.

1.7.1 pH

Since mid-1990s, the role of cytoplasmic and surface pH in RH growth was studied in *Sinapis alba* RHs (Herrmann and Felle 1995). It was shown that an active PM H^+-ATPase is required for growth. pH^{Apo} is associated with RH development in *Arabidopsis* and the processes of tip growth and initiation of RHs show differences in their pH requirements: pH^{Apo} decreased during the initiation of RH, while it increased during the RH growth (Bibikova et al. 1998). Artificially preventing the wall acidification with pH buffers arrested the initiation process but growth resumed when the wall was returned to an acidic pH (Monshausen at al. 2007). These results highlight the role of the spatio-temporal control of pH^{Apo} in cell expansion and morphogenesis in plants (Bibikova et al. 1998). Moreover, the increase in pH^{Apo} of *Medicago* RH could be a signal for the sensing of rhizosphere-associated signaling molecules such as Nod factors (Felle et al. 1996). RHs show oscillations in extracellular pH associated with oscillating growth, where the decrease in growth rate shows lags around 7 s behind the pH increase (Monshausen at al. 2007).

PTs show both a longitudinal cytosolic pH gradient (Feijó et al. 1999) and pH and growth oscillations (Messerli and Robinson 1998). Lily PTs possess a constitutive alkaline band at the base of the "clear zone", and an acidic domain at the extreme apex (Feijó et al. 1999), which may be explained by the localization of the PM H^+-ATPase along the shank but not at the apex (Lefebvre et al. 2005). The "clear zone" is a region just near the apex (so named due to the amyloplasts with highly refractile starch grains) in which vesicles accumulate and fuse, secreting wall material and membrane necessary for tube elongation (Hepler et al. 2013). Intracellular pH oscillations occur several hours after germination and lag the growth rate oscillations by more than 7.5 s (Messerli and Robinson 1998; Lovy-wheeler et al. 2006). Spatially, the pH decreases at RH tip

and travels as far as 60 μm down the shaft of the tube (Messerli and Robinson 1998; Feijó et al. 1999; Messerli et al. 1999). The changes in intracellular pH were associated with a H^+ influx at the extreme apex of the PT (Feijó et al. 1999; Messerli et al. 1999) and an efflux in the region that corresponds to the position of the alkaline band (Feijó et al. 1999). Obviously, the H^+ influx and efflux change pH^{Apo}. The average fluxes at the cell surface during the peaks of the H^+ pulse was 489 ± 81 pmol cm^{-2} s^{-1}. The H^+ pulse has a phase lag of 103 ± 9 degrees with respect to the growth pulses (Figure 1.11) (Messerli et al. 1999; Lovy-Wheeler et al. 2006). Without the distribution of PM H^+-ATPase (Lefebvre et al. 2005), how can H^+ influx and its oscillation occur at the PT apex? Given that the cell wall of PT apex is rich in HG^{HDM} (Bosch et al. 2005) and PME (Rokcel et al. 2008; Tian et al. 2006), it is possible that pH oscillations reflect PME-dependent variations in matrix charge density (details see Matrix Charge section). In agreement with this hypothesis, Ca^{2+} extracellular influx oscillations (~140°, see below) is observed to lags the H^+ influx oscillations by ~30 degrees (Hepler et al. 2013).

Besides pH oscillations in tip growth, there are other factors that may directly or indirectly interplay with pH in the regulation of tip growth, including Ca^{2+}, K^+, PME, ROS, actin dynamics and cell wall deposition (Figure 1.11 and 1.12).

1.7.2 Ca^{2+}

It has been known for decades that Ca^{2+} is essential for PT growth (Brewbaker and Kwack 1963). Only growing PTs possess Ca^{2+} channel activity and tip-focused Ca^{2+} gradients (Malhó et al. 1995). The Ca^{2+} gradient is restricted to a small area of PM at the extreme tube apex in PTs of *Lilium longiflorum*, *Nicotiana sylvestris*, and *Tradescantia virginiana*. Both Ca^{2+} channel activity and Ca^{2+} gradients were involved in PT reorientation (Malhó et al. 1995). Additionally, recovery from mild temperature shock or caffeine is associated with a global swelling of the PT tip, concomitant with a high transient entry of Ca^{2+} into the tip (Pierson et al. 1996). As in other tip-growing cells, the cytosolic Ca^{2+} gradient and an elevated Ca^{2+} in the tip is essential for tip

growth in *Sinapis alba* RHs (Felle and Hepler 1997). The inwardly directed Ca^{2+}-current, localized elevated cytosolic Ca^{2+} in the tip, and constant Ca^{2+}-circulation are pivotal for RHs tip growth (Herrman and Felle 1995).

Cytosolic Ca^{2+} and extracellular influx Ca^{2+} oscillations were extensively studied in Lily PTs. The former is often measured by fluorescent dyes, such as fura-2-dextran and the latter is recorded by non-invasive extracellular, ion-selective Ca^{2+} electrode (Hepler et al. 2013). When pulsatile growth began, the basal Ca^{2+} influx decreased and a pulsatile component appeared, superimposed on the reduced basal Ca^{2+} flux. The peaks of the Ca^{2+} pulses at the cell surface averaged 38.4 ± 2.5 pmol cm^{-2} $second^{-1}$. Longer tubes had large pulsatile Ca^{2+} fluxes with smaller baseline fluxes. Cross-correlation analysis of the oscillatory growth rate and intracellular Ca^{2+} data indicates that the increase in Ca^{2+} slightly follows (+ 10° ~ 40°), rather than leads, the increase in growth rate (Messerli et al. 2000, Cárdenas et al. 2008), while the extracellular influx Ca^{2+} oscillations lags as much as ~ 140° (Messerli et al. 1999; Figure 1.11 and 1.12). Therefore, Ca^{2+} oscillations do not control the oscillations in secretion or in growth rate. It is worthwhile to note that as described above cytosolic Ca^{2+} and extracellular influx Ca^{2+} oscillations lack agreement in the phase relationship (Messerli et al. 2000; Cárdenas et al. 2008; Messerli et al. 1999). One reasonable explanation is that Ca^{2+} of extracellular influx binds to the cell wall, instead of the direct movement into the cytoplasm and equivalently that cell wall could be a "Ca^{2+} sink", delaying Ca^{2+} intracellular influx. Because the calculation of the influx needed to sustain in the cytosolic Ca^{2+} yields values of 0.5 ~ 2.0 pmol cm^{-2} s^{-1}, which is a small fraction of the measured amount, 15 ~ 20 pmol cm^{-2} s^{-1}. By contrast, the predict influx of

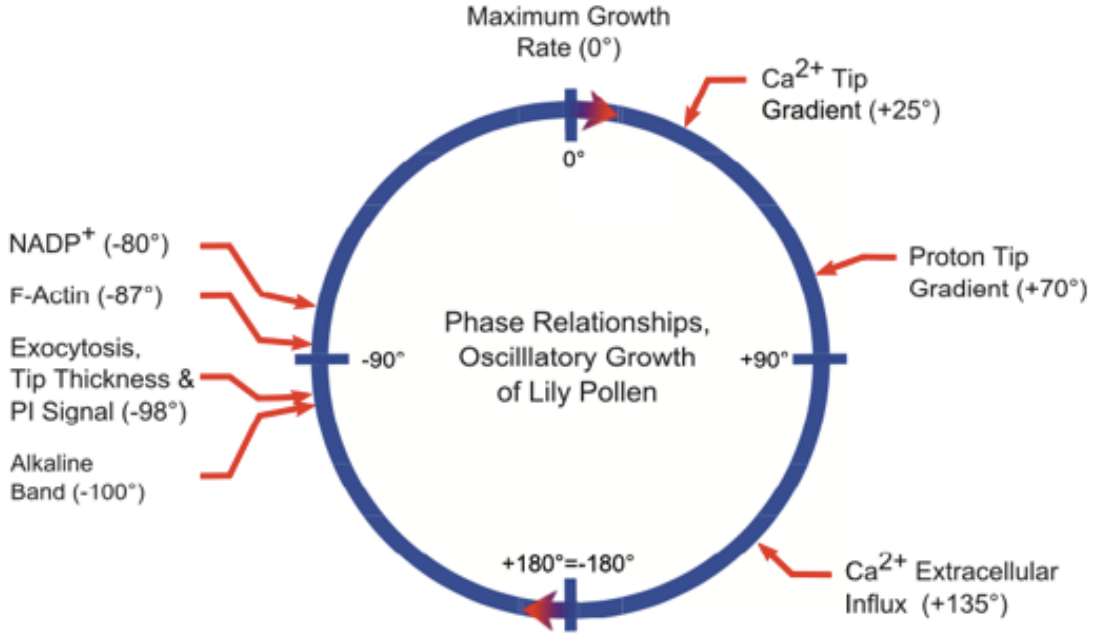

Figure 1.11: Phase Relationships in oscillatory growth in pollen tube. The positive sign (+) indicates that the increase in the particular event follows the increase in growth rate, whereas the negative sign (–) indicates that the increase in the event precedes the increase in growth rate. The increase in the intracellular Ca^{2+} follows the increase in growth rate. In addition, the increase in intracellular Ca^{2+} is out of phase with the increase in extracellular Ca^{2+} influx, and even more out of phase with the process of exocytosis. A series of events including the increase in $NAD(P)^{+}$, F-actin, exocytosis, build-up of wall material at the tip, and alkalinity all precede and thus anticipate the increase in growth rate. These events deserve further attention as potential stimulators of the growth rate. Modified from (Hepler et al. 2013)

35 pmol cm^{-2} s^{-1}, based on the calculations of the amount of wall material and the HG demethylesterification is much closer to the measured amount (Holdway-Clarke et al. 1997; Hepler and Winship 2010). Here again it is possible that Ca^{2+} influx reflects the binding to HG^{LDM} in the cell wall.

1.7.3 K^+

K^+ influx is a component of the current pulses peaks 7.5 s after the peaks of the growth pulses (Messerli and Robinson 1998; Messerli et al. 1999). The average fluxes at the cell surface during the peaks of the K^+ pulse was 688 ± 144 pmol cm^{-2} $second^{-1}$. The K^+ pulses have a phase lag of 100 ± 11 degrees with respect to the growth pulses (Figure 1.12) (Messerli et al. 1999). The K^+ and H^+ pulses are remarkably similar with their timing, average peak amplitude and proportional relationship to the preceding growth pulse. The close correspondence in timing and magnitude of the H^+ and K^+ influx pulses suggests the possibility that a H^+/K^+ cotransporter is responsible for the measured fluxes. The H^+/K^+ cotransporter is thought to aid K^+ uptake under low extracellular K^+ conditions. K^+ influx acts to restore either the total ionic concentration and/or osmotic concentration after the increase in cell volume. The K^+ influx is helping the cell to rapidly recover turgor pressure for the increased volume of the tube during the tip growth (Messerli et al. 1999).

1.7.4 PME

Given the central importance of pectin and its methyesterification state in the mechanics of the cell wall, it can be expected that PME levels also have a profound effect on PT growth (Bosch and Hepler 2005; Mckenna et al. 2009). That this is indeed the case is supported by a number of observations: Exogenous orange PME treatment triggered a dissipation of the Ca^{2+} gradient, the thickening of the apical cell wall and subsequent inhibition of cell elongation. Overexpression of NtPPME1 also inhibited PT growth (Bosch et al. 2005). *Solanum* PTs treated with orange peel PME exhibited a dramatic increase in stiffness and reduction of viscosity at the apex (Parre and Geitmann 2005). In *Arabidopsis*, a relatively small reduction of the total PME activity (in the *atpme1*

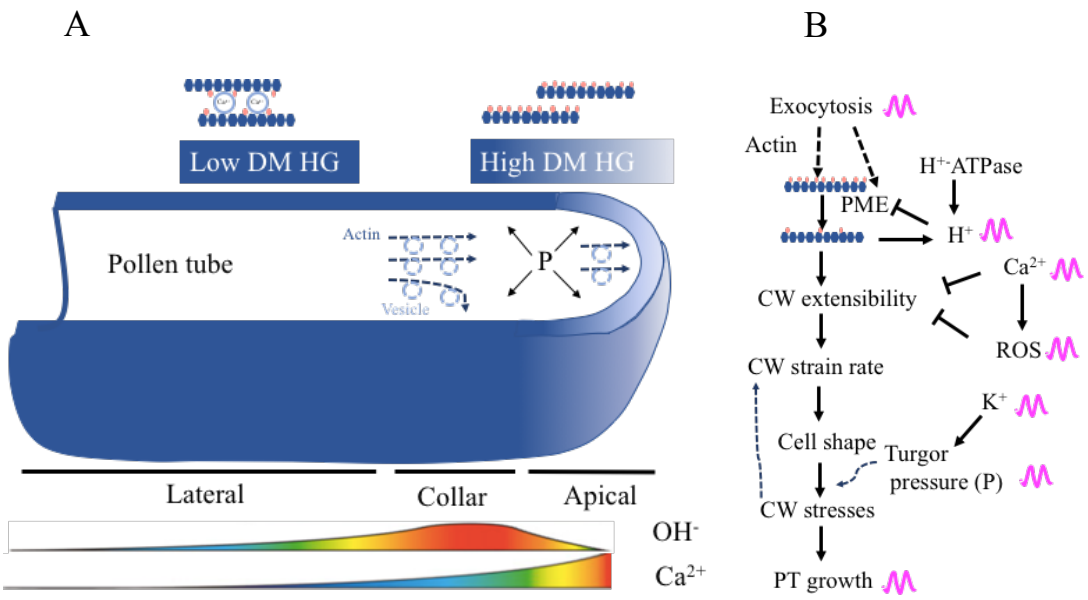

Figure 1.12: Pollen tube tip growth. (A) A model of pollen tube tip growth. The cell wall of flank and apical dome in pollen tube poss LDM (low degree of methylesterification) and HDM (high DM) HG, respectively. Turgor pressure (P) maintains tip growth. Exocytosis deposits cell wall components and controls the growth direction. pH and Ca^{2+} gradients exist and are associated with growth rate oscillations. Color bar, blue to red represents low to high concentration. (B) A simplified diagram for tip growth regulation. Many factors are involved in pollen tube tip growth. During growth rate oscillations, exocytosis, pH, Ca^{2+}, ROS, K^{+} and P concentrations display oscillatory variations (violet wave).

mutant) inhibited PT growth and caused irregular and curved morphology (Tian et al. 2006). Higher PME activity may also explain the inhibition of RH growth in a loss of function mutant for CrRLK1L ERULUS (ERU). Indeed, higher amount of demethylesterified HG accumulated at the RH tip in *eru* relative to the wild type (WT) and this could be prevented, together with the rescue of RH growth, by the chemical inhibition of PME activity (Schoenaers et al. 2018).

1.7.5 ROS

ROS also play a key signaling role in controlling growth of RHs and PTs. In RHs, oscillations in ROS levels are also associated with growth oscillations, which lag growth by ~ 7 s (Monshauson et al. 2007). RHs of the root hair-defective *rhd2-1* mutant, which lack a functional version of the NADPH oxidase ATRBOH C, burst at the transition to tip growth, suggesting a role for ROS in cell wall cross linking. This phenotype could be rescued by elevating the pH of the growth medium to > 6.0, suggesting that PME activity and Ca^{2+}-pectate crosslinks can compensate for the lack of oxidative crosslinks (Schopfer 2001).

1.7.6 Actin dynamics

The actin cytoskeleton is a major component of the PT, where it participates in cytoplasmic streaming. The cortical actin fringe is dynamic, with rapid turnover being necessary to allow it to keep pace with growth. A study of Féijo et al (1999) supposed that the alkaline band correlates with the position of the reverse fountain streaming at the base of the “clear zone”, and may participate in the regulation of actin filament formation through the modulation of pH-sensitive actin binding proteins. Indeed, modifying intracellular pH leads to reorganization of the actin cytoskeleton, especially in the apical domain and a pH-sensitive actin binding protein, actin-depolymerizing factor (ADF), together with actin-interacting protein (AIP) localize to the cortical actin fringe region. Acidification causes actin filament destabilization and inhibits growth by 80%. Increased actin polymerization supports faster growth rates and a H^+ influx, which

inactivates ADF/AIP, decreases actin polymerization, and retards growth. As pH increases, the activity of ADF/AIP again increases, repeating the cycle of events (Lovy-Wheeler et al. 2006). The protein villin/gelsolin may participate in the degradation of the actin fringe. When stimulated by elevated levels of Ca^{2+}, this protein promotes the fragmentation of actin microfilaments (Zhang et al. 2010). In this view, the Ca^{2+} level and the presence of villin/gelsolin at the PT apex could explain the absence of actin microfilaments at this position.

1.7.7 Exocytosis

Cell wall polymer-containing secretory vesicles are transported along actin cables. Exocytosis has been analyzed by using fused PME-YFP, DIC images and propidium iodide (PI) staining. The wall thickness shown by the latter two methods can indirectly reflect the secretion rate. Exocytosis in PT oscillates and leads the increase in growth rate (Rojas et al. 2011); the mean phase difference between exocytosis and growth is –98 ± 3 degrees in lily and –124 ± 4 degrees in tobacco (Figure 1.11). The oscillation in cell wall thickness precedes the Ca^{2+} oscillation (McKenna et al. 2009), and the cell wall thickness is correlated with the extent of the subsequent growth response, suggesting that cell wall deposition rate is the main parameter controlling growth rate (McKenna et al., 2009). In RHs, PI staining of the apical cell wall also shows that the oscillatory increase in fluorescence precedes the changes in the growth rate by an advance of -112° (Rounds et al. 2011). The deposition could actively induce dissociation of Ca^{2+}-pectate cross-links in PT apex, which allows turgor force to stretch the pectic wall. The nascent HG is immediately demethylesterified and then competed for Ca^{2+} to over-turn the load-bearing egg-box (Rojas et al. 2011). This suggested that exocytosis and wall expansion are tightly coupled in the tip growth.

1.8. Two paradoxes related to HG modification

1.8.1 HG demethylesterification can have opposing effects on cell wall stiffness

HG^{LDM} binds to Ca^{2+} and cooperatively forms Ca^{2+}-crosslinked stretches, so called egg-

boxes *in vitro* (Parre and Geitmann 2005). Also in the cell wall, HG demethylesterification is commonly thought to result in stiffer walls. For instance, in growing PTs, HG^{LDM} is associated with stiffer walls and cessation of wall expansion (Geitmann and Parre 2004). Similarly, HG demethylesterification is associated with the decline in the growth rate and increased wall stiffness along the apical-to-basal gradient of growing stems (Phyo et al. 2017). However, a series of elegant experiments with clear but perplexing results show that HG demethylesterification that localized in the shoot apical meristem of *Arabidopsis* results in elastically softer regions of the meristem surface, as measured by AFM (Peaucelle et al. 2008 and 2011). Also in the hypocotyl, HG demethylesterification leads to increase in cell wall elasticity and growth rate (Peaucelle et al. 2015): the transverse walls of slowly-growing cells in hypocotyl contained primarily HG^{HDM}, while rapidly-growing longitudinal walls had more HG^{LDM}.

1.8.2 HG demethylesterification, wall mechanics and growth: controversial results in the literature.

Two recent studies support the observation of Peaucelle et al (2008, 2011, and 2015) that HG demethylesterification also can lead to an *increase* in wall elasticity and cell expansion rate in context of asymmetrical leaf growth in tomato (Qi et al. 2017) and gynoecium morphogenesis (Andres-Robin et al. 2018). This raises the question how the same process (HG demethylesterification) can have opposite effects on cell wall mechanics and cell expansion rate.

One point of view challenges the correctness of the *in vivo* data supporting a cell wall loosening effect of HG demethylesterification. For instance, the model proposed by Qi et al. (2017), which correlates the appearance of HG^{LDM} (revealed using anti-glycan antibody 2F4 recognizing HG^{LDM}), in inner abaxial cell layers, with wall *loosening*, was challenged with an alternative model by Coen and Kennaway (2018). This model in which the epidermis has a constraining role and HG^{LDM}-rich inner wall layers that are *stiffer*, also can predict the observed changes in leaf shape. Qi et al. (2017) reported indeed a PME-induced increase in the elasticity of cell walls in the epidermis but did

not measure the stiffness in inner layers (This is difficult using AFM). Additional experiments are therefore needed to see who is right.

Along the same lines, a recent study (Bou Daher et al. 2018) repeated the experiments of Peaucelle et al. (2015), using the same genetic material, and came to the opposite conclusion that HG demethylesterification stiffens the wall of *Arabidopsis* hypocotyl epidermal cells and inhibits cell expansion. Given the importance of the findings of Peaucelle et al for my PhD thesis, I will here discuss in more detail these contradicting results. Peaucelle et al. (2015) observed in dark grown *Arabidopsis* hypocotyls that the cells that leave the apical hook undergo a transition from isotropic to anisotropic growth and that this symmetry breaking is associated with an increase in the elasticity of the longitudinal anticlinal cell walls as shown using AFM. They also showed increased staining for HG^{LDM} (using 2F4 antibody) in the longitudinal relative to the transverse walls. Finally, inhibition or promotion of PME activity by the inducible overexpression of PMEI3 and PME5, respectively, inhibited and promoted an increase in cell wall elasticity and cell expansion rate. Bou Daher et al. (2018) focused on the growth acceleration of the cells at the base of the hypocotyl that takes place 24 h after germination and also observed an increase in elasticity of the longitudinal cell walls. In contrast to Peaucelle et al. (2015), however, the authors observed preferential demethylesterification in transverse and not in longitudinal walls. To this end, Bou Daher et al. (2018) carried out an immunolabeling using antibodies LM20, LM19 or 2F4, recognizing HG^{HDM}, HG^{LDM} and Ca^{2+}-crosslinked HG^{LDM} [1] respectively, on longitudinal hypocotyl sections at 24 h post germination (hpg). They observed stronger LM20 (HG^{HDM}) labeling of longitudinal walls relative to transverse walls and stronger 2F4 (Ca^{2+}-crosslinked HG^{LDM}) labeling of transverse relative to longitudinal walls, whereas LM19 labeling was symmetric. The images however, are not really convincing and no quantification of the immuno-fluorescence is provided. In addition, our own

[1] 2F4 indeed labels Ca^{2+}-crosslinked HG, but Ca^{2+} is supplied in the immunolabeling buffer. Therefore, in the absence of information on the *in vivo* Ca^{2+} concentration, the assay does not indicate whether the pectate is also crosslinked *in vivo*. The conclusion of the authors: « We concluded that slowly growing transverse walls had more de-methylated pectin which was calcium cross-linked, while faster growing axial walls had more methylated pectin. » is therefore erroneous.

results on 2F4-labeled longitudinal sections of hypocotyls of the same age, showed a large variability in the labeling of the different cells, perhaps related to the growth stage, as well as higher labeling of longitudinal walls in zones that were expected to elongate. This supports the results of Peaucelle et al. (2015). The other discrepancy was that Bou Daher et al. (2018) observed growth inhibition and growth promotion upon ethanol induction of PME5 and PMEI3 respectively, associated with higher and lower wall stiffness respectively. These are responses completely opposite to those observed by Peaucelle et al. (2015). We do not understand why the results are so different, but inspection of the materials and methods section showed that Bou Daher et al. (2018) used very high concentrations of ethanol (100%) to induce the constructs (which may explain why they observed 100% penetrance of the induction as opposed to the 10 - 20% penetrance obtained by Peaucelle et al. (2015). We hypothesize that the induction of PME and PMEI in the presence of such high ethanol levels might be responsible for the phenotypes, especially when considering that a low ethanol concentration itself already leads to the induction of endogenous PME activity Andres-Robin et al. (2018) or a significant reduction in the ester bonds in the cell wall as shown by FTIR (Figure 1.13). Further work is needed to clarify this issue.

In conclusion, the contradicting results of Bou Daher et al. (2018) are to my opinion not sufficiently convincing to invalidate the results of Peaucelle et al. (2015). Furthermore, the results of Qi et al. (2017) and Andres-Robin et al. (2018) also support a wall-loosening and growth promoting effect of PME activity in two different contexts.

Alternative explanations for the dual effects of PME activity on cell wall mechanics depending on the context, may be that it depends on the nature of the PME activity (e.g. pH- or Ca^{2+}-dependence, blockwise or random activity, preferences for certain HG substrates), free Ca^{2+} concentrations in the apoplast, the extent of the demethylesterification or the presence of polygalacturonases or pectate lyases in the cell wall.

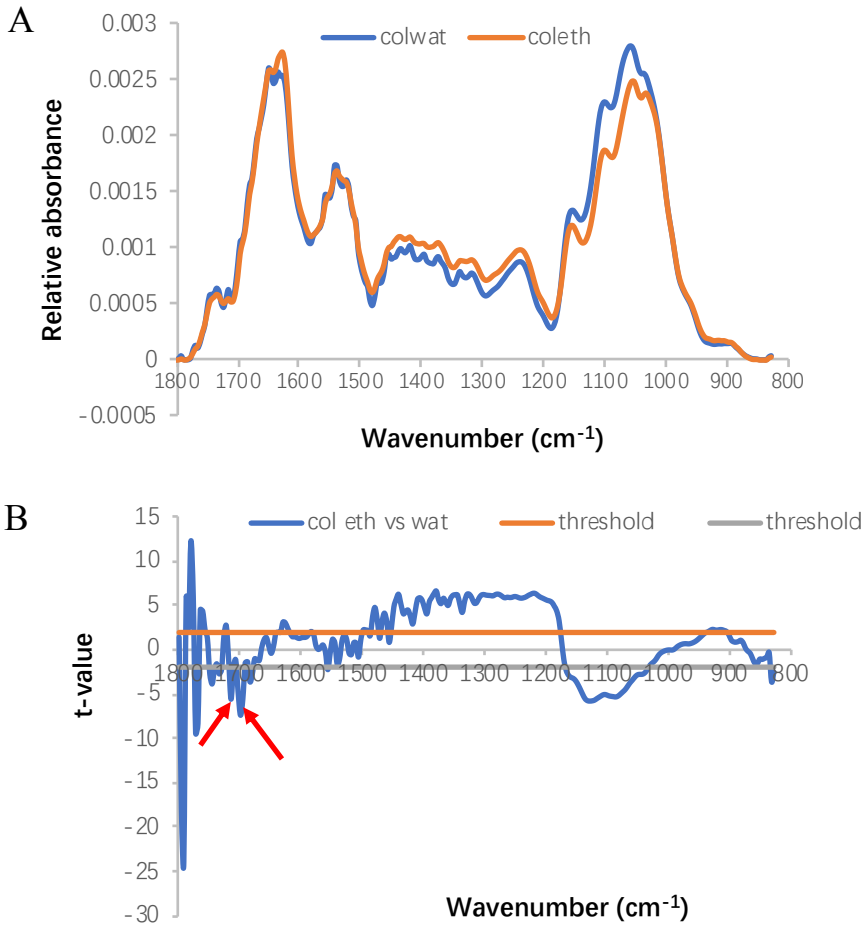

Figure 1.13: Ethanol treatment caused a significant reduction in the amount of ester bonds in the cell wall. (A) Average Fourier Transform Infrared (FTIR) spectra of 5-d-old water- and ethanol-treated Col seedlings (colwat and coleth respectively). (B) Student's t-test: t-value for the comparison between water- and ethanol-treated seedlings (y-axis) is plotted against the wave numbers (x-axis). Horizontal lines refer to the P = 0.05 significancy threshold. Equally significant minima correspond to ester linkages (red arrows) of pectin. n > 20. This suggests that low ethanol concentrations promote de-esterification activity in the cell wall.

1.8.3 Distinct PMEIs showed antagonistic effects on plant growth

Functional studies have been carried out in *Arabidopsis thaliana* for 14 distinct PMEIs (Table 1.1). Interestingly, previous studies showed antagonistic effects of the overexpression of PMEI3 and PMEI5, causing a reduction and an increase in HG^{LDM} respectively (Peaucelle et al. 2008, 2011, and 2015; Wolf et al. 2014), where PMEI5 overexpression enhanced BRI1 signaling with a resultant increase in HG demethylesterification (Wolf et al. 2012 and 2014). Likewise, manipulation of PMEI4 and PMEI9 expression led to opposite root phenotypes. Indeed PMEI4 overexpression and knock-out lines showed a decreased and increased root length respectively and PMEI9 overexpression and knock-down alleles showed an increased and decreased root length respectively (Hocq et al. 2017). These results raise the question how different PMEIs can have antagonistic roles *in vivo*?

To address these two questions, more research is needed. As shown in this introduction there are many interdependent factors that affect the properties of pectins gels and many pathways regulate the expression and activities of PMEs and PMEIs. The study of the control pH^{Apo} may shed some new light this complex issue.

1.9. Objectives of the thesis

At the start of my PhD, it was already known that pectin modification and pH^{Apo} are involved in the control of cell wall extensibility and growth. What remained unclear, however, was the mechanistic link between HG demethylesterification, pH^{Apo} and growth. In my PhD thesis, I have tried to address this issue through a set of linked but different basic questions:

(i) To what extent does the pH^{Apo} depend on HG demethylesterification? Does this also involve the PM H^+-ATPase?

(ii) How does the change in pH^{Apo} triggered by HG demethylesterification in turn affect plant growth *in vivo*? What is the effect of this pH^{Apo} change at the cellular level?

(iii) What is the difference in biochemical properties between PMEI3 and PMEI5 *in vitro*? Do PMEI3 and PMEI5 have different pH optima or target different PMEs?

In this study, I focused on PMEI3 and PMEI5, which, based on previous *in vivo* studies, may have different biochemical specificities. Firstly, I attempted to construct new inducible PMEI3 and PMEI5 overexpression lines and three cell wall-targeted genetically encoded pH sensors in parallel. Secondly, I tried to express these two PMEIs in *Pichia pastoris* and characterized PMEI3 activity *in vitro*. Lastly, I used genetic and pharmacological approaches to manipulate the level of HG demethylesterification in living *Arabidopsis* roots combined with the monitoring of the pH^{Apo} using genetically encoded ratiometric pH sensors and a pH-sensitive fluorescent dye.

Results

Chapter 2 Generation of new inducible PMEI3 and PMEI5 overexpressing lines

PMEs are encoded by remarkably large gene families (69 members in *Arabidopsis thaliana*) and most loss of function mutants analyzed so far did not show obvious changes in PME activity or phenotype suggesting high functional redundancy. To manipulate the PME activity *in vivo*, we therefore explored the use of PMEI overexpressing lines. To identify PMEI gene candidates that inhibit a broad range of PMEs, we analyzed the phylogenetic relationships and expression patterns for the 76 PMEI isoforms of *Arabidopsis thaliana.* The predicted full-length amino acid sequences of the PMEIs were obtained from The Arabidopsis Information Resource (TAIR, https://www.arabidopsis.org). We used the MUSCLE algorithm for the amino acid multiple sequence alignment, and a maximum likelihood tree was constructed using PYHML (Figure 2.1). A similar tree topology was also obtained when a different alignment algorithm was used (t-coffee, ClustalW2) (Figure 2.1). We investigated the expression patterns of the PMEI genes using Genevestigator (data not shown). Twenty-three PMEI genes that showed the relatively higher expression levels, including PMEI1-10, PMEI12-13, At4g12390, At5g62350, At1g14890, At2g01610, At1g23205, At1g70720, At1g23350, At4g15750, At1g47960, At5g64620 and At5g46950. Among those, six genes (PMEI3, 4, 5, 7, 8 and 10) were selected for inducible overexpression based upon their more ubiquitous expression patterns and/or higher expression levels under stress conditions. The work on PMEI3 and PMEI5 is shown in this study, while PMEI4, 7, 8 and 10 are being studied by Jerome Pelloux and colleagues (See Hocq et al. 2017 for PMEI4, Sénéchal et al. 2017 for PMEI7).

A

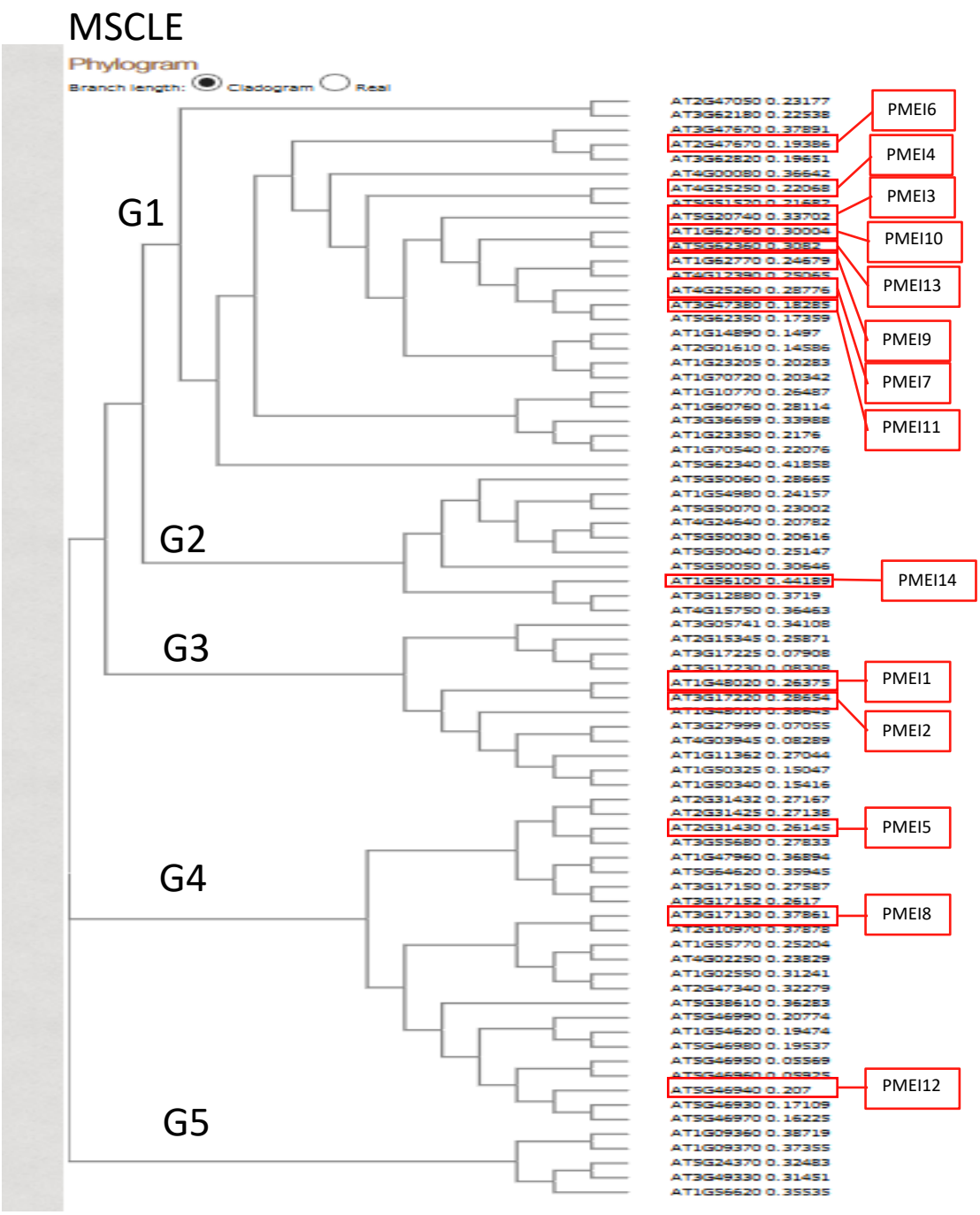
MSCLE
Phylogram
Branch length: Cladogram Real
G1
G2
G3
G4
G5
AT2G47050 0.23177
AT3G62180 0.22538
AT3G47670 0.37891
AT2G47670 0.19386
AT3G62820 0.19651
AT4G00080 0.36642
AT4G25250 0.22068
AT5G20740 0.33702
AT1G62760 0.30004
AT5G62360 0.3082
AT1G62770 0.24679
AT4G25260 0.28776
AT3G47380 0.18285
AT5G62350 0.17359
AT1G14890 0.1497
AT2G01610 0.14586
AT1G23205 0.20283
AT1G70720 0.20342
AT1G10770 0.26487
AT1G60760 0.28114
AT3G36659 0.33988
AT1G23390 0.2176
AT1G70540 0.22076
AT5G62340 0.41858
AT5G50060 0.28665
AT1G54980 0.24157
AT5G50070 0.23002
AT4G24640 0.20782
AT5G50030 0.20616
AT5G50040 0.25147
AT5G50050 0.30646
AT1G56100 0.44189
AT3G12880 0.3719
AT4G15750 0.36463
AT3G05741 0.34108
AT2G15345 0.25871
AT3G17225 0.07908
AT1G48020 0.26375
AT3G17220 0.28654
AT3G27999 0.07055
AT4G03945 0.08289
AT1G11362 0.27044
AT1G50325 0.15047
AT1G50340 0.15416
AT2G31432 0.27167
AT2G31425 0.27138
AT2G31430 0.26145
AT3G55680 0.27833
AT1G47960 0.36894
AT5G64620 0.35945
AT3G17150 0.27587
AT3G17152 0.2617
AT3G17130 0.37861
AT1G55770 0.25204
AT4G02250 0.23829
AT1G02550 0.31241
AT2G47340 0.32279
AT5G38610 0.36283
AT5G46990 0.20774
AT1G54620 0.19474
AT5G46980 0.19537
AT5G46950 0.05569
AT5G46940 0.207
AT5G46930 0.17109
AT5G46970 0.16225
AT1G09360 0.38719
AT1G09370 0.37355
AT5G24370 0.32483
AT3G49330 0.31451
AT1G56620 0.35535
PMEI6
PMEI4
PMEI3
PMEI10
PMEI13
PMEI9
PMEI7
PMEI11
PMEI14
PMEI1
PMEI2
PMEI5
PMEI8
PMEI12

B

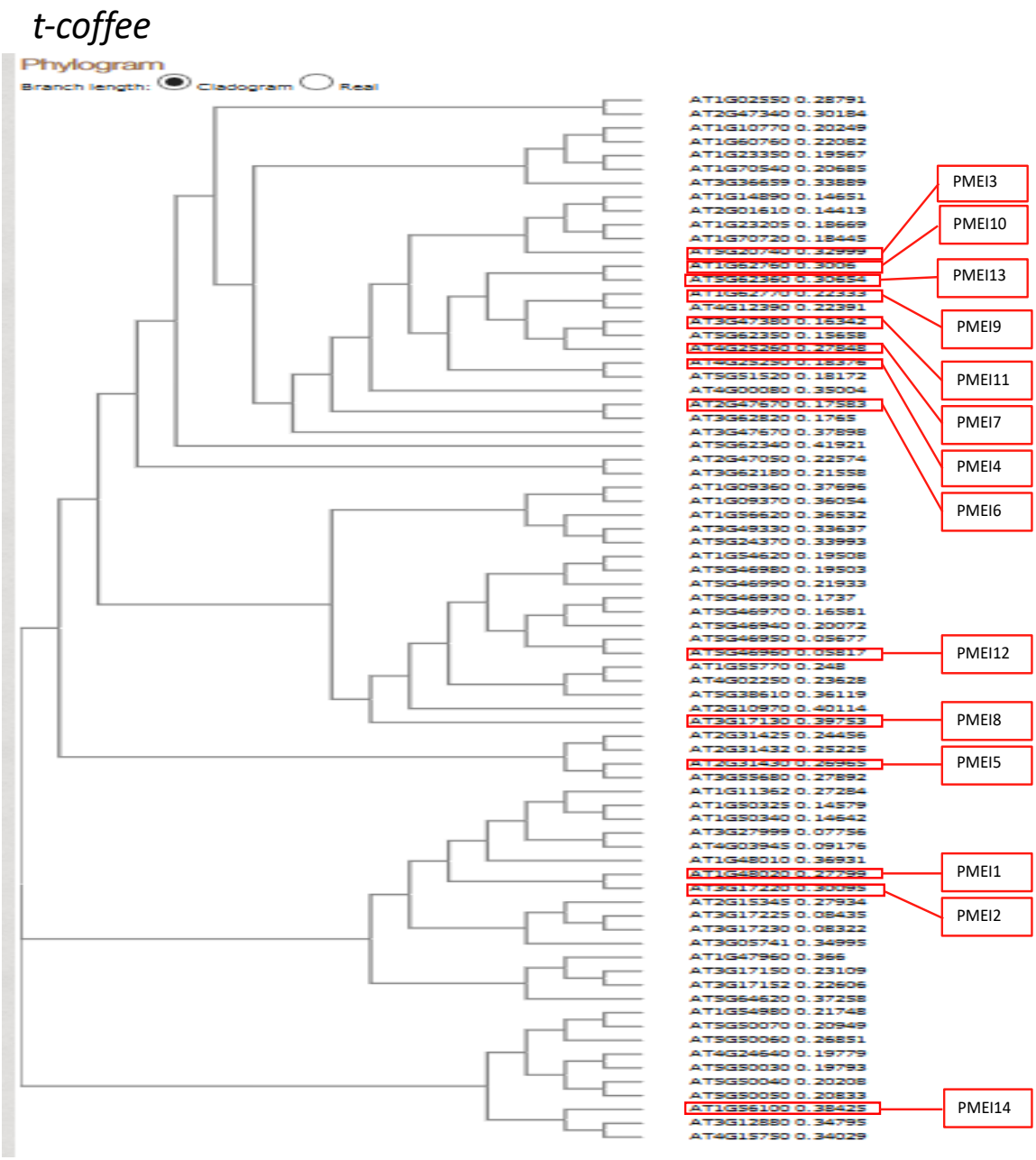

Figure 2.1: Phylogeny of PMEIs in *Arabidopsis*. Phylogenetic analysis of the predicted full-length amino acid sequences of 76 PMEIs was used the MUSCLE algorithm, and a maximum likelihood tree was constructed using PYHML (A). A similar tree topology was also obtained when a different alignment algorithm was used (*t-coffee*, B). PMEIs were divided into 5 groups (G) in left tree. Identified PMEI1-14 are in red boxes, see also Table 1.1.

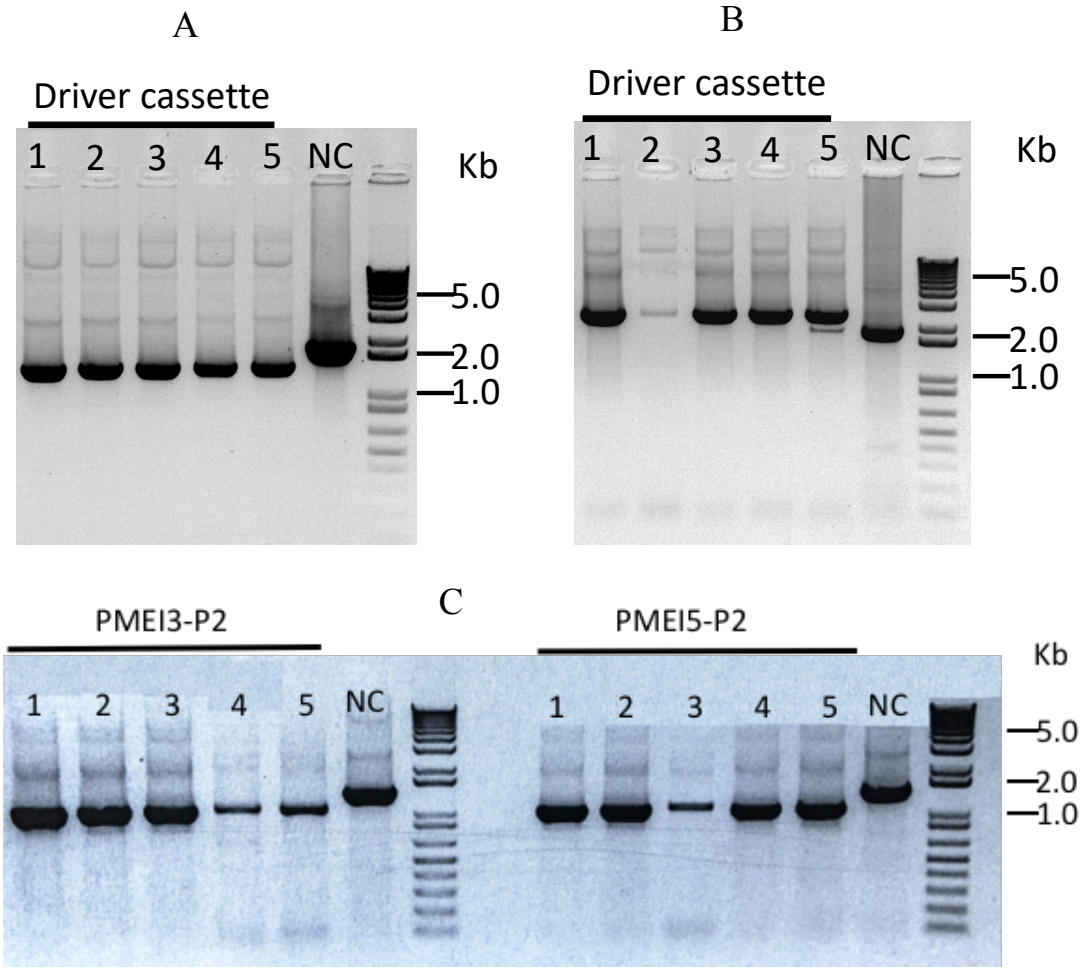

Figure 2.2: Representative agarose gel image showing colony PCR of the intermediate vector. (A and B) Driver cassette intermediate vector. (C) Effector cassette intermediate vector (P2). Five colonies from each group were tested. NC: negative control. Primers: pGGM00-F and pGGM00-R (A), UBQ10-F and pGGM00-R (B), pGGZ001-R and PMEI3-GG-R, PMEI5-GG-R (C).

PMEI3 and PMEI5 belong to group 1 (G1) and group 4 (G4) (Figure 2.1). Previous studies in our laboratory showed that the overexpression of PMEI3 caused, as expected for a PME inhibitor, an increase in pectin methylesterification (as shown in the shoot apical meristem or the hypocotyl epidermis, Peaucelle et al. 2008, 2011, and 2015). Unexpectedly however, the overexpression of PMEI5 caused a decrease in pectin methylesterification (observed in root cells, Wolf et al. 2012 and 2014). The increased PME activity in the PMEI5 overexpression lines was the result of the compensatory overexpression of other PME isoforms, which was mediated by the BRI1 and the receptor-like protein RLP44. These observations suggest that overexpression of PMEI5 but not of PMEI3 triggered compensatory BR signaling. One way to explain this is by assuming that the two proteins inhibit different sets of PMEs, which generate different HG demethylesterification patterns, only one of which is recognized as a signal for RLP44/BRI1 signaling. It should be noted however, that previously reported PMEI3 and PMEI5 inducible overexpression lines used two different induction systems, the ethanol-inducible pAlcA and the estradiol-inducible pMDC7 respectively (Peaucelle et al. 2015; Wolf et al. 2012). To rule out an effect of the induction system on the different response phenotypes, we decided to express the two PMEIs in the same dexamethasone (DEX)-inducible binary transactivation system in a GreenGate cloning system (Lampropoulos et al. 2013) (Figure 7.6 and 7.7). In this system (Figure 7.6), part 2 is the activator construct and part 1 and 3 are acceptor constructs. LhGR encodes a fusion protein between the LacI transcription factor and a glucocorticoid receptor. The latter binds the heat shock protein HSP70. Upon binding to the inducer DEX, LhGR is released from HSP70 and migrates into the nucleus, where it binds to the p4Op promoter driving the transcription of *PMEI3*, *PMEI5* and the "mTURQOUISE (mTUR)" reporter gene. The "REDSEED" reporter gene is a DsRed expressed from the seed-specific promoter (the promoter of the napin gene of *Brassica napus*) and can be used to screen for transformants in T1 seeds. This allows experiments to be carried out one generation earlier than when using resistance genes as selectable markers.

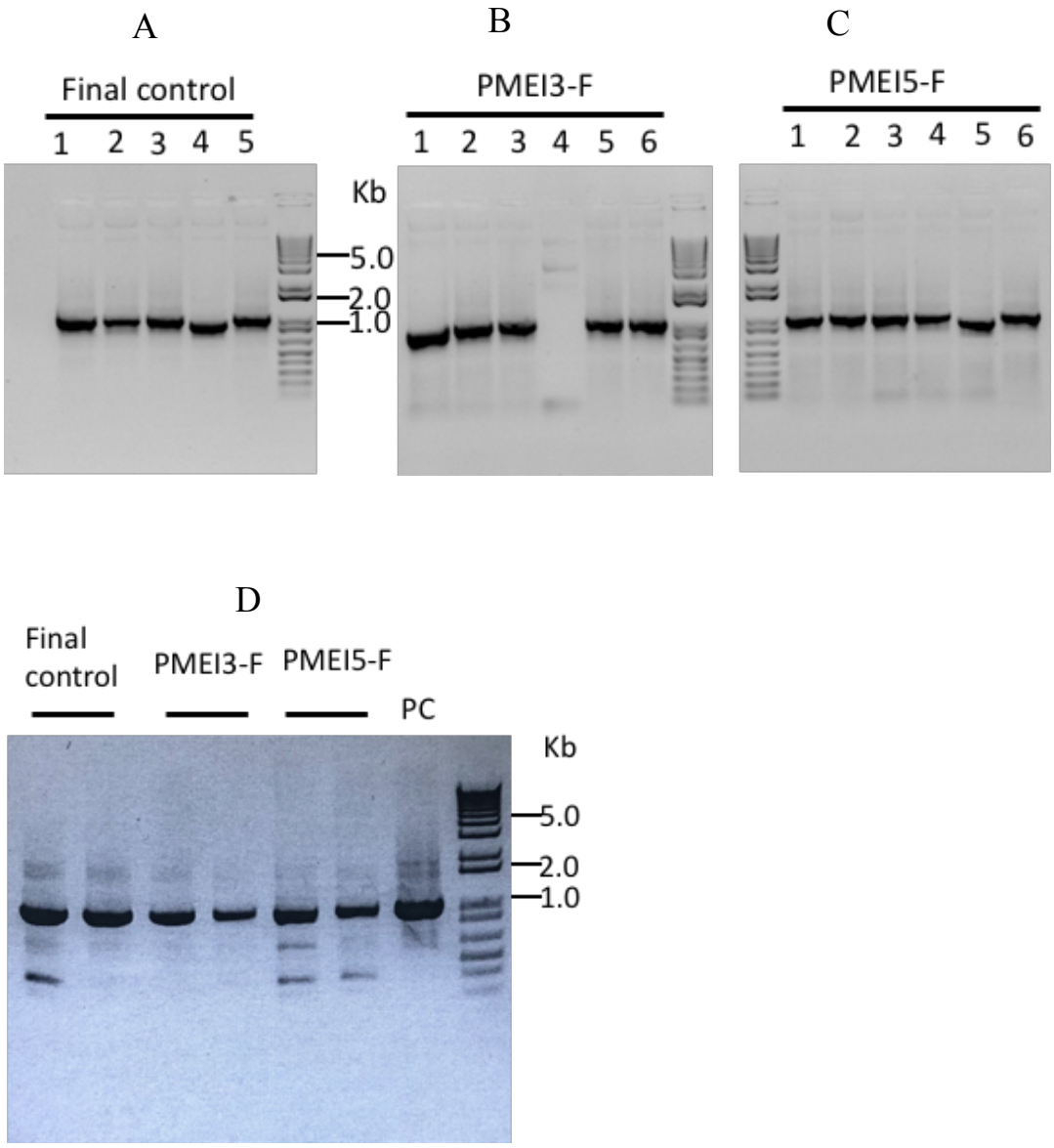

Figure 2.3: Representative agarose gel image showing colony PCR (A, B, and C) and common PCR (D) of the designed destination vector. Five or 6 *E. coli* colonies from Final control, PMEI3-F and PMEI5-F were tested (A, B, and C). Plasmids of two *Agrobacteria* colonies of each group (D). PC: positive control from Final control in (A). Primers: RedSeed-ter-F and Turquoise-R (A, B, C, and D)

The inducible PMEI3 and PMEI5 and control constructs, named PMEI3-F, PMEI5-F and Final control, were created as shown in the Figure 7.7. The intermediate and final vectors were verified, using colony polymerase chain reaction (PCR) and restriction enzyme digestion, for the presence of the desired insert (Figure 2.2). In all but one instance digestion patterns matched the expected sequence, which was finally confirmed by Sanger sequencing of a single clone for each construct. The sequence-verified plasmids were amplified and transformed into *Agrobacterium*. Before flower-dipping transformation, the plasmids from the Agrobacteria carrying PMEI3-F, PMEI5-F and Final control constructs were confirmed by PCR (Figure 2.3).

We transformed the constructs into Columbia-0 (Col-0) and the *xxt1xxt2* mutant. *xxt1xxt2* is a double mutant for XG xylosyl-transferase genes, which entirely lacks XG (Cavalier et al. 2008; Park and Cosgrove 2012). Cell walls in this mutant show reduced stiffness and ultimate stress relative to WT and show greatly reduced acid- and expansin-promoted creep (Park and Cosgrove 2012). Interestingly, in contrast to WT, *xxt1xxt2* mutant walls showed creep in the presence of pectin-degradation enzymes, such as PGases. This suggests that, in the absence of expansin-mediated and XG-dependent growth, HG has a more prominent load bearing role in the cell wall. We therefore reasoned that the effect of the inhibition of PME activity might be more pronounced in the *xxt1/xxt2* background. The plants transformed with Final control, PMEI3-F and PMEI5-F were named shortly Col-FX0, Col-FX3 and Col-FX5 in the Col background and xxt1/xxt2-FX0, xxt1/xxt2-FX3 and xxt1/xxt2-FX5 in the *xxt1/xxt2* background. Ten to 256 red seeds (Figure 2.4) of each group were collected, with transformation efficiencies ranging from 1.7/10,000 to 15.5/10,000 (Table 2.1). This result showed the REDSEED gene was functional in the expression cassette. To identify plants with unique insertion, a Chi-squared test was performed with T2 red seeds of 16 individual Col-FX0, Col-FX3 and Col-FX5 plants and 5, 8 and 8 unique insertion-plants were selected (data not shown). Interestingly, the fluorescence intensity levels allowed homozygote and heterozygote seeds to be distinguished (Figure 2.4). The transformants also showed the sulfadiazine-resistance, indicating that the antibiotic resistance gene was also functional (Figure 2.5).

Table 2.1 T1 red seeds of inducible PMEI3 and PMEI5 overexpressing lines.

Number of seed or plant	Col-FX0	Col-FX3	Col-FX5	xxt1/xxt2-FX0	xxt1/xxt2-FX3	xxt1/xxt2-FX5
Red seeds (T1)	102	256	78	19	10	22
Amplified	16	16	16	-	-	-
Plant with red seeds (T2)	16	16	15	-	-	-
Unique insertion lines	5	8	8	-	-	-
Transformed seeds ratio (1/10000)	7.6	15.5	4.8	3.2	1.7	4.4

Note: FX0: vector control, FX3: PMEI3, FX5: PMEI5.

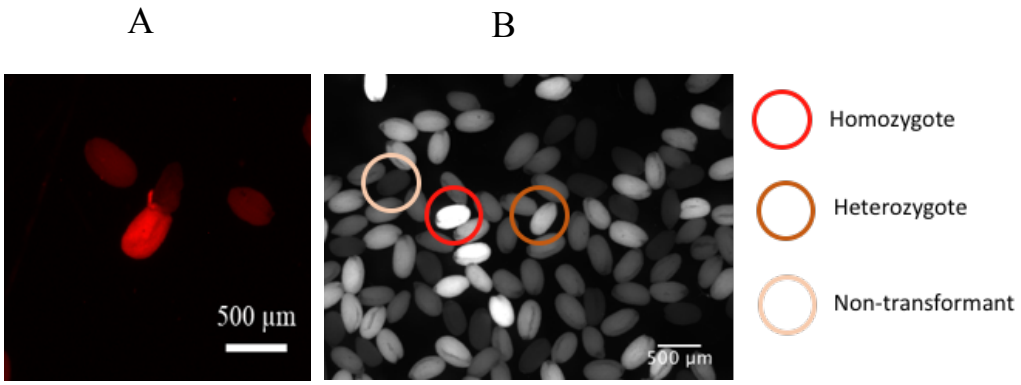

Figure 2.4: Representative red seeds of inducible PMEI3 and PMEI5 overexpressing lines. (A) Red seed of T1 transformant. (B) Heterozygote and homozygote showed different DsRed fluorescence intensity. Black-white image showed the different fluorescence intensities.

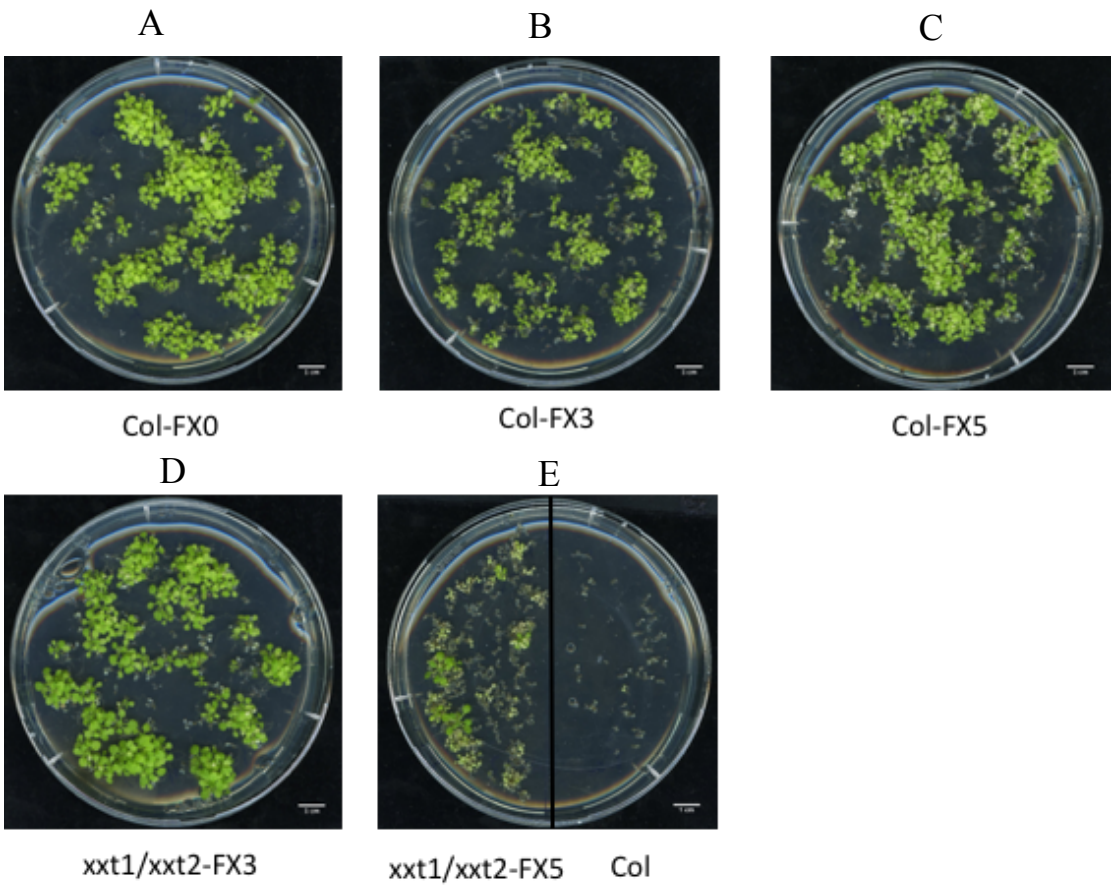

Figure 2.5: Sulfadiazine resistance test of T2 transformants of inducible PMEI3 (FX3) and PMEI5 (FX5) overexpression and vector control (FX0) lines in Col and *xxt1xxt2* background (A, B, C, D, and E). Plants were grown for 7 days in solid 1/2 MS medium complemented with 100 µM sulfadiazine.

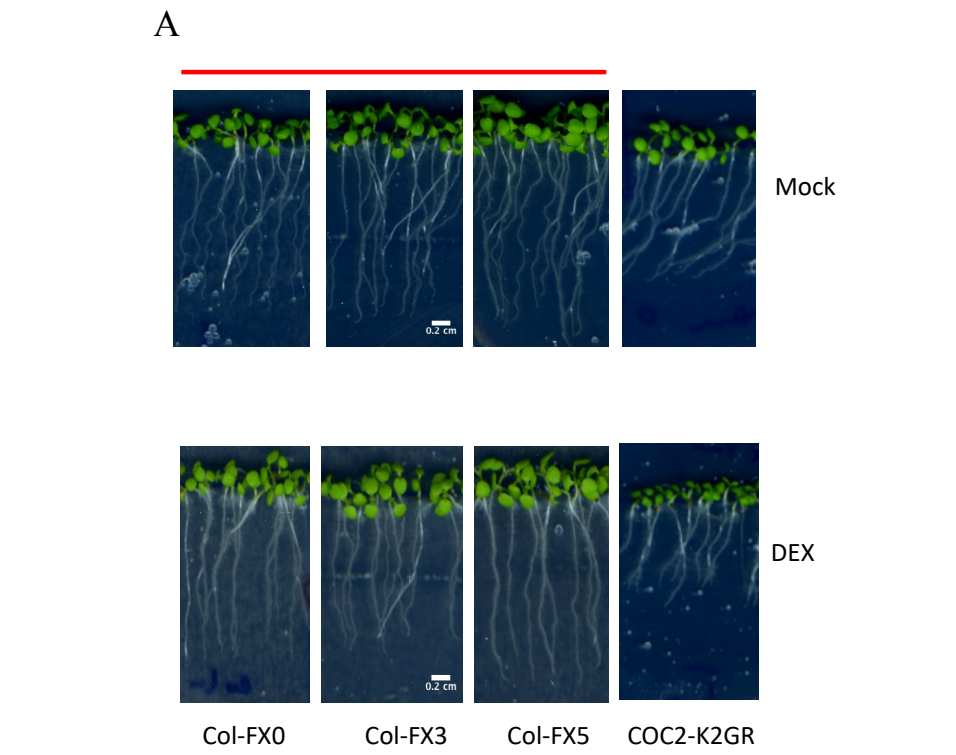

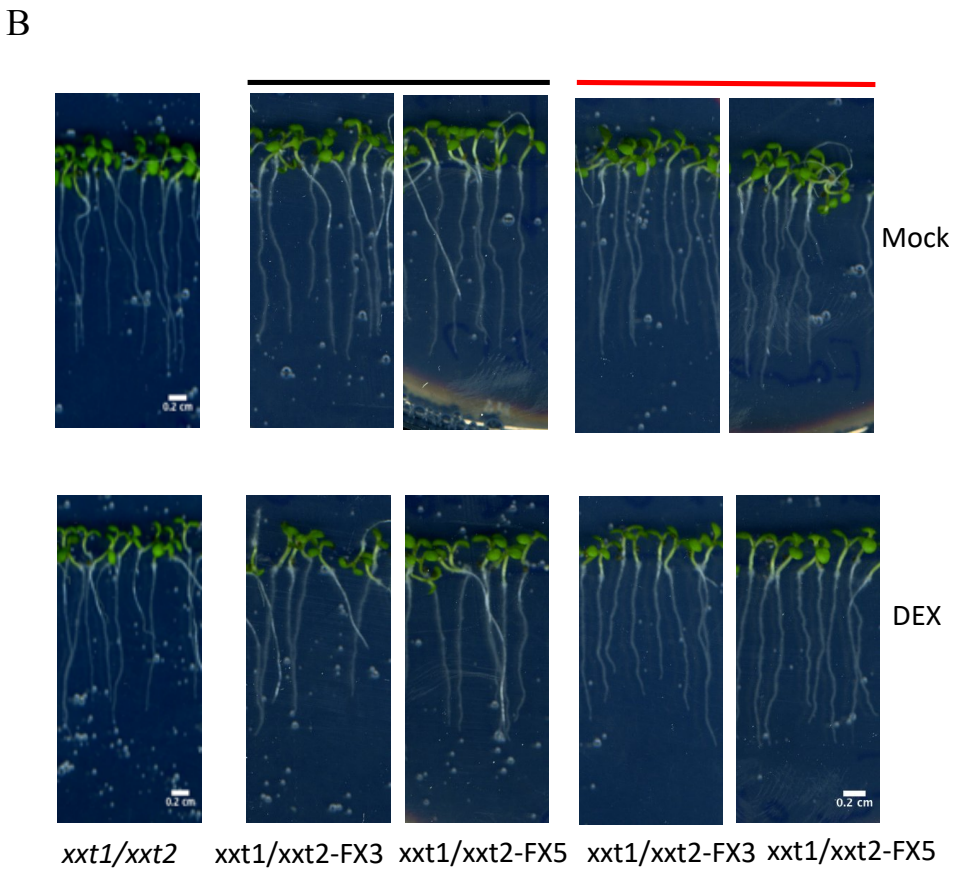

Figure 2.6: T2 transformant phenotyps of inducible PMEI3 (FX3) and PMEI5 (FX5) overexpressing and vector control (FX0) lines grown in Col and *xxt1xxt2* background in the growth chamber (A and B). Plant were

grown in solid 1/2 MS medium complemented 50 µM dexamethasone (DEX) and ethanol (Mock) for 10 days. COC2-K2GR was a positive control of DEX induction, which showed shorter root after induction. Black and red lines represent non-red and red seeds of T1 transformant, respectively.

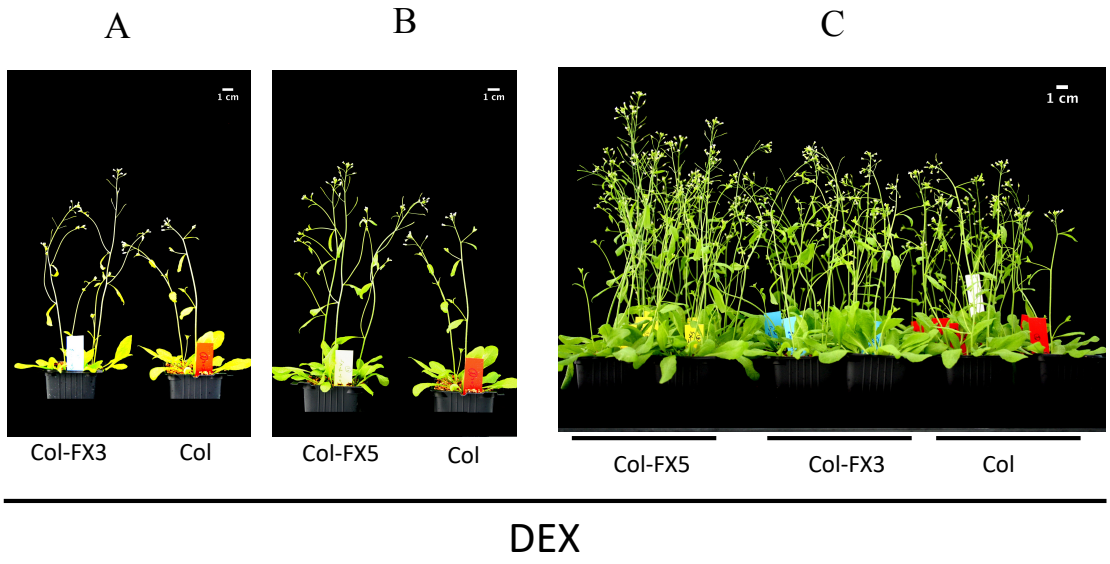

Figure 2.7: T2 transformant phenotype of inducible PMEI3 (FX3) and PMEI5 (FX5) overexpression lines in Col background grown in the green house for 4 weeks (A, B and C). Plants were sprayed with 50 µM dexamethasone (DEX). Induced Col-FX3 and Col-FX5 overexpression lines did not show typical phenotypes associated with PMEI3 or PMEI5 overexpression, such as dwarfism, twisted organ growth, waving roots and abnormal siliques.

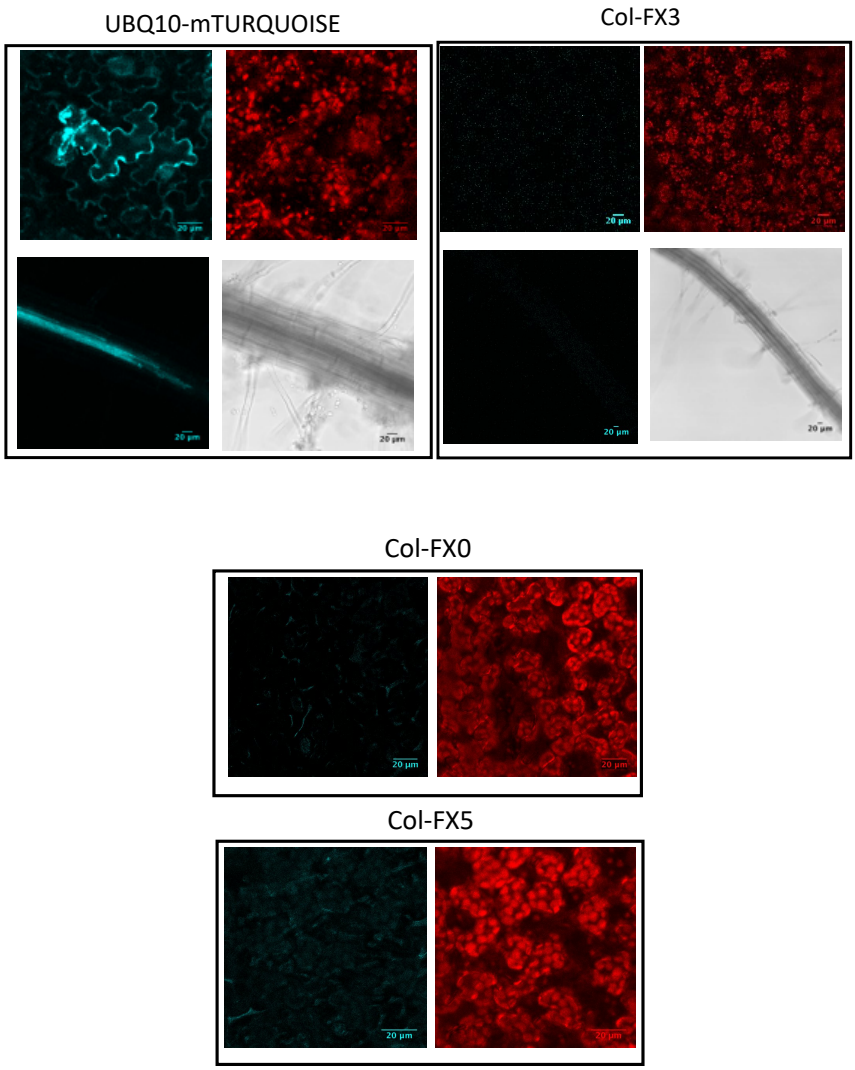

Figure 2.8: mTURQUOISE signal test. mTURQUOISE signal test in leaves or roots of inducible PMEI3 (FX3) and PMEI5 (FX5) overexpression and vector control (FX0) lines in Col background after 24-h 50 µM dexamethasone induction. UBQ10-mTURQUOISE is a positive control. Red is chlorophyll fluorescence.

After amplification of seeds, we looked for phenotypes segregating among the T2 plants. Previous studies reported that the inducible and constitutive PMEI5 overexpression lines showed obvious phenotypes including dwarfism, twisted organ growth, waving roots and abnormal siliques (Wolf et al. 2012 and 2014) and that PMEI3 overexpression lines showed PIN-like apical meristem and smaller plants as compared with WT (Peaucelle et al. 2008). We did not observe such phenotypes among the Col-FX3 and Col-FX5 plants under non-induction conditions. To test the inductivity of transgenic plants, T2 seedlings grown in a growth chamber and in the green house were induced with 50 μM DEX. 24 h after first spraying with DEX, we looked for the growth and developmental phenotypes. Un-induced transgenic plants and induced WT were used as negative controls. Unfortunately, no twisted organ, waving roots or abnormal siliques were observed (Figure 2.6 and 2.7).

We next tested the inducibility of the fluorescent reporter mTUR, which is present the three constructs. To test its signal in our transgenic plants, we induced 4-d old T2 seedlings with 50 μM DEX for 1 h, 4 h, 8 h and 24 h and observed the seedlings using confocal microscopy. No fluorescent mTUR signal could be observed after DEX induction, in contrast to a positive control line containing a DEX-inducible mTUR gene (kindly provided by Sebastian Wolf) (Figure 2.8). Quantative (q)-Real time (RT) PCR was used to quantify *PMEI3*, *PMEI5* and *mTUR* transcripts after DEX induction for 1.5h. We failed to observe an increase in transcript levels for any of the 3 genes. We also measured the PME activity of the cell wall-enriched extracts from the induced T2 transgenic seedlings by 50 μM DEX using a gel diffusion assay (GDA). The PME activity was not altered in transformants relative to the wild type and non-induced controls (Figure 2.9).

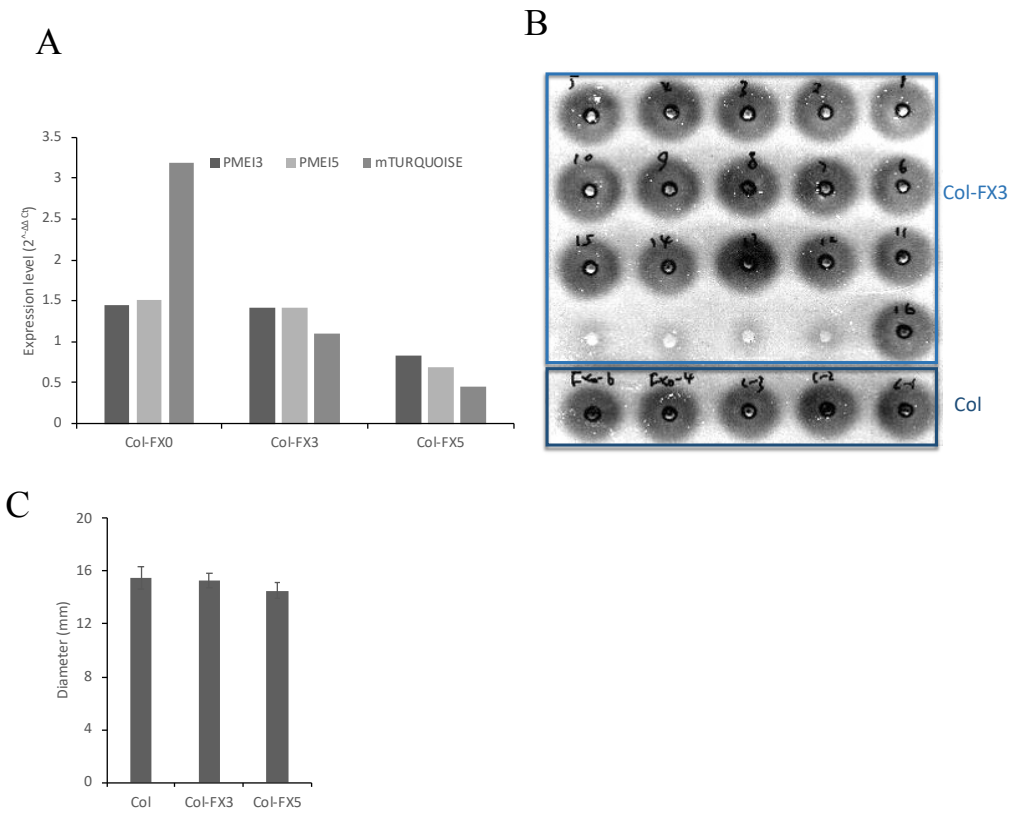

Figure 2.9: qRT-PCR quantification of PMEI3, PMEI5, and mTURQUOISE transcript levels (A) and PME activity measurement (B and C) of inducible PMEI3 (FX3) and PMEI5 (FX5) overexpressing and vector control (FX0) lines in Col background, after1.5-h (A) or 24-h (B and C) 50 µM dexamethasone induction. Representative image of PME activity measurement using a gel diffusion assay (B). Error bar: STD. n > 6 in C.

In conclusion, we successfully obtained transformants for PMEI3-F, PMEI5-F and Final control, but the transformed plants did not show DEX-inducibility of any of the transgenes, including the mTUR reporter. We do not know for the moment why this is the case, it may reflect co-suppression of the repeated promoter fragments in the constructs. Additional studies are required to sort this out. Given the limited time to finish my PhD thesis, I decided not to pursue the analysis of my transgenic lines and to remain focused on the previously defined objectives of my thesis using different tools.

Results

Chapter 3 Biochemical characterization of PMEI3 and PMEI5

3.1 PMEI3 and PMEI5 expression in *Pichia pastoris*.

To investigate the difference in biochemical properties between PMEI3 and PMEI5, they were heterologously expressed in *Pichia pastoris*. The coding sequences and codon-optimized sequences of PMEI3 and PMEI5 minus their signal peptides were cloned downstream and in frame with the poly-Histidine sequence present in an inducible expression vector, pPICZαB. Three types of constructs of PMEI3 and PMEI5 were created (Figure 3.1), named PMEI3/5, PMEI3/5t, and CO-PMEI3/5, respectively. In PMEI3/5t, a poly-Histidine tag and a stop codon were cloned upstream and downstream of gene of interest, respectively. In CO-PMEI3/5, PMEI3 and PMEI5 minus their signal peptides were condon-optimized according to the codon usage frequency of *Pichia pastoris*. All final constructs were checked for the presence of the desired insert using colony PCR and restriction enzyme digestion (Figure 3.1) and confirmed by Sanger sequencing of a single clone for each construct. Precise constructs were transformed into the *Pichia* strain X33. To check if the recombinant protein expressed, supernatants were isolated and concentrated after 4-d cultivation with 0.5% (v/v) methanol induction, and then the recombinants PMEI3 and PMEI5 were analyzed by Western Blotting (WB) using antibodies raised against the poly-Histidine or C-Myc tag (Figure 3.2 and 3.3). Induced cultures harboring the PMEI3 constructs displayed a clear band at the expected molecular mass of about 19.9 kDa (Figure 3.2 and 3.3). In contrast, cultures harboring PMEI5 and CO-PMEI5 constructs showed one or two bands of 35 kDa and 55 kDa, bigger than expected size (17.9 kDa) in WB with the poly-Histidine antibody (Figure 3.2 and 3.3), but not with the c-Myc antibody (Figure 3.3). To assess the inhibiting activity of PMEI3 and PMEI5, concentrated supernatants were tested with 3 types of PME in GDA with a pectin of DM 90% at pH 6.3 (Figure 3.4). The supernatants from cultures harboring PMEI3, PMEI3t and CO-PMEI3 showed clear inhibiting activity on orange PME, *Arabidopsis* flower PMEs and root PMEs, while none of supernatants from PMEI5, PMEI5t and CO-PMEI5 cultures showed inhibiting activity on these PMEs (Figure 3.4).

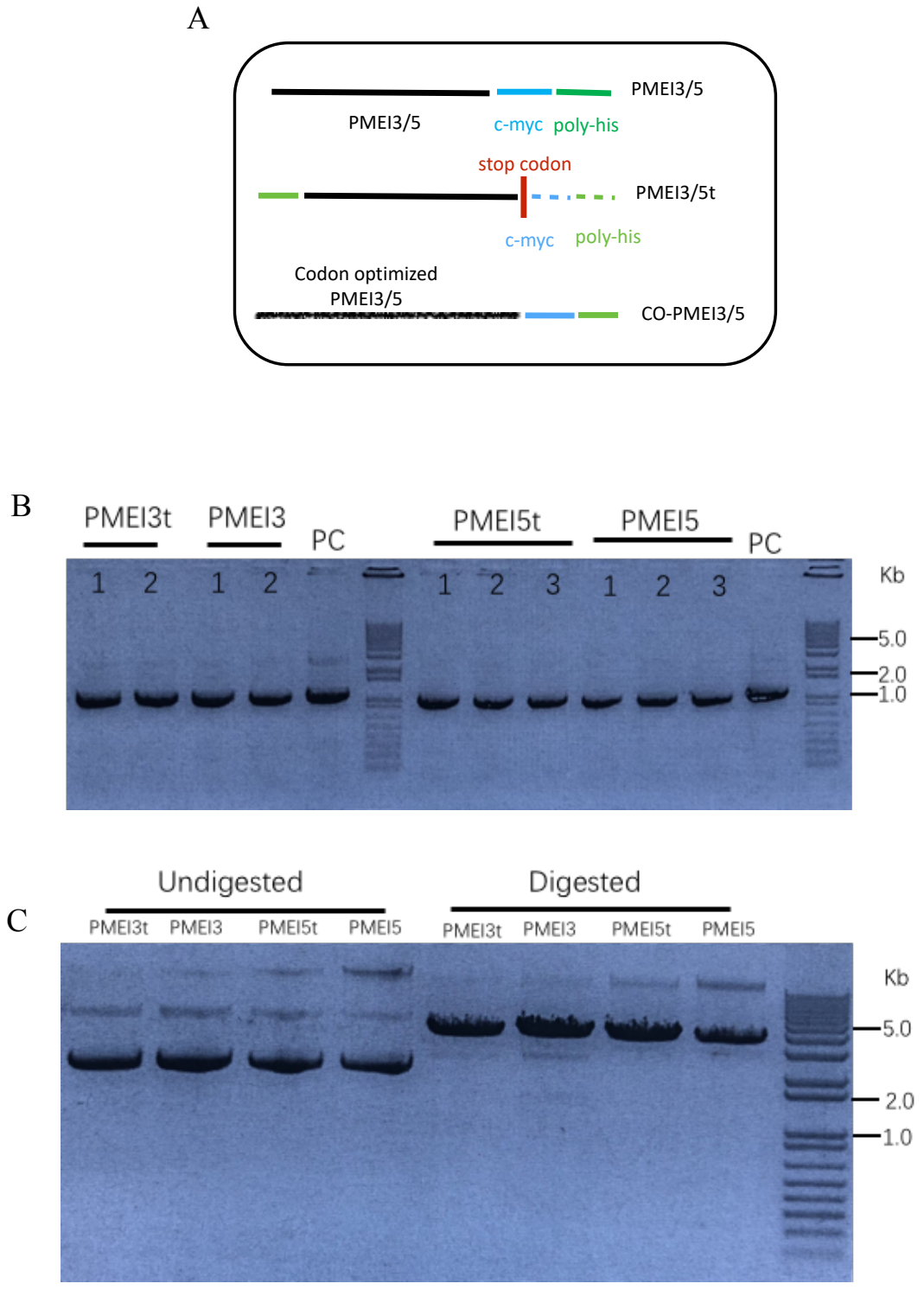

Figure 3.1: constructs for heterologous expression of PMEI3 and PMEI5 in *Pichia pastoris*. (A) Structure of 3 PMEI3 and PMEI5 constructs. See Methods and Materials for vector map. (B) and (C) Representative agarose gel image showing colony PCR of the designed vectors (B) and restriction digestion by Sac I (C). Two or three colonies of each group were tested (B and C). PC: Positive control. Primers: 3'-AOX1 and 5'-AOX1 (B).

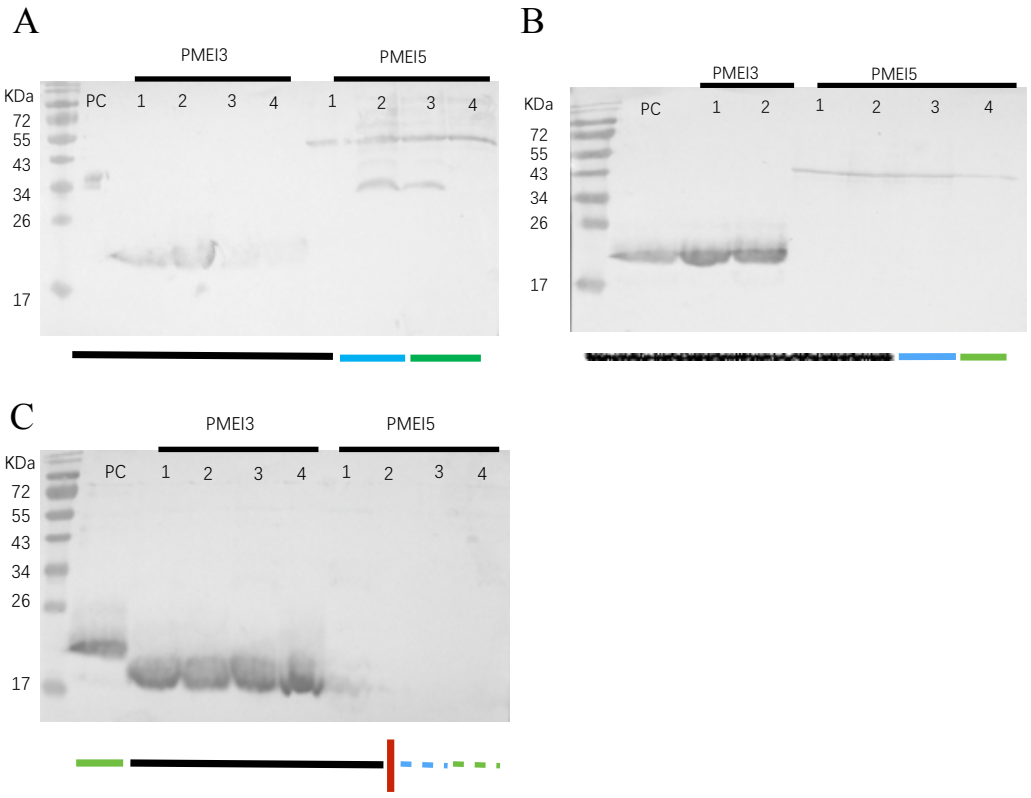

Figure 3.2: Expressioin of PMEI3 and PMEI5 constructs. Two (B) or 4 (A, B, and C) colonies from each group were tested. Construct structures are shown in Figure 3.1. PC: positive control.

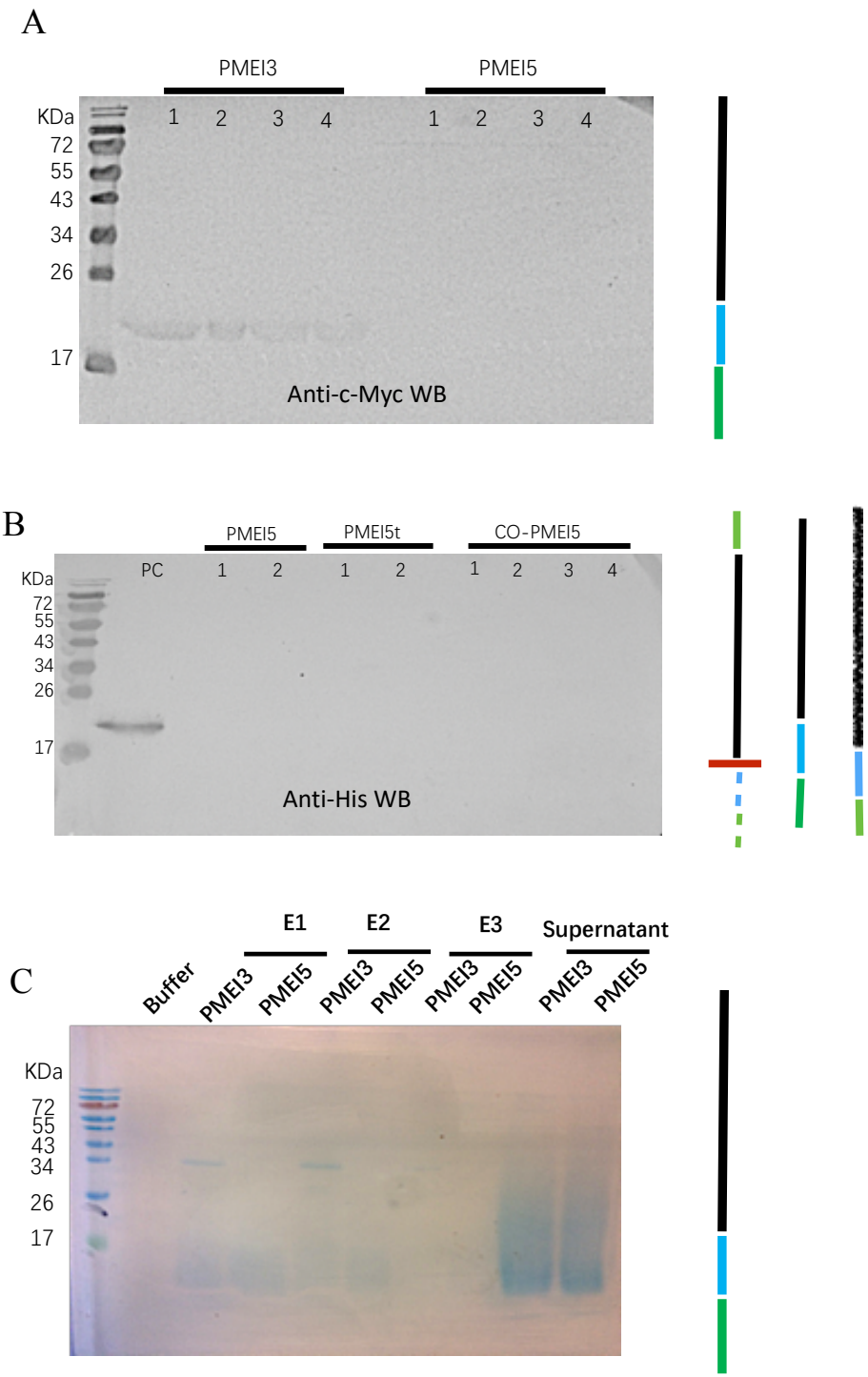

Figure 3.3: Recombinant PMEI5 expression test. Western Blotting (WB) against poly-c-Myc (A) or poly-histidine (His) (B) of supernatant of culture harboring PMEI3 or PMEI5 constructs. (C) SDS-PAGE of purified products by affinity chromatography of the PMEI3 and PMEI5 cultures. Two (B and C) or 4 (A, B, and C) colonies from each group were tested. Construct structures are shown in Figure 3.1. PC: positive control. E_n: elution order.

PMEIs and cell-wall invertase 1 (INV1) inhibitor (CIF) are sequence-related proteins with very similar core structures (Hothorn et al. 2004). Comparing the interface residues in a PMEI-PME complex (Di Matteo et al. 2005) with those of the INV1-CIF complex reveals that both inhibitors directly bind to the substrate-binding cleft of their respective target enzymes. Sequence comparison showed that PMEI5 is more similar to a CIF than to a PMEI (Lionetti et al. 2017). We therefore carried out an invertase activity assay on the supernatant of PMEI5, PMEI5t and CO-PMEI5, but no CIF activity could be observed (Figure 3.5).

Using Mass spectrometry (MS), PMEI3 bands and the "putative" PMEI5 bands were further analyzed (with the INRA Platform PAPSSO). Nineteen peptides corresponded to the AtPMEI3 primary sequence, which confirmed the successful heterologous expression of PMEI3 in *Pichia*. Form the "putative" PMEI5 bands, 21 peptides corresponded to the sequence of formate dehydrogenase (AB472090) in *Pichia* cells (Figure 3.6), indicating that the bands did not correspond to PMEI5. To rule out the possibility that PMEI5 was retained inside yeast cells, we lysed *Pichia* cells containing CO-PMEI3 and CO-PMEI5 constructs. We did not observe a signal inside cells for neither of the PMEIs (Figure 3.7). This showed that the *Pichia* expression system has high secretion efficiency for PMEI3 and that PMEI5 is not expressed in these cells, despite the use of a codon optimized sequence. It is not known why PMEI5 is not expressed, but it is possible that PMEI5 protein accumulation requires the presence of (an) accessory protein(s).

Table 3.1 PMEs used in this study.

Name	Express or extract from	Origin	Reference
Orange PME	Orange peel	Orange	Sigma P5400
Citrus thermo-tolerant PME	*Pichia pastoris*	Citrus	J. Pelloux et al. Unpublished
AtPME2	*Nicotiana tabacum*	*Arabidopsis thaliana*	J. Pelloux et al. Unpublished
AtPME3	*Nicotiana tabacum*	*Arabidopsis thaliana*	Sénéchal et al. 2015 and 2017 ; Hocq et al. 2017
Flower PME	*Arabidopsis* flower	*Arabidopsis thaliana*	This study
Root PME	*Arabidopsis* root	*Arabidopsis thaliana*	This study

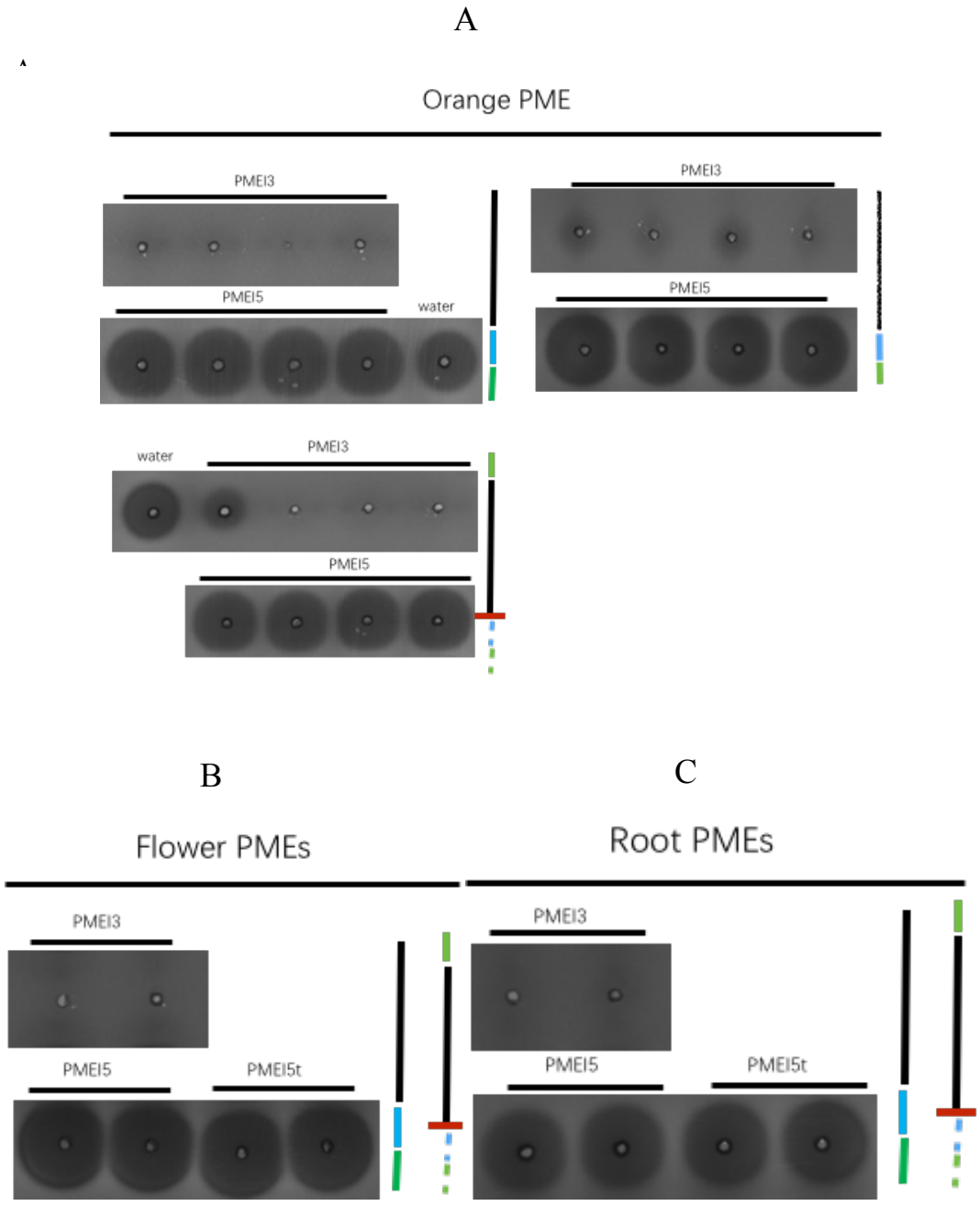

Figure 3.4: PMEI activity measurements using gel diffusion assays. Inhibition assays on orange PME (A) and PME preparations from Arabidopsis flowers (B) and roots (C) using the supernatant of cultures harboring PMEI3 or PMEI5 constructs. Two or 4 colonies from each group were tested in (A, B, and C). Construct structures are shown in Figure 3.1. Water was used as negative control.

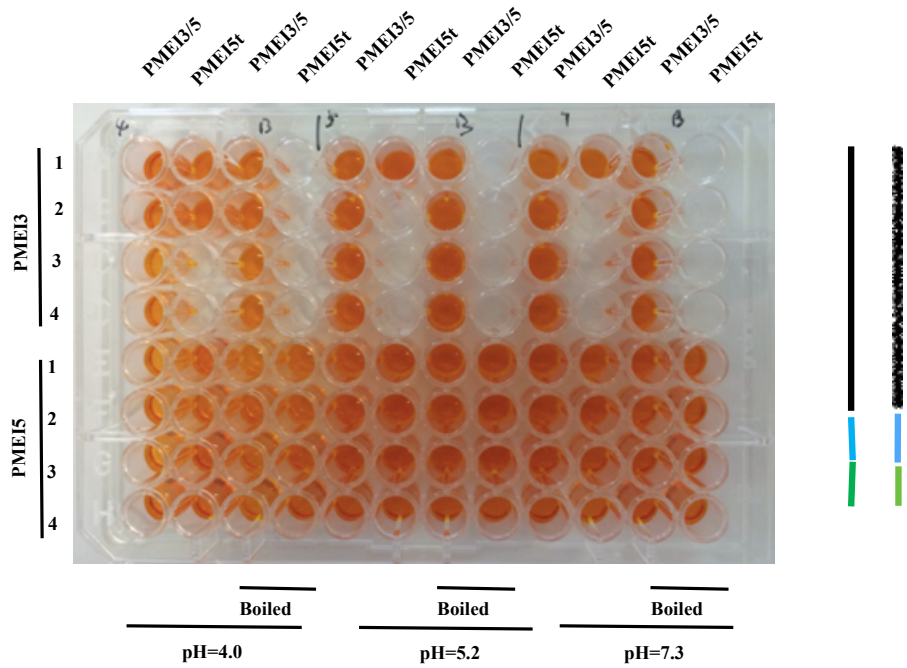

Figure 3.5: Invertase inhibitor activity test on supernatants of cultures harboring PMEI3 or PMEI5 constructs. Four colonies from each group were tested. Boiled supernatant was used as negative control. Construct structures are shown in Figure 3.1.

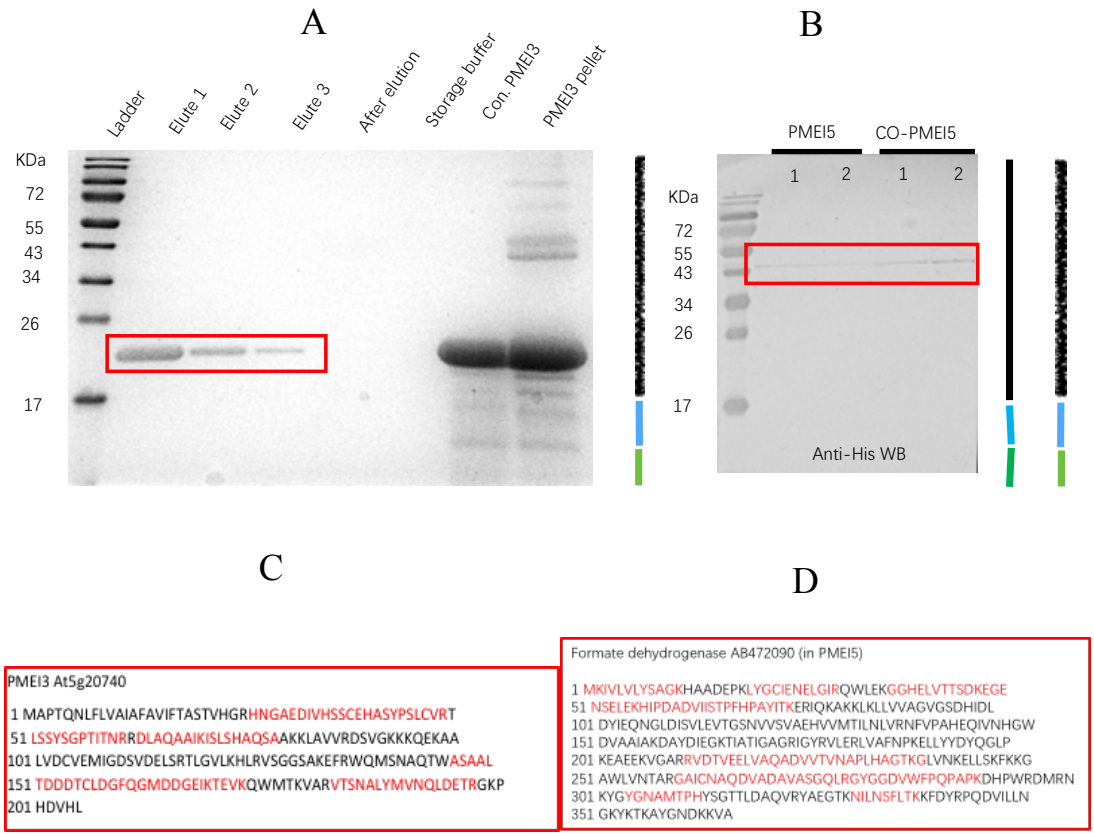

Figure 3.6: Mass spectrometry (MS) analysis of putative recombinant PMEI3 and PMEI5. SDS-PAGE of proteins purified by affinity chromatography of the PMEI3 (A) and PMEI5 (B) cultures. Peptides identified by MS/MS analysis are underlined in red (C and D). Construct structures are shown in Figure 3.1.

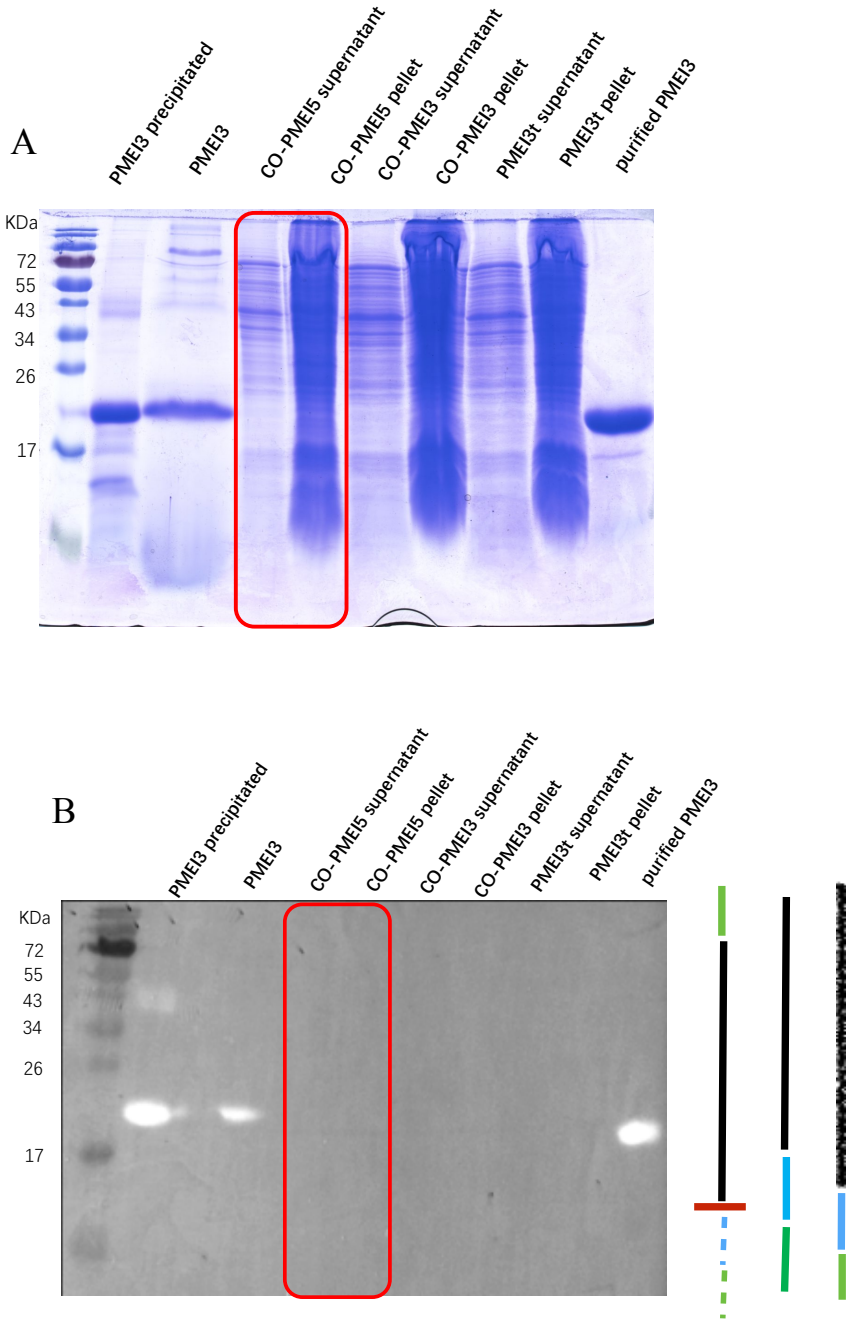

Figure 3.7: Secretion efficiency test of recombinant PMEI3 and PMEI5. Lysed Pichia cells harboring PMEI3 or PMEI5 construct using SDS-PAGE (A) and Western Blotting (B). PMEI5 samples are highlighted by a rectangle. Purified PMEI3 (dissolved PMEI3 after purification by Ni-NTA agarose) and PMEI3 in cell pellet ("PMEI3 precipitated") and culture supernatant ("PMEI3") are used as positive controls. Construct structures are shown in Figure 3.1.

3.2 PMEI3 characterization

PMEI3 recombinant protein was purified subsequently using cOmplete Hig-tag purification Resin and *in vitro* characterized by GDA on six different PME preparation (Table 3.1). In addition, we quantified the binding of PMEI3 to PME3 using MicroScale Thermophoresis (MST).

3.2.1 PMEI3 activity measurement.

Using a colorimetric methanol quantification assay, we first determined the activity of the six PME preparations (Orange PME, citrus thermal-tolerant (TT) PME, AtPME2, AtPME3, *Arabidopsis* flower PMEs and root PMEs) on a reference substrate (citrus pectin) at pH 7.5 and selected a non-saturating enzyme concentration to be used in the inhibition assays (rectangle in Figure 3.8). For the inhibition assays we used a GDA with three concentration (0.025, 0.05 and 0.25 µg) of recombinant PMEI3 along with mock and boiled control samples, incubated with the PME preparation for 1h at pH 5.0, 6.3 or 7.5. The enzyme activity was deduced from the halo diameter after calibration with samples of known PME activity determined by the colorimetric assay.

As shown in Figure 3.9, the PME activity for all preparations was inhibited by PMEI3 in a pH-dependent manner, with strong inhibition at pH 5.0 and no inhibition at pH 7.5. The concentration- and pH-dependence, however, varied between the samples. Concerning the concentration dependence, PME3 and root PMEs showed the highest sensitivity to PMEI3 at pH 5, followed by flower PMEs, AtPME2 and orange PME. Citrus TT PME was the least sensitive to PMEI3. Concerning the pH sensitivity, PME activity in all samples was also inhibited, to a lesser extent, at pH 6.3, except for AtPME2, which did not show any inhibition at this pH. Interestingly, boiling did not affect, or only slightly reduced, the PMEI3 activity indicating a very stable 3D structure for the inhibitor.

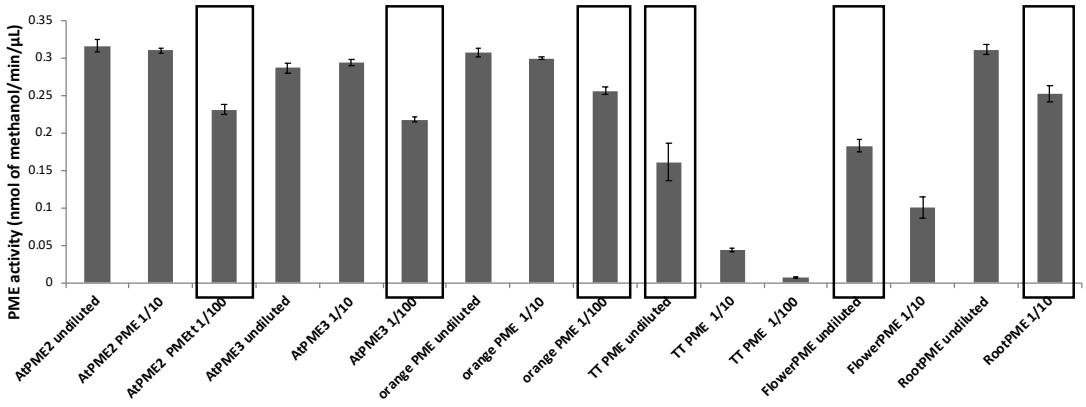

Figure 3.8: PME activity measurement using a methanol colorimetric assay. 1/10, 1/100: fold dilution. TT PME: citrus thermal tolerant PME. The concentrations corresponding to bars surrounded by rectangles were used for the inhibition assays of recombinant PMEI3. Error bar: STD. n=3.

A

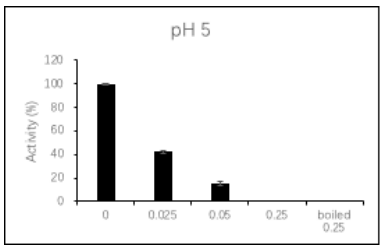

B

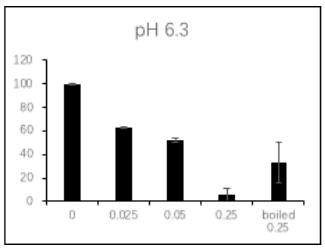

C

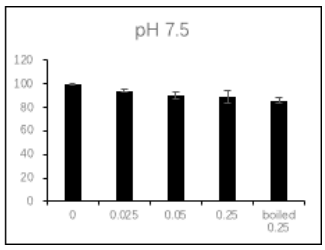

D

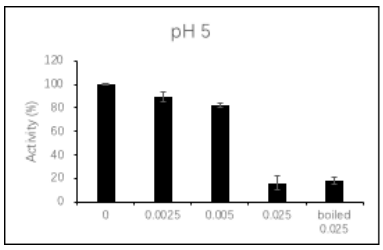

E

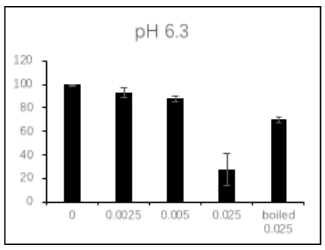

F

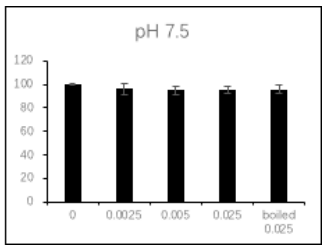

G

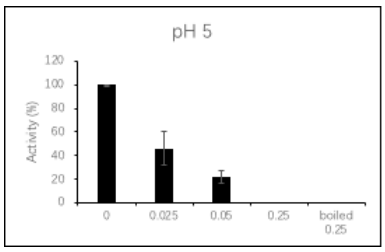

H

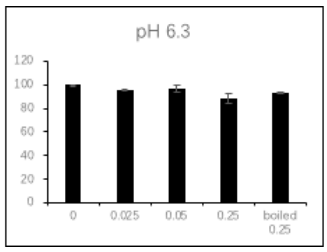

I

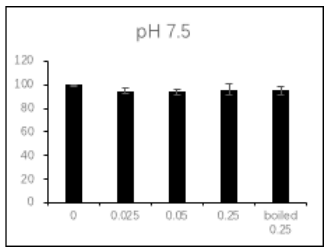

J

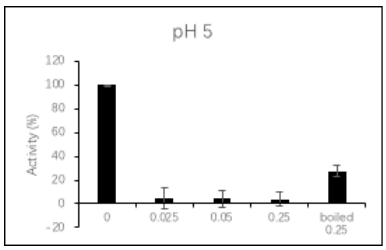

K

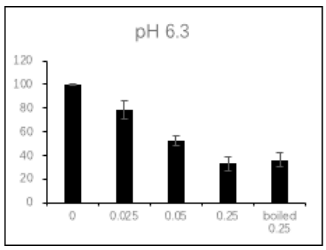

L

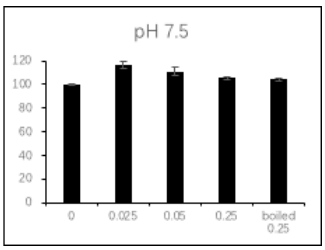

M

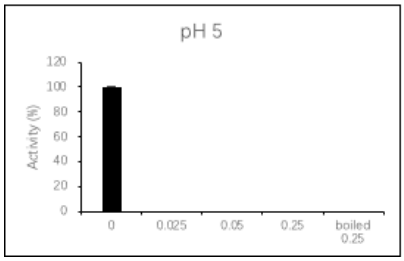

N

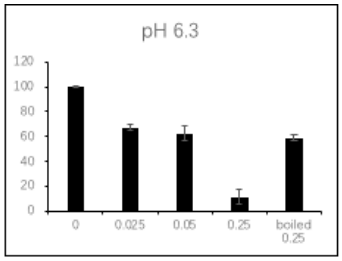

O

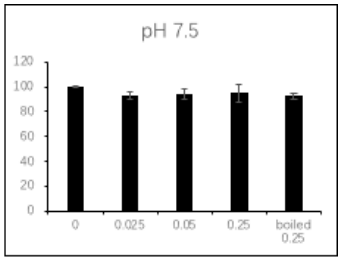

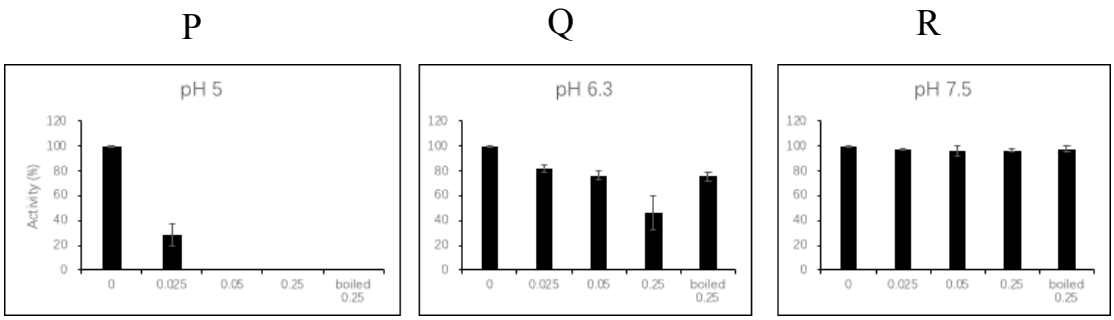

Figure 3.9: PME inhibiting activity of recombinant PMEI3. On orange PME (A, B, and C), citrus thermal-tolerant PME (D, E, and F), AtPME2 (G, H, and I), AtPME3 (J, K, and L), Arabidopsis flower PMEs (M, N, and O) and root PMEs (P, Q, and R). Experiments were carried out using 1.5 milliunits of orange PME, AtPME2, AtPME3, and 1.0 milliunit of citrus TT PME, flower PMEs and root PMEs at pH 5 (A, D, G, J, M, and P), pH 6.3 (B, E, H, K, N, and Q), and pH 7.5 (C, F, I, L, O, and R) and varying quantities of purified PMEI3. PMEI3 concentration unit is µg/µL. Error bar: STD, n=3.

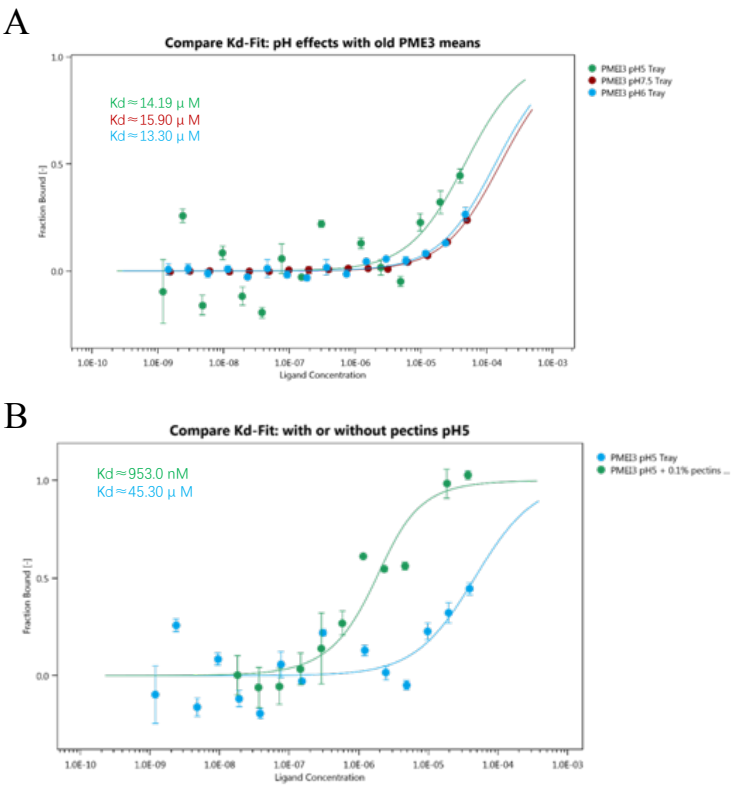

Figure 3.10: Determination of the interaction between PME3 and PMEI3 using microscale thermophoresis. (A) Interaction in binding solution at pH 5.0, 6.3 and 7.5. (B) Interaction in binding solution with or without 0.1 % pectin at pH 5.0. For the binding assay, PME3 was labeled and titrated with decreasing concentrations of PMEI3. The fitted curves and the resulting dissociation constant (Kd) values were calculated by averaging replicates. Kd values represent the mean of 3 replicates. Concentrations on the X axis are nM.

AtPME3 is highly expressed in most tissue and, like AtPME2, highly expressed in young flower and in the inflorescence axis. PMEI3 may therefore inhibit both PMEs *in vivo*. Since flowers and roots express many other PMEs, the inhibition of the total PME activity in these samples confirm the broad substrate range of PMEI3.

The pH sensitivity of the inhibiting activity of PMEI3 appeared very similar to that of PMEI4 (Hocq et al. 2017) and PMEI7 (Sénéchal et al. 2015) tested on AtPME3, but different from recombinant PMEI9 (Hocq et al. 2017), the activity of which did not show any pH dependence in the pH range tested. In AtPMEI7, E75 played an essential role in the pH-dependence of its interaction with AtPME3. Mutating this residue caused a 20-fold decrease in binding affinity. The deprotonation of E75 would shift the conformation so that intramolecular salt bridges are formed with positively charged residues sitting in the vicinity of titratable residue (Sénéchal et al. 2017). The same mechanism may govern the AtPMEI3-PME interactions given the strong sequence similarity between AtPMEI3 and AtPMEI7 (Figure 2.1).

3.2.2 PMEI3/PME3 interaction

Given the strong pH-dependent inhibition of AtPME3 activity by PMEI3, we analyzed the physical AtPME3/PMEI3 interaction *in vitro*. The binding affinities of purified AtPME3 with different concentrations of recombinant AtPMEI3 were determined using MST. This sensitive method assesses the protein-protein interaction *in vitro* by measuring the motion of molecules along microscopic temperature gradients and detects changes in their hydration shell, charge, or size (Wienken et al. 2010; Jerabek-Willemsen et al. 2014). Recombinant AtPME3 was labeled with a blue fluorescent dye, NHS amine. A constant concentration of labeled AtPME3 was added in capillaries with serial dilutions of recombinant unlabeled AtPMEI3. MST curves at pH 5, 6.3 and 7.5 showed a low affinity (Kd ≈ 45 µM) interaction between recombinant AtPME3 and AtPMEI3 (Figure 3.10a), lower affinity than that previously reported for PMEI4-, PMEI7- or PMEI9 (Sénéchal et al. 2015; Hocq et al. 2017). To mimic *in vivo* conditions

the interaction in the conditions of the GDA, purified proteins in acidic buffer were mixed with 0.1% pectin at pH 5. Interestingly, PMEI3-PME3 binding affinity increase 45x in the presence of pectin (Kd ≈ 1 μM) (Figure 3.10b). It will be interesting to see what the underlying mechanism is of this pectin-dependent increase in affinity.

Results

Chapter 4 Comparison of apoplastic pH measurement tools

As discussed in the Introduction, three main standard methods can be used to measure pH^{Apo} in living plants. Among these methods, the genetically encoded fluorescent sensors are reliable, have a high spatiotemporal resolution and are nontoxic. To generate new genetically encoded fluorescent pH sensors in *Arabidopsis* to measure the pH in the cell wall, we built, using the GreenGate cloning system, 3 constructs that fused apoplast targeting signal peptide to the tandem concatenation of a pH-insensitive and a pH-sensitive fluorescent protein (Figure 4.1). Two cell wall targeting domains were chosen from Formin 1 in *Arabidopsis* (AtFH1), which forms a connection between the cell wall and the actin cytoskeleton, and a PME in *Linum usitatissimum* (LuPME1), which localizes to cell wall (plasmid was kindly provided by N. Paris). The pH-sensing moieties comprised either the pH-insensitive mRFP1 and a pH sensitive EGFP used for the ApopHusion (Gjetting et al. 2013), or the pH-insensitive mRFP1 and a pH sensitive BFP (Figure 4.1). *REDSEED* gene was used as a reporter gene in the three pH sensor constructs. The constructs were verified for the presence of the desired insert using colony PCR and restriction enzyme digestion (Figure 4.1) and a single clone for each construct was confirmed by Sanger sequencing of a single clone for each construct. The constructs were first tested in a transient expression assay in *Nicotiana benthamiana* leaves. 72 hours after infiltration, both EGFP and mRFP1 fluorescence were clearly visible in the cell wall in leaves harboring the sensors AtFH1-pHusion and LuPME1-pHusion (Figure 4.2). For AtFH1-mRFP-BFP, only the mRFP1 signal could be detected (Figure 4.2). These results confirmed that the pH sensor constructs were functional. We next generated stable *Arabidopsis* transformants with the 3 constructs. Red seeds from three T1 plants were sown on 1/2 MS medium. Unfortunately, germination rate of red

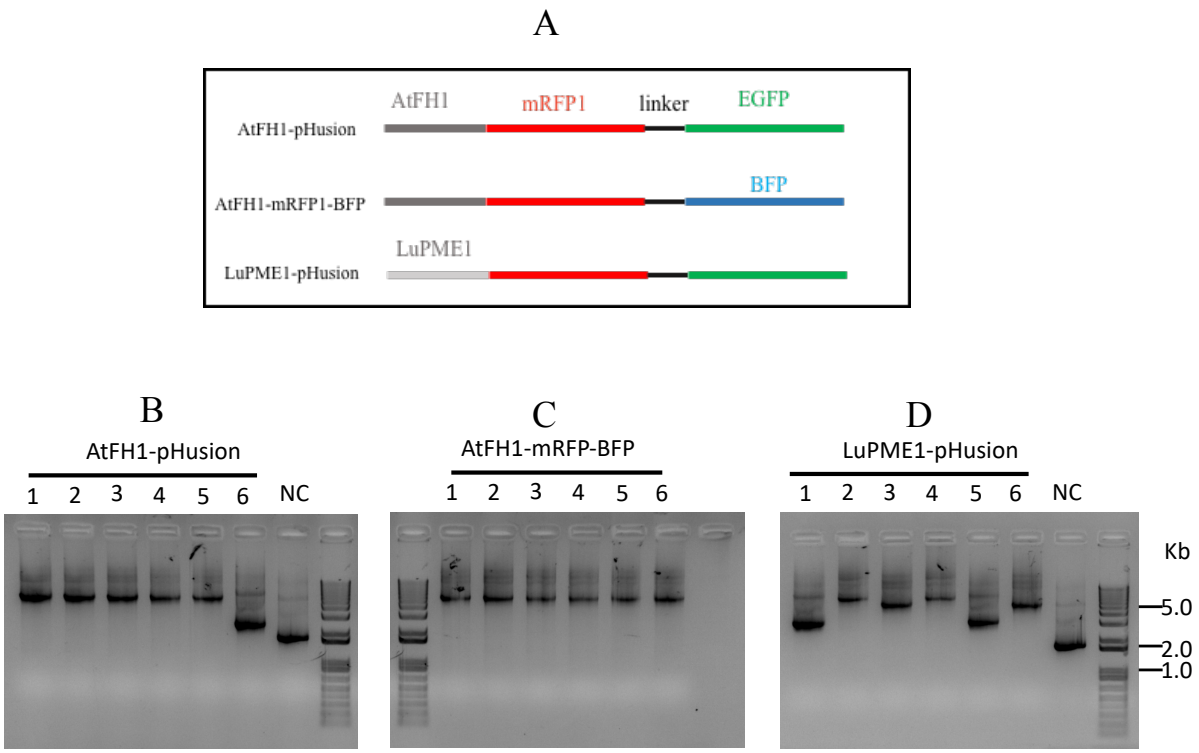

Figure 4.1: Constructs for the expression of cell wall-targeted pH sensors. (A) Scheme of construct structure. See Material and Method for construct map. (B, C, and D): Representative agarose gel images showing colony PCR of the designed vectors. Six colonies for each group were tested. NC: negative control. Primers: pGGZ001-F and pGGZ001-R (B, C, and D).

seed containing AtFH1-pHusion and AtFH1-mRFP-BFP (Figure 4.3) were only 12.3% and 20.3% relative to close to 100% for non-red seeds. LuPME1-pHusion sensor transgenic plant showed a higher germination rate, 60.5% (Figure 4.3). To test if the sensor constructs were functional in the transgenic plants, 6 d old seedlings selected for their red seeds were observed using the Axiozoom. Unfortunately, no fluorescent plants were found for any of the constructs. These results suggested that the cell wall-localized pH sensors interfered with seed germination and that the selection of viable seeds yielded plants in which the expression of the pH sensor was repressed.

Given these disappointing results, we focused on the use of two previously reported pH sensors, one targeted to the apoplast (apopHusion) and one to the apoplastic side of the PM (PM-Apo) to measure pH^{Apo} in *Arabidopsis* roots. PM-Apo comprises pHluorin anchored to the PM by a transmembrane domain. This allows the pH to be measured in a < 10nm range close to the PM (Martinière et al. 2018). The signal of this pH sensor showed a patchy expression in roots, suggesting stochastic co-suppression of the reporter (Figure 4.4) and in the cells that showed high fluorescence intensity, the longitudinal cell walls had less pHluorin signal than transverse cell walls (Figure 4.4), suggesting a selective subcellular targeting. The apopHusion (Gjetting et al. 2012) combines EGFP in a tandem fusion to monomeric mRFP1 fused to the secretory signal peptide, Gjetting et al. (2012) were able to constitutively target the apopHusion to the apoplast in the leaf epidermis, the guard cells, the mesophyll, or the root apex of Arabidopsis. This genetically encoded sensor helped to visualize a fast alkalinization response in the epidermal apoplast of elongating roots in response to external addition of indole-3-acetic acid (Gjetting et al. 2012).

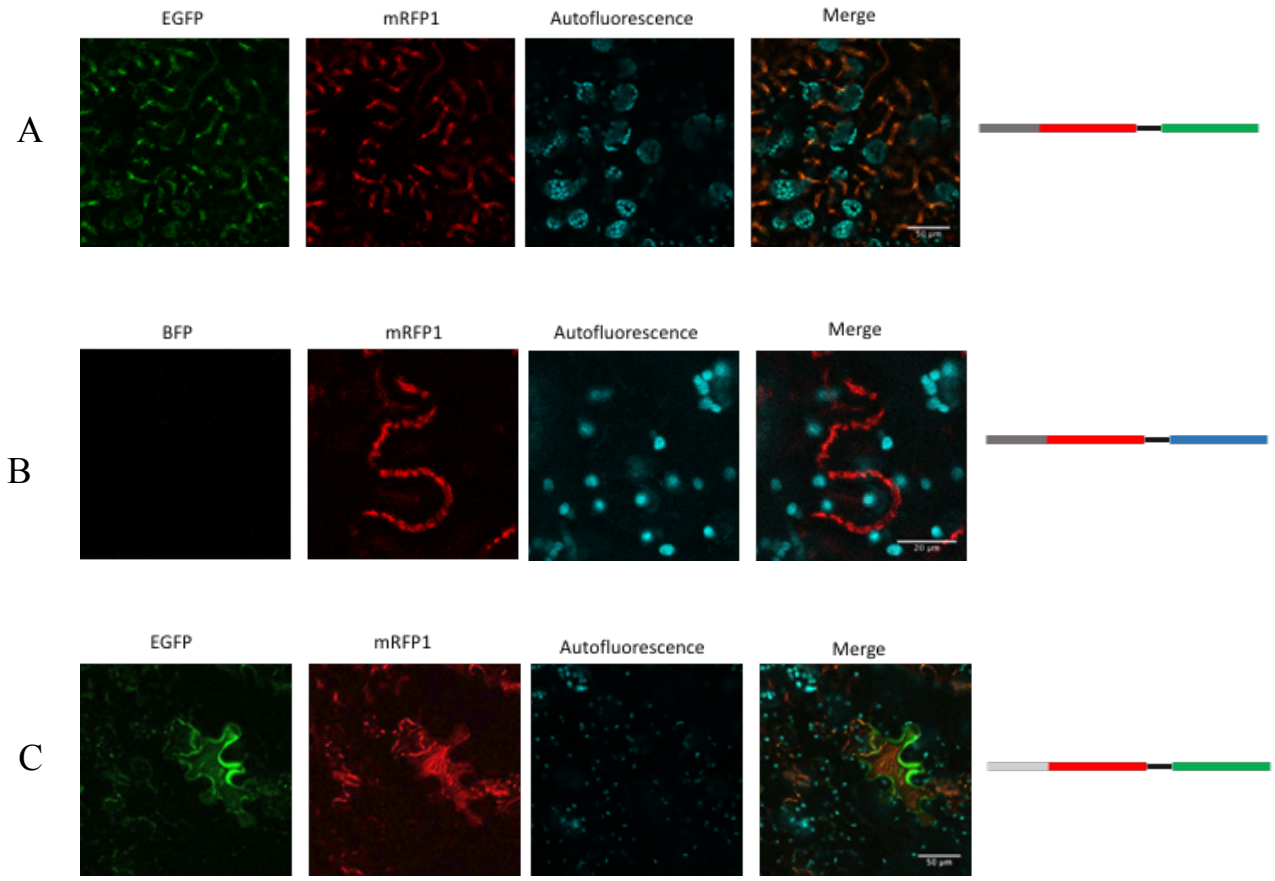

Figure 4.2: Transient expression assay of cell wall targeted pH sensors in tobacco leaves. Confocal images of EGFP, mRFP1 and BFP of AtFH1-pHusion (A), AtFH1-mRFP-BFP2 (B), and LuPME1-pHusion (C). The experiments were repeated at least 3 times. Construct structures are shown also in Figure 4.1.

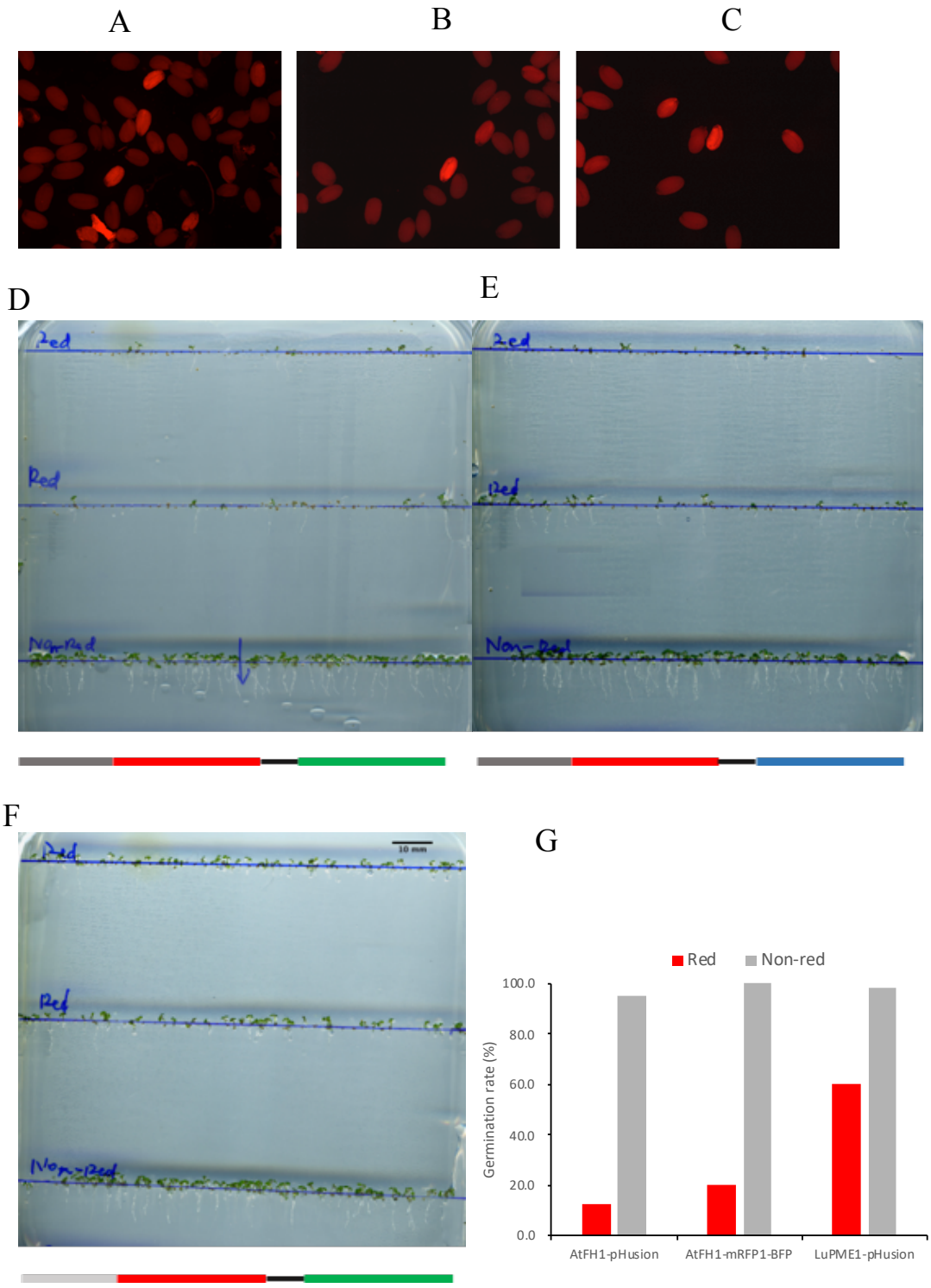

Figure 4.3: Cell wall targeted pH sensor screening. (A), (B) and (C): Red seed of T1 pH sensor transformants. The red seeds are corresponding to those in (D), (E) and (F). Comparison of phenotype between red and non-red seeds for the AtFH1-pHusion (D), AtFH1-mRFP-BFP2 (E), and LuPME1-pHusion (F). Red seeds showed low germination rate. (G) Germination rate of transformants. Construct structures are shown also in Figure 4.1.

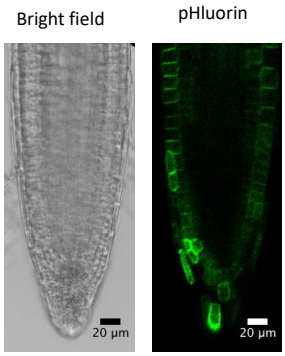

Figure 4.4: PM-Apo showing a patchy expression pattern in root cells.

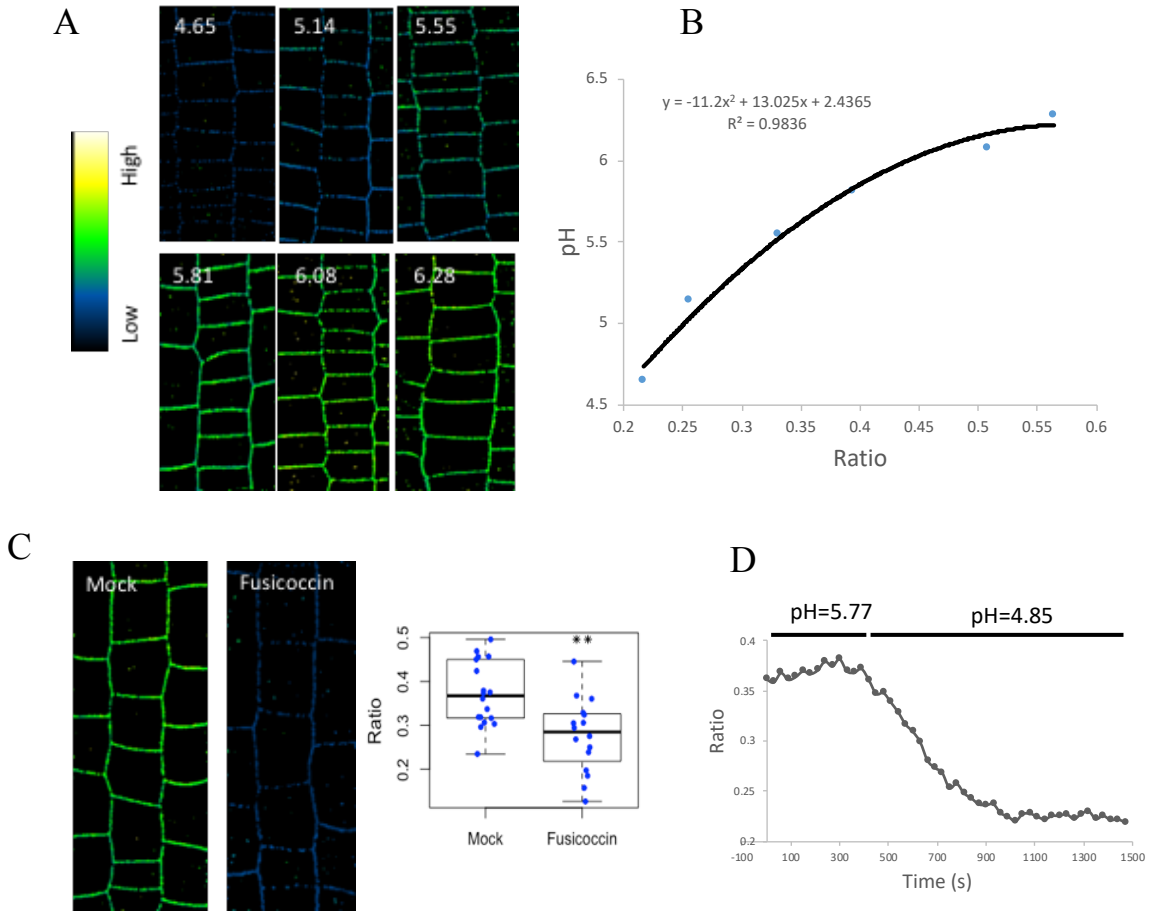

Figure 4.5: HPTS calibration and robustness test *in vivo*. (A): HPTS 458/405 values in transition zone of the seedlings incubated for 30 min in liquid 1/2 MS medium with pH 4.5-6.5. (B): Standard curve of HPTS 458/405 values to pH^{Apo}. Regression analysis derived-equation (top) enabling pH^{Apo} calculation from the obtained 458/405 values. (C) pH^{Apo} measurement of fusicoccin-treated seedlings using HPTS. Significant difference ($P < 0.01$) was determined by two-way ANOVA followed by Tukey's test. $n > 16$ (D) HPTS 458/405 value in living *Arabidopsis* root decreased immediately after addition of 1/2 MS liquid medium with pH 4.85.

We also investigated the use of a new pH indicator, HPTS (8-hydroxypyrene-1,3,6-trisulfonic acid trisodium salt) to measure the pH^{Apo}. HPTS is a water-soluble fluorescent dye displaying pH-dependent spectral characteristics (Barbez et al. 2017; Amali et al. 2011). In plants, HPTS has been used to define the pH of extracted apoplastic fluid from plant tissues (Kasik et al. 2013; Villiers et al. 2013). To test whether HPTS can be used to directly assess pH^{Apo} with a cellular resolution in planta, we immersed 4-day-old seedlings in HPTS- containing liquid growth medium at 6 different pH levels for 30 min and imaged roots using confocal microscopy. A ratiometric image was obtained using 458/405 nm the signal intensity ratio for each pixel, which was calibrated using a standard curve for the 6 pH values of the medium (Figure 4.5). The dye showed a decrease in pH^{Apo} induced by the H^+-ATPase activator fusicoccin (Figure 4.5). To test the capacity of HPTS to dynamically detect changes in pH^{Apo}, we added pH 4.85 medium to roots in a medium of pH 5.77 and observed an almost instantaneous drop in the 458/405 nm intensity ratio (Figure 4.5). These results indicate that HPTS is suitable to detect exogenously-imposed pH^{Apo} changes.

Results

Chapter 5 Effect of homogalacturonan demethylesterification on apoplastic pH in *Arabidopsis* root

The cell wall pH is a key regulator of the cell expansion rate. According to the textbook view, the PM-localized H^+-ATPase directly regulates the pH^{Apo}, which in turn controls the activity of the cell wall loosening agents that affect the cell wall extensibility. As discussed in the introduction, HG demethylesterification is a key element controlling the rheology and extensibility of the cell wall. This reaction increases the negative charge density of the HG, which may contribute to the formation of Ca^{2+}-pectate that is thought to stiffen cell wall (Parre and Geitmann 2005). The reaction also releases H^+ into cell wall. It has been theorized that the released H^+ and the PME-induced increased negative charge density may contribute to the acidification of the cell wall and an increase in the cell wall expansion rate. *In vitro* studies on isolated plant cell walls suggested that PME-catalyzed HG demethylesterification altered the electrical potential and the H^+ concentration between the inside and outside of the wall (Ricard et al. 1981 and 1984). However, no *in vivo* experimental evidence exists so far to support this view. In this study, we addressed this issue by using pharmacological and genetic manipulation of the PME activity to investigate the impact of HG demethylesterification on pH^{Apo} and growth in *Arabidopsis* roots.

5.1. Dose-dependent inhibition of *Arabidopsis* root growth by PME inhibitor EGCG.

To analyze the effect of the inhibition of HG demethylesterification on root growth, we employed a systemic chemical inhibitor of PMEs, (-)-epigallocatechin gallate (EGCG), which inhibits PME activity by binding to PME or to pectin (Lewis et al. 2008; Wolf et al. 2012). *Arabidopsis* Col-0 seedlings were grown under light or dark conditions on solid 1/2 MS medium supplemented 200 μM EGCG and hypocotyl length, primary root length and RH density were measured 2 d after germination (Figure 5.1). The primary root length of EGCG-treated seedlings was significantly shorter than that of mock-

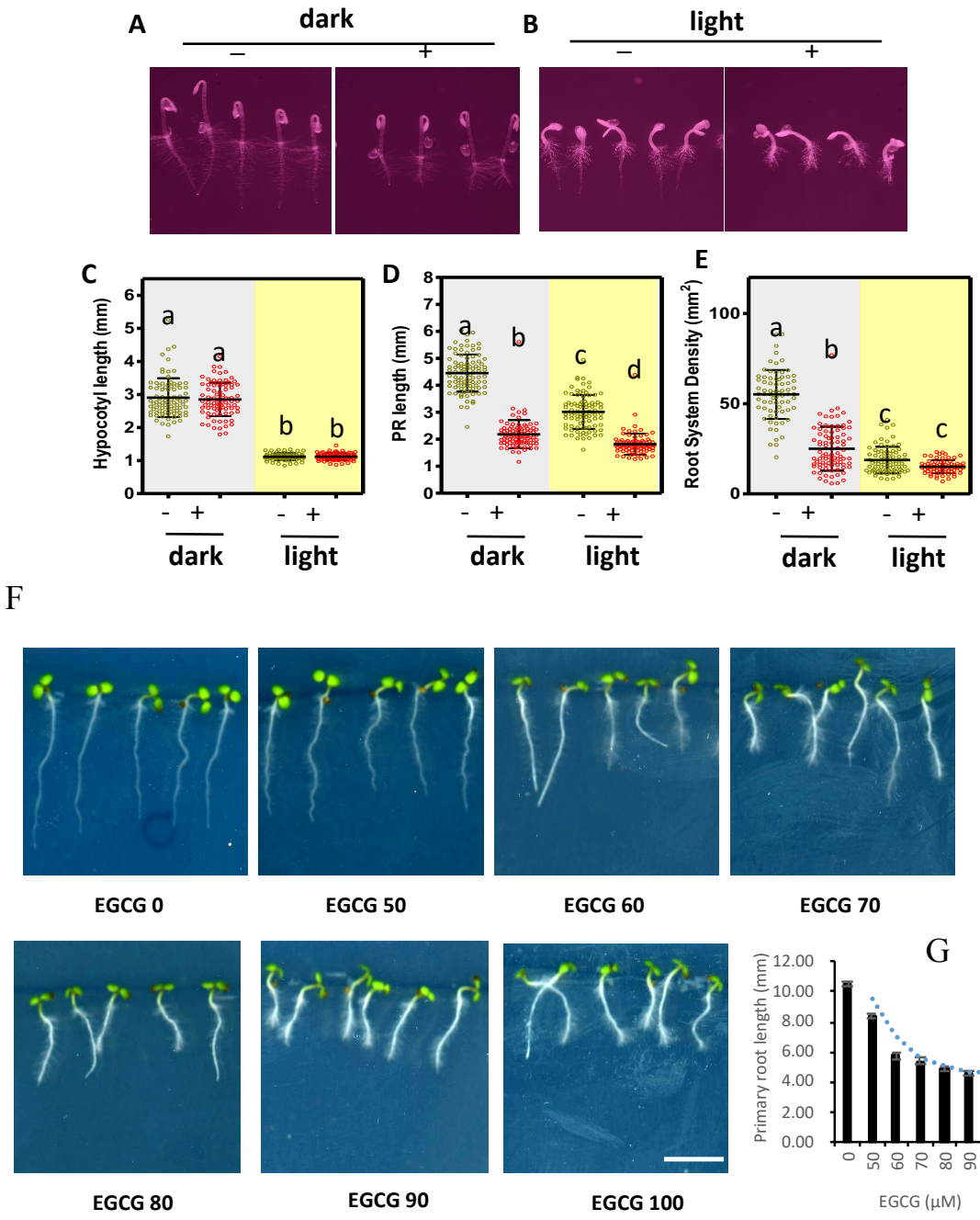

Figure 5.1: Dose-dependent inhibition of *Arabidopsis* root growth by PME inhibitor EGCG. (A) and (B) Col-0 dark- or light-grown seedlings grown for 2 days on solid 1/2 MS medium supplemented with 200 µM EGCG. (C) Hypocotyl length is not affected by ECGC treatment. (D) Primary root (PR) length was inhibited by EGCG treatment under both conditions. (E) Root hair density (Root system density) was reduced by EGCG treatment under dark condition. (C, D, and E) Statistical significance (0.05%) was tested using Kruskal-Wallis non-parametric H test followed by a Dunn's Multiple Comparison posthoc test. $n > 70$. $P < 0.01$. (F). Col-0 seedlings grown on solid 1/2

MS medium supplemented with 0-100 μM of EGCG under light for 4 days. Scale bar: 5 mm. (G) Primary root length decreased with increasing EGCG concentration. n > 30. Error bar: STD。

treated control seedlings both in light- and dark-grown conditions. The hypocotyl length however, was unaffected by the EGCG treatment, suggesting that either pectin metabolism is not important for hypocotyl growth or that the EGCG is not transported to the growing zone in the hypocotyl. The second possibility is the most likely one given the fact that EGCG binds to the cell walls of the root cells. We therefore focused on the root in all subsequent experiments. To confirm the EGCG effect, Col-0 seedlings were grown on solid 1/2 MS solid medium supplemented EGCG at concentrations from 0 to 100 μM. As shown in Figure 5.1, the root length of 4-d-old seedlings decreased with increasing EGCG concentration. 50 μM EGCG-treated plants showed a root waving phenotype (Figure 5.1), which is consistent with previous observations (Wolf et al. 2012) using EGCG or constitutive and inducible PMEI5 overexpressing lines.

PME activity is also involved in RH growth (Schoenaers et al. 2018). RHs show oscillations in growth rate, the peaks of which lag the peaks in the accumulation of demethylesterified HG at the root tip (Rounds et al. 2011). In the present study, EGCG-treated seedling showed more and longer RHs in relative to mock-treated seedlings (Figure 5.1). The same phenotype was observed with polyphenon 60, a catechin extract that also inhibits PME activity in a concentration-dependent manner (Schoenaers et al. 2018). In conclusion, EGCG treatment causes the inhibition and the promotion of root and RH growth respectively. We assume that this effect reflects the inhibition of PME activity.

5.2. EGCG treatment alters cell shape in root

In the EGCG-treated roots, cells in the differentiation zone (DZ) tended to bulge out (Figure 5.2). To determine at which stage the EGCG treatment affects root development, we analyzed the 3D cell shape from the root tip to the elongation zone (EZ). Four-d-old seedlings, grown in solid 1/2 MS medium supplemented with 50 μM EGCG were stained by calcofluor and imaged using confocal microscopy. Images were

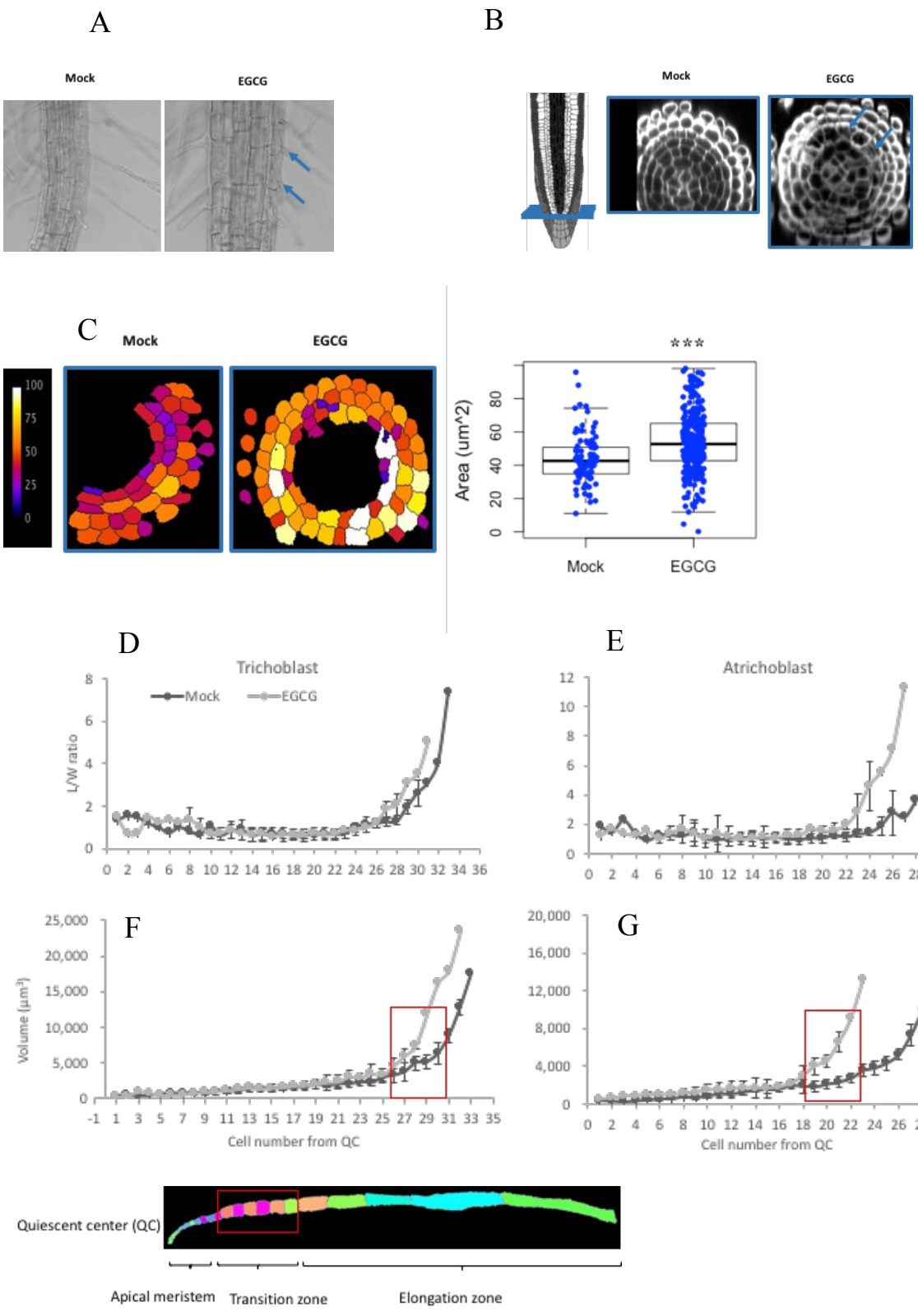

Figure 5.2: EGCG treatment altered cell shape in root. (A) Cells in the differentiation zone (DZ) tended to bulge out (arrows) in EGCG-treated seedlings. (B) Endodermal cells in EGCG-treated seedlings showed irregular cell shapes (arrows). (C) Radial area of epidermis, cortex and endodermis cells at quiescent center (QC) in EGCG-treated seedlings was higher than that in Mock-treated seedlings. False color represents the cell area value. Wilcoxon rank sum test; ***$p < 0.001$. n (cell number) = 91 (Mock) and 290 (EGCG). n = 4 (Mock) and 6 (EGCG) biological

repeats. Ratio of length over width (D and E) and cell volume (F and G) of the trichoblast (D and F) and atrichoblast (E and G) cell lines. Red rectangle represents zone where cell volumes start diverging between Mock- and EGCG-treated seedlings. For D-G, n = 7 biological repeats. Error bar: STD.

segmented using MorphlibJ and trichoblast and atrichoblast cell lines, from quiescent center (QC) to EZ, were extracted (Figure 5.2). The length/width ratio (L/W) and cell volume were determined for the individual cells in the selected cell lines (Figure 5.2). The L/W ratio became significantly higher in EGCG-treated vs mock-treated cells, from cell 27 and 22 (starting for the QC) in trichoblast and atrichoblast respectively indicating that growth symmetry breaking occurred earlier in EGCG-treated relative to mock-treated roots. Similarly, the cell volume became significant higher in EGCG-treated vs control cells, from cell 26 and 19 in trichoblast and atrichoblast respectively (Figure 5.2), indicating that 50 μM EGCG had the first visible effects on cells in the TZ. We therefore focused primarily on the TZ for the analysis of the pH^{Apo}.

5.3. EGCG treatment promotes an increase in pH^{Apo} in root cells

To monitor changes in pH^{Apo} after EGCG treatment, the genetically encoded pH sensor, apopHusion and the pH sensitive fluorescence dye HPTS, were used to measure pH^{Apo} in growing roots. Four-d-old apopHusion expressing seedlings vertically grown on 1/2 MS solid medium were gently mounted onto a home-made root growth chip and fixed by medical adhesive or by covering the seedlings with cotton and a small plastic grid (See Method and materials). To let the mounted seedlings adapt to the new growth conditions, they were grown in unbuffered1/2 MS liquid medium (pH = 5.8) for 15 min. Then the same volume of 1/2 medium supplied with various drugs was inserted into the channel and the seedlings were grown for 45 more min. During this 1 h growth period, EGFP and mRFP1 fluorescence intensity values were acquired in the root within 1 min intervals. Regions of interest (ROIs) in the MT, TZ and EZ were analyzed respectively. We first pharmacologically modulated the activity of the PM H^+-ATPases and analyzed the EGFP/mRFP1 ratio after imaging. Fusicoccin treatment, which activates the PM H^+-ATPases (Barbez et al. 2017), resulted in decreased EGFP/mRFP1 ratio values, indicating a decrease in pH^{Apo} (Figure 5.3). In contrast, treatment with vanadate, which inhibits the PM H^+-ATPases, led to an increased EGFP/mRFP1 ratio values (Figure 5.3). The MT, TZ and EZ in vanadate-treated root showed similar patterns of EGFP/mRFP1 ratio changes, whereas

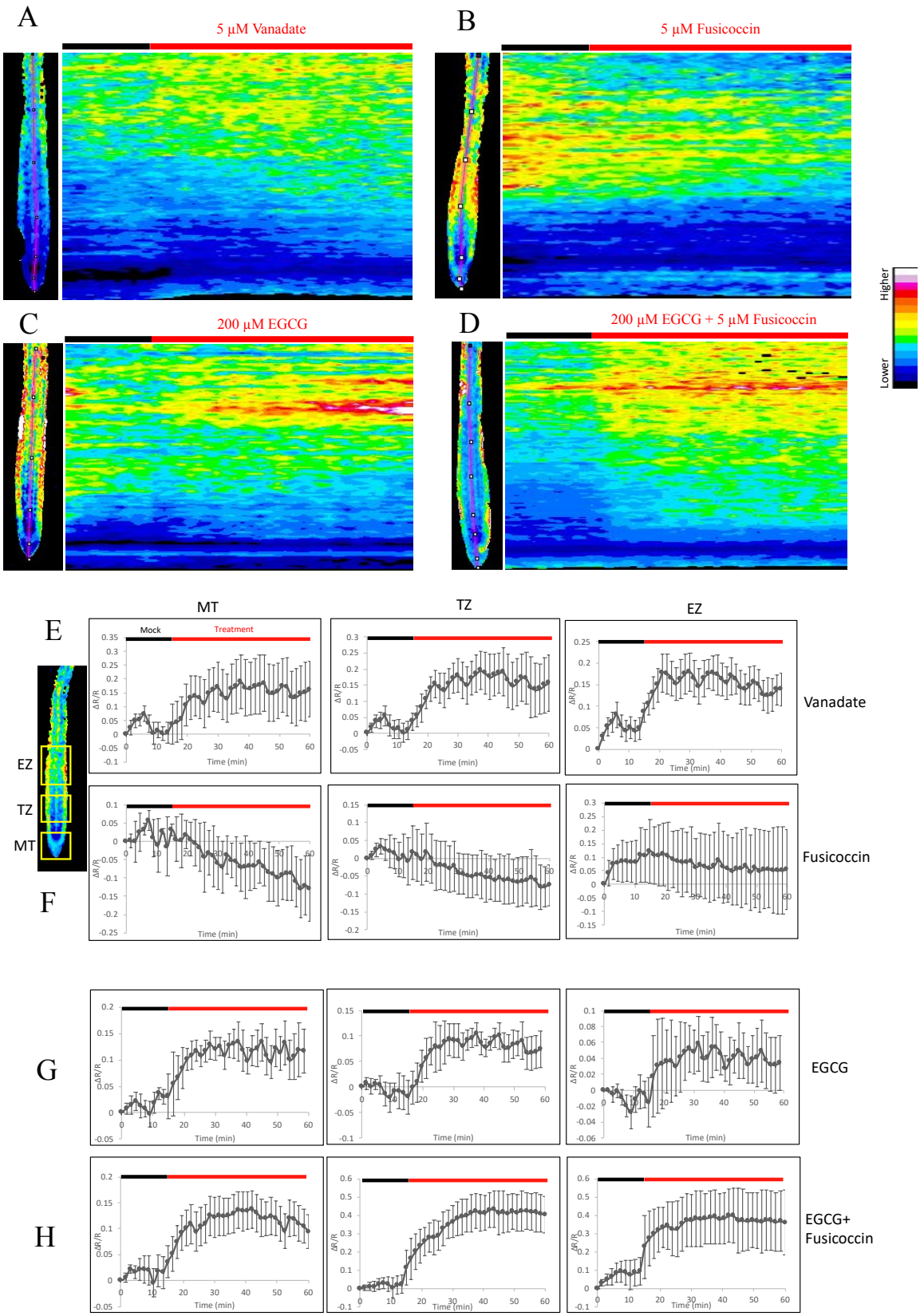

Figure 5.3: EGCG treatment promotes an increase in pH^{Apo} in root cells. pH^{Apo} represented in false color (A-D) and quantification in meristem (MT, left), transition zone (TZ, middle), and elongation zone (EZ, right) (E-H).

Vanadate (A,E) and fusicoccin (B,F) treatments raised and lowered pH^{Apo} in root, respectively. EGCG (C,G) and EGCG+fusicoccin (D,H) application both increased pH^{Apo} in root. n = 6 (vanadate), n = 4 (fusicoccin), n = 4 (EGCG), n = 10 (EGCG+fusicoccin). Black and red bars: 15 min and 45 min. Error bar: STD.

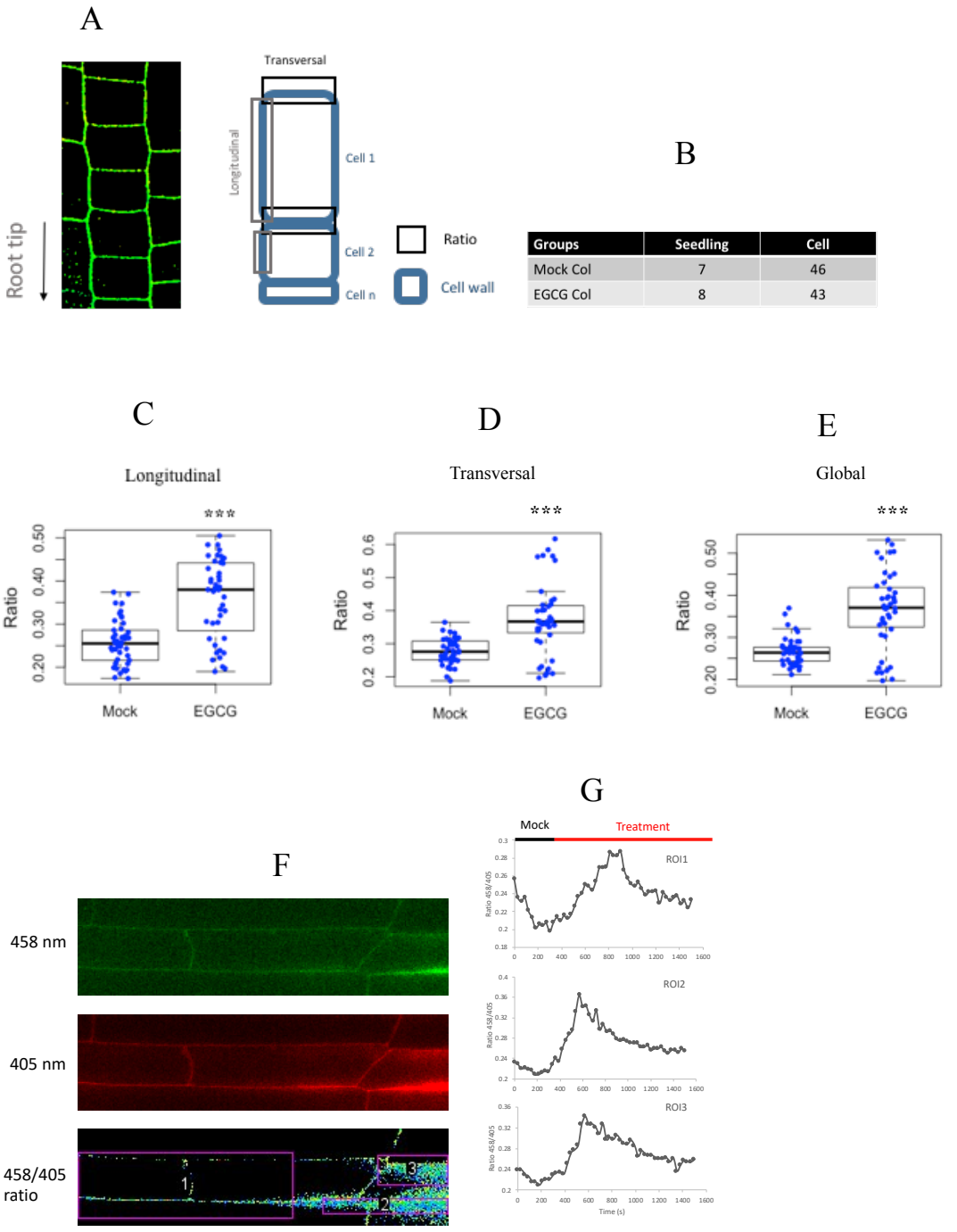

Figure 5.4: EGCG treatment promotes an increase in pH^{Apo} in the root transition zone (TZ). (A) Image of HPTS-stained root epidermal cells and scheme showing zones where 458/405 values of longitudinal and transverse walls in TZ were measured. (B) Specimen number summary. (C, D and E), The ratios of longitudinal (C), transverse (D) and both walls (Global, E) after 60 min treatment with mock or 200µM EGCG. Wilcoxon rank sum test; ***$p < 0.001$. (F) Three ROI in TZ were selected to investigate the kinetics of the pH^{Apo} changes (G). The kinetics showed an increase in pH^{Apo} after EGCG application. For F-G, experiments were repeated twice.

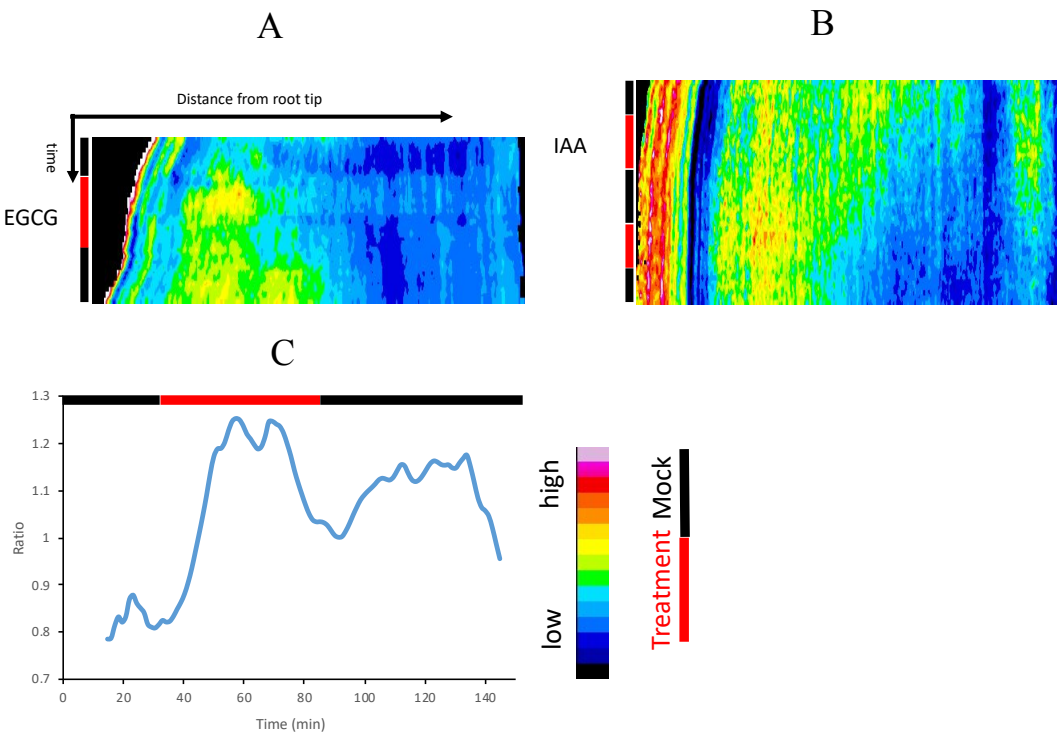

Figure 5.5: EGCG-triggered increase in pH^{Apo} correlates with root growth inhibition. (A,B) : Kymograph of the pH^{Apo} visualized with the apopHusion marker in roots grown in RootChips and (C) : mean ratio of the root in (A). Mock (black bars); Treatment (red bars) with 200µM EGCG (A,C) or 50 µM IAA (B) Experiments were repeated four times.

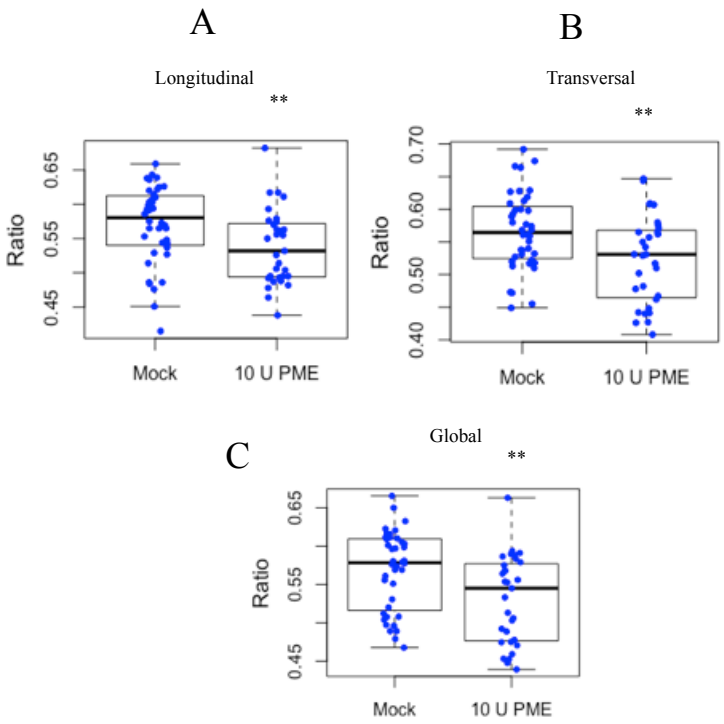

Figure 5.6: Exogenous PME treatment reduced pH^{Apo} in transition zone. (A, B, and C) HPTS 458/405 values of longitudinal (A), transverse (B) and whole wall (Global, C) measured after orange PME (10 U/ml) or mock treatment for 60 min. Wilcoxon rank sum test; **$p < 0.01$. $30 < n < 41$.

the EZ was less sensitive to fusicoccin treatment compared with MT and TZ. EGCG treatment caused also an increase in EGFP/mRFP1 ratio value in MT, TZ and EZ (Figure 5.3), with the strongest effect in the TZ. To confirm the effect of EGCG on the pH^{Apo}, we also used HPTS. HPTS calibration and the effect of fusicoccin on pH^{Apo} was shown in Chapter 4. Four-d-old seedlings were incubated in 1/2 MS liquid medium with EGCG for 30 min and with HPTS plus EGCG for 30 more min. We again observed an increase in 458/405 ratio in EGCG-treated, relative to mock-treated roots in both longitudinal and transverse cell walls in the TZ (Figure 5.4). We also studied the kinetics of the response and observed a transient pH increase within 300 sec after the addition of EGCG. The response peaked more slowly in larger than in smaller cells. Together, combining the use of apopHusion and HPTS, we observed that EGCG treatment led to an increase in pH^{Apo} in the *Arabidopsis* root.

To test whether the EGCG-induced pH increase depended on the inhibition of the H^+-ATPase, we treated the seedlings with a combination of EGCG and fusicoccin. Interestingly, EGCG overruled the effect of fusicoccin on the pH^{Apo} as shown by the increase in the EGFP/mRFP1 ratio in MT, TZ and EZ (Figure 5.3). These results suggest that, irrespective the H^+-ATPase activity, the inhibition of HG demethylesterification triggered an increase in pH^{Apo}, although it cannot be ruled out that EGCG shut down the H^+-ATPase activity downstream of the fusicoccin effect.

5.4. EGCG-triggered increase in pH^{Apo} correlates with root growth inhibition.

According to the acid growth theory, the decrease in pH^{Apo}, triggered by the H^+-ATPase, promotes cell expansion, though the activation of pH-dependent cell wall-loosening proteins (Hocq et al. 2016). To clarify the relationship between the EGCG-triggered increase in pH^{Apo} and root growth, we monitored pH^{Apo} in parallel to root growth in

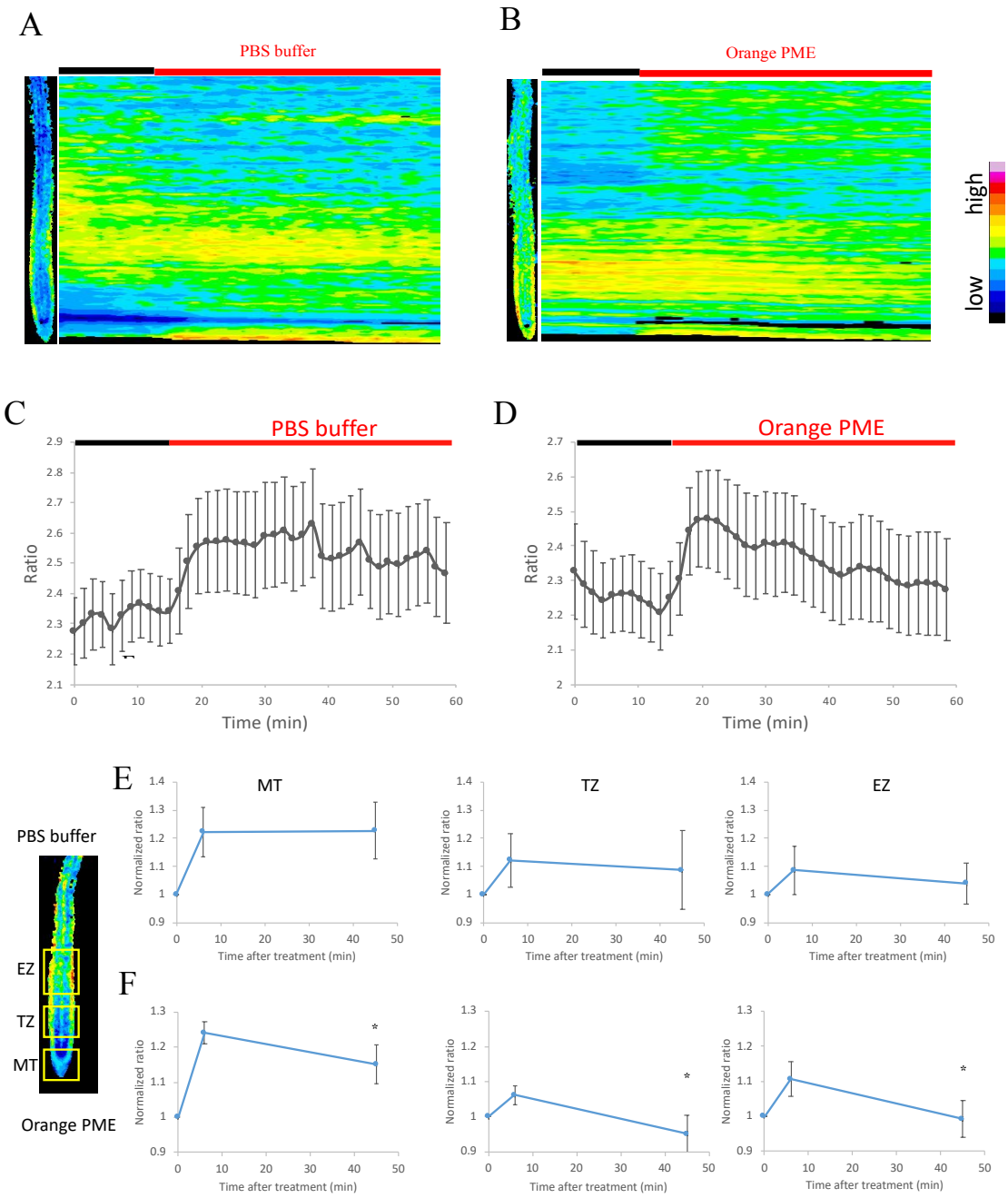

Figure 5.7: Exogenous PME treatment reduced pH^{Apo} in root cells. pH^{Apo} visualized with the apopHusion marker line. (A,B) : pH^{Apo} represented in false colors. (C,F) : mean pH^{Apo} ratios in whole roots (C,D); in meristem (MT), transition zone (TZ), and elongation zone (EZ) (E,F), after application of 0.5 mM PBS buffer pH 7.5 (E) of Orange PME in the same buffer (F). n=6 (mock), n=9 (Orange PME). (E,F) : After the initial pH increase, a significant decrease in pH^{Apo} in PME- but not in mock-treated roots was observed. Significance was determined by two-way ANOVA followed by Tukey's test. * $p < 0.05$. Error bar: STD.

microfluidic RootChips. RootChips can combine live-cell imaging of growth and metabolism of *Arabidopsis* roots with rapid and gentle modulation of environmental conditions (Grossmann et al. 2011). Ten-d-old seedlings were treated with 1/2 MS liquid medium without and with EGCG in the following order: Mock-EGCG-Mock. Six to nine Z-stacks of both EGFP and mRFP1 signals were acquired in a 5 min interval. Image processing is described in Method and materials. The kymograph of EGFP/mRFP1 ratio and root growth was showed in Figure 5.5. EGFP/mRFP1 ratio increased within 5 min by EGCG treatment (Figure 5.5), which is consistent with the results above (Figure 5.3). Simultaneously, the root growth rate diminished, shown by the flatter slope of root tip trace (Figure 5.5). After removal of EGCG, the EGFP/mRFP1 ratio and root growth recovered to lower level within 40 min (Figure 5.5). In conclusion, these preliminary results show that EGCG-induced pH^{Apo} increase coincided with the inhibition of root growth and that these responses were fully reversible.

5.5. Exogenous PME treatment decreased pH^{Apo} in root cells

The EGCG results suggest that the inhibition of PME was responsible for the observed apoplast alkalinization. To confirm this, we measured pH^{Apo} using HPTS in roots after 45min treatment with orange PME (1.0 unit/root). We observed a significant decrease in the 458/405 ratio in both longitudinal, transversal and global cell walls in the TZ in PME-treated roots relative to mock-treated controls (Figure 5.6). We next used the apopHusion to confirm the HPTS data and to study the kinetics of the acidification response. It should be noted that citrus PME is kept in a PBS buffer at pH 7.5. As a result, we observed an initial increase in pH after PME or mock buffer control treatment. However, after the initial pH increase we observed a significant pH decrease in PME- but not in mock-treated roots (Figure 5.7). These data confirm that exogenous PME can promote a decrease in pH^{Apo} in root cells.

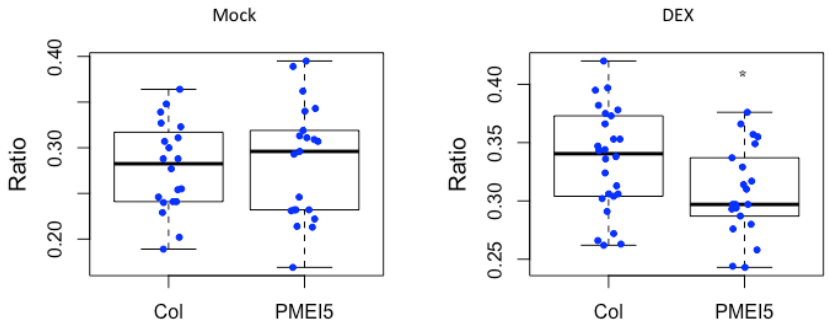

Figure 5.8: pH^{Apo} in transition zone of inducible PMEI5 overexpressing line and WT Col0 was decreased after 24-h induction with 50 µM dexamethasone (DEX). Wilcoxon rank sum test; *$p < 0.05$. $21 < n < 26$.

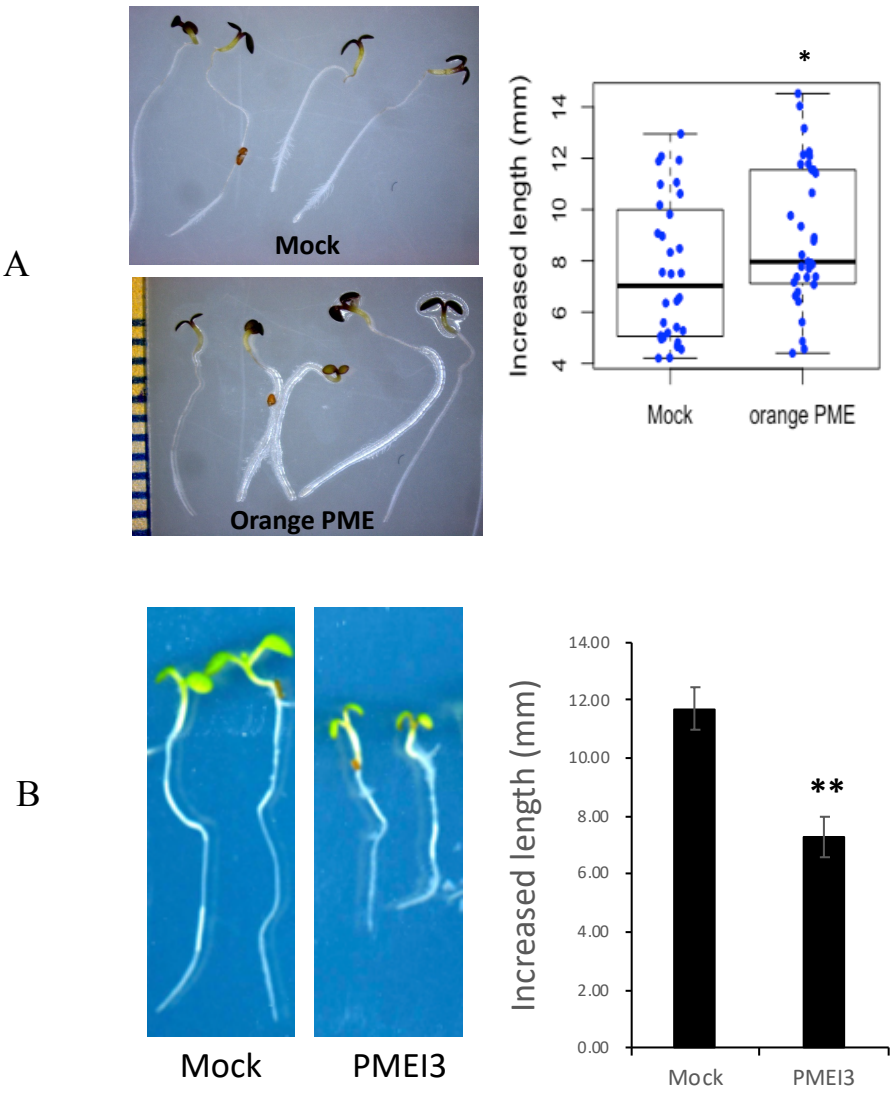

Figure 5.9: Exogenous PME and PMEI3 applications promoted and inhibited root growth, respectively. Two-d-old Col0 seedlings were grown in liquid ½ MS medium containing 10 U/mL orange PME (A) and recombinant PMEI3 14 µg/mL (B) for 2 days. Photographs of the roots (left panels) and root length increase (right panels). n > 35 (A), n > 30 (B). Significance was determined by two-way ANOVA followed by Tukey's test *p < 0.05, ** p < 0.01. Error bar: STD.

5.6. Effect of dexamethasone-induced expression of PMEI5 on pH^{Apo}

Previous studies reported that the overexpression of the putative PME inhibitor PMEI5, promoted a compensatory upregulation of PMEs mediated by activation of BR signaling through a feedback mechanism (Wolf et al. 2012 and 2014). We hypothesized that the elevated PME activity could also lead to a decrease in pH^{Apo}. To test this, we used the dexamethasone-inducible PMEI5 overexpressing line to induce PMEI5 expression for 24 h (sufficient to induce the BRI1-mediated compensatory response, Wolf et al. 2012) after which the pH^{Apo} in root was measured in roots using HPTS. As expected, dexamethasone-induced PMEI5 roots showed a lower 458/405 ratio relative to mock-induced seedlings (Figure 5.8).

5.7. The effect of exogenous PME and PMEI3 on root growth

Given that exogenous PME treatment caused a decrease in pH^{Apo}, we asked if exogenous PME and PMEI3 treatments could affect root growth in long-term. To test this, we treated 2-d-old seedlings for 2 days with 10 U/mL orange PME or 14 µg/mL recombinant PMEI3 using the corresponding buffers as mock control. PME-treated roots were longer than those of mock-treated seedlings. whereas PMEI3-treated roots were shorter than those of mock-treated controls (Figure 5.9). Together, these results show a correlation between PME activity, cell wall pH and root growth.

Chapter 6 Summary and perspectives

6.1 Summary

In this study, we investigated the link between pectin modification, cell wall pH and cell expansion rate. To this end, we used genetic and pharmacological approaches to manipulate the level of HG demethylesterification in living *Arabidopsis* roots combined with the monitoring of the pH^{Apo} using genetically encoded ratiometric pH sensors and a pH-sensitive fluorescent dye.

We first attempted to construct new tools (heterologously expressed purified proteins and inducible overexpression lines) for the *in vivo* manipulation of PME activity. We focused on two PMEIs (PMEI3 and PMEI5), which, based on previous *in vivo* data, might have different biochemical specificities. PMEI3 could be produced in *Pichia pastoris*, whereas PMEI5 was not expressed in this host. Recombinant PMEI3 showed inhibitory activity, at low pH, of a broad range of PME activities. We also used a DEX inducible binary system in GreenGate vectors for expression of the two PMEIs. Unfortunately, none of the transgenic lines showed inducible expression of the PMEIs or the reporter gene. This may be due to the co-suppression of the repeated pOp promoter sequences in the constructs. Next, for the measurement of the cell wall pH, we attempted to generate new genetically-encoded cell wall bound pH sensors. Unfortunately, the constructs appeared to be lethal in transgenic plants and no transformants with stable fluorescence signals were obtained. We therefore relied for our further experiments on the previously reported pH-sensitive dye HPTS and apoplastic ratiometic sensor apopHusion.

Our major finding is that the cell wall pH is not only determined by the activity of the PM H^+-ATPase but also by the PME activity in the cell wall. This conclusion is supported by the following observations: (i) the PME inhibitor EGCG promoted root growth inhibition in parallel with the alkalinization of the apoplast, (ii) EGCG overruled the effect of fusiccocin on the pH^{Apo}, suggesting an effect independent from the H^+-ATPase, (iii) citrus PME promoted an increase in root length and apoplast

acidification, (iiii) enhance endogenous PME activity upon long term induction of PMEI5 was also associated with apoplast acidification. The effect of PMEI3 overexpression and exogenous PMEI3 on the pH^{Apo} remains to be determined.

If confirmed, the results are consistent with the theory of Ricard and colleagues (Crasnier et al. 1985; Moustacas et al. 1986 and 1991; Nari et al. 1986 and 1991; Ricard and Noat 1986), that the cell wall pH reflects the ability of cell wall polymers to sequester H^+. A recent publication also comforts this view. The authors used the PM-anchored pH sensors PM-Apo to show that in a zone < 10 nm above the PM the pH can be up to 2 pH units more basic than in the cell wall (Martinière et al. 2018 and N. Paris personal communication). Given the high diffusion rate of H^+ in solution, such strong H^+ gradients can only be maintained by the local sequestering of H^+ by anionic cell wall polymers. These observations are a valuable addition to the acid growth theory, which stated that cell wall acidification through the activation of the proton pump promotes the activity of cell wall loosening agents (such as expansins) and hence wall relaxation. We propose that PME activity plays a key role in this process by controlling the buffering capacity of the cell wall. This, combined with the high pH optimum of most PMEs, an optimum sharpened by the inhibition of the activity at low pH by PMEs, may explain the oscillations in pH and growth rate observed in tip growing cells (roots and PTs) and possibly also in diffusely growing cells. PME activity at high pH would create anionic sites, leading to the local acidification, the inhibition of PME and wall relaxation. Cell wall expansion and the arrival of new uncharged HG would lead again to cell wall alkalinization, and so forth.

6.2 Perspectives

1. The effect of PME activity on the cell wall pH and growth rate will have to be confirmed using purified PMEI3 and the ethanol-inducible PMEI3 line using the RootChips. It will also be interesting to test PMEI9, which has a pH-independent PME-inhibitory activity (Hocq et al. 2017) and is expected to shut down PME activity

completely, in contrast to PMEI3, which does not inhibit PME at high pH.

2. Other cell wall-bound and non-lethal pH sensors need to be made to measure the pH in specific cell wall domains.

3. Other expression systems must be tested for the expression PMEI5. It is possible that PMEI5 expression requires the presence of a binding partner such as a PME. In this context it might be interesting to try to express tagged PMEI5 in *N. benthamiana* and isolate the protein complex.

4. An important challenge will be to understand the coordination between pectin metabolism and the activity of the PM H^+-ATPase. In this context it will be interesting to study the role of Rapid Alkaliniztion Factor (RALFs) and their CrRLK1L receptors. RALFs are polycationic peptides that trigger cell surface alkalinization upon binding to their receptors, through the repression of the H^+-ATPase activity. An interesting possibility is that the sequestering of the polycationic RALF peptides away from their receptors by polyanionic HG domains may amplify the cell wall acidifying effect of PME by triggering the derepression of the H^+-ATPase. Using the tools developed in this work, it will be possible to study the *in vivo* interaction between RALF signaling and PME activity in the control of cell wall pH and cell expansion.

5. The results of our study suggest that HG demethylesterification may also control the ion balance between apoplast and symplast. This hypothesis is among my future research interests.

Chapter 7 Materials and Methods

7.1. Apoplastic pH measurement using HPTS

Seeds of *Arabidopsis. thaliana* ecotype Colombia and non-fluorescent mutants were sterilized in 70% (v/v) ethanol supplemented with 10% (v/v) NaOCl, rinsed twice in absolute ethanol, and dried overnight under a sterile bench. Seeds were plated 1/2 Murashige and Skoog medium (perliter: 2.16 g MS salts (Duchefa), 2.0% plant agar) at approximately pH 5.8, were stratified at 4°C for 48 h in the dark and seedlings were vertically under long-day conditions at 22°C.

For calibration experiments, 4.7 mM MES in pH between 4.6 and 6.4 in steps of 0.2 or 0.4 units was added the 1/2 MS medium. Plants were grown under long-day conditions at 22°C. HPTS (8-hydroxypyrene-1, 3, 6-trisulfonic acid trisodium salt), EGCG ((−)-Epigallocatechin gallate) and fusicoccin were supplied by Sigma. HPTS stock was made by dissolving 52 mg of HPTS powder in 1 mL distilled water (pH 5.8). EGCG and fusicoccin were dissolved in water and methanol, respectively. These stocks were stored at 4°C.

Four-d-old seedlings were moved gently from 1/2 MS solid medium into 1/2 MS liquid medium supplemented by 1 mM HPTS and incubated for 30 mins. For the treatments, chemicals were added together with HPTS to this medium. Solid medium with the same HPTS concentration was cut into small and thin pieces (length (5 mm) × width (5 mm) × height (1 mm)). For static experiments, such as the calibration, 3 seedlings were mounted flatly and gently on the chip 1 (Figure 7.1 right), soaked with 10 µl of liquid medium and covered by a slice of the solid medium. For dynamic experiments, 1 or 2 seedlings were mounted in the channel of chip 2 (Figure 7.1 left) and gently fixed by a piece of plastic grid covered by cotton. 800 µL or 150 µL of liquid medium (for chip 1 and chip 2, respectively), supplies or not with drugs, was slowly injected into the channel, during the acquisition under the confocal microscopy.

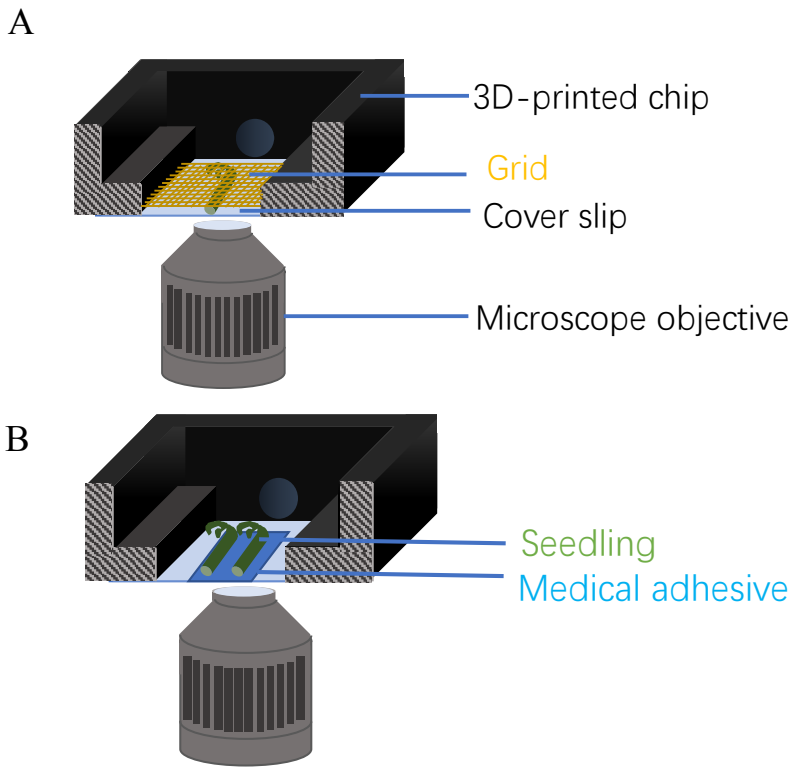

Figure 7.1: Scheme of 3D-printed homemade chip mounted on a microscope stage in which seedlings are immobilized by a grid (A) or by medical-adhesive (B).

Seedling imaging was performed using a LEICA SP5 confocal microscope. Parameters: Objective 63 × 1.4 OIL resolution 512 × 512, speed 700 Hz bidirectional, zoom factor 2.50. Excitation 1: 405 nm (8%), Excitation 2: 458 nm (84%). Emission: 478-534 nm. PMT: 789 V, PMT3: 700 V. Fake colors are red and green. The epidermis near root cap of intact seedling was chosen for the calibration. Images of damaged roots (shown by the penetration of fluorescent signals into the nucleus) were discarded.

Image analysis was performed using the Fiji software (http://fiji.sc/). The experiments described correspond to at least 6 biological repetitions. To avoid potential technical variability between different experiments, we report absolute pH^{Apo} values only when a standard curve was generated in the same experiment. For other experiments, the pH^{Apo} values of treated samples or mutants were given relative to mock-treated or WT seedlings. Because of the saturation of the HPTS signal outside the root, the zones outside the root were removed from the raw images. The trimmed images were processed using a Macro from Barbez et al. (2017) with small modifications. The intensity of the cell wall in processed images was measured manually using Fiji (Image>> Adjust>> Color threshold>> manually set to include all cell walls by the 3rd window>> Measure). The values were used to make a standard curve.

7.2. pH measurement using apopHusion

Four-d-old seedlings were mounted on the home-made devices as described in Figure 7.1. Seedling were immobilized using the grid and cotton as described or, if indicated, medical adhesive, which was spread evenly and air dried for 30 sec after which the seedlings were gently placed on the adhesive. 150 µL of 1/2 MS medium with or without chemicals (EGCG, fusicoccin and vanadate) or proteins (orange PME and PMEI3) was pipetted into the channel of the chip. The whole device was placed on the platform of Leica SP5 confocal laser scanning microscope (Leica Microsystems, Mannheim, Germany). Treatment solution was pipetted during the interval of acquisition at appropriate time points (see Results).

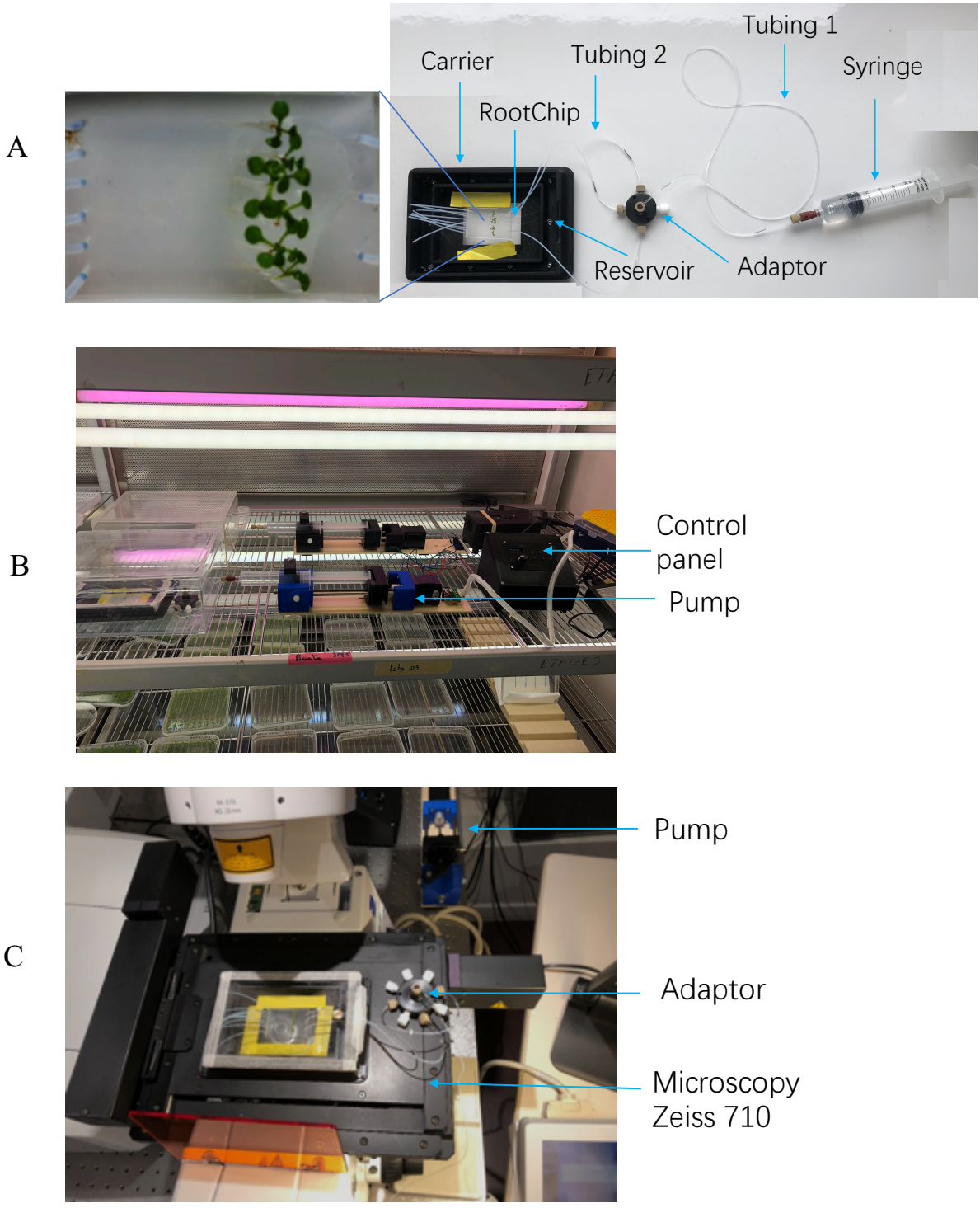

Figure 7.2: Microfluidic RootChip system. Image of microfluidic RootChip mounted on a plastic carrier (A). Image of microfluidic RootChip system in the growth chamber (B) and under a Zeiss 710 confocal microscope (C).

Confocal data acquisition was performed on SP5. For the apopHusion, data were acquired in xyzt mode using multi-positional and sequential scanning of EGFP and mRFP1, respectively. EGFP was excited at 488 nm using a white light laser and detected between 500 nm and 550 nm. mRFP was excited at either 558 nm or 585 nm with a white light laser and detected between 600 nm and 630 nm. 4 to 6 z-stacks were acquired for both channels.

The image analysis was performed using the Fiji software using the macro language (Supplementary data 1), and data were statistically evaluated with Microsoft Excel 2011. The experiments described were performed in at least 3 biological repetitions.

7.3. Rootchip assay

Plant growth and device preparation: apopHusion seeds (Gjetting et al. 2012) were sterilized, plated on solid 1/2 MS medium and stratified as described above. Next, seeds were transferred to solid MS medium pH 5.8, with 0.8% phytoagar (Duchefa) and 1.0% sucrose, that had been poured into pipette tips (Sorenson CAT#35020), from which the base was removed leaving a 5-mm long apical piece. The tips with the seeds on top of the medium were positioned in an upright position in the agar of a Petri dish with solid 1/2 MS medium. After 5 d of incubation in a growth chamber under 16 h light at 22°C, when the root apex had almost reached the lower tip outlet, and the tips were plugged into the Rootchip device (9 or 6 channels, 100 µm) (Grossmann et al. 2011). The Rootchip device was assemblied according to Figure 7.2. The device was sterilized with 70% ethanol and rinsed with distilled water and then with liquid 1/2 MS medium (1% sucrose, pH 5.8). The device was then transferred onto a homemade 3D-printed rectangular chip carrier (Figure 7.2), fixed with adhesive tape, and connected to the pressure lines (line 1: TYGON AAD04103 and line2: Adtech PTFE Tubing 0.56 mm ID ×1.07 mm OD).

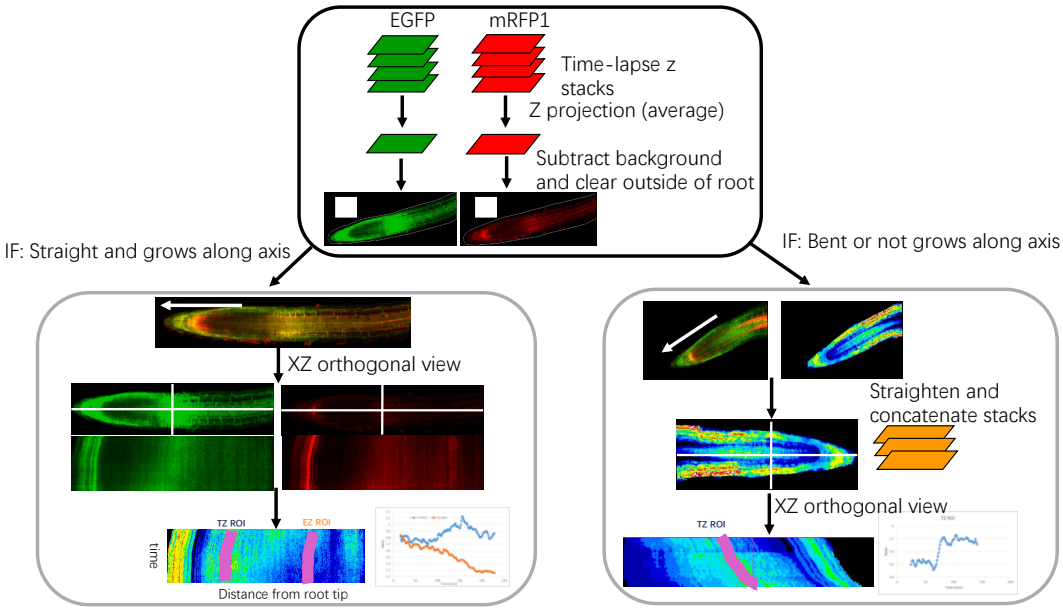

Figure 7.3: Processing of images from microfluidic RootChip experiment. The raw images were pretreated: Z-projection and after subtraction of the background noise (upper panel). The orthogonal views of both channels were used to calculate the ratio (below left panel). If the root was bent or did not grow along the root axis, the ratio image was straightened using Fiji. XZ orthogonal view was used as Kymograph (below right panel). A region of interest (violet) in parallel to the trace of root tip was used to select a specific region on the root.

The Rootchip carrier was covered with a transparent plastic board. 5 ml of distilled water was added into reservoir before covering the carrier in order to keep the inside humid. The whole device was placed in the same growth chamber for 3 d until imaging. The fluid speed was controlled at 1 µL/min/channel by a home-made pump (Figure 7.2). Drug concentration used were 200 µM EGCG-, 50 nM IAA- and 2 µM RALF34-containing dissolved in 1/2 MS medium at 4 µL/min/channel fluid speed.

Imaging and image processing: Roots tips that had reached the channels were imaged on inverted Zeiss 710 microscope (Figure 7.3). Images were taken with a 10× objective. EGFP was excited at 488 nm using a white light laser and detected between 500 nm and 550 nm. mRFP was excited at either 558 nm with a white light laser and detected between 600 nm and 630 nm. Six Z-stacks were acquired for both fluorescent proteins with 5 min intervals. During the acquisition, the seedlings were illuminated with white incandescent light.

Image processing and analysis were performed in FIJI. We first made average Z projections of both EGFP and mRFP1 and then substracted the background from each signal. The noise background outside of root was cut manually. The ratio of XZ orthogonal views of EGFP to that of mRFP were calculated. If the root was bent or did not grow along the root axis, the ratiometric images were straightened (Figure 7.3).

7.4. 3D imaging EGCG treated roots

Calcuofluor staining: Seedlings were grown vertically on 1/2 MS medium with 0, 50 µM, or 200 µM EGCG, respectively, at pH 5.8. Four-d-old seedlings were fixed overnight in an ethanol/acetic anhydride solution (75/25 v/v). Seedlings were then incubated in ethanol for 15 minutes (80% ethanol at 80°C), rehydrated in 50% then 30% ethanol for 10 minutes, then incubated in sodium hydroxyde 0.2N/SDS% for two hours at room temperature. Samples were then rinsed in water and stained for 30 minutes in calcofluor white 0.25% (Fluorescent Brightener 28) to which a few drops of 10 N NaOH were added to obtain complete dissolution. Seedlings were then rinsed in water

and mounted in Citifluor.

Imaging and images processing: Roots were imaged on a Zeiss LSM 710 confocal laser-scanning microscope. Samples were excited at 405 nm with an emission band of 410~550 nm. The distance interval of root Z-stacks was less than 0.45 um.

7.5. MorphlibJ analysis of 3D image

3D images of the root organization were analyzed using the Fiji software. We pretreated 3D images with Gaussian blur 3D (x, y and z = 1) and then performed “Attenuation correction”. A marker-based watershed segmentation of the images was applied with the “Morphological Segmentation” plugin of the MorpholibJ package (Legland et al. 2016), http://imagej.net/MorphoLibJ), under tolerance < 5, connectivity = 6 and “Advanced option” mode. Over-segmentation (one cell split in several parts) and under-segmentation (merged cells) errors were corrected by manually modifying markers before rerunning the watershed transformation. The process was repeated until no segmentation error remained. On the obtained labeled image from the Catchment basin file, we then used in-house developed tools (https://github.com/L-EL/labeledImg_tools) to manually extract cells of interest from cell files. To obtain precise cell files, we used “orthogonal view” and the « 3D Viewer » plugin from Fiji on each segmented cell file. The volume and cell surface were quantified using the "MorpholibJ>>Analyze>>Particle Analysis3D" plugin of Fiji. To map the volume or the surface area, we labeled images with “Assign measure to label”. The transversal width and longitudinal length of root cells were measured manually on the “selected labels” cell files.

7.6. Determination of protein content

The concentration of proteins was determined by the method described by Bradford (1976) using bovine serum albumin (BSA, Sigma, 05479) as the standard in phosphate buffer pH 7.5. Bradford 5X was diluted by double distilled water. 200 µL of Bradford

1X was allocated per well of 96-well plate. The first two columns were added BSA (0.5 µg/µL) in a range of 1 µL to 6 µL, whose values were used to make a standard curve. Wells B1/2, C1/2, D1/2, E1/2, F1/2, G1/2 and H1/2 contained 0-6 µL BSA, respectively. 5-10 µL of protein samples were added in other wells of the same plate and mixed well. After reaction for 5-45 mins, the blue intensity of each well was read using a Biotek microplate reader at 595 nm.

7.7. Cell wall-enriched protein extraction

Fifty mg of frozen material of 10-d-old roots and 4-week-old flowers were ground with liquid nitrogen. 1 ml buffer (containing 50 mM Na_2HPO_4, 20 mM citric acid, 1 M NaCl, 0.01% Tween 20 at pH 7.0) was added. The solution was shaken at 250 rpm for 1 h. The extracts were clarified by centrifugation at 10000 rpm for 30 min at 4°C. The supernatant was filtered using an Amicon ultracentrifuge filter 0.5 ml/10000 MWCO (Millipore, catalog no. UFC5010BK) in order to remove salts. Protein concentration was determined by the Bradford method (details see above).

7.8. Methanol colorimetric assay

Inhibition of AtPME2, AtPME3, citrus PME, citrus thermal-tolerance PME and PMEs from flower and root were determined using a colorimetric microassay adapted from Klavons and Bennett (1986). The reaction solution contained 5 µL of purified protein extract, 90% methylesterfied Citrus pectin (Sigma P9561) at 1mg/ml, 0.008 U of *Pichia pastoris* alcohol oxidase (Sigma A2404) and 50 mM sodium phosphate buffer (pH = 7.5) to a final volume of 100 µl. AtPME2, AtPME3, citrus PME, and citrus thermal-tolerance PME were prepared at 3 concentrations (1, 1/10 and 1/100 of purified proteins) and PMEs from flowers and roots at 2 concentration (1 and 1/10). The mixture was incubated at 28°C for 30 min. A first OD reading 420 nm was done on a BioTek PowerWaveXS2 spectrometer. 100 µL of developing solution (2 mM ammonium acetate, 0.02 M pentane-2,4-dione, 0.05 M glacial acetic acid) was added and the solution was incubated at 68°C for 15 min after which a second reading was done. A

standard dilution series from 0 to 10 nmol of methanol was included in each batch. Results were expressed as nmol MeOH/min/µL of protein using the methanol standard curve.

7.9. Gel diffusion assay

Citrus pectin (Sigma P9561) that was a 90% methylesterfied was dissolved in 0.1 M citric acid and 0.2 M Na_2HPO_4 buffer at pH 5.0, 6.3 and 7.5 (Hocq et al. 2017; Sénéchal et al. 2015 and 2017; Downie et al. 1998). One percent (w/v) agarose was added to the pectin buffer and heated until the agarose had dissolved. The solution was cooled to 60°C and transferred to a petri dish (50 ml per dish) and allowed to solidify. Wells were punched in the gel with a 2-mm-diameter plastic sucker and the gel plug removed by aspiration. The gel was nicked and the orientation of the nick marked on the outside of the petri dish with a marker. Ten µL of enzyme mixture was pipetted in to each well. Once loaded, the lids were placed on the dishes, the wells were incubated at 37°C for 16 h. After incubation, the gels were rinsed briefly with water and stained with 0.02% Ruthenium Red (Sigma) for 1h at room temperature. The dye was then poured off and the gel was rinsed with water again. Diameters of the red halos around each well were measured using the Fiji software.

7.10. Medium pH measurement assay

Ten 4-d old seedlings were transferred to a well containing 1 mL 1/2 MS salts, 1.0% sucrose, pH 5.8, and 14.0 µg/mL PMEI3 protein or the same volume of MES buffer. After 48h incubation, we added a pH indicator, fluorescein-dextran conjugate (MW, 10,000, Sigma, 30 µg/mL) in 200 µL of medium was added. Final fluorescein-dextran concentration is was 30 µL/mL. The fluorescent intensity of the medium (excitation at 485 nm, emission 535 nm) was recorded with a Fluoroscan Ascent (Thermo Scientific). A standard curve for pH was obtained using the 1⁄2 MS media adjusted to pH 6.2, 6.4, and 6.6.

7.11. MicroScale Thermophoresis (MST)

Molecular interaction between purified AtPME3 and AtPMEI3 was analyzed using MST, according to the method previously described (Sénéchal et al. 2015 and 2017; Hocq et al. 2017). For each experiment, lysine residues of AtPME3 were labeled. 30 µL of 100% DMSO was mixed thoroughly with the solid fluorescent dye, Monolith protein labelling kit blue NHS amine reactive (Nano Temper, catalog no. MO-L003). The concentration of the blue dye was adjusted to a 3-fold concentration of the AtPME3 (333 nM) by using the labeling buffer. 100 µL of AtPME3 protein was mixed with 100 µL dye solution in and incubated 30 min at room temperature in the dark. In the meantime, a PD SpinTrap G-25 column was prepared for removing the free dye. Eight ml of final storage buffer (50 mM Na_2HPO_4/NaH_2PO_4 buffer at pH 5.0, 6.3 and 7.5) was added to equilibrate the column. 200 µL of labeling reaction solution was loaded onto the column. The volume was adjusted to 500 µL using the final storage buffer after the sample has entered the bed completely. The flow-through was discarded. 600 µL of storage buffer was added and the eluate was collected after discarding the first few µL. The eluate was stored at 4°C in the dark until use. After the fluorescence intensity and standard capillary (NanoTemper, catalog no. MO-K002) were pretested, the binding affinity test was performed on MST. For each experiment, a constant concentration of labeled AtPME3 was titrated with decreasing concentrations of non-labeled recombinant AtPMEI3 from 100 µM to 24 nM. The resulting mixtures were incubated 15 min at room temperature and then loaded into the capillary. Thermophoresis experiments were performed with 40% of MST power and 90% of LED power for fluorescence acquisition.

7.12. Mass spectrometry

SDS-PAGE samples preparation: Each SDS-PAGE band was manually excised from the gels to be hydrolysed according to (Shevchenko et al. 1996). Each sample was de-stained in a 40% ethanol-10% acetic acid solution (v/v) for 15 min and progressively

dehydrated with 15 min incubations in first a 50% acetonitrile-25 mM ammonium bicarbonate solution and then in 100% acetonitrile. The dehydrated gel pieces were then reduced for 30 min with a 10 mM solution of DTT at 56°C and alkylated for 45 min with 55 mM iodoacetamide. The samples were then dehydrated as above. For digestion, the samples were incubated overnight at 37°C with 0.01 µg/µL of trypsin (Promega, Madison, WI) and dissolved in 50 mM ammonium bicarbonate, pH 8. The tryptic fragments were extracted from the gel by centrifugation after incubation of 15 min in a 0.5% trifluoroacetic acid - 50% acetonitrile (v/v) and in 100% acetonitrile solution, dried in a speed-vac, and reconstituted with 25 µL of a 2% acetonitrile - 0.1% formic acid (v/v) buffer.

LC-MS/MS analysis: HPLC was performed on a NanoLC-Ultra system (Eksigent). A 4 µL sample of the peptide solution was loaded at 7.5 µL min^{-1} on a precolumn cartridge (stationary phase: C18 Biosphere, 5 µm; column: 100 µm inner diameter, 2 cm; Nanoseparations) and desalted with 0.1% AF and 2% ACN. After 3 min, the precolumn cartridge was connected to the separating PepMap C18 column (stationary phase: C18 Biosphere, 3 µm; column: 75 µm inner diameter, 150 mm; Nanoseparations). Buffers A and B respectively were prepared with 0.1% HCOOH in water, and with 0.1% HCOOH in acetonitrile. The peptide separation was achieved at 300 nL min^{-1} with a linear gradient: from minute 0 to 10, at 5 to 30% of B; from minute 10 to 12, at 30 to 95% of B; from minute 12 to 18, at 95% of B (the regeneration step); from minute 18 to 19, at 95 to 5% of B; from minute 19 to 20, at 5% of B (the equilibration step). Remaining percentages are those of buffer A. One run took 45 mins. Eluted peptides were online analyzed with an LTQ XL ion trap (Thermo Electron) using a nanoelectrospray interface. Ionization (1.5 kV ionization potential) was performed with liquid junction and a non-coated capillary probe (10 µm inner diameter; New Objective). Peptide ions were analysed using Xcalibur 2.07 with the following data- dependent acquisition steps: (1) full MS scan (mass-to-charge ratio (m/z) 350-1 400, centroid mode) and (2) MS/MS (isolation width 1m/z, qz = 0.25, activation time = 30 ms, and

normalized collision energy = 35%; centroid mode). Step 2 was repeated for the three major ions detected in step 1. Dynamic exclusion was set to 45s.

Protein identification: A database search was performed with XTandem (version 10-12-01-1) (http://www.thegpm.org/TANDEM/). Enzymatic cleavage was defined as a trypsin digestion with one possible miscleavage. Regarding protein modifications, Cys carboxyamidomethylation was set to static. As potential modifications, Met oxidation, Nter acetylation, Nter deamidation on Gln, Nter deamidation on carbamidomethylated Cys, Nter neutral loss on Glu were set. Precursor mass and fragment mass tolerance were 2.0 and 0.8, respectively. A refinement search was added with similar parameters. The Araport11_genes.201606 database and a contaminant database (trypsin, keratins) were used for peptides identification.

Identified peptides were filtered and grouped using Xtandem according to: (1) A minimum of two different peptides required with an E-value smaller than 0.05, (2) a protein log(E-value) (calculated as the product of unique peptide E-values) smaller than -4.

7.13. PMEI3/5 heterologous expression and purification

Cloning: The coding sequences and codon-optimized sequences (ProteoGenix cn) of PMEI3 and PMEI5 were cloned into the pPICZα B (Invitrogen. Catalog no. V195-20). For codon-optimized constructs, PMEI3 and PMEI5 CDS rare codon analysis was performed on the GenScript platform using the host organism *Pichia pastoris.* Codon-optimized genes (Supplementary data 2) were synthesized by ProteoGenix inc. pPICZα B is a 3.6 kb vectors used to express and secrete recombinant proteins in *Pichia pastoris*. Recombinant proteins are expressed as fusions to an N-terminal peptide encoding the

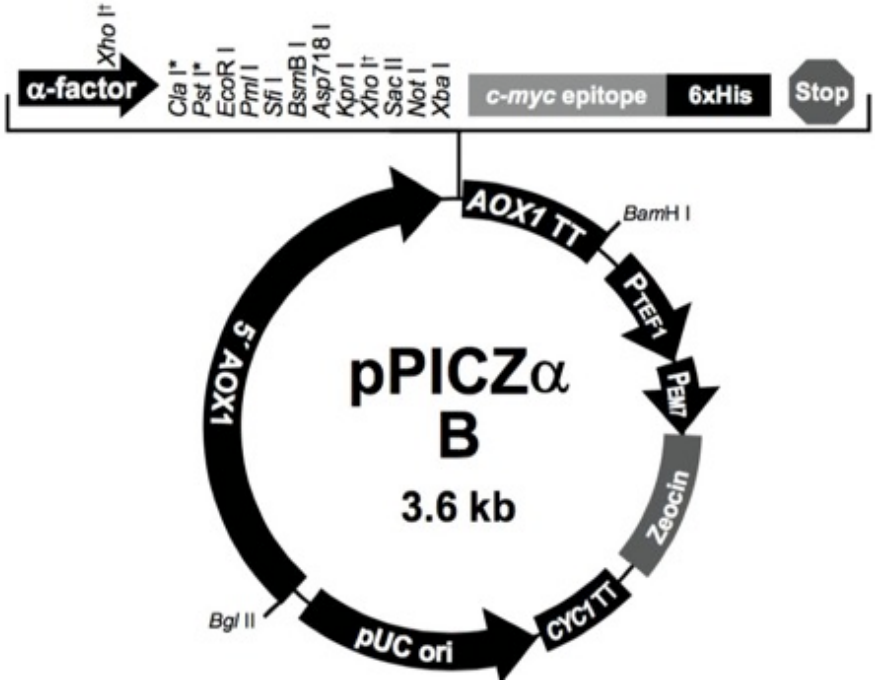

Figure 7.4: Map of pPICZα B vector.

Saccharomyces cerevisiae α-factor secretion signal (Figure 7.4). The vector allows high-level, methanol-inducible expression of the gene of interest in *Pichia*, and can be used in Pichia strain X-33. The coding sequences of PMEI3 and PMEI5 were amplified by using PCR using the primers shown in table (Table 7.1). The PCR products were purified using NucleoSpin Gel and a PCR Clean-up kit (obtained from Machery-Nagel) according to the user manuals. pPICZαB plasmid was propagated by transformation into *E. coli* strain TOP10. The purified PMEI3 and PMEI5 and pPICZαB plasmid were mixed and cleaved with restriction enzymes Pst I and Xba I at 37°C for 1 h. The reaction was terminated by heating at 75°C and the product was cleaned up. T4 ligase was used to ligate the purified DNA at 28°C for 1 h. Two μL of ligated solution was transformed into *E. coli* TOP 10. Transformants was selected on Low Salt LB plates containing 50 μg/mL Zeocin. Eight transformants for each were analyzed by restriction mapping or sequencing to confirm in-frame fusion of PMEI3 and PMEI5 with the α-factor secretion signal and the C-terminal tag. The appropriate transformants were cultivated to collect more plasmid. Plasmids were purified using a DNA purification kit (NucleoBond PC 100/BAC kit, obtained from Machery-Nagel). The recombinant plasmids were purified and then linearized by the Pme I restriction enzyme. Recombinant plasmids (at a concentration > 500 ng/μL) were transformed into *Pichia* pastoris strain X33. Transformed *Pichia* was plated onto YPDS medium containing 50 μg/mL of Zeocin.

Expression and induction: Transformants were selected and then cultivated in BMGY medium (Table 7.2). After 12-h incubation at 37°C with 250 rpm shaking, the OD_{600} of the culture was measured. The recombinant *Pichia* was transferred into BMMY medium in a bigger volume (Table 7.2) for a large-scale expression. The OD_{600} were

Table 7.1 Sequences of oligonucleotide primer used for construct designed for the heterologous expression of PMEI3 and PMEI5.

Primer name	Sequence	Use
PMEI3-F (with additional Hig tag)	ATAAGCTGCAGAGCATCATCATCATCATCATCGTCATAATGGTGCAGAAGATATC	Construction primer
PMEI3-F	ATAAGCTGCAGAGCGTCATAATGGTGCAGAAGATATC	Construction primer
PMEI3-R	CGCTCTCTAGAAATCAAAGATGTACGTCGTGGG	Construction primer
PMEI3-R (with a stop codon)	CGCTCTCTAGAGGTCAAAGATGTACGTCGTGGG	Construction primer
PMEI5-F (with additional Hig tag)	ATAAGCTGCAGAGCATCATCATCATCATCATCGTATTCCAGCCAGAGACATTGACA	Construction primer
PMEI5-F	ATAAGCTGCAGAGATTCCAGCCAGAGACATTGACA	Construction primer
PMEI5-R	CGCTCTCTAGAAATTAGGTCACAAGCTTGTTGA	Construction primer
PMEI5-R (with a stop codon)	CGCTCTCTAGAGGTTAGGTCACAAGCTTGTTGA	Construction primer
AOX1-F	GACTGGTTCCAATTGACAAGC	Sequence testing primer
AOX1-R	GCAAATGGCATTCTGACATCC	Sequence testing primer

measured every 24 h to investigate the *Pichia* growth rate. In the meantime, 100% methanol was added to the medium to keep its final concentration at 0.5% (v/v). To make sure the recombinant proteins expressed correctly, the concentrated supernatant of the culture was tested using SDS-PAGE and/or Immunoblotting (details see above).

Purification: After 4-d expression, *Pichia* were removed by centrifugation at 5000 rpm for 5 min. To the protein-containing supernatant was added PBS buffer 10X (Eurobio, GAUPBS00-01), 400 mM NaCl, 5 mM imidazole and 500 µL cOmplete Hig-tag purification Resin (obtained from Roche, ref 05893682001). The mixture was gently shaken at 4°C for 4 h in dark. The supernatant was removed by centrifugation at 8000 rpm for 5 min at 4°C. The resin was washed by 5 ml of wash buffer 1 (PBS 1X with 400 mM NaCl and 5 mM imidazole), 5 ml of wash buffer 2 (PBS 1X with 400 mM NaCl and 30 mM imidazole) and eluted by elution buffer (PBS 1X with 400 mM NaCl and 400 mM imidazole) for 3 times (800 µL for each). The 3 elutes were collected and centrifuged at 8000 rpm for 30 min by using 3-kDa filter (Amicon Ultra-2 mL, UFC200324). The buffer change was performed using PD SpinTrap G-25 column. Final protein concentration was measured with Bradford assay. The purified PMEI3 was stored at 4°C in the dark until use.

7.14. Cell lysis and immunoblotting

During the purification of PMEI proteins, the cells pellet was collected, rapidly frozen by liquid nitrogen and then stored at -80°C before use. PMEI3 and PMEI5 *Pichia* cells were thawed at room temperature. We resuspended 1 mL of pellet in 2 mL of phosphate buffer pH 7.0. 300 µL of protease inhibitor 1x was (Constant systems Ltd. United Kingdom). The lysate was centrifuged at 5000 rpm for 15 min at 4°C. Both supernatant and pellet were analyzed using immunoblotting.

SDS-PAGE electrophoresis and Immunoblot: The proteins were resolved using a 15% acrylamide/bisacrylamide SDS-PAGE (Table 7.3), using a running buffer composed of 25 mM Tris-base, 192 mM glycine, and 0.1% SDS at pH 8.7. 13 µL of protein was

added to 15 µL Laemmli buffer 2X (4% SDS, 10% 2-mercaptoethanol, 20% glycol, 0.004% bromophenol blue and 0.125 M Tris-HCl) and 2 µL of 1 M imidazole. The protein mix was heated at 95°C for 20 mins. 15 µL of protein mix was loaded into a well of SDS-PAGE gel. After electrophoresis at 100 mA for 100 mins, the gel was stained with Pageblue protein staining solution (Thermo Scientific, catalog no. 24620) and destained with distilled water for 6 h. After migration of proteins, the gel SDS-PAGE was immerged in cathode buffer (25 mM of Tris pH 9.4, 40mM of Glycine, 10% of ethanol) for 15 min. A piece of Hybond-P PVDF membrane (GE Healthcare, catalog no. RPN303F) was placed in 100% ethanol for 15 seconds and rinsed by water for 2 mins. Then the membrane was incubated in anode buffer II (25 mM of Tris pH 10.4, 10% of ethanol) for 5 mins. The membrane, gel, and 7 same-sized Whatmann papers (previously immerged in anode I, anode II and cathode buffers) were placed according to Figure 7.5. The transfer "sandwich" was exposed to 25 V and 1 A for 30 mins by a Trans-Blot TURBO transfer system (Bio-Rad, catalog no. 170- 4155). The membrane was incubated in 4.0% commercial milk for 30 mins and then incubated for 1 h at room temperature under shaking (50 rpm) with 4.0% commercial milk containing 1/5000 of commercial primary antibody raised against poly-His tag directly coupled with peroxidase (Sigma, catalog no. A7058). After washed 3x by PBS 1x, 10 mins for each, the membrane was added 500 µL of DAB substrate for peroxidase was added (Thermo Scientific, catalog no. 34002) before imaging. Imaging was performed with LAS-4000 according to the user manual.

7.15. Fourier Transform InfraRed Spectroscopy

Four-day-old seedlings were collected and immerged in 100% ethanol until use. Before acquisition, the seedlings were squashed between two BaF2 windows and abundantly rinsed in distilled water for 2 min. The samples were then dried on the window at 37°C for 20 min. An area of 30 mm x 30 mm halfway the root, on the side of the central cylinder, was selected for spectra collection. Spectra were collected using a ThermoNicolet Nexus spectrometer with a Continuum microscope accessory.

7.16. Greengate cloning of PMEI3/5 inducible constructs and transformation

All constructs are based on the GreenGate cloning system (Lampropoulos et al. 2013). The structures of final construct were shown in Figure 7.6 and 7.7. The order of building constructs is as follows: entry modules, intermediate vectors and final destination vectors.

Construction of Empty Entry Plasmids: Vector elements were either generated via PCR amplification or via artificially synthesized oligo duplexes. GreenGate vectors and modules used in this study were shown in Table 7.4. Plasmid purification was performed using plasmid DNA purification kit (NucleoBond PC 20/BAC kit, obtained from Machery-Nagel) according to the recommendations of the manufacturer. DNA purification from gel and PCR product was performed using NucleoSpin Gel and PCR Clean-up kit (obtained from Machery-Nagel). All constructs were verified by sequencing and test digestion. PCRs were done with Phusion High-Fidelity DNA Polymerase (Fisher Scientific - Germany GmbH, Schwerte, Germany). PCR products and intermediate plasmids were cut with conventional restriction endonucleases (obtained from Fisher Scientific - Germany GmbH, Schwerte, Germany) and ligated with T4 DNA ligase (Fisher Scientific - Germany GmbH, Schwerte, Germany). For complex PCR products, the single elements were amplified separately with primers shown in Table 7.5. Bsa I restriction enzyme sites were added to the primers, the single PCR products were digested with the respective enzymes, ligated and the reaction products used as templates for subsequent PCRs. pGGF000 entry plasmid was used to directly mutagenesis, changing the G site (GTAT) into a H site (TAGG). The new entry plasmid was called pGGFH000. p4Op DNA and the expression cassette 2 were a gift from the laboratory of Sebastian Wolf (University of Heidelberg, Germany). *E. coli* cells electro-transformed with the resulting plasmids were grown in medium with 50 mg/mL spectinomycin or 50 mg/mL kanamycin. For *Agrobacterium. tumefaciens*, ampicillin and spectinomycin were used at 100 mg/mL and kanamycin at 50 mg/mL,

Table 7.2 BMGY and BMMY components

Components	Buffered Glycerol-complex medium (BMGY)	Buffered Methanol-complex medium (BMMY)
Yeast extract	1.0%	1.0%
Peptone	2.0%	2.0%
Potassium phophate	100 mM	100 mM
Yeast nitrate base	1.34%	1.34%
Biotin	4×10^{-5} %	4×10^{-5} %
Glycerol	1.0 %	-
Methanol	-	0.5%

Table 7.3 SDS-PAGE gel components

Components	Resolving Gel (10 mL)	Stacking Gel (8 mL)
H_20	1.0 mL	5.0 mL
30% Acryl/Bis	5 mL	1.0 mL
1 M Tris pH 8.8	3.75 mL	1.0 mL
10% SDS	100 µL	80 µL
10% APS	100 µL	80 µL
TEMED	10 µL	8 µl

respectively. Plasmid from Agrobacterium was extracted using Nucleospin Plasmid Kit (obtained from Machery-Nagel) and its sequence was verified by test digestion. Construction of the Intermediate Vectors for Two Constructs on One T-DNA: pGGM000 and pGGN000 were created from two PCR products each. The PCR products were digested with these enzymes and ligated.

Methylated oligonucleotide duplex synthesis and annealing: The oligonucleotide duplex was created by annealing oligonucleotides A02827 (59-taggaccttgagacCgaaaaggtggtctCa-39) and A02828 (59-atactgagacCacctttcggtctCaaggt-39), in which the nucleotides in capital letters are methylated. Equal volumes of both complementary oligos at equimolar concentration were mixed in a 1.5 ml eppendorf tube. The tube was heated at 95°C for 5 mins and cooled at room temperature for 1 h. The oligonucleotide duplex was stored on ice until use.

GreenGate Reaction: Plasmids were purified from the bacterial hosts using the innuPREP Plasmid Mini Kit (Analytik Jena AG, Jena, Germany) according to the user manual. DNA was eluted with 100~125 µL elution buffer. The DNA concentration was usually not determined exactly but estimated after gel electrophoresis estimated to be around 100 ng/µL judging from earlier preparations done with the same kit. For the GreenGate reaction itself 1.5 µL plasmid of each of the six modules were mixed with 1 µL of the destination vector, 1.5 µL CutSmart Buffer, 1.5 µL ATP (10 mM), 1 µL T4 DNA ligase (30 U/µL) and 1 µL BsaI-HF in a total volume of 15 µL. We performed 50 cycles of 37°C for 5 minutes and 16°C for 5 minutes each, followed by 50°C for 5 minutes and 80°C for 5 minutes. Later, we reduced the incubation time to 2 min each and the cycle number to 30. 6 µL of the reaction were used for heat-shock transformation of ccdB-sensitive *E. coli* TOP10. The products of the first GreenGate reactions were analyzed by both restriction endonuclease test digestions and sequencing of the ligation sites. When creating the intermediate supermodules for two

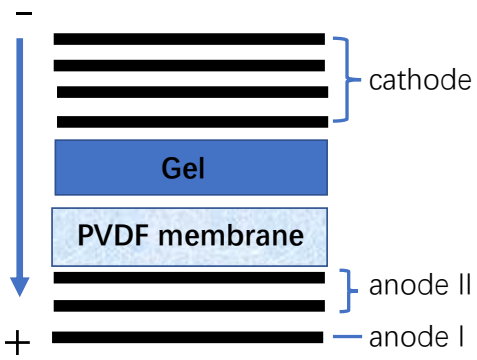

Figure 7.5: Scheme of protein transfer onto membrane in for immune-blotting.

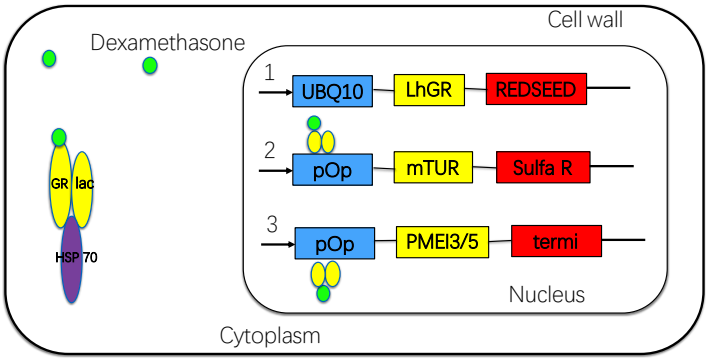

Figure 7.6: Cartoon of the binary activated dexamethasone-inducible system. In the absence of dexamethasone, the GR-lac-HSP70 complex is maintained in cytoplasm without activating the expression cassette. In the presence of inducer, the complex releases HSP70 and drives expression in nucleus. 1: activator cassette, 2 and 3: expression cassette. HSP70: heat shock protein 70, GR: glucocorticoid receptor. lac: lac transcription. UBQ10: ubiquitin 10 promoter. pOp: p4Op promoter. mTUR: mTURQUOISE. Sulfa R: sulfadiazine resistance. Termi: terminator.

constructs on one T-DNA approach, ligase and ATP were added again after the GreenGate reaction and the mixture incubated for one more hour at room temperature before heat-inactivation and heat-shock transformation. When using the methylated oligonucleotide pair, BsaI was added after the GreenGate reaction and digestions carried out for one hour at 37°C prior to heat-inactivation and transformation.

***Arabidopsis* transformation and plant selection**: Colombia and *xxt1xxt2* mutant plants were transformed by a modified version of the floral dip protocol (Clough and Bent 1998), where only the tips of the inflorescences were dipped into the Agrobacterium suspension. For selection on soil, BastaTM (glufosinate-ammonium; Bayer CropScience Deutschland GmbH, Langenfeld, Germany) was used at a concentration of 20 mg/L, both for spraying and watering. The concentrations of sulfadiazine, BastaTM, and kanamycin for selection on MS plates were 0.75-7.5 mg/mL, 10 mg/mL, and 50 mg/mL, respectively.

7.17. Greengate cloning of pH sensor constructs and *Arabidopsis* and tobacco transformation

The main steps of pH sensor construct building and *Arabidopsis thaliana* transformation and plant selection are similar to those of the inducible PMEIs lines (see above), with tiny modifications. The map of constructs was shown in Figure 7.8. Primers used for pH sensor constructs are shown in Table 7.6.

***Nicotiana Benthamiana* Infiltration:** *Agrobacterium. tumefaciens* strain ASE was transformed with the respective constructs. Transgenic clones were cultured in liquid selective LB medium for 2 nights at 28°C, resuspended in infiltration medium (10 mM $MgCl_2$, 10 mM MES, 150 mM acetosyringone, pH 5.7) and pressed with a blunt syringe through the stomata at the abaxial site of leaves of approximately 4-week-old plants. The plants were put back in the incubators for 48 or 72 h before analyzing the fluorescence levels.

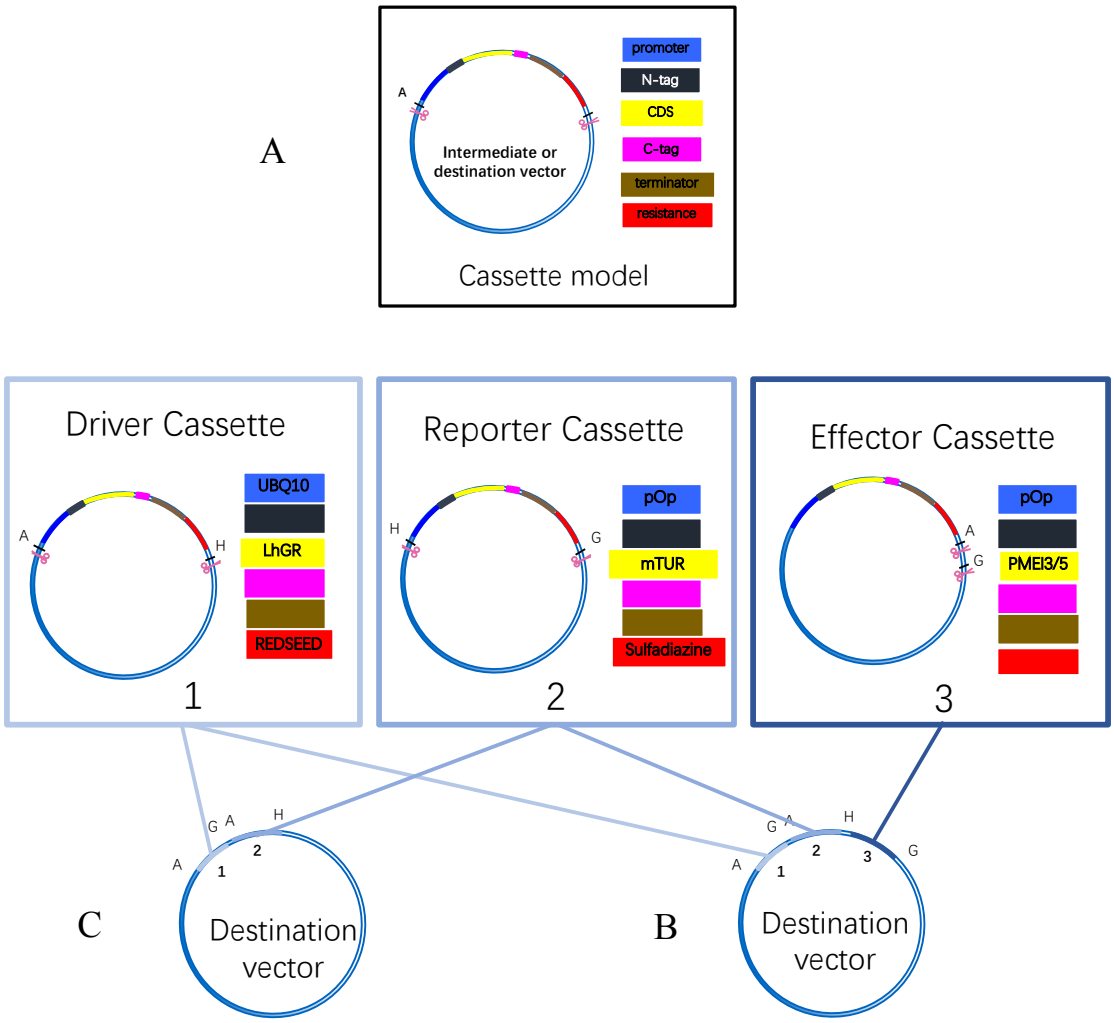

Figure 7.7: Map of GreenGate construct of inducible PMEIs overexpressing lines (B) and vector control (C). (A) GreenGate cassette model containing six modules shown in different colors. capital letter: GreenGate overhang. (B) Constructs of inducible PMEIs overexpression line consists of three expression cassettes that harbors inducible transcription factor, reporter gene and gene of interest. (C) Vector control consists of driver cassette and reporter cassette which as same with (B). UBQ10: ubiquitin 10 promoter. pOp: p4Op promoter. mTUR: mTURQUOISE. LhGR: glucocorticoid receptor.

Table 7.4 GreenGate vectors and modules used in this study.

Modules	Name	Type	Overhangs	Resistance	Addgene ID
Empty entry vectors	pGGC000	CDS	C–D	Carbenicillin	48858
	pGGE000	Plant terminator	E–F	Carbenicillin	48860
	pGGF000	Plant resistance cassette	F–G	Carbenicillin	48861
	pGGH000	N-tag + CDS + C-tag + terminator	B–F	Carbenicillin	48862
Empty intermediate vectors	pGGM000	Assembly of expression cassette # 1	A–H	Kanamycin	48864
	pGGN000	Assembly of expression cassette # 2	H–G	Kanamycin	48865
Empty destination vectors	pGGZ001	Plant resistance at RB	A–G	Spectinomycin	48868
Plant promoters	pGGA006	UBQ10 (UBIQUITIN10) promoter	A–B	Carbenicillin	48816
N-tags	pGGB003	B-dummy	B–C	Carbenicillin	48821
C-tags	pGGD002	D-dummy	D–E	Carbenicillin	48834
Plant terminators	pGGE003	At1g04880 terminator	E–F	Carbenicillin	48854
Adapters	pGGG001	FH-adapter	F–H	Carbenicillin	48850
Adapters	pGGG002	HA-adapter	H–A	Carbenicillin	48851

Table 7.5 Sequences of oligonucleotide primers used for inducible PMEI overexpressing constructs.

Primer name	Sequence	Use
PMEI5-GG-F	AACAGGTCTCAGGCTGTATGGCCACAATGCTAATAAA	Greengate constructs
PMEI5-GG-R	AACAGGTCTCACTGATTAGGTCACAAGCTTGTTGA	Greengate constructs
PMEI3-GG-F	AACAGGTCTCAGGCTGTATGGCTCCTACACAAAATCT	Greengate constructs
PMEI3-GG-R	AACAGGTCTCACTGATCAAAGATGTACGTCGTG	Greengate constructs
LhGR-GG-F	AACAGGTCTCAGGCTGTATGGCTAGTGAAGCTCGAAA	Greengate constructs
LhGR-GG_R	AACAGGTCTCACTGATTACTCTTTTTTTGGGTTTGGTGGG	Greengate constructs
RedSeed-GG-F	AACAGGTCTCAACTACATCGGTGATTGATTCCTTT	Greengate constructs
RedSeed-GG-R	AACAGGTCTCACCTACCCGATCTAGTAACATAGATGAC	Greengate constructs
pGGN000-F	AACGTTGTGAAGCAACGGCCCGGA	Greengate constructs
pGGN000-R	ATTGCCCGACATTATCGCGAGCCC	Greengate constructs
Turquoise-R	AGTCGATGCCCTTCAGCTCGATGC	Greengate constructs
Sulf-promoter-F	CAGTGCGCAAGACGTGACGTAAGT	Greengate constructs
Sulf-promoter-R	CAGTGCGCAAGACGTGACGTAAGT	Greengate constructs
UBQ10-F	GATTTGTGATTTCTATCTAGATCTGGT	Colony PCR
pGGZ001-R	CTTTTGCTCACATGAGATCTCAAAC	Colony PCR
pGGM00-F	GAGCGGATTTGAACGTTGTGAAGC	Colony PCR
pGGM00-R	GATTGCCCGACATTATCGCGAGCC	Colony PCR
RedSeed-ter-F	GAATCCTGTTGCCGGTCTTGC	Colony PCR

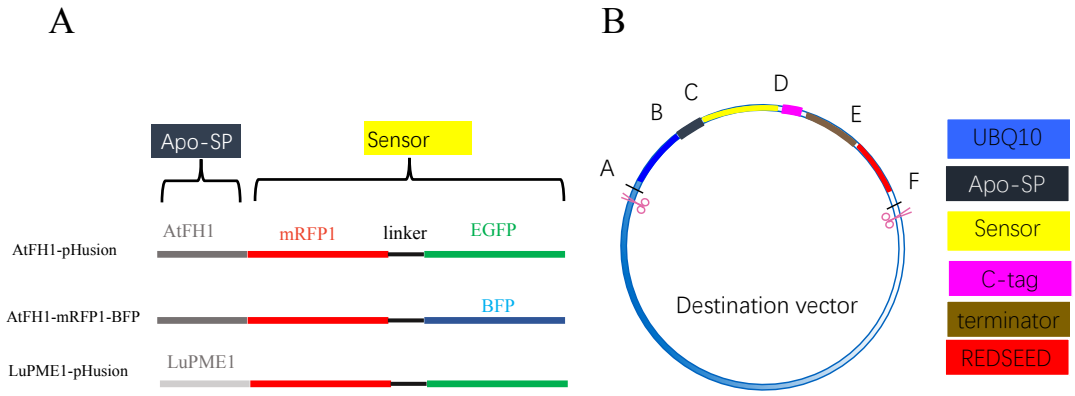

Figure 7.8: Map of GreenGate construct of cell wall-targeted pH sensor. (A) pH sensor constructs consist of an apoplast targeting signal peptide (Apo-SP) and a fluorescent sensor. AtFH1: N terminal of Arabidopsis Formin1. LuPME1: mutated and non-functional flax PME. (B) GreenGate construct structures. See also Figure 6.

Confocal acquisition was performed on SP5. For apopHusion, EGFP was excited at 488 nm using a white light laser and detected between 500 nm and 550 nm. mRFP1 was excited at either 558 nm or 585 nm with a white light laser and detected between 600 nm and 630 nm. Fluorescence intensities were measured with the Fiji software. BFP in AtFH1-mRFP1-BFP sensor was excited at 405 nm and emitted at 515 nm.

7.18. q-RT-qPCR

Leaves or roots of each line were collected and rapidly frozen using liquid nitrogen. Samples were stored at -80°C until grinding. Grinding was performed in a mortar with freezing by liquid nitrogen. The extraction of total RNA was performed using RNeasy Plant Mini kit (QIAGEN, Cat No. 74904) following the manufacturer's recommendations and treated with Room Temperature Stable (RTS) DNase (QIAGEN Cat No 79254) only when RNA was prepared for quantitative q-RT-PCR (Mobio). Degradation and genomic DNA contamination were analyzed before cDNA synthesis. The following cycle was used: 95°C for 3 min, 40 cycles of 95°C for 5 s and 60°C for 20s, followed by 65°C for 5s and 95°C for 30s. Specific probes were amplified by PCR using primers indicated in Table 7.7.

7.19. GUS staining and GUS activity measurement

Ten 4-d-old seedlings were immerged in GUS staining solution (Table 7.8). The well plate was placed in a container that can be vacuumed. The plate was kept in half-vacuum condition over night at room temperature. The seedlings were immerged by 100% ethanol for 2 h to remove chlorophyll and rinsed by water for 3 times.

Table 7.6 Sequences of oligonucleotide primers used for pH sensors

Primer name	Sequence	Use
AtFH1-GG-F	AACAGGTCTCAAACAGCATGCTCTTCTTCTTATTCTTC	Greengate constructs
AtFH1-GG-R	AACAGGTCTCAAGCCGAGTTTTTTGGAGTTAGGTGG	Greengate constructs
LuPME1-GG-F	AACAGGTCTCAAACAGCATGTCGACCTTCTCCCATGCA	Greengate constructs
LuPME1-GG-R	AACAGGTCTCAAGCCGACACCAATCAAGCCGGCGTCAA	Greengate constructs
mR-BFP2-GG-F	AACAGGTCTCAGGCTGGATGGCCTCCTCCGAGGACGT	Greengate constructs
mR-BFP2-GG-R	AACAGGTCTCACTGAACCTTTGGACGGCAGGTCACA	Greengate constructs
pHusion-GG-F	AACAGGTCTCAGGCTGGATGGCCTCCTCCGAGG	Greengate constructs
pHusion-GG-R	AACAGGTCTCACTGATTACTTGTACAGCTCGTCC	Greengate constructs
Redseed-GG-F	AACAGGTCTCAACTACATCGGTGATTGATTCCTTTA	Greengate constructs
Redseed-GG-R	AACAGGTCTCAATACCCCGATCTAGTAACATAGATGAC	Greengate constructs
pGGZ001-F	CCCGGAATTAGATCTTGGCA	Colony PCR

GUS activity test: Fresh or frozen samples were ground in GUS buffer. The mixture was centrifuged at 10000 rpm for 30 min at 4°C. Supernatant was collected for the activity test. Total protein concentration was measured using Bradford assay (details see above). One or 0.5 µg total protein was added to the well. 150 µL 2 mM MUG was mixed in each well just before the acquisition. The kinetics of fluorescent intensity (excitation at 355 nm, emission 460 nm,) was recorded with a Fluoroscan Ascent (Thermo Scientific) at 37°C for 30 min.

Table 7.7 Sequences of oligonucleotide primer used for qRT-PCR

Primer name	Sequence	Use
PMEI3-20740_F	AAACGGAGGTGAAGCAGTGGATG	PMEI3
PMEI3-20740_R	GACCATGTAAAGCGCGTTGCTC	PMEI3
PMEI5-31430_F	AAACGCGATTCCAGCCAGAGAC	PMEI5
PMEI5-31430_R	AGGCAGAAGGGCACATCAGTTG	PMEI5
mTurquoise-F	ACGTAAACGGCCACAAGTTC	mTURQUOISE
mTurquoise-R	CTTCATGTGGTCGGGGTAGC	mTURQUOISE
At1g13440-F	GGTACGACAACGAATGGGGT	Standard gene
At1g13440-R	TGACTGCGCATGGAATCAGT	Standard gene

Table 7.8 GUS staining solution components

Components	Final concentration
Phosphate buffer pH 7.0	100 mM
Triton 100X	0.1% (v/v)
Ferrocyanide white	0.5 mM
Ferrocyanide orange	0.5 mM
X-Glucose	1.9 mM
H_2O	To 1 ml

References

Ammann, D. (2013). Ion-selective Microelectrodes: Principles, Design and Application (Vol. 50) (Berlin, Heidelberg: Springer Science & Business Media).

Amtmann, A., and Sanders, D. (1999). Mechanisms of Na^+ uptake by plant cells. Adv. Bot. Res. *29,* 75–112.

Andres-Robin, A., Reymond, M.C., Dupire, A., Battu, V., Dubreulle, N., Mouille, G., Lefebvre, V., and Moneger, F. (2018). Evidence for the regulation of gynoecium morphogenesis by ETTIN via cell wall dynamics. Plant. Physiol. DOI:10.1104/pp.18.00745

Atmodjo, M.A., Sakuragi, Y., Zhu, X., Burrell, A.J., Mohanty, S.S., and Atwood, J.A. (2011). Galacturonosyltransferase (GAUT)1 and GAUT7 are the core of a plant cell wall pectin biosynthetic homogalacturonan: galacturonosyltransferase complex. Proc. Natl. Acad. Sci. USA. *108(50)*. 20225-20230.

Axelos, M.A.V., and Thibault, J.F. (1991). Influence of the substituents of the carboxyl groups and of the rhamnose content on the solution properties and flexibility of pectins. Int. J. Biol. Macromol. *13(2)*, 77–82.

Barbez, E., Dünser, K., Gaidora, A., Lendl, T., and Busch, W. (2017). Auxin steers root cell expansion via apoplastic pH regulation in *Arabidopsis thaliana*. Proc. Natl. Acad. Sci. USA. *114 (24),* 4884-4893.

Barbier-Brygoo, H., De Angeli, A., Filleur, S., Frachisse, J.M., Gambale, F., Thomine, S., and Wege, S. (2011). Anion channels/transporters in plants: from molecular bases to regulatory networks. Annu. Rev. Plant Biol. *62*, 25–51.

Basak, R., and Bandyopadhyay, R. (2014). Formation and rupture of Ca^{2+} induced pectin biopolymer gels. Soft Matter. *10(37)*, 7225–7233.

Baxter, I., Tchieu, J., Sussman, M.R., Boutry, M., Palmgren, M.G., Gribskov, M., Harper, J.F., and Axelsen, K.B. (2003). Genomic comparison of P-type ATPase ion pumps in Arabidopsis and rice. Plant. Physiol. *132,* 618–628.

Beauzamy, L., Nakayama, N., and Boudaoud, A. (2014). Flowers under pressure: Ins and outs of turgor regulation in development. Ann. Bot. *114*, 1517–1533.

Bergonci, T., Ribeiro, B., Ceciliato, P.H.O., Guerrero-Abad, J.C., Silva-Filho, M.C., and Moura, D.S. (2014). *Arabidopsis thaliana* RALF1 opposes brassinosteroid effects on root cell elongation and lateral root formation. J. Exp. Bot. *65*, 2219–2230.

Bibikova, T.N., Jacob, T., Dahse, I., and Gilroy, S. (1998). Localized changes in apoplastic and cytoplasmic pH are associated with root hair development in *Arabidopsis thaliana*. Development *125*,

2925–2934.

Biswal, A.K., Atmodjo, M. A., Li, M., Baxter, H.L., Yoo, C.G., Pu,Y.Q., et al. (2018). Sugar release and growth of biofuel crops are improved by downregulation of pectin biosynthesis. Nat. Biotechnol. *36,* 249-257.

Bizzarri, R., Serresi, M., Luin, S., and Beltram, F. (2009). Green fluorescent protein based pH indicators for *in vivo* use: a review. Anal. Bioanal. Chem. *393*, 1107–1122.

Blackford, S., Rea, P.A., and Sanders, D. (1990). Voltage sensitivity of H^+/Ca^{2+} antiport in higher plant tonoplast suggests a role in vacuolar calcium accumulation. J. Biol. Chem. *265,* 9617–20.

Bosch, M., and Hepler, P.K. (2005). Pectin methylesterases and pectin dynamics in pollen tubes. Plant. Cell. *17*, 3219–3226.

Bosch, M., and Hepler, P.K. (2006). Silencing of the tobacco pollen pectin methylesterase NtPPME1 results in retarded *in vivo* pollen tube growth. Planta. *223*, 736–745.

Bosch, M., Cheung, A.Y., and Hepler, P.K. (2005). Pectin methylesterase, a regulator of pollen tube growth. Plant. Physiol. *138*, 1334–1346.

Bou Daher, F., Chen, Y.J., Bozorg, B., Clough, J., Jonsson, H., Braybrook, S., (2018). Anisotropic growth is achieved through the additive mechanical effect of material anisotropy and elastic asymmetry. elife. 7: e38161.

Braccini, I., Grasso, R.P., and Pérez, S. (1999). Conformational and configurational features of acidic polysaccharides and their interactions with calcium ions: A molecular modeling investigation. Carbohydr. Res. *317*, 119–130.

Braccini, I., Rodríguez-Carvajal, M.A., and Pérez, S. (2005). Chain-chain interactions for methyl polygalacturonate: Models for high methyl-esterified pectin junction zones. Biomacromolecules *6*, 1322–1328.

Bradford, M.M. (1976). A rapid and sensitive method for the quantitation of microgram quantities of protein utilizing the principle of protein-dye binding. Anal. Biochem. *72,* 248–254.

Braybrook, S.A., and Peaucelle, A. (2013). Mechano-chemical aspects of organ formation in *Arabidopsis thaliana*: the relationship between auxin and pectin. PLoS ONE. 8.

Brewbaker, J.L., and Kwack, B.H. (1963). The essential role of calcium ion in pollen germination and pollen tube growth. Amer. J. Bot. *50,* 859–865.

Buchanan, B. B., Gruissem, W., Jones, R. L. (2001). Biochemistry and Molecular Biology of Plants. American Society of Plant Physiologists.

Burton, R.A., Gidley, M.J., Fincher, G.B. (2010). Heterogeneity in the chemistry, structure and function of plant cell walls. Nat. Chem. Biol. *6,*724–32.

Bush, D.R. (1988). Amino acid transport into membrane vesicles isolated from *Zucchini*: evidence of a proton-amino acid symport in the plasmalemma. Plant. Physiol. *88,* 487-90.

Bush, D.R. (1990). Electrogenicity, pH-dependence, and stoichiometry of the proton-sucrose symport. Plant. Physiol. *93,* 1590-96.

Bush, D.R. (1993). Proton-coupled sugar and amino acid transportation in plants. Annu. Rev. Plant. Physiol, Plant. Mol. Biol. *44,* 513-542.

Caesar, K., Elgass, K., Chen, Z.H., Huppenberger, P., Witthoft, J., Schleifenbaum, F., et al. (2011). A fast brassinolide-regulated response pathway in the plasma membrane of *Arabidopsis thaliana*. Plant J. *66,* 528-540.

Caffall, K.H., and Mohnen, D. (2009). The structure, function, and biosynthesis of plant cell wall pectic polysaccharides. Carbohydr. Res. *344*, 1879–1900.

Campbell, P., and Braam, J. (1999). *In vitro* activities of four xyloglucan endotransglycosylases from Arabidopsis. Plant J. *18,* 371-382

Cannon, M.C., Terneus, K., Hall, Q., Tan, L., Wang, Y. Wegenhart, B.L., Chen, L.W. et al. (2008). Self-assembly of the plant cell wall requires an extensin scaffold. Proc. Natl. Acad. Sci. USA. *105,* 2226–223.

Cárdenas, L., Lovy-Wheeler, A., Kunkel, J.G., and Hepler, P.K. (2008). Pollen tube growth oscillations and intracellular calcium levels are reversibly modulated by actin polymerization. Plant Physiol. *146*, 1611–1621.

Chan., S.Y., Choo., W.S., Young., D.J., and Loh., X.J. (2017). Pectin as a rheology modifier: origin, structure, commercial production and rheology. Carbohydrate. Polymers. *161*, 118-139.

Chebli, Y., Kaneda, M., Zerzour, R., Geitmann, A. (2012). The cell wall of the Arabidopsis pollen tube-spatial distribution, recycling, and network formation of polysaccharides. Plant Physiol. *160*, 1940–1955.

Chen, J., Chen, X., Zhang, Q., Zhang, Y., Ou, X., An, L., Feng, H., Zhao, Z. (2018). A cold-induced pectin methylesterase inhibitor gene contributes negatively to freezing tolerance but positively to salt tolerance in *Arabidopsis*. J. Plant Physiol. *222,* 67–78.

Chen, J., Yu, F., Liu, Y., Du, C., Li, X., Zhu, S., Wang, X., and Lan, W. (2016). FERONIA interacts with ABI2-type phosphatases to facilitate signaling cross-talk between abscisic acid and RALF peptide in *Arabidopsis*. Proc. Natl. Acad. Sci. USA. *113(37)*, 5519–5527.

Chun, J.P., and Huber, D.J. (1998). Polygalacturonase-mediated solubilization and depolymerization of pectic polymers in tomato fruit cell walls. Regulation by pH and ionic conditions. Plant Physiol, *117,* 1293-1299

Clough, S.J., and Bent, A.F. (1998) Floral dip: a simplified method for Agrobacterium-mediated transformation of *Arabidopsis thaliana*. Plant J. 16, 735–743

Coen, E., and Kennaway, R. (2018). Early shaping of a leaf. Nat. Plants.*4*, 618-619.

Conde, A., Chaves, M.M., and Gerós, H. (2011). Membrane transport, sensing and signaling in plant adaptation to environmental stress. Plant Cell Physiol. *52*, 1583–1602.

Cosgrove, D.J., (2014). Re-constructing our models of cellulose and primary cell wall assembly. Cur.

Opinion Plant Bio. *22C,* 122–131.

Cosgrove, D.J. (2015). Plant cell wall extensibility: connecting plant cell growth with cell wall structure, mechanics, and the action of wall-modifying enzymes. J. Exp. Bot. *62*, 463–476.

Crasnier, M., Moustacas, a M., and Ricard, J. (1985). Electrostatic effects and calcium ion concentration as modulators of acid phosphatase bound to plant cell walls. Eur. J. Biochem. *151*, 187–190.

Crombie, H.J., Chengappa, S., Jarman, C., Sidebottom, C., and Reid, J.S.G. (2002). Molecular characterisation of a xyloglucan oligosaccharide-acting α-D- xylosidase from nasturtium (*Tropaeolum majus* L.) cotyledons that resembles plant apoplastic α-D-glucosidases. Planta. *214,* 406–413.

da Silva, J.A.L., Gonc¸alves, M.P., and Rao, M.A. (1995). Kinetics and thermal behaviour of the structure formation process in HMP/sucrose gelation. Int. J. Biol. Macromol. *17(1)*, 25–32.

Deslauriers, S.D., and Larsen, P.B. (2010). FERONIA is a key modulator of brassinosteroid and ethylene responsiveness in *Arabidopsis* hypocotyls. Mol. Plant. *3,* 626–640.

Doblas, V.G., Gonneau, M., and Höfte, H. (2018). Cell wall integrity signaling in plants: Malectin-domain kinases and lessons from other kingdoms. The Cell Surface *3,* 1-11.

Downie, B., Dirk, L.M.A., Hadfield, K.A., Wilkins, T.A., Bennett, A.B., and Bradford, K.J. (1998). A gel diffusion assay for quantification of pectin methylesterase activity. Anal. Biochem. 264, 149–157.

Du, S., Qu, L.J., and Xiao, J. (2018). Crystal structures of the extracellular domains of the CrRLK1L receptor-like kinases ANXUR1 and ANXUR2. Protein. Sci. *27*, 886–892.

Duan, Q., Kita, D., Johnson, E. A., Aggarwal, M., and Cheung A, Y., (2014). Reactive oxygen species mediate pollen tube rupture to release sperm for fertilization in *Arabidopsis*. Nat. Commun. *5,* 3129.

Duan, Q., Kita, D., Johnson, E.A., Aggarwal, M., Gates, L., Wu, H.M., and Cheung, A.Y. (2014). Reactive oxygen species mediate pollen tube rupture to release sperm for fertilization in *Arabidopsis*. Nat. Commun. *5*, 3129.

Duan. Q., Kita. D., Li. C., Cheung. A.Y., and Wu. H.M. (2010). FERONIA receptor-like kinase regulates RHO GTPase signaling of root hair development. Proc. Natl. Acad. Sci. USA. *107(41)*, 17821–17826.

Gilroy, S., Fricker, M.D., Read, N.D., Trewavas, A.J. (1990). Fluorescence ratio imaging and photometry of calcium in living plant cells. J. R. Microsc. Soc. *1,* 475–478.

Escobar-Restrepo, J.M., Huck, N., Kessler, S., Gagliardini, V., Gheyselinck, J., and Grossniklaus U., (2007). The FERONIA receptor-like kinase mediates male-female interactions during pollen tube reception. Science. *317(5838),* 656–660.

Fasano, J.M., Swanson, S.J., Blancaflor, E.B., Dowd, P.E., Kao, T.H., and Gilroy, S. (2001). Changes in root cap pH are required for the gravity response of the *Arabidopsis* root. Plant Cel. *13,* 907–921.

Feijó, J.A., Sainhas, J., Hackett, G.R., Kunkel, J.G., and Hepler, P.K. (1999). Growing pollen tubes possess a constitutive alkaline band in the clear zone and a growth-dependent acidic tip. J. Cell Biol. *144*, 483–496.

Felle, H.H. (1998). The apoplastic pH of the Zea mays root cortex as measured with pH-sensitive microelectrodes: aspects of regulation. J. Exp. Bot. *49,* 987–995.

Felle, H.H., and Hanstein, S. (2002). The apoplastic pH of the substomatal cavity of *Vicia faba* leaves and its regulation responding to different stress factors. J. Exp. Bot. *53*, 73–82.

Felle, H.H., and Hepler, K.P. (1997). The cytosolic Ca^{2+} concentration gradient of *Sinapis alba* root hairs as revealed by CA^{2+}-selective microelectrode tests and fura-dextran imaging. Plant Physiol. *114*, 39–45.

Felle, H.H., Kondorosi, É., Kondorosi, Á., and Schultze, M. (1996). Rapid alkalinization in alfalfa root hairs in response to rhizobial lipochitooligosaccharide signals. Plant J. *10*, 295–301.

Felle, H.H., Waller, F., Molitor, A., and Kogel, K.H. (2009). The mycorrhiza fungus *Piriformospora indica* induces fast root-surface pH signaling and primes systemic alkalinization of the leaf apoplast upon powdery mildew infection. Mol. Plant. Microbe. Interact. *22,* 1179–1185.

Fendrych, M., Leung, J., and Friml, J. (2016). TIR1/AFB-Aux/IAA auxin perception mediates rapid cell wall acidification and growth of *Arabidopsis* hypocotyls. eLife *5*, 1–18.

Feng, W., Kita, D., Peaucelle, A., and Wu, H. (2018). The FERONIA receptor kinase maintains cell-wall integrity during salt stress through Ca^{2+} signaling. Curr. Bio. *28,* 1–10.

Franck, C.M., Westermann, J., and Boisson-Dernier, A. (2018). Plant malectin-like receptor kinases: from cell wall integrity to immunity and beyond. Annu. Rev. Plant Biol. *69,*1–28.

Fry, S. C. (1998). Oxidative scission of plant cell wall polysaccharides by ascorbate-induced hydroxyl radicals. Biochem. J. *332,* 507–515.

Fry, S.C., Smith, Rachel.C., Renwick, K. F., Martin, D.J., Hodge, S.K., and Matthews, K.J. (1992). Xyloglucan endotransglycosylase, a new wall-loosening enzyme activity from plants. Biochem. J. *282,* 821–828.

Fu, J.T., Rao, and M.A. (2001). Rheology and structure development during gelation of low-methoxyl pectin gels: The effect of sucrose. Food Hydrocoll. *15(1)*, 93–100.

Gao, D., Knight, M.R., Trewavas, A.J., Sattelmacher, B., and Plieth, C., (2004). Self-reporting *Arabidopsis* expressing pH and Ca^{2+} indicators unveil ion dynamics in the cytoplasm and in the apoplast under abiotic stress. Plant. Physiol. *134,* 898–908.

Ge, Z., Bergoncii, T., Zhao, Y., Du, S., Hou, S., Huang, Q., Lai, L., Moura, D.S., Gu, H., Cheung, A.Y., et al. (2017). *Arabidopsis* pollen tube integrity and sperm release are regulated by RALF-mediated signaling. Science. *1600*, 1596–1600.

Geilfus, C., Mühling, K.H., Kaiser, H., and Plieth, C. (2014). Bacterially produced Pt-GFP as ratiometric dual-excitation sensor for in planta mapping of leaf apoplastic pH in intact *Avena sativa* and *Vicia faba*. Plant. Methods. *10:*31.

Geilfus, C.M. (2017). The pH of the apoplast: dynamic factor with functional impact under stress. Mol. Plant. *10*, 1371–1386.

Geitmann, A., and Parre, E. (2004). The local cytomechanical properties of growing pollen tubes correspond to the axial distribution of structural cellular elements. Sex. Plant. Reprod. *17,* 9–16.

Gendre, D., McFarlane, H.E., Johnson, E., Mouille, G., Sjodin, A., Oh. J., Levesque-Tremblay. G., Watanabe, Y., Samuels, L., and Bhalerao, R.P. (2013). Trans-Golgi network localized ECHIDNA/Ypt interacting protein complex is required for the secretion of cell wall polysaccharides in *Arabidopsis*. Plant Cell. *25,* 2633–2646.

Gevaudant, F., Duby, G., vonstedingk, E., Zhao, R., Morsomme, P., and Boutry, M. (2007). Expression of a constitutively activated plasma membrane H^+-ATPase alters plant development and increases salt tolerance. Plant. Physiol. *144,* 1763–1776.

Gigli, J., Garnier, C., and Piazza, L. (2009). Rheological behaviour of low-methoxyl pectin gels over an extended frequency window. Food. Hydrocolloids, *23(5)*, 1406–1412.

Gilsenan, P.M., Richardson, R.K., and Morris, E.R. (2000). Thermally reversible acid-induced gelation of low-methoxy pectin. Carbohydr. Polym. *41*, 339–349.

Gjetting, S.K., Ytting, C.K., Schulz, A., and Fuglsang, A.T. (2012). Live imaging of intra- and extracellular pH in plants using pHusion, a novel genetically encoded biosensor. J. Exp. Bot. *63*, 3207–3218.

Gonneau, M., Desprez, T., Martin, M., Doblas., V.G., Bacete, L., Miart, F. et al. (2018). Receptor kinase THESEUS1 is a Rapid Alkalinization Factor 34 receptor in *Arabidopsis*. Curr. Bio. *28,*1-7.

González-Fontes, A., Navarro-Gochicoa, M.T., Ceacero, C.J., Herrera-Rodríguez, M.B., Camacho-Cristóbal, J.J., and Rexach, J. (2017). Understanding calcium transport and signaling, and its use efficiency in vascular plants (Elsevier Inc.). Plant Macronutrient Use Efficiency. 165-180.

Grignon, C., and Sentenac, H. (1991). pH and ionic conditions in the apoplast. Annu. Rev. Plant. Biol. *42,* 103–128.

Guimarães, G.C., Coelho Júnior, M.C., and Garcia Rojas, E.E. (2009). Density and kinematic viscosity of pectin aqueous solution. J. Chemi. Engineering. Data. *54(2)*, 662–667.

Guo, H., Li, L., Ye, H., Yu, X., Algreen, A., and Yin, Y. (2009). Three related receptor-like kinases are required for optimal cell elongation in *Arabidopsis thaliana*. Proc. Natl. Acad. Sci. USA. *106(18)*, 7648–7653.

Guzel Deger, A., Scherzer, S., Nuhkat, M., Kedzierska, J., Kollist, H., Brosche, M., Unyayar, S., Boudsocq, M., Hedrich, R., and Roelfsema, M.R.G. (2015). Guard cell SLAC1-type anion channels mediate flagellin-induced stomatal closure. New Phytol. *208*, 162–173.

Harholt, J., Suttangkakul, A., and Vibe Scheller, H. (2010). Biosynthesis of pectin. Plant Physiol. *153(2)*, 384-95.

Haruta, M., and Sussman, M.R. (2012). The effect of a genetically reduced plasma membrane proton motive force on vegetative growth of *Arabidopsis*. Plant Physiol. *158*, 1158–1171.

Haruta, M., Burch, H.L., Nelson, R.B., Barrett Wilt, G., Kline, K.G., Mohsin, S.B., Young, J.C., Otegui, M.S., and Sussman, M.R. (2010). Molecular characterization of mutant Arabidopsis plants with reduced plasma membrane proton pump activity. J. Biol. Chem. *285,* 17918–17929.

Haruta, M., Sabat, G., Stecker, K., Minkoff, B.B., and Sussman, M.R. (2014). A peptide hormone and its receptor protein kinase regulate plant cell expansion. Science. *343(6169),* 408–411.

Haughn, G.W, and Western, T.L. (2012). *Arabidopsis* seed coat mucilage is a specialized cell wall that can be used as a model for genetic analysis of plant cell wall structure and function. Front. Plant. Sci. *3,* 64.

Hayashi, Y., Takahashi, K., Inoue, S.I., and Kinoshita, T. (2014). Abscisic acid suppresses hypocotyl elongation by dephosphorylating plasma membrane H^+-ATPase in arabidopsis thaliana. Plant Cel. Physiol. *55*, 845–853.

Hedrich, R., Busch, H., and Raschke, K. (1990). Ca^{2+} and nucleotide dependent regulation of voltage dependent anion channels in the plasma membrane of guard cells. EMBO. J. *9*, 3889–92.

Herrman, A., and Felle, H.H. (1995). Tip growth in root hair cells of *Sinapis alba L*: significance of internal and external Ca^{2+} and pH. New Phytol. *129*, 523–533.

Herron, S.R., Benen, J.A.E., Scavetta, R.D., Visser, J., and Jurnak, F. (2000). Structure and function of pectic enzymes : virulence factors of plant pathogens. Proc. Natl. Acad. Sci. USA. *97(16)*, 8762–8769.

Hocq, L., Pelloux, J., and Lefebvre, V. (2016). Connecting homogalacturonan-type pectin remodeling to acid growth. Trends Plant Sci. *22(1)*, 20–29.

Hocq, L., Sénéchal, F., Lefebvre, V., Lehner, A., Domon, J., Mollet, J., Dehors, J., Pageau, K., Marcelo, P., Guérineau, F., et al. (2017). Combined experimental and computational approaches reveal distinct pH dependence of pectin. Plant Physiol. *173*, 1075–1093.

Hoffmann, B., and Kosegarten, H. (1995). FITC-dextran for measuring apoplast pH and apoplastic pH gradients between various cell types in sunflower leaves. Plant Physiol. *95*, 327–335.

Holdaway-Clarke, T.L. Feijo, J. A., Hacket, G. R., Kunkel, J, G., and Hepler, P.K., (1997). Pollen tube growth and the intracellular cytosolic calcium gradient oscillate in phase while extracellular calcium influx is delayed. Plant Cell. *9(11)*, 1999–2010.

Hrmova, M., and Fincher, G.B. (2001). Structure-function relationships of beta-D-glucan endo- and exohydrolases from higher plants. Plant Mol. Biol. *47,* 73-91

Huffaker, A., Pearce, G., and Ryan, C.A. (2006). An endogenous peptide signal in *Arabidopsis* activates components of the innate immune response. Proc. Natl. Acad. Sci. USA. *103*, 10098–10103.

Ishii, T. (1997). O-acetylated oligosaccharides from pectins of potato tuber cell walls. Plant Physiol. *113*, 1265–1272.

Javed, M.T., Lindberg, S., and Greger, M., (2014). Cellular proton dynamics in *Elodea canadensis* leaves induced by cadmium. Plant Physiol. Biochem. *77,* 15-22.

Jia, W., and Davies, W.J. (2007). Modification of leaf apoplastic pH in relation to stomatal sensitivity to root-sourced abscisic acid signals. Plant Physiol. *143,* 68–77.

Kanczewska, J., Marco, S., Vandermeeren, C., Maudoux, O., Rigaud, J.-L., and Boutry, M. (2005). Activation of the plant plasma membrane H^+-ATPase by phosphorylation and binding of 14-3-3 proteins converts a dimer into a hexamer. Proc. Natl. Acad. Sci. USA. *102*, 11675–11680.

Kars, I., Krooshof, G.H., Wagemakers, L., Joosten, R., Benen, J.A., and van Kan, J.A. (2005). Necrotizing activity of five *Botrytis cinerea* endopolygalacturonases produced in *Pichia pastoris*. Plant J. *43,* 213–225

Kars, I., Krooshof, G.H., Wagemakers, L., Joosten, R., Benen, J.A.E., Kan, J.A.L. Van, and Group, F.G. (2005). Necrotizing activity of five *Botrytis cinerea* endopolygalacturonases produced in *Pichia pastoris*. *43(2):* 213–225.

Kastner, H., and Senge, B. (2012). Food hydrocolloids structure formation in sugar containing pectin gels influence of Ca^{2+} on the gelation of low-methoxylated pectin at acidic pH. Food Hydrocoll. *27*, 42–49.

Kim, S.J., and Brandizzi, F. (2014). The plant secretory pathway: an essential factory for building the plant cell wall. Plant Cel. Phyiol. *55(4)*, 687–693.

Kim, S.J., Held, M.A., Zemelis, S., Wilkerson, C., and Brandizzi, F. (2015). CGR2 and CGR3 have critical overlapping roles in pectin methylesterification and plant growth in *Arabidopsis thaliana*. Plant J. *82,* 208–220.

Klavons, J.A., and Bennett, R.D. (1986). Determination of methanol using alcohol oxidase and its application to methyl ester content of pectins. J. Agric. Food Chem. *34,* 597–599.

Kneen, M., Farinas, J., Li, Y., and Verkman, A.S., (1998). Green fluorescent protein as a noninvasive intracellular pH indicator. Biophys. J. *74,* 1591–1599.

Kohorn, B.D., and Kohorn, S.L. (2012). The cell wall-associated kinases, WAKs, as pectin receptors. Front. Plant Sci. *3*, 1–5.

Krupkova, E., Immerzeel, P., Pauly, M., and Schmulling, T. (2007). The tumorous shoot development gene of *Arabidopsis* encoding a putative methyltransferase is required for cell adhesion and coordinated plant development. Plant. J. *50*:735–75.

Kurkdjian, A., and Guern, J. (1989). Intracellular pH: measurement and importance in cell activity.

Lagarde, D., Basset, M., Lepetit, M., Conejero, G., Gaymard, F., Astruc, S., and Grignon., C. (1996). Tissue-specific expression of *Arabidopsis* AKT1 gene is consistent with a role in K^+ nutrition. Plant. J. *9,* 195–203.

Lalonde, S., Boles, E., Hellmann, H., Hellmenn, H., Barker, L., Patrick, J.W., Frommer, W,B., and Ward, J.M., (1999). The dual function of sugar carriers: transport and sugar sensing. Plant Cel. *11,* 707–726.

Lampropoulos, A., Sutikovic, Z., Wenzl, C., Maegele, I., Lohmann, J.U., and Forner, J. (2013).

GreenGate - A novel, versatile, and efficient cloning system for plant transgenesis. PLoS One 8.

Lampugnani, E.R., Khan, G.A., Somssich, M., and Persson, S. (2018). Building a plant cell wall at a glance. J. Cel. Sci. *131,* 1-6.

Lefebvre, B., Arango, M., Oufattole, M., Crouzet, J., Purnelle, B., and Boutry, M. (2005). Identification of a *Nicotiana plumbaginifolia* plasma membrane H^+-ATPase gene expressed in the pollen tube. Plant. Mol. Bio. *58,* 775-787.

Legland, D., Arganda-Carreras, I., and Andrey, P. (2016). MorphoLibJ: Integrated library and plugins for mathematical morphology with ImageJ. Bioinformatics *32,* 3532–3534.

Levesque-Tremblay, G., Müller, K., Mansfield, S.D., Haughn, G.W. (2015). HIGHLY METHYL ESTERIFIED SEEDS is a pectin methyl esterase involved in embryo development. Plant Physiol. 167, 725–737

Li, C., Wu, H., and Cheung, A.Y. (2016). FERONIA and her pals: functions and mechanisms. Plant Physiol. *171*, 2379–2392.

Li, C., Yeh, F.L., Cheung, A.Y., Duan, Q., Kita, D., Liu, M.C., Maman, J., Luu, E.J., Wu, B.W., Gates, L., et al. (2015). Glycosylphosphatidylinositol-anchored proteins as chaperones and co-receptors for FERONIA receptor kinase signaling in *Arabidopsis*. eLife *4*, 1–21.

Li, X., Leck, C., Sun, L., Hede, T., Tu, Y., and Agren, H. (2013). Cross-linked polysaccharide assemblies in marine gels: An atomistic simulation. J. Phys. Chem. Lett. *4*, 2637–2642.

Li, Z.C., and Bush, D.R. (1990). pH-dependent amino acid transport into plasma membrane vesicles isolated from sugar beet leaves: I. Evidence for carrier-mediated, electrogenic flux through multiple transport systems. Plant Physiol. *94,* 268–77.

Lin, D., Lopez-Sanchez, P., and Gidley, M.J. (2015). Binding of arabinan or galactan during cellulose synthesis is extensive and reversible. Carbohydr. Polym. *126*, 108–121.

Lin, W.W., Tang, W.X., Anderson, C.T., Yang, Z.B. (2018). FERONIA's sensing of cell wall pectin activates ROP GTPase signaling in *Arabidopsis*. bioRxiv. doi: http://dx.doi.org/10.1101/269647

Linder, B., and Raschke, K. (1992). A slow anion channel in guard cells, activating at large hyperpolarization, may be principal for stomatal closing. FEBS. Lett. *313,* 27–30.

Lionetti, V., Fabri, E., De Caroli, M., Hansen, A.R., Willats, W.G.T., Piro, G., Bellincampi, D. (2017). Three pectin methylesterase inhibitors protect cell wall integrity for *Arabidopsis* immunity to *Botrytis*. Plant Physiol. *173*, 1844–1863.

Lionetti, V., Raiola, A., Camardella, L., Giovane, A., Obel, N., Pauly, M., Favaron, F., Cervone, F., and Bellincampi, D. (2007). Overexpression of Pectin Methylesterase Inhibitors in Arabidopsis Restricts Fungal Infection by *Botrytis cinerea*. Plant Physiol. *143,* 1871-1880.

Lovy-wheeler, A., Kunkel, J.G., Allwood, E.G., Hussey, P.J., and Hepler, P.K. (2006). Oscillatory increases in alkalinity anticipate growth and may regulate actin dynamics in pollen tubes of Lily. Plant

Cell *18*, 2182–2193.

Malhó, R., Read, N.D., Trewavaqb, A.J., Pais, M.S., Vegetal, D.D.B., Lisboa, F.D.C., Vasconcelos, R.E., and Bloco, C. (1995). Calcium channel activity during pollen tube growth and reorientation. Plant Cell *7*, 1173–1184.

Mansel, B.W., Chu, C.Y., Leis, A., Hemar, Y., Chen, H.L., Lundin, L., and Williams, M.A.K. (2015). Zooming in: Structural investigations of rheologically characterized hydrogen-bonded low-methoxyl pectin networks. Biomacromolecules. *16(10)*, 3209–3216.

Mao, D., Yu, F., Li, J., Van de Poel, B, Tan, D., Li, J., Liu, Y., Li, X., Dong, M., Chen, L., Li, D., and Luan, S., (2015). FERONIA receptor kinase interacts with S-adenosylmethionine synthetase and suppresses S-adenosylmethionine production and ethylene biosynthesis in *Arabidopsis*. Plant Cell Environ. *38,* 2566–74.

Maris, A., Kaewthai, N., Eklof, J.M., Miller, J.G., Brumer, H., Fry, S.C., Verbelen, J.P., and Vissenberg, K. (2011). Differences in enzymic properties of five recombinant xyloglucan endotransglucosylase/hydrolase (XTH) proteins of *Arabidopsis thaliana*. J. Exp. Bot. *62,* 261–271.

Marschner, H., Romheld, V., and Ossenberg-Neuhaus, H. (1982). Rapid method for measuring changes in pH and reducing processes along roots of intact plants. Z. Pflanzen physiol. *105*, 407–416.

Martinière, A., Desbrosses, G., Sentenac, H., and Paris, N. (2013). Development and properties of genetically encoded pH sensors in plants. Front. Plant Sci. *4*, 1–6.

Martinière, A., Gibrat, R., Sentenac, H., Dumont, X., Gaillard, I., and Paris, N. (2018). Uncovering pH at both sides of the root plasma membrane interface using noninvasive imaging. Proc. Natl. Acad. Sci. USA. *115(25),* 6488-6493.

Masachis, S., Segorbe, D., Turrà, D., Leon-Ruiz, M., Fürst, U., El Ghalid, M., Leonard, G., López-Berges, M.S., Richards, T.A., Felix, G., et al. (2016). A fungal pathogen secretes plant alkalinizing peptides to increase infection. Nat. Microbiol. *1*, 16043.

Master, E.R., Rudsander, U.J., Zhou, W., Henriksson, H., Divne, C., Denman, S., Wilson, D.B., and Teeri, T.T. (2004). Recombinant Expression and Enzymatic Characterization of PttCel9A, a KOR Homologue from *Populus tremula* x *tremuloides*. Biochemi. *9,* 10080–10089.

McFarlane, H.E., Watanabe, Y., Gendre, D., Carruthers, K., Levesque-Tremblay, G., Haughn, G.W., Bhalerao, R.P., and Samuels, L. (2013). Cell wall polysaccharides are mislocalized to the Vacuole in *echidna* mutants. Plant. Cell. Physiol. *54,* 1867–1880.

Mckenna, S.T., Kunkel, J.G., Bosch, M., Rounds, C.M., Vidali, L., Winship, L.J., and Hepler, P.K. (2009). Exocytosis precedes and predicts the increase in growth in oscillating pollen tubes. Plant Cell. *21*, 3026–3040.

McLachlan, D.H., Lan, J., Geilfus, C.M., Dodd, A.N., Larson, T., Baker, A., Horak, H., Kollist, H., He, Z., Graham, I., and Hetherington, A, M., (2016). The breakdown of stored triacylglycerols is required

during light-induced stomatal opening. Curr. Biol. *26,* 707–712.

McQueen-Mason, S., and Cosgrove, D. J. (1994). Disruption of hydrogen bonding between plant cell wall polymers by proteins that induce wall extension. Proc. Natl Acad. Sci. USA. *91,* 6574–6578.

McQueen-Mason, S., Durachko, D. M. and Cosgrove, D. J. (1992). Two endogenous proteins that induce cell wall expansion in plants. Plant Cell. *4,* 1425–1433.

Mecchia, M.A., Santos-fernandez, G., Duss, N.N., Somoza, S.C., Boisson-dernier, A., Gagliardini, V., Martínez-bernardini, A., Fabrice, T.N., Ringli, C., Muschietti, J.P., et al. (2017). RALF4/19 peptides interact with LRX proteins to control pollen tube growth in *Arabidopsis*. Science *358*, 1600–1603.

Grossmann, G., Guo, W.J., Ehrhardt, D.W., Frommer, W.B., Sit, R.V., Quake, S.R., and Meier, M. (2011). The RootChip : An Integrated Microfluidic Chip for Plant Science. Plant Cell. 23, 4234–4240.

Merlot, S., Leonhardt, N., Fenzi, F., Valon, C., Costa, M., Piette, L., Vavasseur, A., Genty, B., Boivin, K., Muller, A., Giraudat. J., and Leung, J., (2007). Constitutive activation of a plasma membrane H^+-ATPase prevents abscisic acid-mediated stomatal closure. EMBO. J. *26,* 3216–3226.

Messerli, M.A., and Robinson, K.R. (1998). Cytoplasmic acidification and current influx follow growth pulses of Lilium longiflorum pollen tubes. Plant J. *16*, 87–91.

Messerli, M.A., Creton, R., Jaffe, L.F., and Robinson, K.R. (2000). Periodic increases in elongation rate precede increases in cytosolic Ca^{2+} during pollen tube growth. Dev. Biol. *222*, 84–98.

Messerli, M.A., Danuser, G., and Robinson, K.R. (1999). Pulsatile influxes of H^+, K^+ and Ca^{2+} lag growth pulses of *Lilium longiflorum* pollen tubes. *1509*, 1497–1509.

Mierczynska, J., Cybulska, J., Sołowiej, B., and Zdunek, A. (2015). Effect of Ca^{2+}, Fe^{2+} and Mg^{2+} on rheological properties of new food matrix made of modified cell wall polysaccharides from apple. Carbohydr. Polym. *133*, 547–555.

Mølhøj, M., Ulvskov, P., and Degan, F.D. (2001). Characterization of a Functional Soluble Form of a Heterologously Expressed in *Pichia pastoris.* Plant Physiol. *127,* 674–684.

Monshausen, G.B., Bibikova, T.N., Messerli, M.A., Shi, C., and Gilroy, S. (2007). Oscillations in extracellular pH and reactive oxygen species modulate tip growth of *Arabidopsis* root hairs. Proc. Natl. Acad. Sci. USA. *104*, 20996–21001.

Monshausen, G.B., Bibikova, T.N., Weisenseel, M.H., and Gilroy, S. (2009). Ca^{2+} regulates reactive oxygen species production and pH during mechanosensing in *Arabidopsis* roots. Plant Cell. *21*, 2341–2356.

Monshausen, G.B., and Gilroy, S. (2009), Feeling green: mechanosensing in plants. Trends Cell Biol. *19,* 228–235.

Morato do Canto, A., Ceciliato, P.H.O., Ribeiro, B., Ortiz Morea, F.A., Franco Garcia, A.A., Silva-Filho, M.C., and Moura, D.S. (2014). Biological activity of nine recombinant AtRALF peptides: Implications for their perception and function in *Arabidopsis*. Plant Physiol. Biochem. *75*, 45–54.

Morsomme, P., and Boutry, M., (2000). The plant plasma membrane H^+-ATPase: structure, function and regulation. Biochimica et Biophysica Acta. *1465,* 1-16

Moustacas, A., Nari, J., Noat, G., Diamantidis, G., Woudstra, M., and Ricard, J. (1986). Electrostatic effects and the dynamics of enzyme reactions at the surface of plant cells. *202*, 199–202.

Moustacas, A.M., Nari, J., Borel, M., Noat, G., and Ricard, J. (1991). Pectin methylesterase, metal ions and plant cell-wall extension. The role of metal ions in plant cell-wall extension. Biochem. J. *279*, 351–354.

Müller, K., Levesque-Tremblay, G., Bartels, S., Weitbrecht, K., Wormit, A., Usadel, B., Haughn, G., and Kermode, A.R. (2013). Demethylesterification of cell wall pectins in Arabidopsis plays a role in seed germination. Plant Physiol. *161,* 305-316.

Nari, J., Noat, G., and Ricard, J. (1991). Pectin methylesterase, metal ions and plant cell-wall extension. Hydrolysis of pectin by plant cell-wall pectin methylesterase. Biochem. J. *279 (2)*, 343–350.

Nari, J., Noat, G., Diamantidis, G., Woudstra, M., and Ricard, J. (1986). Electrostatic effects and the dynamics of enzyme reactions at the surface of plant cells. *202*, 199–202.

Ngo, Q.A., Vogler, H., Lituiev, D.S., Nestorova, A., and Grossniklaus, U. (2014). A calcium dialog mediated by the FERONIA signal transduction pathway controls plant sperm delivery. Dev. Cell *29*, 491–500.

Ngouémazong, D.E., Jolie, R.P., Cardinaels, R., Fraeye, I., Van Loey, A., Moldenaers, P., and Hendrickx, M. (2012). Stiffness of Ca^{2+}-pectin gels: Combined effects of degree and pattern of methylesterification for various Ca^{2+} concentrations. Carbohydr Res. *348*, 69–76.

Nieves-Cordones, M., Alemán, F., Martínez, V., and Rubio, F. (2014). K^+ uptake in plant roots: the systems involved, their regulation and parallels in other organisms. J. Plant Physiol. *171*, 688–695.

Nogata,Y., Ohta, H., and Voragen, A.G.J. (1993). Polygalacturonase in strawberry fruit. Phytochemistry, *34,* 617-620

O'Neill, M. A., and York, W. S. (2013). The composition and structure of primary cell walls. Rose JKC, editor. The Plant Cell Wall. Blackwell Publishers, Oxford, pp 1–54.

Oakenfull, D., and Scott, A. (1984). Hydrophobic interaction in the gelation of high methoxyl pectins. J. Food. Sci. *49(4)*, 1093–1098.

Okazaki,Y., and Tazawa, M. (1990). Calcium ion and turgor regulation in plant cells. J. Membrane. Biol. *114*, 189-194.

Pacheco-Villalobos D, Diaz-Moreno, S.M., van der Schuren, A., Tamaki, T., Kang, Y.H., Gujas, B., et al. (2016). The effects of high steady state auxin levels on root cell elongation in *brachypodium*. Plant Cell *28,*1009–1024.

Parre, E., and Geitmann, A. (2005). Pectin and the role of the physical properties of the cell wall in pollen tube growth of *Solanum chacoense*. Planta. *220*, 582–592.

Pathak, N. and Sanwal G.G. (1998). Multiple forms of polygalacturonase from banana fruits. Phytochemistry, *48,* 249-255.

Pearce, G., Moura, D.S., Stratmann, J., and Ryan, C.A. (2001). RALF, a 5-kDa ubiquitous polypeptide in plants, arrests root growth and development. Proc. Natl Acad. Sci. USA. *98*, 12843–12847.

Pearce, G., Yamaguchi, Y., Munske, G., and Ryan, C.A. (2010). Structure-activity studies of RALF, rapid alkalinization factor, reveal an essential YISY-motif. Peptides *31*, 1973–1977.

Peaucelle, A., Braybrook, S.A., Guillou, L. Le, Bron, E., and Kuhlemeier, C. (2011). Report Pectin-induced changes in cell wall mechanics underlie organ initiation in *Arabidopsis.* Curr. Biol. *21(20),* 1720–1726.

Peaucelle, A., Louvet, R., Johansen, J.N. Hofte, H., Laufs, P., Pelloux, J., and Mouille, G., (2008). *Arabidopsis* phyllotaxis is controlled by the methyl-esterification status of cell-wall pectins. Curr. Biol. *18(24),* 1943–1948.

Peaucelle, A., Wightman, R., and Hofte, H. (2015). The control of growth symmetry breaking in the *Arabidopsis* hypocotyl. Curr. Biol. *25*, 1746–1752.

Pelletier, S., Van Orden, J., Wolf, S., Vissenberg, K., Delacourt, J., Ndong, Y.A., Pelloux, J., Bischoff, V., Urbain, A., Mouille, G., et al. (2010). A role for pectin de-methylesterification in a developmentally regulated growth acceleration in dark-grown *Arabidopsis* hypocotyls. New Phytol. *188,* 726–739.

Pelloux, J., Rusterucci, C., and Mellerowicz, E.J. (2007). New insights into pectin methylesterase structure and function. Trends Plant Sci. *12,* 267–277.

Phyo, P., Wang, T., Kiemle, S.N., Neill, H.O., Pingali, V., Hong, M., and Cosgrove, D.J. (2017). Gradients in wall mechanics and polysaccharides along growing inflorescence stems. Plant Physiol. *175*, 1593–1607.

Phyo, P., Wang, T., Kiemle, S.N., Neill, H.O., Pingali, V., Hong, M., and Cosgrove, D.J. (2017). Gradients in wall mechanics and polysaccharides along growing inflorescence stems. Plant Physiol. *175*, 1593–1607.

Pierson, E.S., Miller, D.D., Callaham, D.A., van Aken, J., Hackett, G., and Hepler, P.K. (1996). Tip-localized calcium entry fluctuates during pollen tube growth. Dev. Biol. *174*, 160–173.

Pitann, B., Kranz, T., and Muhling, K.H. (2009). The apoplastic pH and its significance in adaptation to salinity in maize (*Zea mays L.*): comparison of fluorescence microscopy and pH-sensitive microelectrodes. Plant. Sci. *176,* 497–504.

Pollack, G.H, (2001). Cells, gels and the engines of life. Ebner and Sons Publishers.

Popper., Z.A., and Fry., S.C., (2005). Widespread occurrence of a covalent linkage between xyloglucan and acidic polysaccharides in suspension-cultured angiosperm Cells. Annals. Bot. *96*, 91-99.

Purugganan, M. M., Braam, J. and Fry, S. C. (1997). The *Arabidopsis* TCH4 xyloglucan endotransglycosylase. Substrate specificity, pH optimum, and cold tolerance. Plant Physiol. **115**, 181–

190.

Qi, JY., Wu, Bb., Feng, Sl., Lu, Sq., Guan, Cm., Zhang, X., and Jiao, Yl., (2017). Mechanical regulation of organ asymmetry in leaves. Nat. Plants. *3*, 724-733.

Ricard, J., and Noat, G. (1986). Electrostatic effects and the dynamics of enzyme reactions at the surface of plant cells. Euro. J. Biochem. *202*, 199–202.

Ricard, J., Noat, G., and Nari, J. (1984). pH-induced co-operative effects in hysteretic enzymes: 1. A theoretical model of a new type of co-operative behaviour controlled by pH. Eur. J. Biochem. *145,* 311–317.

Ricard, J., Noat, G., and Nari, J. (1984). pH-induced co-operative effects in hysteretic enzymes: A theoretical model of a new type of co-operative behaviour controlled by pH. Eur. J. Biochem. *145*, 311–317.

Ricard, J., Noat, G., Crasnier, M., and Job, D. (1981). Ionic control of immobilized enzymes. Kinetics of acid phophatase bound to plant cell walls. Biochem. J. *195*, 357–367.

Röckel, N., Wolf, S., Kost, B., Rausch, T., and Greiner, S. (2008). Elaborate spatial patterning of cell-wall PME and PMEI at the pollen tube tip involves PMEI endocytosis, and reflects the distribution of esterified and de-esterified pectins. Plant J. *53*, 133-143.

Rojas, E.R., Hotton, S., and Dumais, J. (2011). Chemically mediated mechanical expansion of the pollen tube cell wall. Biophysi. J. *101,* 1844-1853.

Rounds, C.M., Lubeck, E., Hepler, P.K., and Winship, L.J. (2011). Propidium iodide competes with Ca^{2+} to label pectin in pollen tubes and *Arabidopsis* root hairs. Plant. Physiol. *157*, 175–187.

Rubio, F., Santa Maria, G.E., and Rodríguez Navarro, A. (2000). Cloning of Arabidopsis and barley cDNAs encoding HAK potassium transporters in root and shoot cells. Physiol. Plant. *109,* 34–43.

Rubio, L., Garcıa, D., Garcıa-Sanchez, M.J., Xavier Niell, F., Felle, H.H., and Fernandez, J.A. (2017). Direct uptake of HCO_3^- in the marine angiosperm *Posidonia oceanica* (L.) Delile driven by a plasma membrane H^+ economy. Plant Cell Environ. https://doi.org/10.1111/ pce.13057.

Saez-Aguayo, S., Ralet, M.C., Berger, A., Botran, L., Ropartz, D., Marion-Poll, A., and North, H.M. (2013). PECTIN METHYLESTERASE INHIBITOR6 promotes Arabidopsis mucilage release by limiting methylesterification of homogalacturonan in seed coat epidermal cells. Plant Cell. *25,* 308–323

Sampedro, J., Sieiro, C., Revilla, G., Gonzalez-Villa, T., and Zarra, I. (2001). Cloning and expression pattern of a gene encoding an α-xylosidase active against xyloglucan oligosaccharides from *Arabidopsis*. Plant Physiol. *126,* 910–920.

Sampedro, J., Valdivia, E.R., Fraga, P., Iglesias, N., Revilla, G., and Zarra, I. (2017). Soluble and membrane-bound beta-glucosidases are involved in trimming the xyloglucan backbone. Plant Physiol, *173,* 1017-1030.

Schallus, T., Jaeckh, C., Feher, K., Palma, A.S., Liu, Y., et al. (2008). Malectin: a novel carbohydrate-

binding protein of the endoplasmic reticulum and a candidate player in the early steps of protein N-glycosylation. Mol. Biol. Cell *19,* 3404-14.

Schlosser, A., and Volkmer-Engert, R. (2003). Volatile polydimethylcyclosiloxanes in the ambient laboratory air identified as source of extreme background signals in nanoelectrospray mass spectrometry. J. Mass Spectrom. *38,* 523–525.

Schopfer, P. (2001). Hydroxyl radical-induced cell-wall loosening *in vitro* and *in vivo*: implications for the control of elongation growth. Plant. J. *28*, 679–688.

Schulte, A., Lorenzen, I., Böttcher, M., and Plieth, C. (2006). A novel fluorescent pH probe for expression in plants. Plant Methods. *2*, 1–13.

Schoenaers, S., Balcerowicz, D., Breen, G., Hill, K., Zdanio, M., Mouille, G., Holman, T.J., Oh, J., Wilson, M.H., Nikonorova, N., et al. (2018). The auxin-regulated CrRLK1L kinase ERULUS controls cell wall composition during root hair tip growth. Curr. Biol. *28,* 722–732.

Sénéchal, F., Enfant, M.L., Domon, J., Rosiau, E., Crépeau, M., Surcouf, O., Bonnin, E., Jamet, E., Kihara, D., Lerouge, P., et al. (2015). Tuning of pectin methylesterification: PECTIN METHYLESTERASE INHIBITOR 7 MODULATES THE PROCESSIVE ACTIVITY OF CO-EXPRESSED PECTIN METHYLESTERASE 3 IN A pH-DEPENDENT MANNER. Planta. *290*, 23320–23335.

Sénéchal, F., Habrylo, O., Hocq, L., Domon, J., Marcelo, P., Lefebvre, V., Pelloux, J., and Mercadante, D. (2017). Structural and dynamical characterization of the pH-dependence of the pectin methylesterase-pectin methylesterase inhibitor complex. J. Biol. Chem. *292*, 21538–21547.

Sentenac, H., Bonneaud, N., Minet, M., Lacroute, F., Salmon, J.M., Gaymard, F., and Grignon., C. (1992). Cloning and expression in yeast of a plant potassium ion transport system. Science. *256*, 663–5.

Shen, J., Zeng, Y., Zhuang, X., Sun, L., Yao, X., Pimpl, P., and Jiang, L. (2013). Organelle pH in the *Arabidopsis* endomembrane system. Mol. Plant. *6*, 1419–1437.

Shevchenko, A., Wilm, M., Vorm, O., and Mann, M. (1996). Mass spectrometric sequencing of proteins from silver-stained polyacrylamide gels. Anal. Chem. *68,* 850–858.

Shi, D., Ren, A., Tang, X., Qi, G., Xu, Z., Chai, G., Hu, R., Zhou, G., Kong, Y. (2018). MYB52 negatively regulates pectin demethylesterification in seed coat mucilage. Plant Physiol.*176,* 2737–2749.

Shih, H.W., Miller, N.D., Dai, C., Spalding, E.P., and Monshausen, G.B. (2014). The receptor-like kinase FERONIA is required for mechanical signal transduction in *Arabidopsis* seedlings. Curr. Biol. *24*, 1887–1892.

Sorek, N., Szemenyei, H., Sorek, H., Landers, A., Knight, H., Bauer, S., Wemmer, D.E., and Somerville, C.R. (2015). Identification of MEDIATOR16 as the Arabidopsis COBRA suppressor MONGOOSE1. Proc. Natl. Acad. Sci. USA. *112*, 16048–16053

Spartz, A.K., Ren, H., Park, M.Y., Grandt, K.N., Lee, S.H., Murphy, A.S., Sussman, M.R., Overvoorde,

P.J., and Gray, W.M. (2014). SAUR Inhibition of PP2C-D phosphatases activates plasma membrane H^+-ATPases to promote cell expansion in *Arabidopsis*. Plant Cell. *26*, 2129–2142.

Stegmann, M., Monaghan, J., Smakowska-Luzan, E., Rovenich, H., Lehner, A., Holton, N., Belkhadir, Y., and Zipfel, C. (2017). The receptor kinase FER is a RALF-regulated scaffold controlling plant immune signaling. Science. *355*, 287–289.

Sterling, J.D., Quigley, H.F., Orellana, A., and Mohnen, D. (2001). The catalytic site of the pectin biosynthetic enzyme alpha-1, 4-galacturonosyltransferase is located in the lumen of the Golgi. Plant. Physiol. *127*, 360–371.

Strom, A., Ribelles, P., Lundin, L., Norton, I., Morris, E. R., and Williams, M. A. K., (2007). Influence of pectin fine structure on the mechanical properties of calcium–pectin and acid–pectin gels Biomacromolecules. *8*, 2668–74.

Suárez, C., Zienkiewicz, A., Castro, A. J., Zienkiewicz, K., Majewska-Sawka, A., and Rodríguez-García, M. I. (2013). Cellular localization and levels of pectins and arabinogalactan proteins in olive (*Olea europaea L.*) pistil tissues during development: Implications for pollen–pistil interaction. Planta. *237(1)*, 305–319.

Sussman, M.R. (1994). Molecular analysis of proteins in the plant plasma membrane. Annu. Rev. Plant Physiol. Plant. Mol. Biol. *45*, 211–234.

Swanson, S.J., Choi, W.-G., Chanoca, A., and Gilroy, S. (2011). *In vivo* Imaging of Ca^{2+}, pH, and reactive oxygen species using fluorescent probes in plants. Annu. Rev. Plant Biol. *62*, 273–297.

Sze, H., Padmanaban, S., Cellier, F., Honys, D., Cheng, N.H., Bock, K.W., Conéjéro, G., Li, X., Twell, D., and Ward, J.M. (2004). Expression patterns of a novel AtCHX gene family highlight potential roles in osmotic adjustment and K^+ homeostasis in pollen development. Plant Physiol. *136,* 2532–2547.

Taiz L, and Zeiger E. 2010. Plant physiology, 5th edn. Sunderland, MA: Sinauer Associates.

Takahashi, K., Hayashi, K. I., and Kinoshita, T. (2012). Auxin activates the plasma membrane H^+-ATPase by phosphorylation during hypocotyl elongation in *Arabidopsis*. Plant Physiol. *159*, 632–641.

Tan, L., Eberhard, S., Pattathil, S., Warder, C., Glushka, J., Yuan, C., Hao, Z., Zhu, X., Avci, U., Miller, J.S., et al. (2013). An Arabidopsis cell wall proteoglycan consists of pectin and arabinoxylan covalently linked to an arabinogalactan protein. Plant Cell. *25*, 270–287.

Talmadge, K. W., Keegstra, K., Bauer, W. D., and Albersheim, P. (1973). The structure of plant cell walls. I. The macromolecular components of the walls of suspension-cultured sycamore cells with a detailed analysis of the pectic polysaccharides. Plant physiol. *51,*158-173.

Tanaka, T. (1981). Gels. Scientific American. 124–138.

Thakur, B.R., Singh, R.K., Handa, A.K., and Rao, M.A. (1997). Chemistry and uses of pectin - A review. Crit. Rev. Food Sci. Nutr. *37(1)*, 47–73.

Thibault, J.F., and Ralet, M.C. (2003). Physico-chemical properties of pectins in the cell walls and after

extraction. In F. Voragen, H. Schols, R. Visser (Eds.), Advances in pectin and pectinase research (pp. 91–105). Netherlands, Dordrecht: Springer.

Tian, G.W., Chen, M.H., Zaltsman, A., and Citovsky, V. (2006). Pollen-specific pectin methylesterase involved in pollen tube growth. Dev. Biol. *294*, 83–91.

Valentin, R., Cerclier, C., Geneix, N., AguieBeghin, V., and Gaillard, C. (2010). Elaboration of extensin-pectin thin film model of primary plant cell wall. Langmuir. *26,* 9891–98.

Verlent, I., Van Loey, A., Smout, C., Duvetter, T., and Hendrickx. M.E. (2004). Purified tomato polygalacturonase activity during thermal and high pressure treatment. Biotechnol and Bioengin, *86,* 63-71.

Vincent, R.R., and Williams, M.A.K. (2009). Microrheological investigations give insights into the microstructure and functionality of pectin gels. Carbohydr. Res. *344*, 1863–1871.

Vincken, J. P., Schols, H. A., Oomen, R.J.F.J., McCann, M.C., Ulvskov, P., Voragen, A.G.J. et al. (2003). If homogalacturonan were a side chain of rhamnogalacturonan I. Implications for cell wall architecture. Plant Physiol. 132, 1781–1789.

Vitart, V., Baxter, I., Doerner, P., and Harper, J.F. (2001). Evidence for a role in growth and salt resistance of a plasma membrane H^+- ATPase in the root endodermis. Plant. J. *27,* 191–201.

Voxeur, A., and Höfte, H. (2018). Cell wall integrity signaling in plants: To grow or not to grow that' s the question. Glycobiology. *26*, 950–960.

Wang, Y., and Wu, W.H. (2017). Regulation of potassium transport and signaling in plants. Curr. Opin. Plant Biol. *39*, 123–128.

Weisenseel, M.H., Dorn, A., and Jaffe, L.F. (1979). Natural H^+ currents traverse growing roots and root hairs of barley (*Hordeum vulgare L.*). Plant. Physiol. *64*, 512–518.

Willats, W. T., McCartney, L., Mackie, W., and Knox, J. P. (2001). Pectin: cell biology and prospects for functional analysis. In N. C. Carpita, M. Campbell, & M. Tierney (Eds.), Plant cell walls (pp. 9–27). Netherlands: Springer.

Wolf, S., Mouille, G., and Pelloux, J. (2009). Homogalacturonan methyl-esterification and plant development. Mol. Plant. *2*, 851–860.

Wolf, S., Mravec, J., Greiner, S., and Mouille, G. (2012). Plant cell wall homeostasis is mediated by brassinosteroid feedback signalling. Curr. Biol. *22*: 1730-7.

Wolf, S., van der Does, D., Ladwig, F., Sticht, C., Kolbeck, A., Schürholz, A.-K., Augustin, S., Keinath, N., Rausch, T., Greiner, S., et al. (2014). A receptor-like protein mediates the response to pectin modification by activating brassinosteroid signaling. Proc. Natl. Acad. Sci. USA. *111*, 15261–15266.

Wu, J., Kurten, E.L., Monshausen, G., Hummel, G.M., Gilroy, S., and Baldwin, I.T. (2007). NaRALF, a peptide signal essential for the regulation of root hair tip apoplastic pH in *Nicotiana attenuata*, is required for root hair development and plant growth in native soils. Plant J. *52*, 877–890.

Yu, F., Li, J., Huang, Y., Liu, L, Li, D, P., and Luan, S., (2014). FERONIA receptor kinase controls seed size in *Arabidopsis thaliana*. Mol. Plant *7(5),* 920–922.

Yu, F., Qian, L., Nibau, C., Duan, Q., Kita, D., Levasseur, K., Li, X., Lu, C., Li, H., Hou, C., and Luan, S., (2012). FERONIA receptor kinase pathway suppresses abscisic acid signaling in *Arabidopsis* by activating ABI2 phosphatase. Proc. Natl. Acad. Sci. USA. *109*, 14693–14698.

Yu, Q., Tang, C., and Kuo, J. (2000). A critical review on methods to measure apoplastic pH in plants. Plant Soil. *219*, 29–40.

Zablackis, E., Huang, J., Muller, B., Darvill, A.G., Albersheim, P. (1995). Characterization of the cell-wall polysaccharides of Arabidopsis thaliana leaves. Plant Physiol. *107,*1129–1138.

Zhang, H., Qu, X., Bao, C., Khurana, P., Wang, Q., Xie, Y., Zheng, Y., Chen, N., Blanchoin, L., Staiger, C.J., and Huang., S.J., (2010). *Arabidopsis* VILLIN5, an actin filament bundling and severing protein, is necessary for normal pollen tube growth. Plant Cell. *22*, 2749–2767.

Zhao, J., Cheng, N.H., Motes, C.M., Blancaflor, E.B., Moore, M., Gonzales, N., Padmanaban, S., Sze, H., Ward, J.M., and Hirschi, K.D. (2008). AtCHX13 is a plasma membrane K^+ transporter. Plant. Physiol. *148,* 796–807.

Zhao, J., Li, P., Motes, C.M., Park, S., and Hirschi, K.D. (2015). CHX14 is a plasma membrane K-efflux transporter that regulates K^+ redistribution in *Arabidopsis thaliana*. Plant Cell Environ. *38,* 2223–2238.

Zhao, Q., Ren, Y.R., Wang, Q.J., Yao, Y.X., You, C.X., and Hao, Y.J. (2016). Overexpression of MdbHLH104 gene enhances the tolerance to iron deficiency in apple. Plant. Biotechnol. J. *14*, 1633–1645.

Zhu, C., Yang, N., Ma, X., Li, G., Qian, M., Ng, D., Xia, K., and Gan, L. (2015). Plasma membrane H^+-ATPase is involved in methyl jasmonate-induced root hair formation in lettuce (*Lactuca sativa* L.) seedlings. Plant Cell Rep. *34*, 1025–1036.

Zhu, J.K. (2003). Regulation of ion homeostasis under salt stress. Curr. Opin. Plant Biol. *6*, 441–445.

Zimmermann, M.R., Maischak, H., Mithofer, A., Boland, W., and Felle, H.H. (2009). System potentials, a novel electrical long-distance apoplastic signal in plants, induced by wounding. Plant Physiol. *149*, 1593–1600.

Zimmermann, M.R., Mithofer, A., Will, T., Felle, H.H., and Furch, A.C. (2016). Herbivore-triggered electrophysiological reactions: candidates for systemic signals in higher plants and the challenge of their identification. Plant Physiol. *170*, 2407–2419.

ANNEXES

Supplementary Data 1. Macro used in this study.

(1) /**This Macro creates a ratiometric image of plant cell walls stained with a ratiometric dye. It takes a two-channel image, applies smoothing to reduce noise, applies a Laplacian of Gaussian filter to shape out cell walls, creates a Mask, uses it to cut out the cell walls, shows the image in a defined LUT to emphasize the different ratios. This Macro needs the FeatureJ Plugin of Fiji. Best use the Fiji Life-Line version, 2015 December 22 without updates. Two images are created as an output, the original ratiometric image and an RGB using the predifined scaling

If you reset Brightness and Contrast in the ratiometric image, you have to redo the Calibration Bar (Analyze/Tools/Calibration Bar)

**/

```
//Choose Channel used for Segmentation
Segment=2;
//Predefine the amount of Gaussian Blur
Blur=1.5;
//Predefine the sigma for the Laplace Filter (higher value for bigger structures)
Laplace=1;
//Predefine the Radius for Background subtraction
Backsubtract=20;
//Minimum and Maximum Value for output Image
min=0;
max=1;
inDir = getDirectory("Choose a Source Folder with images to process.");
outDir = getDirectory("Choose a Destination Folder.");
fileList = getFileList(inDir);
fileListOut = getFileList(outDir);
setBatchMode(false);
roiManager("Reset");
run("Close All");
for (i=0; i<fileList.length; i++) {
```

```
        showProgress(i+1, fileList.length);
        file = inDir + fileList[i];
        inFileCut = lengthOf(file)-4;
        inFile=substring(file,0,inFileCut);
        outFileTemp = outDir + fileList[i];
        cut=lengthOf(outFileTemp)-4;
        outFile=substring(outFileTemp,0,cut);
        print("Outfile= "+outFile);
        run("Bio-Formats Importer", "open=" + file + " color_mode=Default view=[Hyperstack]
stack_order=XYCZT");
        TitleImage=getTitle();
        cut=lengthOf(TitleImage)-4;
        TitleImage2=substring(TitleImage,0,cut);
        run("32-bit");
        run("Gaussian Blur...", "sigma="+Blur+" stack");
//Split into single Images
        selectWindow(TitleImage);
        setSlice(1);
        run("Duplicate...", "title=Ch1");
        selectWindow(TitleImage);
        run("Next Slice [>]");
        run("Duplicate...", "title=Ch2");
        selectWindow(TitleImage);
        run("Close");
//Filter for Segmentation
        selectWindow("Ch"+Segment);
        run("Duplicate...", " ");
        rename("Backsubtract");
        run("Subtract Background...", "rolling="+Backsubtract+"");
        run("FeatureJ Laplacian", "compute smoothing="+Laplace+"");
        setAutoThreshold("Triangle");
        waitForUser("Set manual Threshold, then click OK");
        setOption("BlackBackground", true);
```

```
        run("Convert to Mask");
        run("32-bit");
        setAutoThreshold("Default dark");
        run("NaN Background");
        run("Divide...", "value=255");
//Create Ratiometric Image
        imageCalculator("Divide create 32-bit", "Ch2","Ch1");
        imageCalculator("Multiply create 32-bit", "Result of Ch2","Backsubtract Laplacian");
//Set Display and save
        run("Green Fire Blue");
        run("Select None");
        setMinAndMax(min, max);
        run("Calibration Bar...", "location=[U Right] fill=White label=Black number=5 decimal=3 font=12
zoom=1 overlay");
        saveAs("Tiff", outFile+"_ratio");
        setMinAndMax(min, max);
        run("Calibration Bar...", "location=[U Right] fill=White label=Black number=5 decimal=3 font=12
zoom=1");
        saveAs("Tiff", outFile+"_calibration");

        run("Close All");
}
```

(2) Raw data processing for apopHusion images

// Raw data processing is to split images,z project and merge images of the multipositional data, which has 4 z stacks and 4 channels. After this process, the merged images can be used to ratiometic and registration analyze.

```
run("Split Channels");
selectWindow("C3-example.tif");
run("Z Project...", "projection=[Average Intensity] all");
selectWindow("C1-example.tif");
run("Z Project...", "projection=[Average Intensity] all");
run("Merge Channels...", "c1=AVG_C1-example.tif c2=AVG_C3-example.tif create");
```

```
saveAs("Tiff", "/Users/xufan/Desktop/output/Merged.tif");
selectWindow("C1-example.tif");
close();
selectWindow("C3-example.tif");
close();
selectWindow("C4-example.tif");
close();
selectWindow("C2-example.tif");
close();
```

(3) Ratiometric analyse for apopHusion images

```
// Registration
selectWindow("Merged.tif");
run("Correct 3D drift", "channel=1 multi_time_scale sub_pixel only=0 lowest=1 highest=1");
saveAs("Tiff", "/Users/xufan/Desktop/output/registered time points.tif");
// Retiometrics analyze
run("Split Channels");
selectWindow("C2-registered time points.tif");
run("Duplicate...", "title=Ch2 duplicate");
selectWindow("C1-registered time points.tif");
run("Duplicate...", "title=Ch1 duplicate");
selectWindow("Ch2");
run("32-bit");
setAutoThreshold("Huang dark")
run("NaN Background", "stack");
waitForUser("Set manual threshold, then click OK")
imageCalculator("Divide create 32-bit stack", "Ch1","Ch2");
// Set display and save
selectWindow("Result of Ch1");
run("16 colors");
saveAs("Tiff", "/Users/xufan/Desktop/output/Result of Ch1.tif");
close();
```

```
selectWindow("Ch1");
close();
selectWindow("C1-registered time points.tif");
close();
close();
close();
```

Supplementary Data 2. Codon-optimized sequences of PMEI3 and PMEI5

>PMEI3

CTGCAGgaAGACATAACGGTGCTGAGGATATCGTTCACTCTTCTTGTGAGCACGCTTCTTAC
CCATCCTTGTGTGTTAGAACCTTGTCCTCTTACTCCGGTCCAACCATCACTAACAGAAGAGA
CTTGGCTCAGGCCGCTATCAAGATTTCTTTGTCTCACGCTCAATCCGCCGCTAAGAAGTTGG
CTGTTGTTAGAGACTCCGTCGGTAAGAAGAAGCAAGAGAAGGCTGCTTTGGTTGACTGCG
TTGAGATGATTGGTGACTCCGTTGACGAGTTGTCCAGAACCTTGGGTGTTTTGAAGCACTT
GAGAGTTTCTGGTGGTTCCGCCAAAGAATTCAGATGGCAAATGTCCAACGCTCAGACTTGG
GCTTCTGCTGCTTTGACTGATGACGACACTTGTCTGGATGGTTTCCAAGGTATGGACGACG
GTGAGATCAAGACTGAGGTTAAGCAGTGGATGACCAAGGTTGCTAGAGTTACTTCCAACGC
CTTGTACATGGTCAACCAGTTGGACGAGACTAGAGGTAAGCCACACGACGTTCACTTGttTC
TAGA

>PMEI5

CTGCAGgaATTCCAGCTAGAGACATCGACAAGCTGTGCAAAGAGACTACCGACGTTCCATT
CTGCTTGAAGTACTTGGGTACTGACCCAAGAATCCCAGCTGCTAGAGATTTGACCGACGTT
TTGTTGATCGCTATCACCCAGTCCAAGATGCAAGTTGACGATGCTACTACCCACATCGACAG
AGTCAGAAGAAAGTTCAACGGTCCACACGGTAGAAGAAGAATCGAGGTCTGTAAGACCAA
CTACGGTATCGCTTCTGCTAGATTCCACACTGCTTGGGAGTTGGGATTGCAAAAGTCTTTCT
GGGACGTTGAGAAGCTGGCCAGAATTGGAACTAACGCCGTTATCGACTGTGAGAACGTTT
GGAGAAGAGATGGTCCAATCCAGACTTCCCCACTGACCTTCTACAACATGAACGTGTTCAA
GCTGTCCGGTATCATCCTGCTGATCTTCAACAAGTTGGTTACTttTCTAGA

Résumé

Les pectines sont des polysaccharides abondants dans la paroi primaire et caractérisés par la présence d'acide galacturonique (GalA). Les pectines jouent un rôle clé dans le contrôle de la porosité de la paroi et aussi dans les mécanismes de régulation de la croissance et du développement de la plante. L'homogalacturonane (HG) constituant majeur des pectines, est un homopolymère α-1,4-GalA linéaire qui représente 20% des polysaccharides pariétaux. Ce polymère est sécrété sous forme méthylestérifiée et ne porte donc pas ou peu de charges. La déméthylestérification d'HG par des pectine méthylestérases (PMEs) fait apparaître des charges négatives ce qui a des conséquences importantes sur les propriétés physico-chimiques de la paroi, affectant des processus physiologiques et développementaux comme l'ouverture des stomates, l'initiation d'organes et la croissance cellulaire anisotrope. De nombreuses PME existent (69 isoformes chez *Arabidopsis thaliana*) qui peuvent être inhibées par des inhibiteurs protéiques (les « PME Inhibitors » ou PMEI) endogènes également représentés par de multiples isoformes (76 chez *Arabidopsis thaliana*). Cette abondance d'isoformes illustre la complexité de la régulation de la densité de charges dans la paroi. L'HG déméthylestérifiée peut former des liaisons Ca^{2+}-pectate qui peuvent rigidifier la paroi, mais des études récentes montrent que la déméthylestérification de l'HG peut également promouvoir une augmentation de l'élasticité de la paroi ainsi que la vitesse de l'expansion cellulaire à travers un mécanisme inconnu. Au cours de ma thèse je me suis interrogé sur ce paradoxe en étudiant le lien entre le métabolisme des pectines, le pH et l'extensibilité de la paroi. A cette fin, j'ai développé et utilisé des outils génétiques et pharmacologiques pour la manipulation *in vivo* de l'activité PME. J'ai généré des lignées permettant la surexpression inductible de deux PMEIs différents, mais qui malheureusement se sont avérés non fonctionnels. J'ai également produit une PMEI dans la levure *Pichia pastoris* afin d'étudier son activité *in vitro* et *in vivo*. Ainsi, j'ai pu observer que la protéine a une activité inhibitrice pH-dépendante sur un large éventail de PMEs *in vitro*. Par ailleurs, j'ai utilisé des senseurs ratiométriques pour la mesure du pH dans l'apoplaste de la cellule et j'ai contribué à générer des senseurs permettant de mesurer le pH dans des microdomaines au sein de la paroi. Enfin j'ai participé au développement de nouveaux outils permettant de maintenir les plantes dans des conditions optimales pour l'observation simultanée de la croissance et du pH

apoplastique dans la racine suite à un changement du milieu de culture. A l'aide de tous ces outils, j'ai ensuite étudié l'impact de la modification de l'activité PME sur le pH et la croissance cellulaire. D'abord, j'ai pu observer que le traitement avec un inhibiteur chimique de la PME, l'epigallocatechin gallate (EGCG) provoquait une inhibition de la croissance et une perte de l'anisotropie des cellules de la racine et que ces réponses étaient accompagnées d'une augmentation du pH apoplastique (pH^{Apo}) à priori indépendamment de l'activité de l'H^+-ATPase dans le plasmalemme. Par ailleurs, l'addition d'une PME dans le milieu de culture augmentait la croissance racinaire et réduisait le pH^{Apo}, tandis que l'addition d'un PMEI ralentissait la croissance et augmentait le pH^{Apo}. Enfin, l'induction de l'activité PME dans des plantes transgéniques provoquait également une diminution du pH^{Apo} dans la racine. En conclusion, mes résultats montrent que la déméthylesterification de l'HG peut induire une acidification de l'apoplaste et une augmentation de la croissance. Pour expliquer ce phénomène, je propose que des domaines anioniques générés par l'activité PME dans la paroi aient la capacité de séquestrer des protons. Cette acidification locale pourrait ensuite activer des facteurs de relâchement de la paroi, comme les expansines, entraînant ainsi une augmentation de la vitesse de croissance. En revanche, les résultats ne permettent pas d'exclure que la modification de l'HG active également des voies de signalisation affectant le pH^{Apo} et l'expansion cellulaire. Cette question fera l'objet d'études ultérieures.

université PARIS-SACLAY
ÉCOLE DOCTORALE
Sciences du végétal : du gène à l'écosystème

Titre : Le rôle du métabolisme des pectines dans le contrôle du pH et de la rhéologie de la paroi

Mots clés : pectine, paroi, pH, rhéologie, croissance

Résumé : La pectine, un composant de la matrice de la paroi primaire, joue un rôle dans le contrôle de la porosité de la paroi, l'élongation et l'adhésion cellulaire et est un facteur important dans le développement de la plante. Homogalacturonane (HG), le polymère pectique le plus abondant, est sécrété sous forme methylestérifiée et ne porte donc peu ou pas de charges négatives. La déméthylestérification d'HG par des pectine méthylestérases (PMEs) expose ensuite des charges négatives et a des conséquences importantes sur les propriétés mécaniques de la paroi, affectant des processus physiologiques et développementaux comme l'ouverture des stomates, l'initiation d'organes et la croissance cellulaire anisotropique. De multiples PME existent (chez Arabidopsis thaliana) qui peuvent être inhibées par des « PME inhibitors » (PMEIs) endogènes. L'HG déméthylestérifiée peut former des liaisons Ca^{2+}-pectate qui peuvent rigidifier la paroi, mais des études récentes montrent que la déméthylestérification de HG peut également promouvoir le relâchement de la paroi et l'expansion cellulaire à travers un mécanisme inconnu. Dans ma thèse j'ai adressé ce paradoxe en étudiant le lien entre le métabolisme des pectines, le pH et l'extensibilité de la paroi. A cette fin j'ai dévelopé et utilisé des outils génétiques et pharmacologiques pour la manipulation in vivo de l'activité PME. J'ai généré des lignées permettant la surexpression inductible de deux PMEIs différents, mais qui malheureusement s'avéraient non fonctionnelles. J'ai produit PMEI3 dans une levure ce qui m'a permis de montrer que la protéine a une activité inhibitrice pH-dépendante sur un large éventail de PMEs. Par ailleurs, j'ai utilisé et développé des senseurs ratiométriques pour la mesure du pH à la surface de la cellule. En dehors des senseurs existants, j'ai aussi essayé d'adresser les mêmes biosenseurs à la paroi. A l'aide de ces outils, j'ai ensuite étudié l'impact de la modification de l'activité PME sur le pH et la croissance cellulaire. J'ai pu observer qu'un inhibiteur chimique de la PME, l'(-)-epigallocatechin gallate (EGCG) entrainait une augmentation du pH apoplastique (pH^{Apo}) dans la racine, et ceci indépendamment de la H^+-ATPase ; une inhibition de la croissance et une perte de l'anisotropie des cellules. Par ailleurs, un traitement avec PMEI3 ralentissait la croissance et un apport de PME entrainait une réduction du pH^{Apo} et une augmentation de la croissance. Enfin, une induction de 24h de PMEI5 causait une réduction du pH^{Apo}, ce qui est en accord avec l'activation compensatoire d'autres PMEs suite à une signalisation liée eux brassinostéroide accrue décrit précédemment. En conclusion, nos résultats suggèrent que la démethylesterification des HG crée domaines anioniques qui peuvent séquestrer des protons ce qui pourrait activer localement des protéines qui stimulent le relâchement de la paroi avec un pH optimum acide entrainant une augmentation de la vitesse de croissance cellulaire.

Université Paris-Saclay
Espace Technologique / Immeuble Discovery
Route de l'Orme aux Merisiers RD 128 / 91190 Saint-Aubin, France

université PARIS-SACLAY | ÉCOLE DOCTORALE Sciences du végétal : du gène à l'écosystème

Title : The role of pectin metabolism in the control of cell wall pH and rheology

Keywords : pectin, cell wall, pH, rheology, growth

Abstract : Pectin, a matrix component in the primary cell wall, plays a role in controlling cell wall porosity, cell elongation and cell adhesion and constitutes an important factor in plant development. The demethylesterification of homogalacturonan (HG), the most abundant pectic polymer, has vast consequences on the mechanical properties of the cell wall, and affects developmental processes such as stomata opening, organ initiation and anisotropic cell growth. HG is selectively demethylesterified *in muro* by pectin methylesterases (PME), which in turn can be inhibited by endogenous PME inhibitor proteins (PMEIs). Demethylesterified HG is thought to form Ca^{2+}-pectate complexes, which contribute to wall stiffening, but recent evidence suggest that it can also promote cell wall loosening and expansion, through a so far unknown mechanism.

In this study I addressed this paradox by investigating the link between pectin metabolism, cell wall pH and extensibility. To this end I developed and used genetic and pharmacological tools for the *in vivo* manipulation of PME activity. I generated inducible overexpression lines for two distinct PMEIs, which unfortunately were not functional. I also produced PMEI3 from *Arabidopsis* in a yeast and showed that the protein displayed an inhibiting activity on a broad range of PMEs.

In addition, I developed and used tools to monitor the cell surface pH. In addition to using existing genetically-encoded ratiometric apoplastic pH sensors, I also tried to generate similar sensors targeted to the cell wall. Using these tools I then studied the impact of changes in pectin methylesterification on the cell wall pH and cell expansion. I discovered that a chemical inhibitor of PME, (-)-epigallocatechin gallate (EGCG), promoted an increase in apoplastic pH (pH^{Apo}) in root cells, independently from the inhibition of the H^+-ATPase, and triggered root growth inhibition and abnormal cell shape. Exogenous PMEI3 application also inhibited root growth. In addition, PME application caused a decrease in pH^{Apo} and enhanced root growth. Interestingly, long-term induction of PMEI5 could reduce pH^{Apo}, consistent with the previously described activation of brassinosteroid signaling causing a compensatory increase in PME activity. Together, my study provides evidence that HG demethylesterification leads to a decrease in pH^{Apo} and an increase in cell growth in the *Arabidopsis* root. Our results support the view that the negatively charged pectate can sequester protons and thus may contribute to the activation of cell wall loosening proteins and cell growth.

Université Paris-Saclay
Espace Technologique / Immeuble Discovery
Route de l'Orme aux Merisiers RD 128 / 91190 Saint-Aubin, France